SOLAR RADIATION CONTROL BY PYROLYTIC OXIDE THIN FILMS

by

Thomas R. Viverito

Dissertation submitted to the Graduate Faculty of the
Virginia Polytechnic Institute and State University
in partial fulfillment of the requirements for the degree of
MASTER OF SCIENCE
in
Ceramic Engineering

APPROVED:

L. H. Slack
L. H. Slack, Chairman

W C Hackler
W. C. Hackler

J J Brown Jr
J. J. Brown, Jr.

J. H. Steele, Jr.

October, 1974

Blacksburg, Virginia

ACKNOWLEDGMENTS

This author wishes to thank all those who have aided him in any way in the preparation of this thesis and in the research connected with it. Special thanks must go to Dr. Lyle H. Slack, Associate Professor of Ceramic Engineering at the Virginia Polytechnic Institute and State University for his never ending patience, encouraging advice and for reviewing the manuscript of this thesis.

The author would also like to thank Dr. William C. Hackler, Professor and Chairman of Ceramic Engineering, Dr. Jesse J. Brown, Jr., Associate Professor of Ceramic Engineering, and Dr. James H. Steele, Jr., Assistant Professor of Metallurgical Engineering for their many helpful suggestions and willingness to serve on the graduate committee.

Special thanks must go to ASG Industries, Kingsport, Tennessee. Without their generous financial assistance, this project could not have been undertaken. The author is thankful to Dr. Agett and Mr. Cook of the ASG Industries for their inspiring suggestions that contributed much to the direction of this research.

The author gratefully acknowledges Mr. Lee Roy Durden for aiding in the designing of the computer plot routine and Miss Lynn Shelton, Mrs. Teresa Belcher and Miss Nora Phillips for typing this manuscript.

The author would also like to extend his personal thanks to his colleagues Mr. Donald Griffin and Mr. Orville Steininger for their technical assistance and continuous enthusiasm.

Finally, to my parents and family, my heartiest thanks and deepest appreciation for making my education possible and for their everlasting love and encouragement.

TABLE OF CONTENTS

Page

III. EXPERIMENTS AND MEASUREMENTS

Page

V. DISCUSSION OF RESULTS

Page

APPENDIX E

ABSTRACT

LIST OF TABLES

LIST OF FIGURES

Figure Page

Figure Page

I. INTRODUCTION

Within the last decade, thin films for optical as well as electrical applications have been receiving much attention. Thin films economically yield desired properties that could never be achieved with regular plate glass. An ordinary sheet of glass can be transformed into an optical filter, a transparent thermal insulator, a solar collector, or into a highly conducting mass with thin films. With the growing concern for energy conservation, the glass industry has found it feasible to block out solar radiation from buildings to conserve electrical energy, resulting in the lower usage of air conditioning. At the present time, the films for this purpose are mainly metallic. Films of gold and copper exhibit excellent visible through near infrared reflection and absorption, but disadvantages such as instability to the weather and its elements, plus a high cost, deem it necessary to examine the stable, less expensive oxides.

Solar collectors made from glass, on the other hand, should not reflect solar energy but transmit it. However, it is important that the solar energy be trapped under the glass. Usually the solar energy is absorbed on a dark layer of painted metal. This surface becomes hot and emits long wavelength radiation. In this case, it is important that the glass transmits short wavelength solar energy, but reflects the long wavelength thermal energy being emitted from the heated surface. Once the heat has been entrapped between the glass and a black surface, then the thermal energy may be carried away to be used at another location.

The purpose of this thesis is to investigate with single and multilayered oxide thin films, those compositions and combinations that exhibit high reflectance and absorbance in this critical visible through the near infrared region of light wavelength (.3-2.5μ).(1) It is a major aim of this research to not only determine correct compositions, but to examine the crystal and band structures, in order to gain an understanding of the optical behavior of the coatings.

A prime practical objective of this research is to find an oxide which has the optical properties of gold. The following is a brief review of why metallic films have such high reflectances at solar wavelength. According to Fresnels equations, reflection, at least in the visible wavelengths, is dependent upon the film's index of refraction. The law governs less in the infrared region, since index of refraction usually decreases with increasing wavelengths.(2) A more basic question is why do metals have a high index of refraction or what do metals do to light to slow it down so, since index of refraction,

$$N = \frac{\text{Velocity Light in the Material}}{\text{Velocity Light in a Vacuum}} .$$

The key to this phenomenon is involved with the mobility and concentration of a metal's free electrons which interact with the light as it passes through the film. The reasonable oxides to investigate then are the transition metal oxides. With their unpaired 3d electrons and resulting high index of refraction, they are likely candidates for aesthetic coatings similar to the appearance of gold and with optical properties that are equally good. In order for an oxide film to have a high reflectance, it too must have a high concentration of free electrons. This can be accomplished by heavy doping. For this reason, this study includes oxides which contain large amounts of other oxides.

Oxide thin films with high solar reflectances are not the only ones of importance. Films with a high solar absorbance also have important practical applications. A thin film exhibiting a high absorption is a possible alternative for the screening of solar energy. This absorption has the disadvantage of heating the glass, thus causing it to become a thermal radiator. Stresses could also be induced into the glass, if the temperature reached significant levels. It is conceivable though that a system could be devised where there is a layer of insulating air between the glass with the absorbing film and another plate of glass (see Fig. 1).

With possible schemes such as this in mind, absorption will also be studied in this thesis.

There are four mechanisms for absorption on the atomic scale. They include (1) lattice absorption, (2) band gap transitions, (3) intra-atom transitions, and (4) charge transfer transitions. Lattice absorption arises from the transverse vibrations which occur in the lattice due to energy from light radiation. It primarily depends on the mean atomic spacing, which is directly related to the materials thermal expansion coefficient and temperature. Band gap transitions, where electrons obtain the energy to advance into the conductance band from the valence band, yield absorption also. This is why insulators such as Al_2O_3, which have a large band gap, are white. Semiconductors, on the other hand, have a low energy of activation for electrical conduction and usually have many energy levels; therefore, they are often

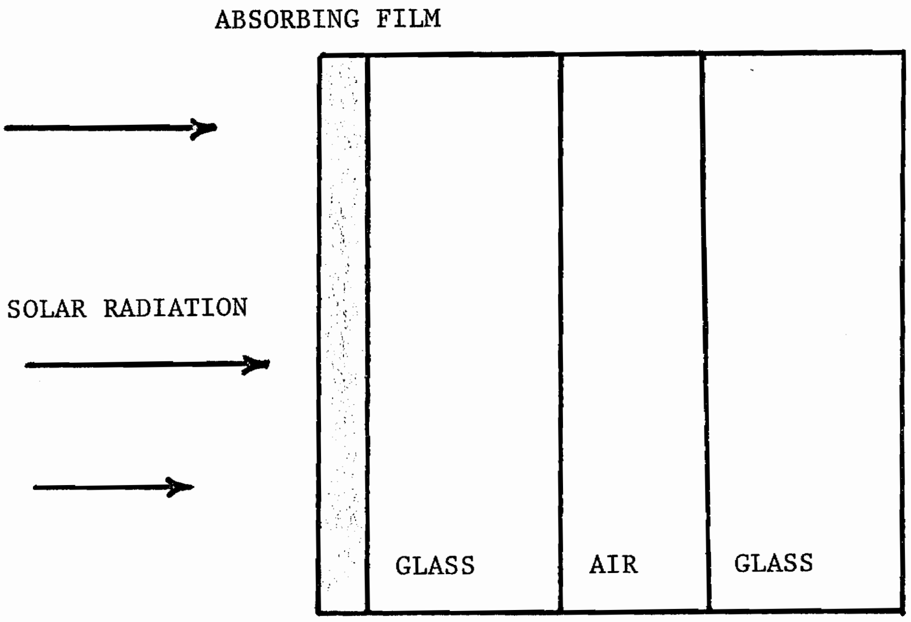

Figure 1. Solar Insulating Window Utilizing an Absorbing Thin Film.

black. This mechanism for absorption is especially significant in the near infrared - visible region of light energy. Intra-atom transitions, where electrons "jump" into energy levels which are unfilled in the same atom or ion, are the primary mechanisms for color in pigments and glasses. When an electron drops an energy level, a color is emitted. This selective absorption is especially prevalent in the rare earths, where there exists unfilled lower energy levels (the 4f), which are screened from the outer environment by filled 5P, 6S and 5d shells. The transition metal ions tend to produce color because their d-electrons are split in energy. Bloss(2) suggests that color arises in the transition metals because their electrons are held loosely in their outer shells and that they have the ability to adopt several valence states. Coordination is also important in the transition metal ions for specific colors. Co^{2+} produces a deep blue color in compounds in which it is tetrahedrally coordinated to four oxygen ions, but a pink color if octahedrally coordinated to six oxygen ions.(2) Atomic number, valence state, site radius, symmetry and coordination number all effect the intra-atom absorption bands. Color in the thin films studied in this research is of primary interest for commercial value. Absorption, due to charge-transfer transition, arises from the high energies such as that present in the ultraviolet. This mechanism involves the "jumping" of electrons from an anion to a cation or vice versa.

Crystals usually display sharp, sometimes intense absorption bands, whereas glasses exhibit broad smooth absorption bands.

Polycrystalline thin films are expected to exhibit absorption bands somehwere in between, probably more like those in a glass.

A wide range of optical properties are needed from thin films on glass. A considerable amount of information has been found on the bulk materials, but the relations of optical properties of oxide thin films to their compositions and methods of deposition are still largely unknown. It is the purpose of this thesis to relate the optical characteristics of oxide thin films to a number of parameters such as composition, method of deposition, sequentially deposited films, the composition of the gas used during the deposition process, annealing of the films after deposition, and the effect of the gas used.

With these objectives in mind, generalities relating optical behavior to the above parameters will be deduced.

II. LITERATURE REVIEW

In the literature, many authors have investigated one or more fields of interest concerning the optical and electrical properties of various thin films. This section reviews the scientific literature as it relates to:

(1) The electrical and optical properties of the bulk oxides and thin films of Cobalt, Iron, Titanium, Tin and Vanadium, the oxides studied in this thesis.

(2) Pyrolytic film deposition.

(3) The effects of oxidizing and reducing atmospheres on chemical reactions.

(4) Multilayered oxide films on glass.

(1) - (A) Bulk and Thin Film Co_3O_4

Very little has been reported concerning the optical and electrical properties of bulk Co_3O_4. This is probably due to the fact that it is not the stable phase of Cobalt. At 900°C, Co_3O_4 decomposes to CoO, the more common oxide(3). Takada et al.(3) grew crystals of Co_3O_4 by a chemical transport reaction. They noticed that Co_3O_4 has the normal spinel structure and is an antiferromagnetic substance. It was determined by Goodenough(4) that both CoO and Co_3O_4 are insulators with approximate resistivities of 10 Ωcm.

Kingery(5) reported that Co_3O_4 is amphoteric which means it can behave both as a p-type or n-type semiconductor. Co_3O_4 reduced to CoO is p-type. Co_3O_4 is black and handbook indices of refraction are not reported.

The thin film of Co_3O_4, on the other hand, has been receiving much attention, especially by the Russian scientists. As reported by Brekhovskikh and Borisova(6) in their literature review, ordinary window glass with a cobalt oxide film becomes heat protecting, since this coating does have a high reflectance and a selective transparency. Such glass is profitably distinguished from heat absorbing glass, since it does not become as heated and consequently is not as great a secondary source of radiation(7).

These films were produced by the pyrolytic decomposition of salt vapors at temperatures close to the softening-point of the glass. The high adhesion of the film to the glass, the mechanical strength and chemical resistance all lead to the assumption of a chemical bond to the substrate(8).

Botvinkin and Borisova(9) stated that sun-protective glass should possess a low radiation transmission in the spectral distribution range of the sun's radiation (Fig. 2). For health reasons the spectral characteristics of the glass should also correspond to the spectral distribution of the sensitivity of the eye to light; that is, maximum transluency of the yellow-green wavelength portions. An outstanding feature of the cobalt-oxide coating is that it has a transmission maximum in the yellow-green part of the spectrum(10).

Botvinkin and Borisova(9) prepared their films from cobalt acetate, $Co(C_2H_3O_2)_2\cdot 4H_2O$ - water, water-alcohol solutions. The thermal dissociation took place according to the equations:

$$Co(C_2H_3O_2)_2\cdot 4H_2O \rightleftarrows [Co(H_2O)_6] + 2\ (C_2H_3O_2) \longrightarrow$$

$$\xrightarrow[\text{glass surface}]{\text{at the}} \underset{\text{glass}}{\underset{\downarrow}{\underline{Co_xO_y}}} \quad + \quad 2CH_3\ COOH \uparrow$$

X-ray analysis showed that with a glass temperature of 550°-750°, the films form from colloidal Co_3O_4(9).

An investigation for the formation of cobalt oxide coatings on glass was made by Borisova and Botvinkin(11). They determined that films sprayed with cobalt acetate solutions in the limits 400°-800°C, form Co_3O_4, however, above 750°-800°C the Co_3O_4 undergoes partial dissociation to form CoO.

It was determined that water-alcohol solutions used for the application of cobalt oxide coatings have considerable drawbacks compared

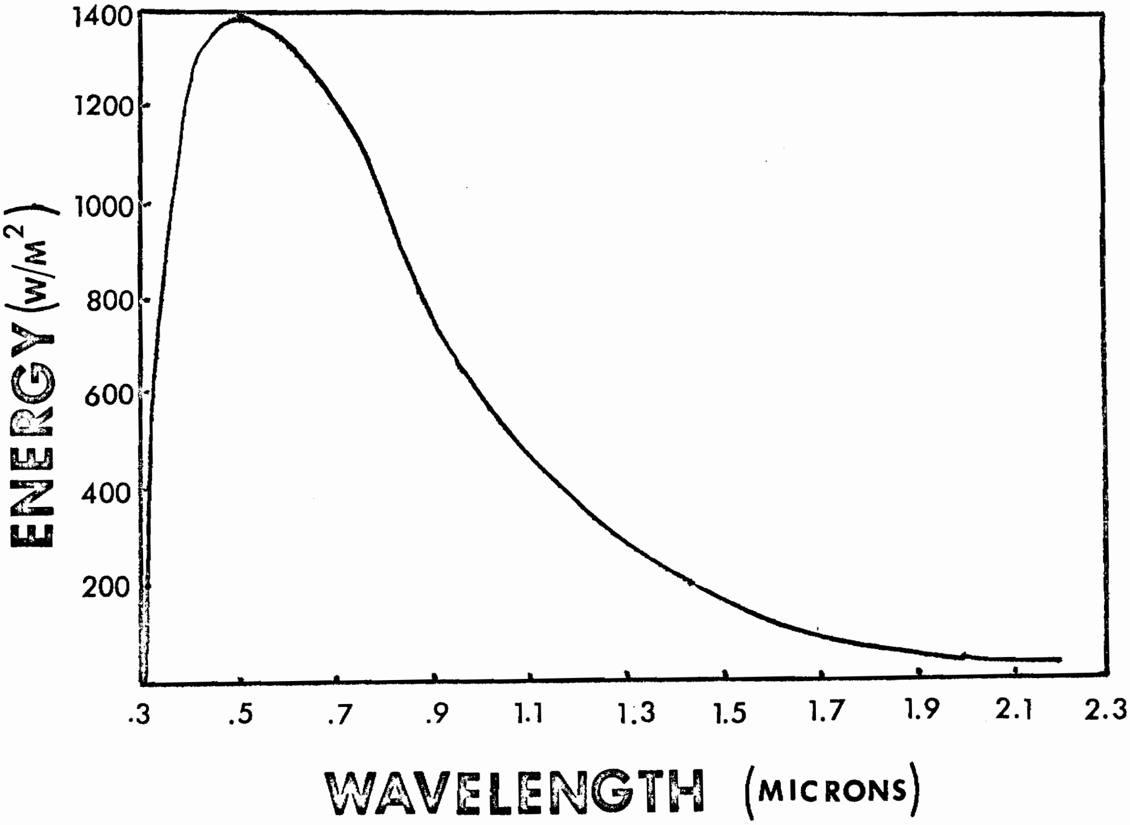

Figure 2. Average Spectral Distribution Range of the Sun's Radiation. (Vorob'eva and Bessonova (1))

with water solutions, since they reduce the useful consumption of the cobalt.

The structure of cobalt oxide films was studied by Borisova and Botvinkin(11). They compared X-ray and electron microscope studies. It occurred to them, that the structure of the coating is different than the structure of most colloids. The films are compared of distinct particles which are crystalline and have a crystalline lattice which is no different from the lattice of well formed crystals. However, they found that the coating on the whole is not ordered, its particles are chaotically arranged and are not always cohesive.

It was established that one of the peculiarities of Co_3O_4 coatings is that there is nearly a linear increase in reflectance with increasing film thickness up to a given value (0.10 - 0.12 μ), where a maximum is attained. Following that, there is a sharp drop in reflectance at greater film thickness. Rekant & Borisova(12,13) suggest that this peculiarity is caused by changes in the film macrostructure. Increase in reflectance is associated with the formation of a denser film, however, as the film thickness increases, excess of the film forming material results in a rougher surface which scatters light.

It was summarized by Rekant & Borisova(12,13) that the ability to reflect near-infrared radiation (0.7 - 2.2 μ) in the solar spectrum is particularly pronounced in films 0.075 - 0.150 μ thick. Evidently, the film thickness most effectively protects the glass from excessive absorption of solar energy (and consequently, from heating) while permitting a significant (up to 40%) transmission of visible light(12,13).

(B) Bulk and Thin Film Fe_2O_3

Bulk iron oxide occurs as three different phases; Wustite (FeO), magnetite (Fe_2O_3) and Hematite (Fe_2O_3). This discussion will be limited to α Fe_2O_3, since this is the oxide phase that exists when $FeCl_3 \cdot 6H_2O$ undergoes pyrolytic decomposition(14). Tannhauser(15) concluded that the Hematite phase of iron is insulating, that the phase is narrow and does not exhibit any significant Fe^{2+} and Fe^{3+} "hopping" conduction as does Fe_3O_4. Gardner _et al._(16) also studied the electrical properties of high purity polycrystalline α Fe_2O_3. They did concentrate on its high temperature behavior from 200°C to 1350°C and came to the conclusion that charge carriers were due to deviations from stoichiometry and to the electron transfer from an oxygen ion to a ferric ion. A value of 10^9 Ωcm for the resistivity of α Fe_2O_3 was reported by Verwey _et al._(17). Hackler(18) found that crystalline iron oxide films generally had lower electrical resistivities than amorphous films. This agreed well with the theory that impurities in amorphous semiconductors (Fe^{2+} ions, Fe^{3+} ions, or oxygen vacancies) have no effect on the resistivity, while in the crystalline phase the impurities contribute substantially to electrical conductivity.

Hematite occurs with an intense red color pointing to the fact that it absorbs much in the visible. Bulk α Fe_2O_3 has an index of refraction of 3.3(19), which is quite high.

The thin films of α Fe_2O_3 are of interest primarily because of their optical properties. Like the bulk oxide α Fe_2O_3 films(15,18) are insulators and possess little interest for electrical applications.

With this in mind, only the optical properties of α Fe_2O_3 thin films will be discussed.

Short-wave radiation from the sun is generally useful since it stimulates life. On the other hand, it is known that the ultraviolet rays destroy certain materials such as paper and paint. It was shown by Vorob'eva and Bessonova(14) that thin layers of iron oxide (Fe_2O_3) as a rule, have a weak transmission in the short wavelength region. Certain types completely hold back ultraviolet rays.

Iron-oxide films, like cobalt-oxide, have a very high transmission in the long wavelengths of the spectrum (0.75 - 2.5)(14). They are less transparent than cobalt oxide and hold back 50% or more of the radiation from the sun by absorbance.

The total integral reflection of solar energy by films of iron oxide was found to be less than 30% by Vorob'eva & Bessonova(14). Thin layers of iron oxide (1 μ) possess selective transmission bands in the visible spectrum(14), so when applied to ordinary glass, they can be used as light filters.

Vorob'eva & Bessonova(14) reported optical data for Fe_2O_3 - SnO_2 mixtures. It is worth noting that preceeding this research little has been done with the effects of composition mixtures on optical properties. Vorob'eva _et al_.(14) found that additions of tin, not more than 10%, scarcely changed the spectral characteristics of the coatings, but they do increase their thermal, mechanical and chemical resistance. More than 10% tin oxide destroyed the optical character. Coatings with large tin-oxide additions alter the transmission curves of Fe_2O_3 radically and they become similar to the curve for SnO_2 films.

Colors of the film varied from orange to a light green and coatings with more than 80% SnO_2 were colorless. One great advantage of SnO_2 - Fe_2O_3 films is that they have the power to sustain high-temperature heating in a reducing atmosphere(14).

(C) Bulk and Thin Film TiO_2

Titanium dioxide exists in two tetragonal structures, anatase and rutile, plus orthorhombic brookite. Rutile is the thermodynamically stable form at all temperatures. Anatase and brookite retain their structures until heated to fairly high temperatures, at which time they transform irreversibly to rutile. Temperatures for significant rates of conversion to rutile are 800°C - 1100°C for anatase and 700°C - 1300°C for brookite.(20,21)

According to Hollander(22) rutile single crystals exhibit a conductivity of about $10^{-13}\ \Omega^{-1}cm^{-1}$. The forbidden gap was reported as 3 ev by Baer(23). The cation Ti^{4+} has no outer d-electrons and is located at the center of its anion interstice. With no outer d-electrons, d-band conductivity cannot occur.

Non-stoichiometric rutile TiO_{2-x} is classified as a metal-excess, n-type semiconductor on the basis of experimental observations of both Grant(24) and Frederikse(25). TiO_{2-x} contains only a few anion vacancies and conductivity takes place via excitation to the antibonding S-P bands and a "hopping" of localized electrons(26). Some other investigators(27-29) explain this conduction with a defect model consisting of quasi-free electrons and titanium interstitials in one or more states of ionization. Blumenthal(26) went one step further and concluded that the non-stoichiometric effect structure of rutile can be rationalized in terms of quasi-free electrons and both triply and quadruply ionized titanium interstitials. In addition, they concluded that there is a contribution to electrical conduction due to impurity conduction or intrinsic conduction.

Stoichiometric TiO_2 as a thin film is an insulator with a high dielectric constant(30). Katsuta, Akahane and Yahagi(30) reported conductance as $2 \times 10^{-13}\ \Omega^{-1}cm^{-1}$. The activation energy was estimated as 0.5 ev in the region of high temperature and 0.5 ev in that of low temperature.

TiO_2 (anatase) has an index of refraction of 2.565(20), while (rutile) has an index of refraction equal to 2.75(31). The single crystal of rutile exhibits an absorption edge(32) at 0.41 μm (3.0 ev). TiO_2 is commonly utilized as an opacifier in glazes and enamels, since it has a high index of refraction enabling it to scatter light.

It can be seen from the following Table I that the crystal structure of TiO_2 films is controlled by the deposition process, along with this, refractive index and density are altered, thereby controlling optical properties.

Since TiO_2 (rutile) possesses a high index of refraction, it is surely a candidate for highly reflection coatings.

Fitzgibbons et al.(33) reported the optical transmission spectrum of a TiO_2 (anatase) film annealed 350°C in the visible wavelengths of light. They attribute maxima and minima above 0.35 μm to interference due to multiple internal reflection and the strong absorption peak at 0.32 μm (3.9 ev) to an electronic transition. Transmission in an amorphous TiO_2 film was also measured and similar results were obtained, except that the strong absorption peak was much broader,

TABLE I

Comparison of TiO_2 Films (Yokozawa et al.(32))

Author	Method	Structure	Refractive Index	Density
Haas(20)	Thermal oxidation of Evaporated Ti Metal Film 300-700°C	Rutile (Electron Diffraction)	2.70	-
Sakurai and Watanabe (21)	Thermal Decomposition of $Ti(C_3H_7O)_4$,$Ti(C_2H_5O)_4$ in vacuum >900°C	Rutile (X-Ray Diffraction)	-	4.22
Feursanger (34)	Hydrolysis of $TiCl_4$ >160°C	-	2.55	-
Yokozawa, Iwasa, and Teramoto (32)	Thermal Decomposition of $Ti(C_3H_7O)_4$ in N_2 410-750°C	Anatase (X-Ray Diffraction) (Electron Diffraction)	2.08-2.13	2.50-2.60
	Thermal Decomposition of $Ti(C_3H_7O)_4$ in $N_2 + O_2$ 320-540°C	"Amorphous" (X-Ray Diffraction) Anatase (Electron Diffraction)	2.00-2.05	2.40-2.49
Anatase	Single Crystal(32)		2.565	3.80-3.95
Rutile	Single Crystal(32)		2.75	4.26

although still centered at 0.32 μm. This agreed well with Maserjian(35) who also found an absorption peak at 0.32 μm with a rutile film. In contrast as mentioned before, single crystal rutile exhibits an absorption edge(32) at 0.41 μm (3.0 ev). The cause of this discrepancy between bulk single crystal and thin film TiO_2 is not known.

(D) Bulk and Thin Film SnO_2

A pure tin oxide crystal is a broad-band semiconductor (36,37). Kohnke determined a value of 0.72 ev for the activation energy of conduction while Foex calculated it to be 0.77 ev from his data on polycrystalline samples.(37) Loch(36) calculated the electron mobility μ to be 10.9 to 12 cm^2-v^{-1}-sec^{-1} which compared well with Hall mobilities measured on SnO_2 films by Ishiguro(36) 17-32 cm^2-v^{-1}-sec^{-1}]. Kohnke's value for very pure crystals was 50 cm -v^{-1}-sec^{-1} which was in reasonable agreement, since one expects higher values of μ in single crystals than in polycrystalline compacts.

Pure polycrystalline SnO_2 is white and is sometimes used as an opacifier in glazes. The handbook value of index of refraction is 2.00.(19)

Tin dioxide thin films, on the other hand, are fairly conducting. They exhibit resistivities in the order of 0.05 Ω-cm and activation energies of 0.0175 ev for electrical conduction(38). Vincent(39) concluded from thermodynamic considerations that this high conductivity is probably due to the inclusion of chlorine ions in the lattice. Rohatgi(38) et al. argues that conduction may also be due to the presence of Sn^{2+} which results from the pyrolytic process.

These films are generally prepared by the pyrolytic decomposition of $SnCl_4 \cdot 5H_2O$ or $SnCl_2 \cdot 2H_2O$-alcohol solutions(38), with the reaction taking place upon a hot glass substrate near the softening point of glass (650-700°C).

SnO_2 films consistently form with the cassiterite structure (38,40). SnO_2 is nearly unique among electronic materials in being a fairly good conductor when oxygen deficient yet having a high degree of transparency to visible light. A typical tin dioxide film displays intense interference colors which may be used for thickness determinations.

It is known(13) that tin dioxide coatings transmit the solar spectrum (.3 - 2.2) well, but at the same time reflect the natural infrared radiation (5-15 μ). This is important since tin oxide on the internal surface (towards a radiation receiver) significantly reduces heat losses which would otherwise be absorbed in the surface layers of the glass, returned to the receiver thus heating it. This heating is harmful for two reasons: (1) It uselessly consumes a portion of energy lost by the receiver in the form of radiation and (2) The increased temperature of the transparent insulation causes reinforcement of convective and radiative losses from the glass into the surrounding space. A coating for this purpose as reported by Rekant _et al._(13) is 98% SnO_2 - 2% F, where the fluorine is introduced to the solution by means of hydrofluoric acid. These coatings are generally 0.2 - 0.4 μ thick (Fig. 3).

It is interesting to note that the optical properties of their tin oxide films are directly related to their composition, determined on the basis of the specific surface resistivity (in ohms)(13). Rekant found that in general the lower the resistivity the greater the reflection in the long wavelength region (4 - 20 μ). The optimum

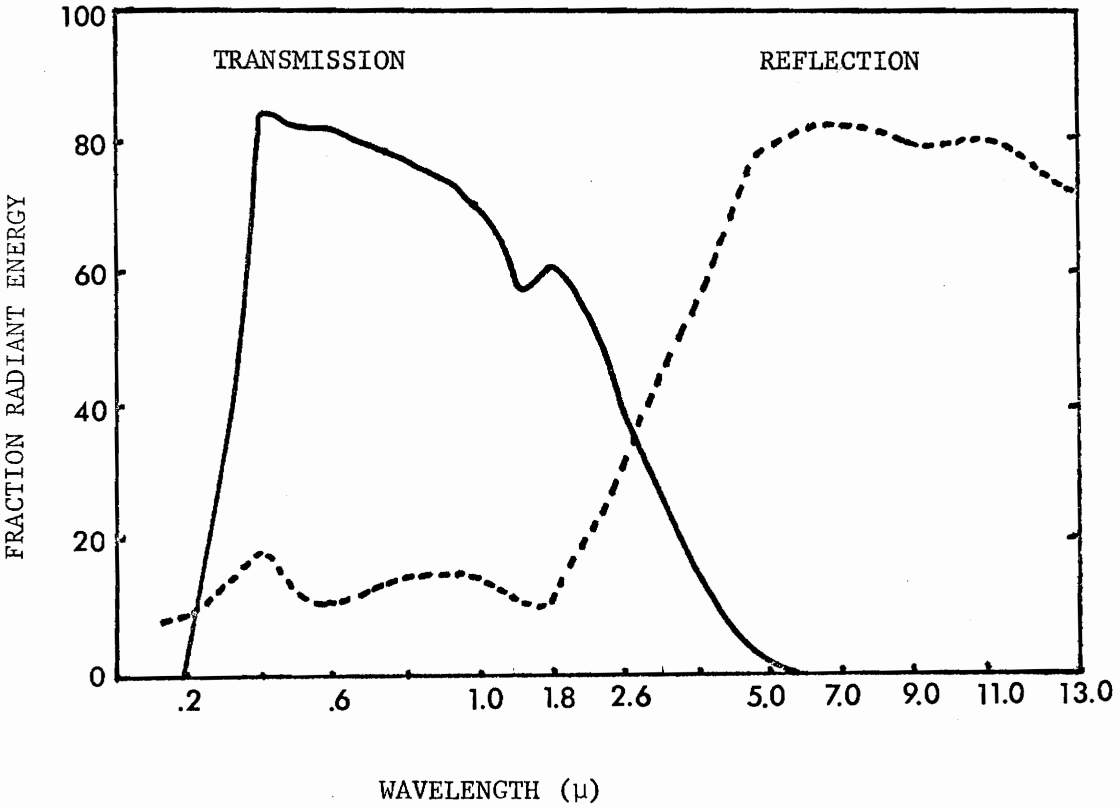

Figure 3. Optical Properties of a SnO_2 Film in the Visible Through Far Infrared Region. (Rekant et al.$^{(13)}$)

value of reflection with relatively high transparency was observed in tin oxide films with surface resistivities of 15 to 100 ohms.

Since SnO_2 films display low resistivities and are transparent, they find application as heated, non-frosting viewing windows, glass or ceramic heating elements and transparent thermostats.

It was determined by Rohatgi *et al.*(38) and others(41), that a 2-5% addition of Sb_2O_5 (Group V), to SnO_2 films enhances conductance an order of magnitude, whereas transmission decreases from 80% to 5% (at 2 μm). A 2% addition of indium, on the other hand, (Group III) increases sheet resistance four orders of magnitude while transmission increased slightly from 80% to 83%. It was reasoned that this behavior was due to the multivalency (II & IV) of the tin ion where the addition of trivalent or pentavalent ions would control the Sn^{+2}/Sn^{+4} ratio. Thus, changing the electrical and optical properties.

It is realized that electrical properties such as band gap and conduction are closely related to optical properties. Vincent(39) explained that free electrons are able to absorb energy from electromagnetic radiation only when they can interact with a crystal lattice. Since absorption is a function of electron-lattice interaction frequency, it is closely connected with the conductance of the crystal(39).

(E) Bulk Oxides and Thin Films of Vanadium

The vanadium-oxygen system is very complex and contains many oxide and sub-oxide compounds. Since this system is complex it is difficult to grow films of stoichiometric V_2O_3 and VO_2. For a complete discussion on the methods of growing such films one should refer to Fan(42). The difficulties in forming oxide films of vanadium could be attributed to the many valence states of vanadium which permit it to combine with oxygen in various proportions. The ratio of vanadium to oxygen has to be exactly right and very well controlled to grow reproducible films. A deposition method far more sophisticated than the pyrolytic decomposition process would have to be utilized. Generally a vapor transport technique is used which yields the correct reactions with controlled atmospheres, i.e. $VOCl_3 + H_2O + 1/2H_2 \longrightarrow VO_2 + 3HCl$ or $2\ VOCl_3 + H_2O + 2H_2 \longrightarrow VO_2O_3 + 6HCl$, etc.

Vanadium oxides of V_2O_3 and VO_2 are of major interest since they both display semiconductor-metal transitions(42). These oxides though, will not be discussed further, since an oxide of vanadium was not produced in this research.

There are also many hydrates of vanadium(43). This is logical since the V-OH system is probably just as complex as the V-O system. Phase equilibria concerning the V-OH system has not been reported in the literature. These hydrates are not stable and do not have interesting optical properties.

(2) Pyrolytic Film Deposition

The pyrolytic decomposition process offers an economical, practical method for oxide film deposition on glass. This process consists of spraying a salt solution, either a chloride or an organometallic dissolved in water, alcohol or water-alcoholic mixtures, onto a heated substrate onto which the solvent evaporates. The salt decomposes and its cation combines with atmospheric oxygen to form the oxide film on the substrate. When the salt decomposition and subsequent oxidation provides a negative free energy change, the oxide film is formed(43). The decomposition process proceeds as follows:

$$a\mathrm{Me}_m\mathrm{R}_n \xrightarrow{\mathrm{H_2O,\ Heat}} b\mathrm{Me}_x\mathrm{O}_y + c\mathrm{H}_p\mathrm{R}\ (\mathrm{gas})$$

The ratio x/y and the amount of oxide formed is determined by the conditions of thermal dissociation of the film forming solution (44). Most metal oxide films that develop on the glass surface are quite adhesive. This is a result of a chemical reaction between the hot glass substrate and the highly reactive dispersal elements forming a strong Si-O-Me bond.

It was determined by Rohatgi & Slack(44) that by utilizing a conventional sprayer, the optimum spray parameters for an experimental set up are as follows:

(1)	Spray Time	5 - 15 sec
(2)	Spray Rate	1 cc/sec
(3)	Spray Distance	12 inches
(4)	Furnace Temperature	550° - 750°C

With this system it was necessary to use solutions with fairly high concentrations, since the glass' surface cooled quickly from the 5-6 cfm air flow rate of the sprayer.

Both the conventional and an improved process for pyrolytic film deposition is reported by Viverito(45) *et al*. which is also included in Appendix A.

(3) Effect of Oxidizing and Reducing Atmospheres on Chemical Reactions

As mentioned in the previous section, the pyrolytic process obeys the reaction:

$$aMe_mR_n \xrightarrow{H_2O,\ Heat} bMe_xO_y + cH_pR\ (gas)$$

The ratio x/y and the amount of oxide formed is governed by the conditions of thermal dissociation. In a reducing atmosphere x/y is larger than in oxidizing conditions(44,14). A specific example concerning this, is the reaction: $TiCl_4 + O_2 \longrightarrow TiO_2 + 2Cl_2 \uparrow$ with an oxygen excess atmosphere; TiO_2 is formed. Yokozawa _et al_.(32) determined that the deposition rate at low temperatures is strikingly increased by the addition of oxygen in the reactant gas. They determined that the rate of deposition in an ozidizing atmosphere reached the same rate as an oxygen-free atmosphere at elevated temperatures. The apparent activation energy for film formation in the oxygen-free atmosphere was estimated to be about 36 Kcal/mole, whereas, if oxygen is present it is about 6.5 Kcal/mole regardless of the oxygen content within 5-60%(20). X-Ray diffraction revealed that the film deposited in the oxygen-free atmosphere had the anatase structure. For the film deposited in the presence of oxygen, X-Ray diffraction did not reveal any crystalline phase.

It is certainly reasonable to predict the reaction $TiCl_4 + N_2 + O_2 \longrightarrow TiO_{2-x} + 2Cl_2 \uparrow$ when oxygen is deficient(23). This type of oxygen deficiency would occur with most n-type oxides depending on the oxygen affinities of the cation forming the oxide.

Rohatgi(44) reported the effect of annealing stannic oxide films in oxidizing, air and reducing atmospheres. Annealing in air at about 50°C below the spraying temperatures for half an hour increased the sheet resistance by a factor of almost 2. This increase in sheet resistance was accompanied by the diffusion of substrate compounds such as silicon and sodium, to the film surface at an estimated level of 10% of Sn^{2+} present, using ESCA. Annealing in air at a temperature close to or above the spraying temperature produces line fissures in the film which reduce its transparency.

Rohatgi(44) determined that annealing in a reducing atmosphere at 650°C for a half hour removes all interference colors and leaves the film completely non-conductive. The glass did acquire a pale gray color which Rohatgi suggests may be due to a deposit of tin metal resulting from the reduction of stannic oxide. ESCA studies seemed to indicate some trace of stannous oxide. Transmission decreased with annealing of the film in a reducing atmosphere(44).

Fitzgibbons _et al._(33) produced thin films of TiO_2 at 150°C by chemical vapor deposition using the hydrolysis of tetraisopropyl titanate. The films were amorphous as grown, but annealing in air caused the crystallization of anatase beginning at 350°C and rutile at 700°C. Density and index of refraction increased substantially with increasing annealing temperature.

It was shown by Rozgonyi and Polito(46) that desired oxides of vanadium could be achieved with different annealing conditions. These are summarized in Table II.

TABLE II

Optimum Conditions for Preparation of Vanadium Oxide Films (Rozgongi and Polito (46)).

Desired film	Initial or recrystallized film	Annealing Conditions		
		ATM	TEMP	TIME
V_2O_5	Amorphous V-O or Polycrystalline V	90% N_2 - 10% O_2	500°C	4
V_2O_3	Recrystallized V_2O_5 amorphous V-O	Wet H_2	550°C	1
VO_2	Amorphous V-O recrystallized V_2O_5	Water vapor	450°C	4

There was no effort made by the authors to determine the exact partial pressure of their annealling conditions.

It can be realized from examining other investigators' work that with n-type oxides , oxygen should promote stoichiometry while a reducing atmosphere such as N_2 should produce an oxide which is oxygen deficient. Annealing is one way to achieve this. It was also determined that crystal structure can be altered with oxidizing and reducing atmosphere.

(4) Multilayered Oxide Films on Glass

Interference light filters have been known for some time now. These filters selectively reflect and transmit specific wavelength regions. One such filter as reported by Gisin and Nesmelov(47) incorporated 9 layers with quarter-wave optical thicknesses with high (H) and low (L) refractive indexes so that the system DHLHLHLHLH was formed. D denotes the index of refraction of the substrate 1.5, H = 2.5 and L = 1.4. Sb_2S_3 was used for the high index material while SrF_2 was utilized for the low index material. This filter had the capabilities of transmitting the short-wave part of the spectrum while reflecting the long-wave part, in which the transition point lay in the near infrared region.

Vijayalaxmi and Rao(48) proved the feasibility of thin film multilayer systems by evaluating performance with computer simulation. The program calculates the reflectance and transmittance of periodic multilayer systems under varying conditions, such as refractive index of the multilayer components, angle of incidence, film thickness and wavelength for any number of layers. It was determined that the 3 layer stack in the ZrO_2 (H) - MgF_2 (L) multilayer system produces a reflection of 54.9%, while a 9 layer stack yielded a reflectance of 95.3%. For a fixed number of layers, the reflectance is higher for a system with large differences in refractive indices of the films in the basic period. However, if the difference in refractive index is small, high reflectances can be achieved by stacking more layers. Table III lists the handbook values(19) of the oxides studied in this thesis.

TABLE III

Handbook Values of Index of Refraction(19)

Oxide	O-Ray	E-Ray
SnO_2	1.997	2.093
Co_3O_4	N/D	N/D
TiO_2 (Rutile)	2.616	2.903
TiO_2 (Anatase)	2.56	2.56
VO_xH_y	N/D	N/D
Fe_2O_3	3.22	2.94

The dependence of angle of incidence and thickness of the multilayered components has also been investigated theoretically. The variation of reflectance with angle of incidence is well known(48). Reflection decreases as the angle of incidence increases from 1° to 90°.

For desired reflectances in a specified wavelength, thickness equal to λ/4 provides the optimum for interference reflection. It was determined by Vijayalaxmi and Rao(48) that the thickness of the higher index film should be controlled more critically than that of the lower index film, while fabricating a multilayer system, especially that with a small number of layers.

There are many practical problems associated with multilayered systems. The first is an economical consideration. Each layer demands its own deposition process. Most workers in multilayer preparation have sometimes found that their otherwise satisfactory coatings become crazed, cloudy, or even detached from the substrate on removal from the coating plant. This disturbing experience is now known to be associated with the intrinsic stress manifested in some degree by virtually all films. Recent studies(49) have shown that a number of courses may be taken to alleviate the effects of stress. Component materials having balancing tensile and compressive stresses may be chosen to produce a multilayer of low overall stress. The use of an elevated substrate temperature will often not only reduce stress but minimize the chance of it causing disrupture by improving film adhesion(50). The dependence of reflectance on thickness can in some cases be so remote from theoretical expectation that the monitoring method is wholly invalidated. These anomalies can often be explained in terms of the inhomogeneity that can occur in films, that is, a variation of refractive index through the thickness of the film. Such inhomogeneities can be represented as "couches de passage" - films occurring at the boundaries of each layer with a refractive index dissimilar from that of the bulk(51,52). These inhomogeneities are dependent upon the deposition parameters which may induce voids or defects in the films' physical structure(50). Recent work has shown that few dielectric films are free from such inhomogeneities and their effect on light measurements can be particularly severe(53).

Another discrepancy between theory and practice multilayer systems is attributable to the effects of optical scattering. Light losses by this means can not only cause undesirable glare in image forming systems, but may place a limit on the maximum reflectance of a dielectric stack(54) or resolution of an interference filter. Four major examples of sources of scattering are structural breakdown within films due to stress, dust particles, substrate surface roughness (which may be inherited or even amplified by subsequently deposited layers), and "spattered" solid particles of evaporant(50).

At the present time, most multilayered systems are utilized in lasar mirrors or for enhancing reflection and protection of metal mirrors. These systems are usually applied by vacuum evaporation techniques(50). The use of multilayers for the enhancement of reflection on architectural glass has not been reported in the literature.

III. EXPERIMENTS AND MEASUREMENTS

(1) Preparation of Salt Solutions

Appendix C lists all of the chloride and organo-metallic compounds that were used to prepare solutions. Of the solutions tested, only $TiCl_4$, $FeCl_3 \cdot 6H_2O$, $SnCl_4 \cdot 5H_2O$, $VO(C_5H_7O_2)_2$ and $Co(C_5H_7O_2)_2$* successfully deposited pyrolytic films. This fact limited this thesis to the study of only these compositions and combinations of them.

Since the organo-metallics of cobalt and vanadium were insoluble in H_2O, acetone, ether, benzene and only slightly soluble in alcohol, .04M alcohol-salt solutions were mixed. The calculated amounts of raw materials were weighed with a Sartorius balance** and then were added to a premeasured amount of absolute anhydrous alcohol. A magnetic stirrer was used to insure a complete solution. Mole fraction for the combination of two or more compounds were measured accurately with a buret.

It was assumed that the film contained the same ratio of metal ions as did the starting solutions, since the exact chemical analysis of the deposited film could not be determined. This is justified because whenever pure solutions are sprayed at the glass temperature, the individual oxides form.

(2) Spray Set-Up and Procedure

The sprayer used in these experiments is described in Appendix A, and a discussion of it will soon appear in the Ceramic Bulletin as an Engineering Note (45). The sprayer set-up is shown in Figures 4 and 5.

---

*Ventron Corporation, Alfa Products, P.O. Box 159, Beverly, Mass.

**Preiser Scientific, Inc., Charleston, West Virginia.

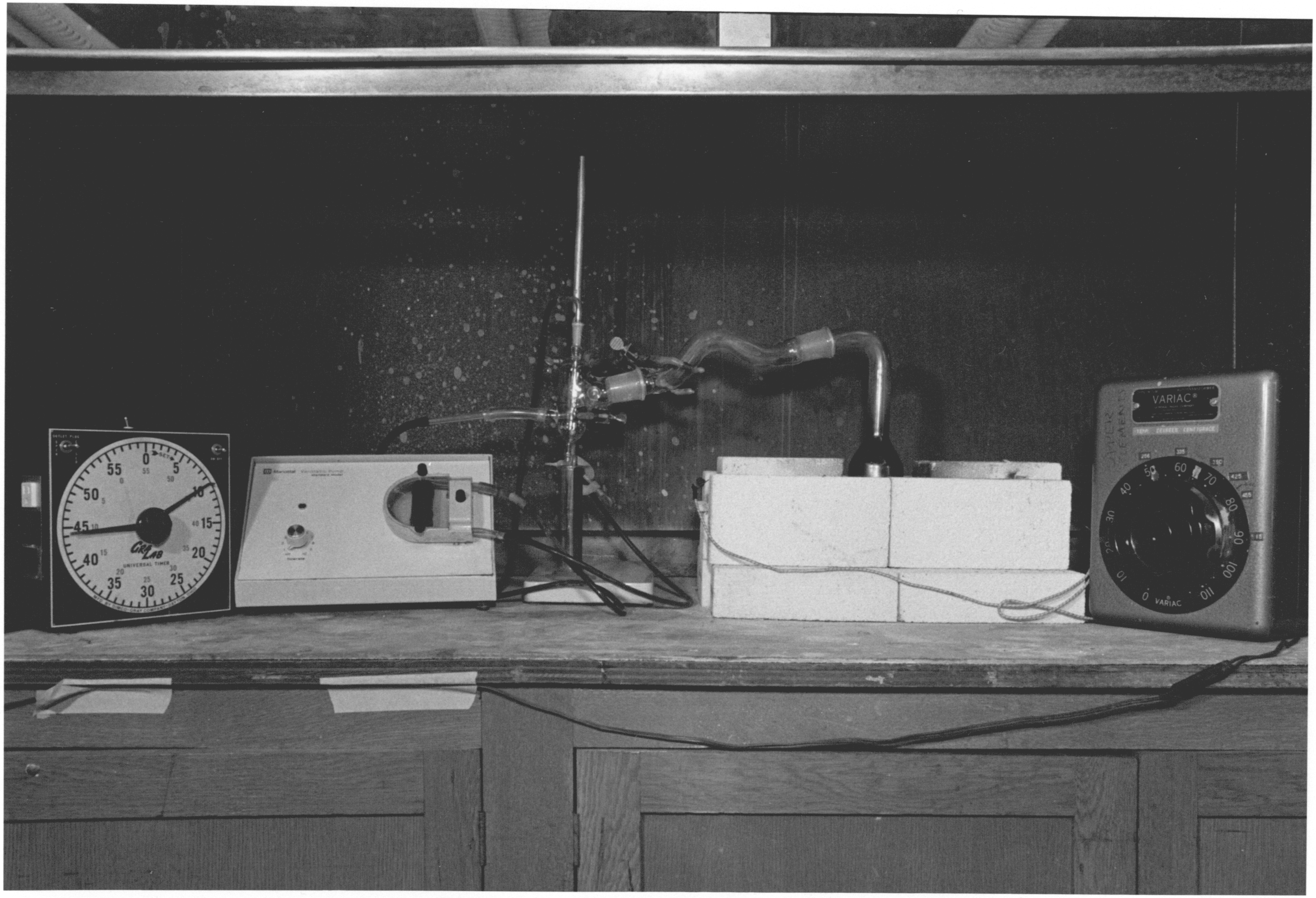

Figure 4. Spray set-up

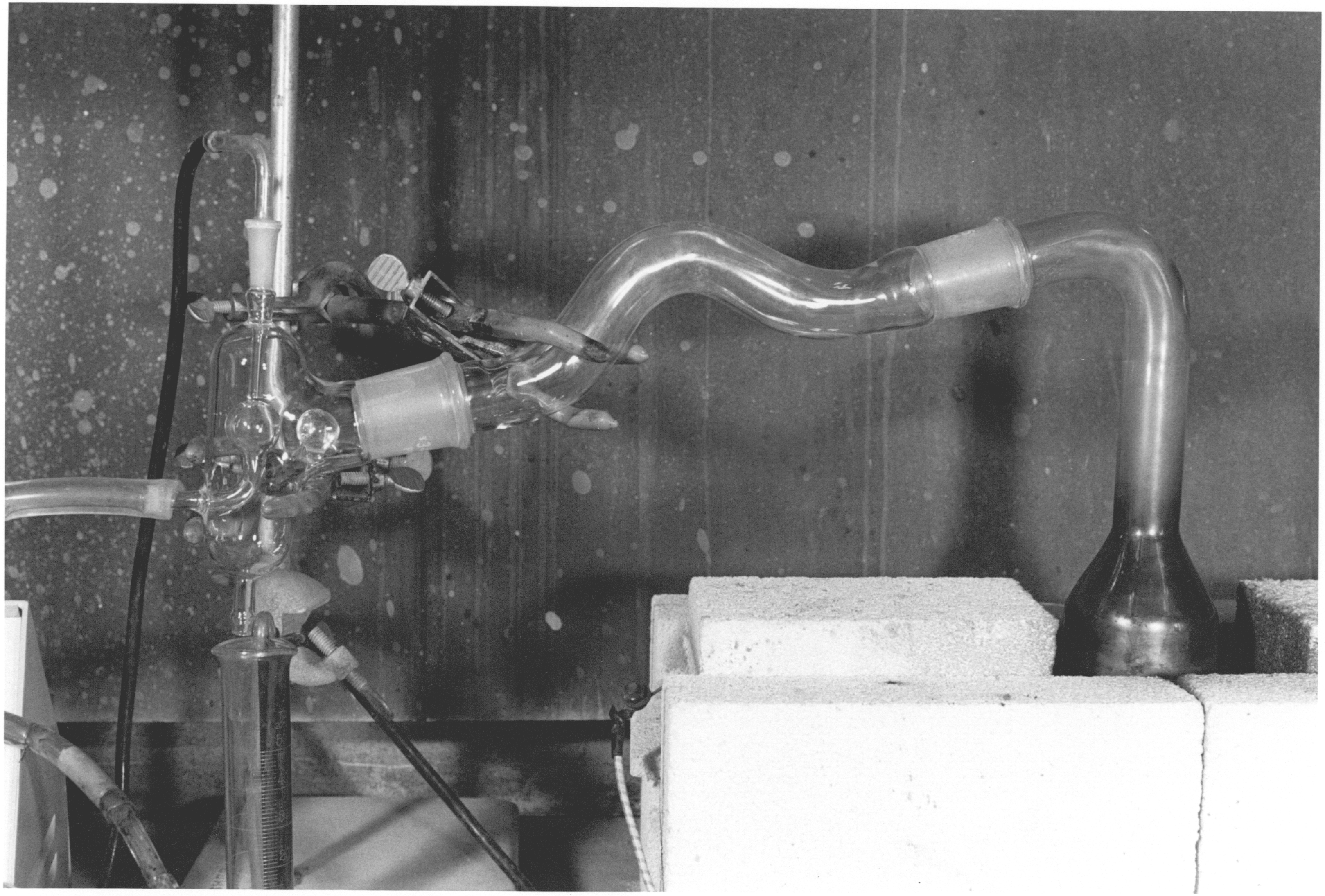

Figure 5. Sprayer

The conditions used in the spraying of the films are listed as follows: Temperature - 360°c, Air Flow Rate - .6 cfm, Solution Concentration - 0.4M, Sample Heating Time - 15 min., Spray Time - 15 min. In order to keep the substrates surface temperature above the reaction temperature for the deposition of these films, the films were sprayed at alternate one-minute intervals. Thus, a 15 minute deposition took a total of 30 minutes.

A cooling curve for the substrate's top surface is present in Figure 6. This curve was drawn with a X-Y recorder* which connected to a chrome-alumel thermalcouple that was cemented to the top surface of the glass substrate. This procedure was used in the deposition of all of the films, with a few exceptions to be mentioned later.

The solutions were also mixed systematically to produce films in the following systems: (1) Fe_2O_3-Co_3O_4, (2) TiO_2-Co_3O_4, (3) VO_xH_y - -Co_3O_4, (4) Fe_2O_3-TiO_2, (5) SnO_2-Co_3O_4, (6) TiO_2- VO_xH_y , (7) $Fe_2O_3TiO_2$ -Co_3O_4.

(3) Experiments with O_2, Air, N_2 and Forming Gas (95% N_2-5% H_2)

The low flow rates of this sprayer enables one to spray with gases such as O_2, N_2 and 95% N_2-5% H_2; substituting for air. This could also be done with a conventional sprayer, but its large flow rate of 5 cfm would render it uneconomical.

Only the pure films of Co_3O_4, SnO_2, TiO_2, VO_xH_y and Fe_2O_3 were sprayed with O_2, air, N_2 and 95% N_2-5% H_2.

---

* 520 X-Y Recorder, Honeywell, San Diego.

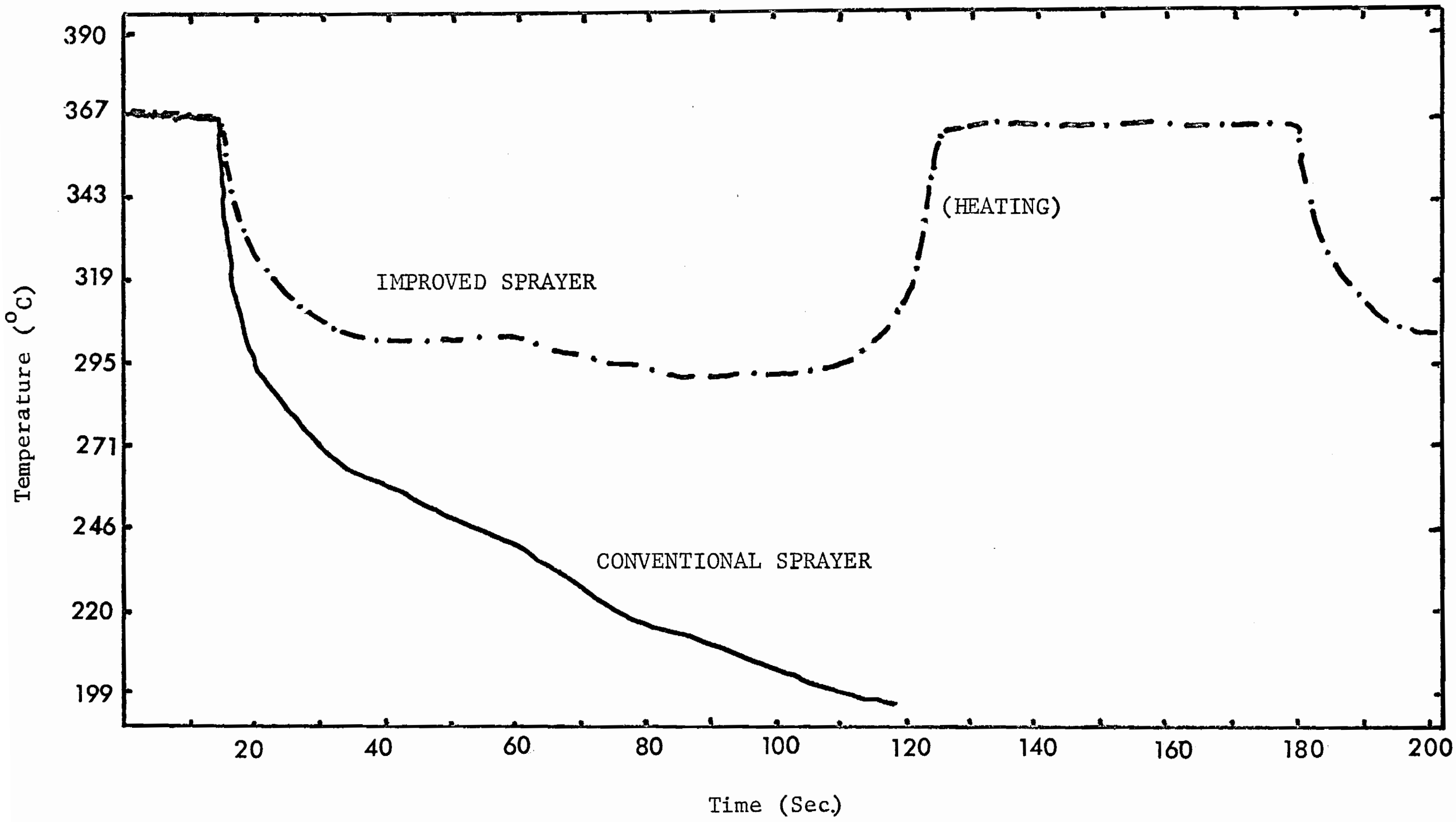

Figure 6. Cooling Curves for the Glass Substrate's Top Surface.

(4) Annealing Experiments

The pure films of VO_xH_y, Co_3O_4 and Fe_2O_3 were annealed in oxygen and forming gas to yield oxidizing and reducing conditions, respectively. The annealing set-up is shown in Figure 7. The actual conditions for annealing are listed in Table IV .

(5) Thickness Variation Experiment

The composition 60% Fe_2O_3 - 40% Co_3O_4, which showed promising optical characteristics and displayed a gold appearance, was sprayed at various times of 5, 10, 15, 20, 30, and 60 minutes to obtain a variation in thickness. Again, the films were sprayed, alternating one minute intervals of spraying and heating.

(6) Multilayered Experiments

Iron oxide has the highest refractive index of the five oxides studied and tin oxide has the lowest. Alternate layers of these high and low refractive index oxides were fabricated. Utilizing .6M solutions of $FeCl_3 \cdot 6H_2O$ and $SnCl\ \cdot 5H_2O$, alternate layers of Fe_2O_3 and SnO_2 were sprayed for one minute, 45 second and 30 second intervals. These were compared to the optical properties of three equivalent layers of Fe_2O_3.

(7) Thickness Measurements

The attenuation of X-rays of a film on a glassy substrate was chosen as the method for thickness determination. This technique is described by Evans and Fisher(55). This method compares the intensity of the glassy halo of an uncoated and coated substrate and knowing the film's absorption coefficient and density, thickness can be calculated using the equation:

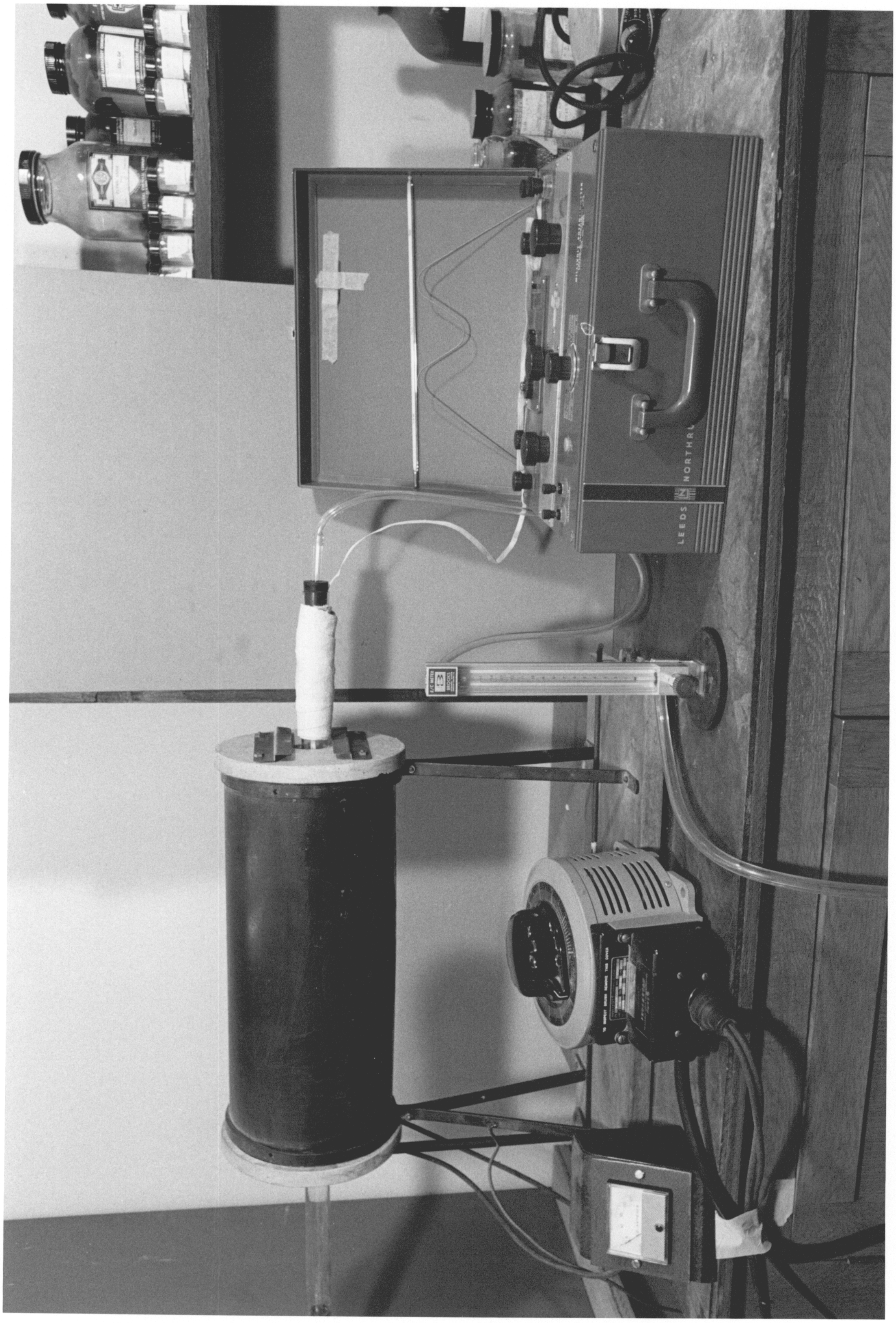

Figure 7. Annealing set-up

TABLE IV

Annealing Conditions

Atmosphere - Oxygen, Air or 95% N_2 - 5% H_2

Flow Rate - 200 cc/min.

Temperature - 500°C

Time - 4 hours

Volume of Reaction Tube - 28.3 sq. inches

$$t = \frac{\sin\theta \ln \frac{I\ \text{uncoated surface}}{I\ \text{coated surface}}}{2(\mu/\rho)\rho}$$

The mass absorption coefficients of the pure and doped compositions was calculated using the equation:

$$(\mu/\rho)\text{cpd.} = X_1(\mu/\rho)_1 + X_2(\mu/\rho)_2 + \cdots + X_n(\mu/\rho)_n{}^{(55)}$$

where X_1, X_2 $\cdots$ X_n are the weight fractions of each compound. A refinement of Evans and Fisher's method was made. Utilizing a low range, high time constant and a very slow chart speed, statistics yielding an average intensity were accumulated at a constant 2θ on the amorphous halo. The area under the intensity curve was determined with a polar planimeter. Dividing by the constant 2-inch scan, produced an average intensity that was significant to the tenth place. This accuracy was necessary to achieve, since a small deviation in intensity yielded a gross error in the thickness measurement.

(8) Determination of Crystal Structure

X-Ray Diffraction Analysis* was utilized for the purpose of crystal structure determination. Scans were made using the following conditions:

Voltage	40 kv
Current	15 ma
Range	500
T.C.	2 cps
Scan	$2\theta = 10°$ to $2\theta = 60°$.

The ASTM standard files were used for the crystal evaluation.

---

* Norelco Diffractometer, North American Philips, Mount Vernon, N. Y.

(9) Scanning Electron Microscopy

The Scanning Electron Microscope** was also used to examine the crystal structure of select films. The actual surface was examined closely to see if there was any reaction with the glass substrate.

(10) Optical Property Measurements

The Varian Instrument, Cary 14 Spectrophotometer***, was utilized for reflection and absorption vs. wavelength measurements. A scan from 2.5μ to .3μ was investigated.

Air was used as the zero reference for the absorption scans, while the reference for the reflection measurements was an aluminum mirror which supposedly had 99% reflectance. It should be noted that the absorption measurements include reflection, therefore 100% - A = %T, the transmission. The absorption measurements were straight forward and very reproducible.

The reflection measurements, on the other hand, were dependent on the instrument's beam size, shape and intensity. Alignment of the beam, which was dependent upon the alignment of the mirrors, phototube and IR source, was critical to get reproducible readings. This measurement utilized an angle of incidence equal to 8° to determine the specular component of reflectance.

The data could not be interpreted directly from the Cary 14 plots. A computer plot routine (Appendix B) was designed to plot simultaneously reflection and transmission. Since A + T + R = 1, absorption was included.

** AR 900, Burlington, Mass.

*** Cary 14, Varian Instrument, New York, New York.

(11) Electrical Measurements

To obtain orders of magnitude of the film's resistance, a two point probe technique was utilized. Of course, this did not eliminate contact resistance, but only orders of magnitude were desired.

For select films that showed possible signs of conductance, a four probe technique was utilized(18). To determine activation energies, resistance was measured as a function of temperature for Co_3O_4, Fe_2O_3, SnO_2 and VO_xH_y films.

IV. RESULTS

A. Appearance

The samples prepared in this investigation appear in Figures 8 and 9. The corresponding identification keys are Tables V and VI.

B. Thickness

The approximate film thicknesses for each film are listed in Table VII.

C. Structure

Identification of each oxide film as determined by X-ray diffraction is also listed in Table VII. These phases were identified using the ASTM files and selected references. The X-ray patterns for the annealed samples of VO_xH_y, Fe_2O_3 and Co_3O_4 are sketched in Figures 10, 11 and 12.

Selected Scanning Electron Micrographs of VO_xH_y, Co_3O_4 and SnO_2 are shown in Figures 14 through 21.

D. Optical Properties

Reflection (R), absorption (A), and transmission(T), as a function of wavelength (.3μ - 2.5μ) for the samples are shown in Appendix A. An index for these figures is included in Table VII. Figures 21 through 27 summarize the findings for the compositional study, where the optical properties at representative infrared (2.5μ and .9μ) and visible (.6μ) wavelengths are plotted as a function of composition. The shaded area represents the amount of light that is not transmitted.

A similar scheme depicting the effect of thickness, instead of composition on the optical properties for the single composition 60% Fe_2O_3 - 40% Co_3O_4 is shown in Figure 28. Figures 29 through 34 progressively show the effects of thickness over the entire $.3\mu$ - 2.5μ spectrum.

Those samples that were sprayed and annealed with various gases are compared with their equivalent sample sprayed with air in Figures 49 through 54. The multilayered systems Fe_2O_3-SnO_2-Fe_2O_3 are compared with the multilayered systems Fe_2O_3-Fe_2O_3-Fe_2O_3 in Figures 55 through 57. Figures 58 and 59 illustrate the effects of stacking successive layers of Co_3O_4 and TiO_2.

Figures 60, 61, and 62 present the optical characteristics of films on glass which the glass industry is currently using to screen solar energy. Figures 60 and 61 show the optical properties of "ASG Gray" and "ASG Bronze"* glasses which contain coloring ions. Figure 62 illustrates the properties of vapor deposited gold ("ASG Gold")*.

E. Electrical Properties

The results of the simple two-point probe measurement for film resistance is presented in Table VII. Plots of log resistance vs $\frac{1}{T}$ for selected samples are shown in Appendix E.

---

*Samples compliments of ASG Industries, Kingsport, Tennessee.

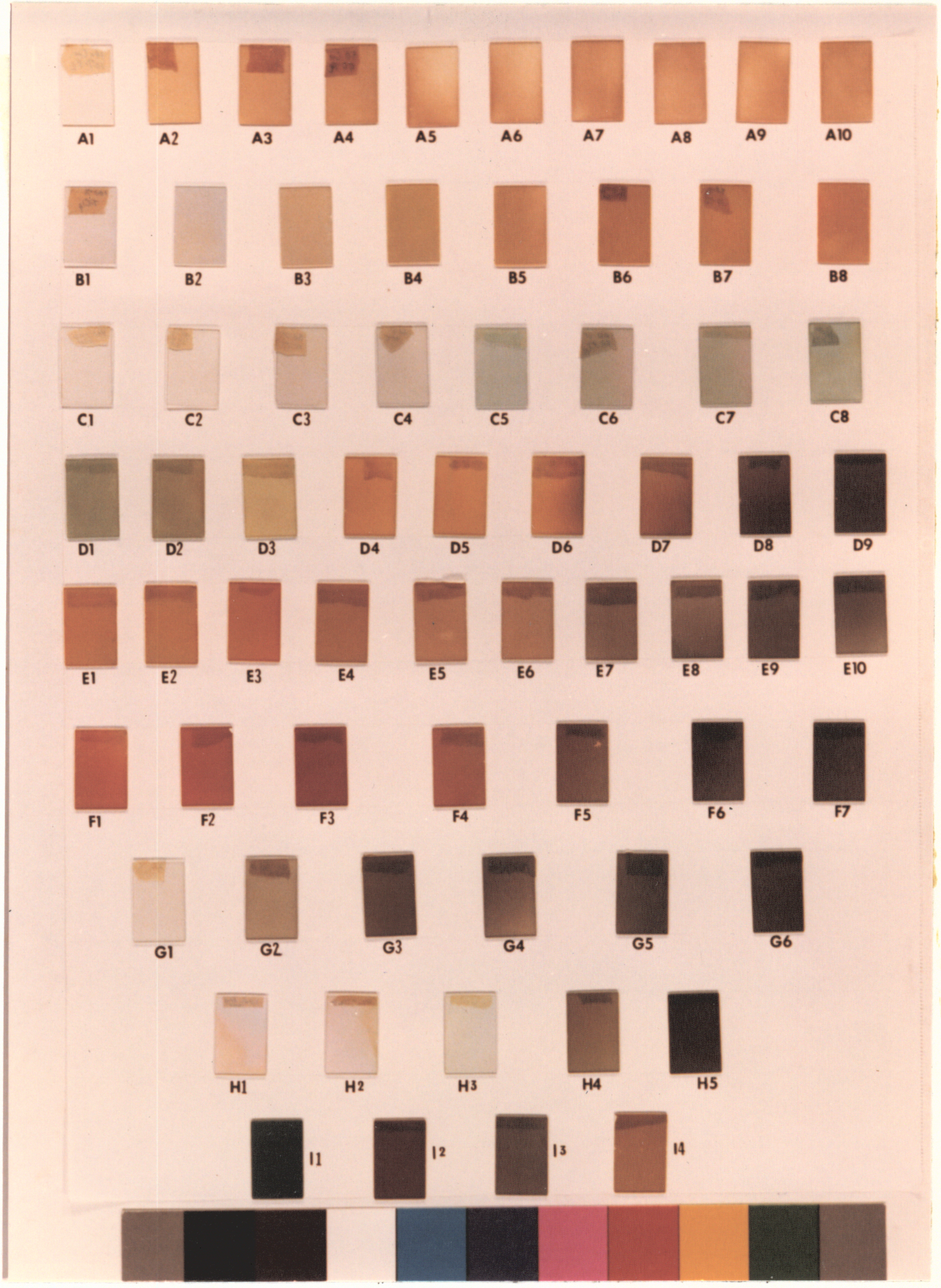

Figure 8. Samples of the Compositional Systems.

TABLE V

Identification of Oxide Films Shown in Figure 8

A1	90% Co_3O_4 10% Fe_2O_3
A2	70% Co_3O_4 30% Fe_2O_3
A3	60% Co_3O_4 40% Fe_2O_3
A4	50% Co_3O_4 50% Fe_2O_3
A5	40% Co_3O_4 60% Fe_2O_3
A6	30% Co_3O_4 70% Fe_2O_3
A7	20% Co_3O_4 80% Fe_2O_3
A8	10% Co_3O_4 90% Fe_2O_3
A9	5% Co_3O_4 95% Fe_2O_3
A10	100% Fe_2O_3
B1	100% TiO_2
B2	90% TiO_2 10% Fe_2O_3
B3	70% TiO_2 30% Fe_2O_3
B4	50% TiO_2 50% Fe_2O_3
B5	30% TiO_2 70% Fe_2O_3
B6	25% TiO_2 75% Fe_2O_3
B7	20% TiO_2 80% Fe_2O_3
B8	10% TiO_2 90% Fe_2O_3
C1	100% TiO_2
C2	80% TiO_2 20% VO_xH_y
C3	60% TiO_2 40% VO_xH_y
C4	40% TiO_2 60% VO_xH_y
C5	30% TiO_2 70% VO_xH_y
C6	20% TiO_2 80% VO_xH_y
C7	10% TiO_2 90% VO_xH_y
C8	100% VO_xH_y
D1	90% VO_xH_y 10% Co_3O_4
D2	80% VO_xH_y 20% Co_3O_4
D3	70% VO_xH_y 30% Co_3O_4
D4	60% VO_xH_y 40% Co_3O_4
D5	50% VO_xH_y 50% Co_3O_4
D6	40% VO_xH_y 60% Co_3O_4
D7	30% VO_xH_y 70% Co_3O_4
D8	20% VO_xH_y 80% Co_3O_4
D9	10% VO_xH_y 90% Co_3O_4

TABLE V (Continued)

Identification of Oxide Films Shown in Figure 8

E1	100% Fe_2O_3
E2	90% Fe_2O_3 10% Co_3O_4
E3	80% Fe_2O_3 20% Co_3O_4
E4	60% Fe_2O_3 40% Co_3O_4
E5	65% Fe_2O_3 35% Co_3O_4
E6	50% Fe_2O_3 50% Co_3O_4
E7	40% Fe_2O_3 60% Co_3O_4
E8	20% Fe_2O_3 80% Co_3O_4
E9	10% Fe_2O_3 90% Co_3O_4
E10	100% Co_3O_4

15 min. $FeCl_3 \cdot 6H_2O$ - $Co(C_5H_7)_2)_2$

F1	100% Fe_2O_3
F2	80% Fe_2O_3 20% Co_3O_4
F3	60% Fe_2O_3 40% Co_3O_4
F4	50% Fe_2O_3 50% Co_3O_4
F5	40% Fe_2O_3 60% Co_3O_4
F6	10% Fe_2O_3 90% Co_3O_4
F7	100% Co_3O_4

$TiCl_4$ - $Co(C_5H_7O_2)_2$

G1	100% TiO_2
G2	50% TiO_2 50% Co_3O_4
G3	40% TiO_2 60% Co_3O_4
G4	30% TiO_2 70% Co_3O_4
G5	20% TiO_2 80% Co_3O_4
G6	100% Co_3O_4

$SnCl_4 \cdot 5H_2O$ - $Co(C_5H_7O_2)_2$

H1	100% SnO_2
H2	80% SnO_2 20% Co_3O_4
H3	60% SnO_2 40% Co_3O_4
H4	20% SnO_2 80% Co_3O_4
H5	100% Co_3O_4

TABLE V (Continued)

Identification of Oxide Films Shown in Figure 8

Ternary Coatings

I1	VAP dep Gold
I2	55% Co_3O_4 15% TiO_2 30% Fe_2O_3
I3	58% Co_3O_4 27% TiO_2 15% Fe_2O_3
I4	48% Co_3O_4 7% TiO_2 45% Fe_2O_3

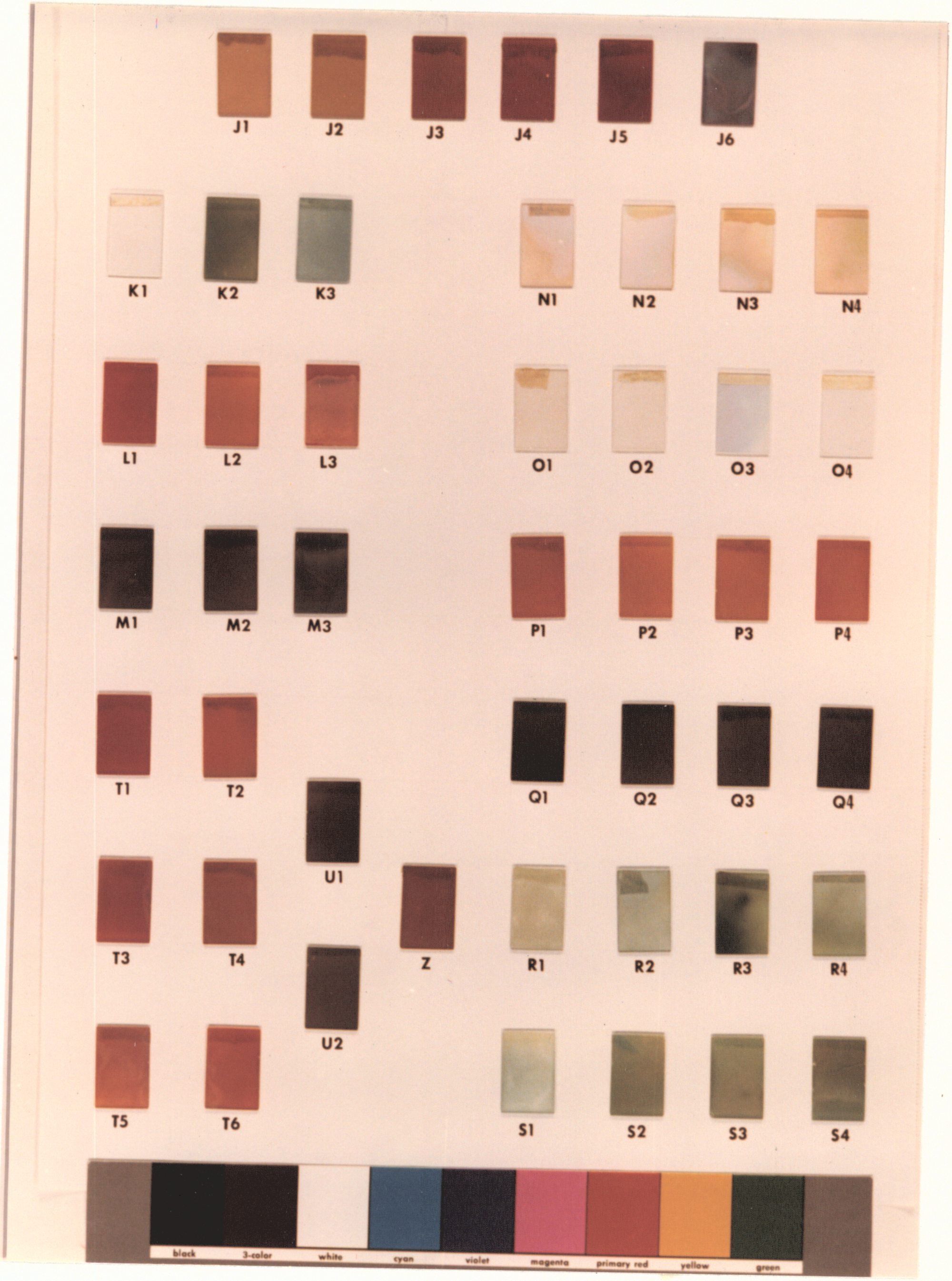

Figure 9. Samples for Thickness Variation, Annealing, Multilayer and Spraying with Gases Experiments.

TABLE VI

Key for Figure 9

60% Fe_2O_3 - 40% Co_3O_4
Thickness Variation

Appearance	Spray Time (Min)	Thickness (Å)
J1	5	265
J2	10	441
J3	15	815
J4	20	907
J5	30	1759
J6	60	5980

K1	VO_xH_y	Annealed 4 hrs 500°C in 100% O_2
K2	VO_xH_y	Before Annealing
K3	VO_xH_y	Annealed 4 hrs 500°C in 95% N_2 - 5% H_2
L1	αFe_2O_3	Annealed 4 hrs 500°C in 100% O_2
L2	αFe_2O_3	Before Annealing
L3	αFe_2O_3	Annealed 4 hrs 500°C in 95% N_2 - 5% H_2
M1	Co_3O_4	Annealed 4 hrs 500°C in 100% O_2
M2	Co_3O_4	Before annealing
M3	Co_3O_4	Annealed 4 hrs 500°C in 95% N_2 - 5% H_2

		Sprayed with
N1	SnO_2	O_2
N2	SnO_2	Air
N3	SnO_2	N_2
N4	SnO_2	95% N_2 - 5% H_2

		Sprayed with
O1	TiO_2	O_2
O2	TiO_2	Air
O3	TiO_2	N_2
O4	TiO_2	95% N_2 - 5% H_2

TABLE VI (Continued)

		Sprayed with
P1	αFe_2O_3	O_2
P2	αFe_2O_3	Air
P3	αFe_2O_3	N_2
P4	αFe_2O_3	95% N_2 - 5% H_2

		Sprayed with
Q1	Co_3O_4	O_2
Q2	Co_3O_4	Air
Q3	Co_3O_4	N_2
Q4	Co_3O_4	95% N_2 - 5% H_2

		Sprayed with
R1	VO_xH_y	O_2
R2	VO_xH_y	Air
R3	VO_xH_y	N_2
R4	VO_xH_y	95% N_2 - 5% H_2

			Temp.	Sprayed with
S1	VO_xH_y	+ H_2O	450°C	N_2
S2	VO_xH_y	+ H_2O	360°C	Air
S3	VO_xH_y	+ H_2O	450°C	Air
S4	VO_xH_y	+ Alcohol	360°C	Air

T1	Fe_2O_3	3 layers	.6 solution	1 min each layer
T2	Fe_2O_3-SnO_2-Fe_2O_3		.6 solution	1 min each layer
T3	Fe_2O_3	3 layers	.6 solution	45 sec each layer
T4	Fe_2O_3-SnO_2-Fe_2O_3		.6 solution	45 sec each layer
T5	Fe_2O_3	3 layers	.6 solution	30 sec each layer
T6	Fe_2O_3-SnO_2-Fe_2O_3		.6 solution	30 sec each layer

U1	Co_3O_4-TiO_2-Co_3O_4-TiO_2-Co_3O_4	5 min each layer
U2	Co_3O_4-TiO_2-Co_3O_4	5 min each layer

Z	60% Fe_2O_3 - 40% Co_3O_4 sprayed	12 min both sides

TABLE VII

Properties of Oxide Thin Films

Starting Solution (conc.)	Thickness (A)	Final Phase	Room Temperature Resistance	Identification and Optical Properties
100% $CoCl_2$ (.6M)	N/D	Amorphous	10^{12}	A1
70% $CoCl_2$-30% $FeCl_3 \cdot 6H_2O$	N/D	Amorphous	10^{12}	A2
60% $CoCl_2$-40% $FeCl_3 \cdot 6H_2O$	N/D	Amorphous	10^{12}	A3
50% $CoCl_2$-50% $FeCl_3 \cdot 6H_2O$	N/D	Amorphous	10^{12}	A4
40% $CoCl_2$-60% $FeCl_3 \cdot 6H_2O$	N/D	Amorphous	10^{12}	A5
30% $CoCl_2$-70% $FeCl_3 \cdot 6H_2O$	N/D	Amorphous	10^{12}	A6
20% $CoCl_2$-80% $FeCl_3 \cdot 6H_2O$	N/D	Amorphous	10^{12}	A7
10% $CoCl_2$-90% $FeCl_3 \cdot 6H_2O$	N/D	Amorphous	10^{12}	A8
5% $CoCl_2$-95% $FeCl_3 \cdot 6H_2O$	N/D	Amorphous	10^{12}	A9
100% $FeCl_3 . 6H_2O$	N/D	Amorphous	10^{12}	A10

TABLE VII (Continued)

Starting Solution (conc.)	Thickness (A)	Final Phase	Room Temperature Resistance	Identification and Optical Properties
100% $TiCl_4$	400	Amorphous	10^{12}	B1 Fig. D-1
90% $TiCl_4$-10% $FeCl_3.6H_2O$	410	Amorphous	10^{12}	B2 Fig. D-2
70% $TiCl_4$-30% $FeCl_3\cdot 6H_2O$	405	Amorphous	10^{12}	B3 Fig. D-3
50% $TiCl_4$-50% $FeCl_3\cdot 6H_2O$	415	Amorphous	10^{12}	B4 Fig. D-4
30% $TiCl_4$-70% $FeCl_3\cdot 6H_2O$	400	Amorphous	10^{12}	B5 Fig. D-5
25% $TiCl_4$-75% $FeCl_3\cdot 6H_2O$	405	Amorphous	10^{12}	B6 Fig. D-6
20% $TiCl_4$-80% $FeCl_3\cdot 6H_2O$	410	Amorphous	10^{12}	B7 Fig. D-7
10% $TiCl_4$-90% $FeCl_3\cdot 6H_2O$	400	Amorphous	10^{12}	B8 Fig. D-8

TABLE VII (Continued)

Starting Solution	Thickness (Å)	Resulting Phase as Determined by X-ray	Room Temperature Resistance	Appearance
$VO(C_7H_5O_2)_2$	600	VO_xH_y	2.0×10^8	C_8 Fig. D-17
$90VO(C_7H_5O_2)_2-10TiCl_4$	670	VO_xH_y	1.0×10^{10}	C_7 Fig. D-16
$80VO(C_7H_5O_2)_2-20TiCl_4$	668	VO_xH_y	4.1×10^{10}	C_6 Fig. D-15
$70VO(C_7H_5O_2)_2-30TiCl_4$	679	VO_xH_y	2.6×10^{10}	C_5 Fig. D-14
$60VO(C_7H_5O_2)_2-40TiCl_4$	688	Amorphous	2.9×10^{10}	C_4 Fig. D-13
$40VO(C_7H_5O_2)_2-60TiCl_4$	684	Amorphous	2.5×10^{11}	C_3 Fig. D-12
$20VO(C_7H_5O_2)_2-80TiCl_4$	658	Amorphous	3.5×10^{11}	C_2 Fig. D-11
$TiCl_4$	667	Amorphous	1.2×10^{12}	C_1 Fig. D-10

TABLE VII (Continued)

Starting Solution (conc.)	Thickness (Å)	Resulting Phase as Determined by X-ray	Room Temperature Resistance	Appearance
$VO(C_7H_5O_2)_2$	600	VO_xH_y	2.0×10^8	D_1 Fig. D-17
$90VO(C_7H_5O_2)_2$-$10Co(C_7H_5O_2)_2$	595	VO_xH_y	1.5×10^{10}	D_2 Fig. D-18
$80VO(C_7H_5O_2)_2$-$20Co(C_7H_5O_2)_2$	593	Trace VO_xH_y	2.0×10^{11}	D_3 Fig. D-19
$70VO(C_7H_5O_2)_2$-$30Co(C_7H_5O_2)_2$	580	Amorphous	3.2×10^{11}	D_4 Fig. D-20
$60VO(C_7H_5O_2)_2$-$40Co(C_7H_5O_2)_2$	584	Amorphous	3.6×10^{11}	D_5 Fig. D-21
$50VO(C_7H_5O_2)_2$-$50Co(C_7H_5O_2)_2$	583	Amorphous	4.6×10^{11}	D_6 Fig. D-22
$40VO(C_7H_5O_2)_2$-$60Co(C_7H_5O_2)_2$	590	Amorphous	1.0×10^{11}	D_7 Fig. D-23
$30Vo(C_7H_5O_2)_2$-$70Co(C_7H_5O_2)_2$	580	Amorphous	2.6×10^{11}	D_8 Fig. D-24
$20Vo(C_7H_5O_2)_2$-$80Co(C_7H_5O_2)_2$	585	Trace Co_3O_4	1.6×10^{10}	D_9 Fig. D-25
$10Vo(C_7H_5O_2)_2$-$90Co(C_7H_5O_2)_2$	590	Co_3O_4	4.9×10^9	D_{10} Fig. D-26
$Co(C_7H_5O_2)_2$	600	Co_3O_4	1.0×10^8	D_{11} Fig. D-27

TABLE VII (Continued)

Starting Solution (conc.)	Thickness (A)	Resulting Phase as Determined by X-ray	Room Temperature Resistance	Appearance
$FeCl_3 \cdot 6H_2O$	496	αFe_2O_3	2.5×10^{11}	E_1 Fig. D-28
$90FeCl_3 \cdot 6H_2O-10Co(C_7H_5O_2)_2$	548	αFe_2O_3	2.0×10^{11}	E_2 Fig. D-29
$80FeCl_3 \cdot 6H_2O-20Co(C_7H_5O_2)_2$	615	Amorphous	1.0×10^{11}	E_3 Fig. D-30
$65FeCl_3 \cdot 6H_2O-35Co(C_7H_5O_2)_2$	650	Amorphous	1.5×10^{11}	E_4 Fig. D-31
$60FeCl_3 \cdot 6H_2O-40Co(C_7H_5O_2)_2$	717	Amorphous	1.0×10^{11}	E_5 Fig. 30
$50FeCl_3 \cdot 6H_2O-50Co(C_7H_5O_2)_2$	700	Amorphous	3.1×10^{11}	E_6 Fig. D-32
$40FeCl_3 \cdot 6H_2O-60Co(C_7H_5O_2)_2$	750	Amorphous	3.3×10^{11}	E_7 Fig. D-33
$20FeCl_3 \cdot 6H_2O-80Co(C_7H_5O_2)_2$	775	Amorphous	2.3×10^{11}	E_8 Fig. -
$10FeCl_3 \cdot 6H_2O-90Co(C_7H_5O_2)_2$	770	Co_3O_4	1.5×10^{11}	E_9 Fig. D-34
$Co(C_7H_5O_2)_2$	550	Co_3O_4	1.5×10^{8}	E_{10} Fig.D-35

TABLE VII (Continued)

Starting Solution (conc.)	Thickness (A)	Resulting Phase as Determined by X-ray	Room Temperature Resistance	Appearance
$FeCl_3 \cdot 6H_2O$	537	αFe_2O_3	2.8×10^{11}	F_1 Fig. D-36
80 $FeCl_3 \cdot 6H_2O$-20$Co(C_7H_5O_2)_2$	717	αFe_2O_3	4.2×10^{11}	F_2 Fig. D-37
60 $FeCl_3 \cdot 6H_2O$-40$Co(C_7H_5O_2)_2$	815	αFe_2O_3	4.0×10^{11}	F_3 Fig. 31
50 $FeCl_3 \cdot 6H_2O$-50$Co(C_7H_5O_2)_2$	800	Amorphous	1.4×10^{11}	F_4 Fig. D-38
40 $FeCl_3 \cdot 6H_2O$-60$Co(C_7H_5O_2)_2$	805	αFe_2O_3	3.7×10^{11}	F_5 Fig. D-39
10 $FeCl_3 \cdot 6H_2O$-90$Co(C_7H_5O_2)_2$	862	Co_3O_4	1.4×10^{11}	F_6 Fig. D-40
$Co(C_7H_5O_2)_2$	600	Co_3O_4	1.0×10^{8}	F_7 Fig. D-46

TABLE VII (Continued)

Starting Solution	Thickness (Å)	Resulting Phase as Determined by X-ray	Room Temperature Resistance	Appearance
$TiCl_4$	667	Amorphous	1.2×10^{12}	G_1 Fig. D-10
$50TiCl_4$-$50Co(C_7H_5O_2)_2$	650	Amorphous	6×10^{11}	G_2 Fig. D-42
$40TiCl_4$-$60Co(C_7H_5O_2)_2$	647	Amorphous	5×10^{11}	G_3 Fig. D-43
$30TiCl_4$-$70Co(C_7H_5O_2)_2$	620	Amorphous	7.3×10^{10}	G_4 Fig. D-44
$20TiCl_4$-$80Co(C_7H_5O_2)_2$	617	Co_3O_4	2.0×10^{10}	G_5 Fig. D-45
$Co(C_7H_5O_2)_2$	600	Co_3O_4	1.5×10^8	G_6 Fig. D-46
$SnCl_4 \cdot 5H_2O$	1782	SnO_2	2.6×10^4	H_1 Fig. D-47
$80SnCl_4 \cdot 5H_2O$-$20Co(C_7H_5O_2)_2$	1504	SnO_2	3.9×10^5	H_2 Fig. D-48
$40SnCl_4 \cdot 5H_2O$-$60Co(C_7H_5O_2)_2$	1104	Amorphous	4.9×10^{11}	H_3 Fig. D-49
$20SnCl_4 \cdot 5H_2O$-$80Co(C_7H_5O_2)_2$	904	Amorphous	4.0×10^{11}	H_4 Fig. D-50
$Co(C_7H_5O_2)_2$	600	Co_3O_4	1.6×10^7	H_5 Fig. D-46

TABLE VII (Continued)

Starting Solution	Thickness (Å)	Resulting Phase as Determined by X-ray	Room Temperature Resistance	Appearance
Ternary Systems				
$60FeCl_3 \cdot 6H_2O-40\%Co(C_7H_5O_2)_2$	815	αFe_2O_3	4.0×10^{11}	Z Fig. D-54
$45FeCl_3 \cdot 6H_2O-48Co(C_7H_5O_2)_2-7TiCl_4$	780	Amorphous	1.8×10^{11}	I_4 Fig. D-51
$30FeCl_3 \cdot 6H_2O-55Co(C_7H_5O_2)_2-15TiCl_4$	775	Amorphous	2.1×10^{11}	I_3 Fig. D-52
$15FeCl_3 \cdot 6H_2O-62Co(C_7H_5O_2)_2-23TiCl_4$	770	Amorphous	3.2×10^{11}	I_2 Fig. D-53
Vapor Deposited Gold	400	Amorphous	----------	I_1 Fig. 62
$60FeCl_3 \cdot 6H_2O-40Co(C_7H_5O_2)_2$	265	Amorphous	4.0×10^{11}	J_1 Fig. 29
$60FeCl_3 \cdot 6H_2O-40Co(C_7H_5O_2)_2$	414	Amorphous	1.0×10^{11}	J_2 Fig. 30
$60FeCl_3 \cdot 6H_2O-40Co(C_7H_5O_2)_2$	815	αFe_2O_3	4.0×10^{11}	J_3 Fig. 31
$60FeCl_3 \cdot 6H_2O-40Co(C_7H_5O_2)_2$	907	αFe_2O_3	4.5×10^{11}	J_4 Fig. 32
$60FeCl_3 \cdot 6H_2O-40Co(C_7H_5O_2)_2$	1759	αFe_2O_3	8×10^{10}	J_5 Fig. 33
$60FeCl_3 \cdot 6H_2O-40Co(C_7H_5O_2)_2$	5980	αFe_2O_3	5×10^{10}	J_6 Fig. 34

TABLE VII (Continued)

Starting Solution	Thickness (Å)	Resulting Phase as Determined by X-ray	Room Temperature Resistance	Appearance
VO_xH_y Annealed in O_2	No Film	Amorphous	3×10^{11}	K_1 Fig. 49
VO_xH_y - Air reference	650	VO_xH_y	8×10^{8}	K_2 Fig. D-17
VO_xH_y Annealed in 95%N_2-5%H_2	600	VO_xH_y	2.1×10^{10}	K_3 Fig. 50
αFe_2O_3 Annealed in O_2	415	αFe_2O_3	5×10^{11}	L_1 Fig. 51
αFe_2O_3 - Air reference	537	Amorphous	4.0×10^{11}	L_2 Fig. D-36
αFe_2O_3 Annealed in 95%N_2-5%H_2	300	αFe_2O_3	6×10^{9}	L_3 Fig. 52
Co_3O_4 Annealed in O_2	600	Co_3O_4	2.5×10^{7}	M_1 Fig. 53
Co_3O_4 Air reference	600	Co_3O_4	1.0×10^{8}	M_2 Fig. D-46
Co_3O_4 Annealed in 95%N_2-5%H_2	600	Co_3O_4	5.0×10^{10}	M_3 Fig. 54
$SnCl_4 \cdot 5H_2O$ w/O_2	717	Amorphous	6.8×10^{4}	N_1 Fig. 46
$SnCl_4 \cdot 5H_2O$ w/air	1782	Strong SnO_2	2.6×10^{4}	N_2 Fig. D-47
$SnCl_4 \cdot 5H_2O$ w/N_2	948	Weak SnO_2	4.0×10^{6}	N_3 Fig. 47
$SnCl_4 \cdot 5H_2O$ w/95N_2-5H_2	935	Amorphous	7.0×10^{6}	N_4 Fig. 48

TABLE VII (Continued)

Starting Solution	Thickness (Å)	Resulting Phase as Determined by X-ray	Room Temperature Resistance	Appearance
$TiCl_4$ w/O_2	500	Amorphous	10^{11}	O_1 Fig. 35
$TiCl_4$ w/air	667	Amorphous	10^{11}	O_2 Fig. D-10
$TiCl_4$ w/N_2	900	Amorphous	10^{11}	O_3 Fig. 36
$TiCl_4$ w/95%N_2-5%H_2	No Film	Amorphous	10^{11}	O_4 Fig. -
$FeCl_3 \cdot 6H_2O$ w/O_2	500	Amorphous	4.0×10^{11}	P_1 Fig. 37
$FeCl_3 \cdot 6H_2O$ w/air	537	αFe_2O_3	2.8×10^{11}	P_2 Fig. D-36
$FeCl_3 \cdot 6H_2O$ w/N_2	774	Amorphous	3.0×10^{9}	P_3 Fig. 38
$FeCl_3 \cdot 6H_2O$ w/95%N_2-5%H_2	300	αFe_2O_3	4.0×10^{10}	P_4 Fig. 39
$Co(C_7H_5O_2)_2$ w/O_2	885	Co_3O_4	3.0×10^{7}	Q_1 Fig. 43
$Co(C_7H_5O_2)_2$ w/air	600	Co_3O_4	1.5×10^{8}	Q_2 Fig. D-46
$Co(C_7H_5O_2)_2$ w/N_2	554	Slight Co_3O_4	1.0×10^{8}	Q_3 Fig. 44
$Co(C_7H_5O_2)_2$ w/95%N_2-5%H_2	590	Amorphous	4.0×10^{8}	Q_4 Fig. 45

TABLE VII (Continued)

Starting Solution	Thickness (Å)	Resulting Phase as Determined by X-ray	Room Temperature Resistance	Appearance
$VO(C_7H_5O_2)_2$ w/O_2	300	Amorphous	10^{11}	R_1 Fig. 40
$VO(C_7H_5O_2)_2$ w/air	600	VO_xH_y	2.0×10^8	R_2 Fig. D-17
$VO(C_7H_5O_2)_2$ w/N_2	615	VO_xH_y	1.7×10^6	R_3 Fig. 41
$VO(C_7H_5O_2)_2$ w/95%N_2-5%H_2	590	VO_xH_y	1.1×10^7	R_4 Fig. 42
Van. + H_2O + N_2 450° C	N/D	VO_xH_y	N/D	S_1 Fig. D-55
Van. + H_2O + Air 360° C	N/D	VO_xH_y	N/D	S_2 Fig. D-56
Van. + H_2O + Air 450° C	N/D	VO_xH_y	N/D	S_3 Fig. D-57
Van. + Alcohol + Air 360° C	N/D	VO_xH_y	N/D	S_4 Fig. D-58

TABLE VII (Continued)

Starting Solution	Thickness (Å)	Resulting Phase as Determined by X-ray	Room Temperature Resistance	Appearance
$FeCl_3 \cdot 6H_2O$ - 3 Layers	Each 300	N/D	N/D	T_1 Fig. 57
$FeCl_3$-$SnCl_4$-$FeCl_3$	Each 300	N/D	N/D	T_2 Fig. 57
$FeCl_3 \cdot 6H_2O$ - 3 Layers	Each 500	N/D	N/D	T_3 Fig. 56
$FeCl_3$-$SnCl_4$-$FeCl_3$	Each 500	N/D	N/D	T_4 Fig. 56
$FeCl_3 \cdot 6H_2O$ - 3Layers	Each 1000	N/D	N/D	T_5 Fig. 55
$FeCl_3$-$SnCl_4$-$FeCl_3$	Each 1000	N/D	N/D	T_6 Fig. 55
$Co(C_7H_5O_2)_2$-$TiCl_4$-$Co(C_7H_5O_2)_2$	Each 600	N/D	N/D	U_1 Fig. 58
$Co(C_7H_5O_2)_2$-$TiCl_4$-$Co(C_7H_5O_2)_2$-$TiCl_4$-$Co(C_7H_5O_2)_2$	600	N/D	N/D	U_2 Fig. 59

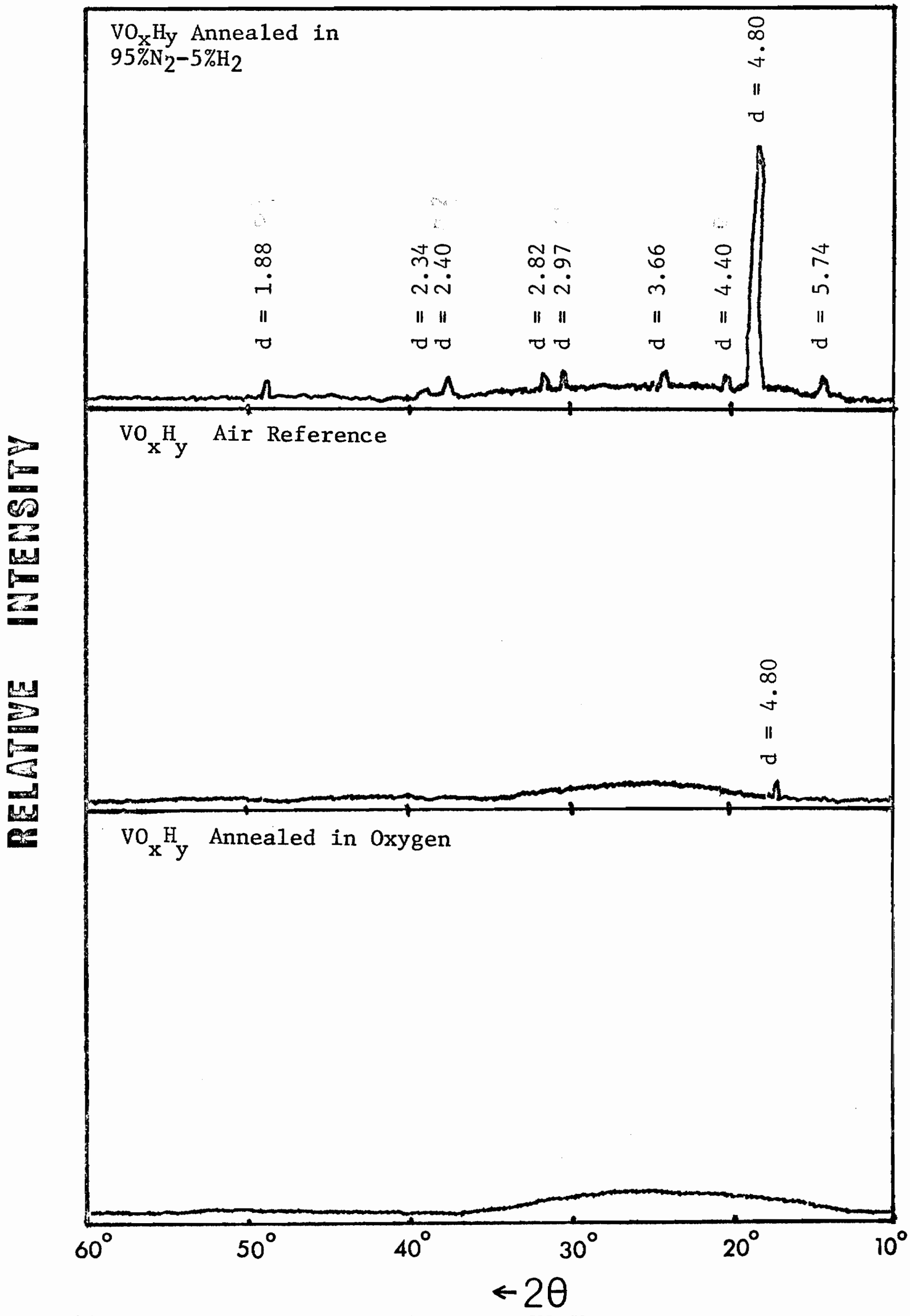

Figure 10. X-Ray Diffraction of Annealed VO$_x$H$_y$.

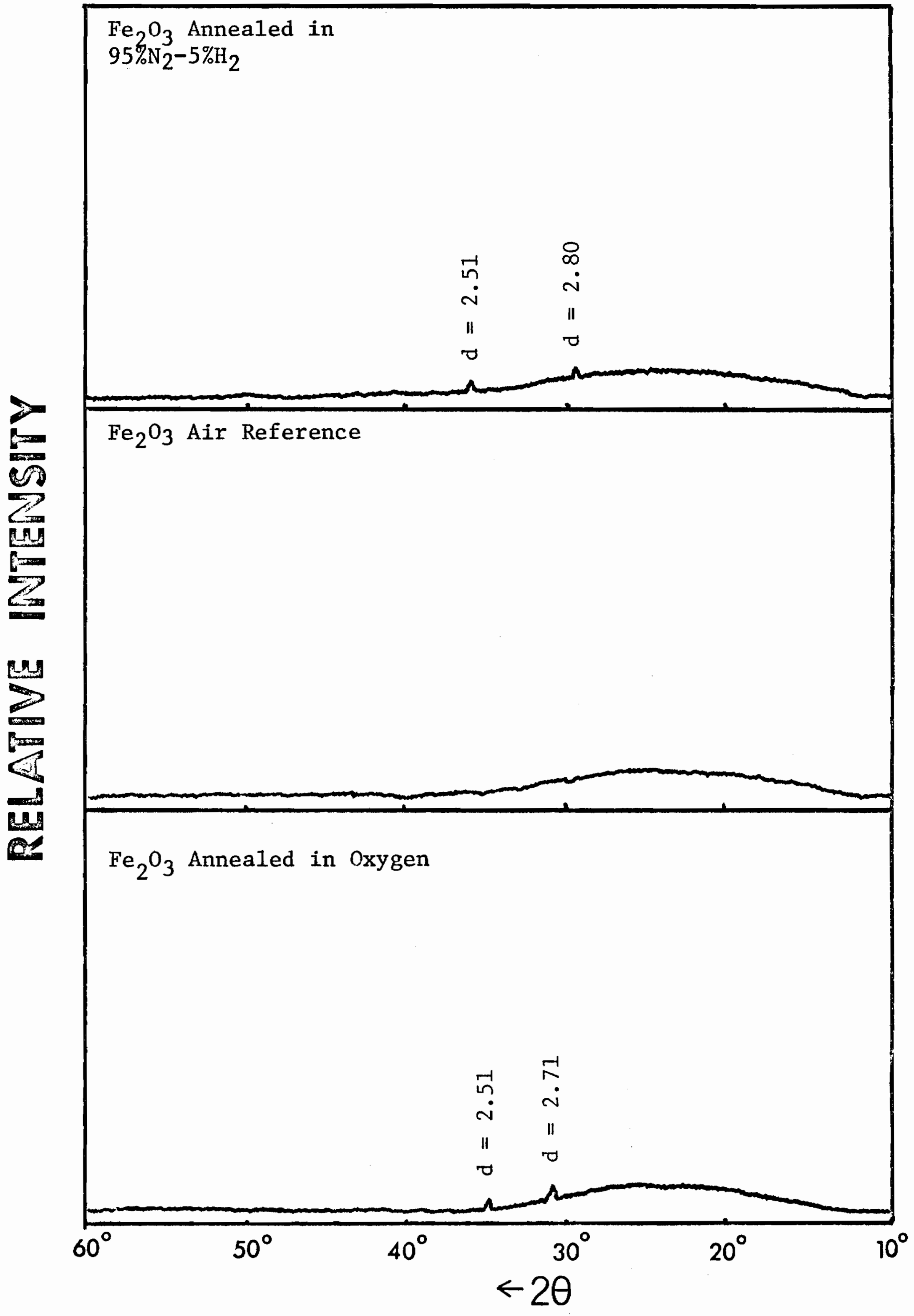

Figure 11. X-Ray Diffraction of Annealed Fe_2O_3.

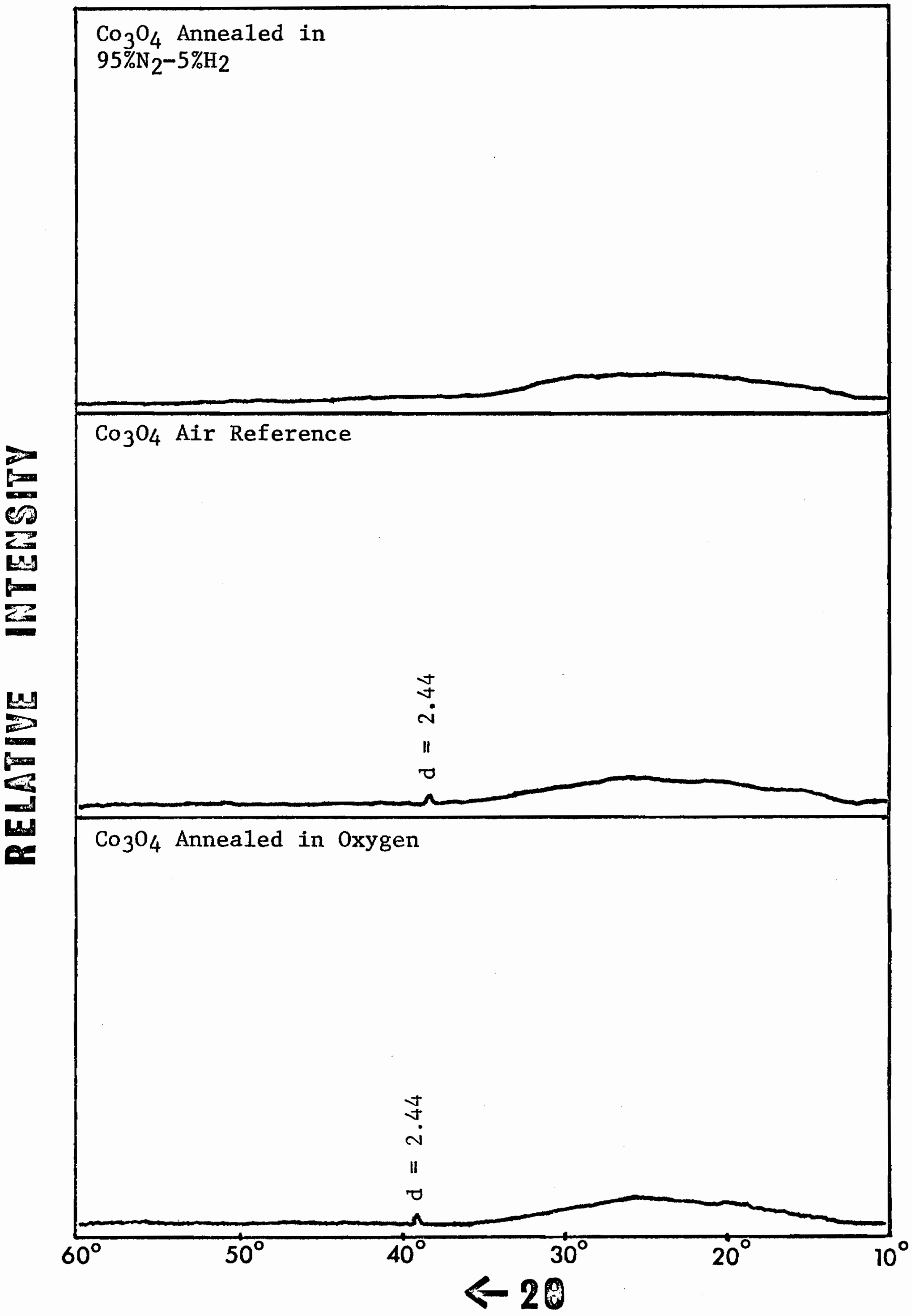

Figure 12. X-Ray Diffraction of Annealed Co_3O_4.

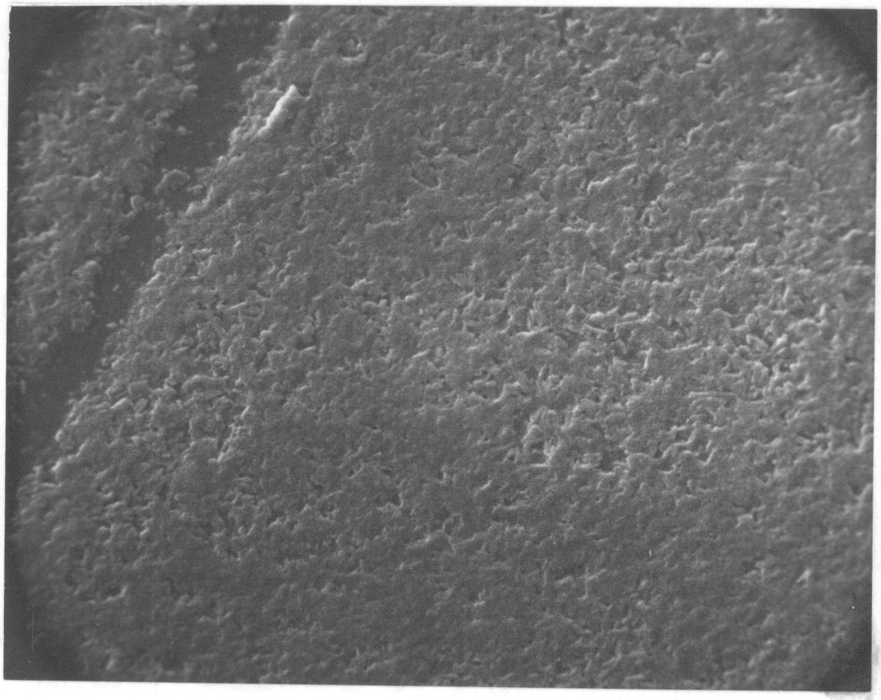

Figure 13a. SEM VO_xH_y Air Reference (4,900X)

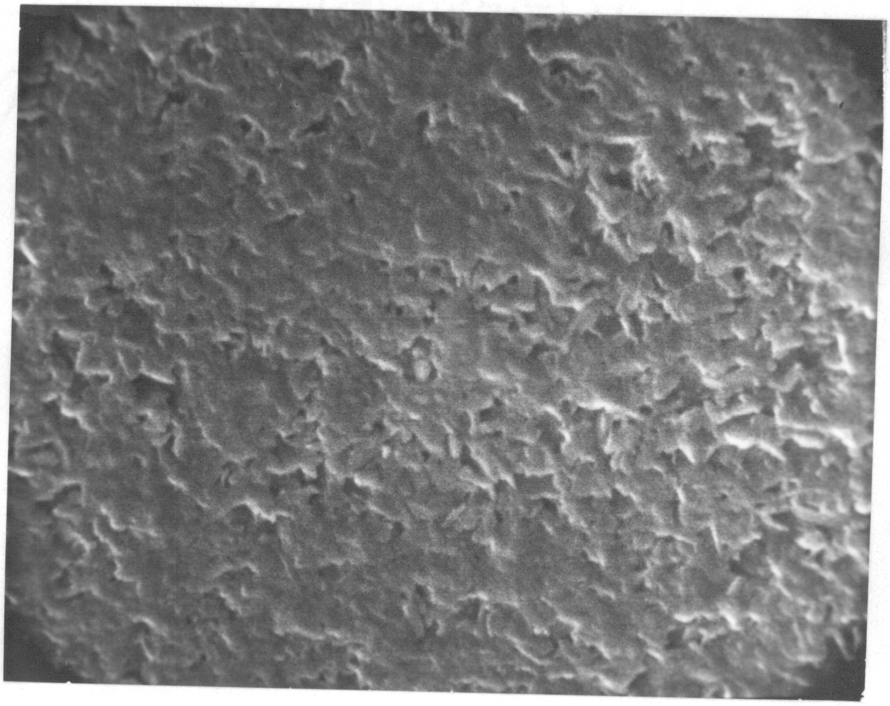

Figure 13b. SEM VO_xH_y Air Reference (9,800X)

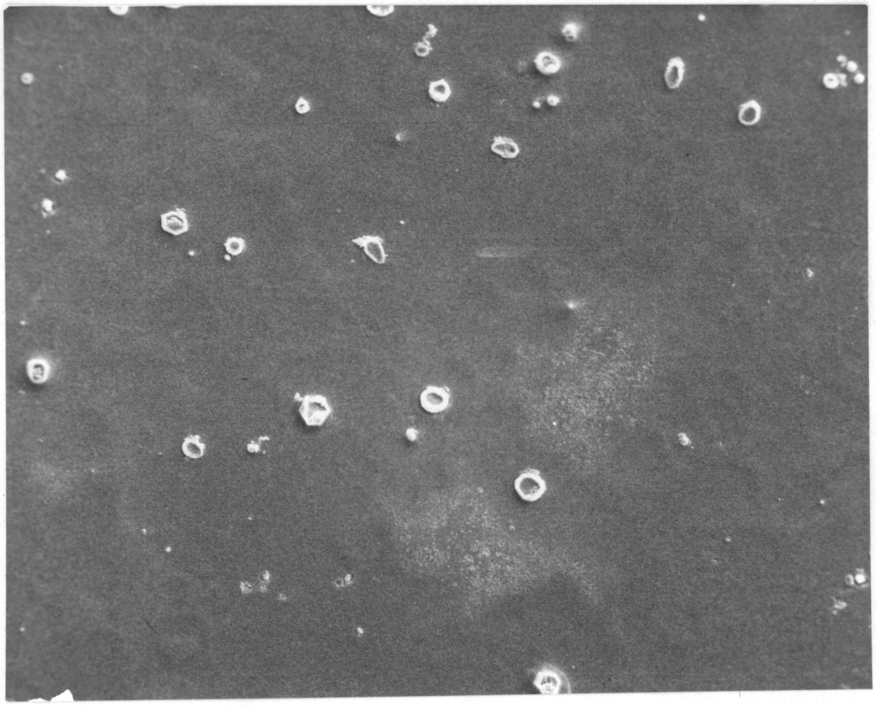

Figure 14a. SEM VO_xH_y Annealed in Oxygen (190X)

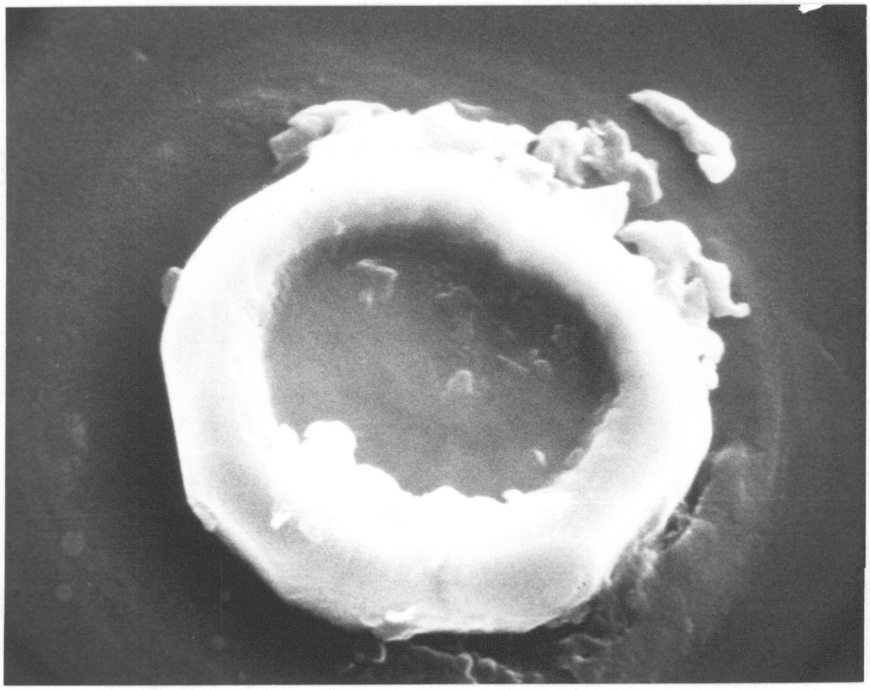

Figure 14b. SEM VO_xH_y Annealed in Oxygen (4,900X)

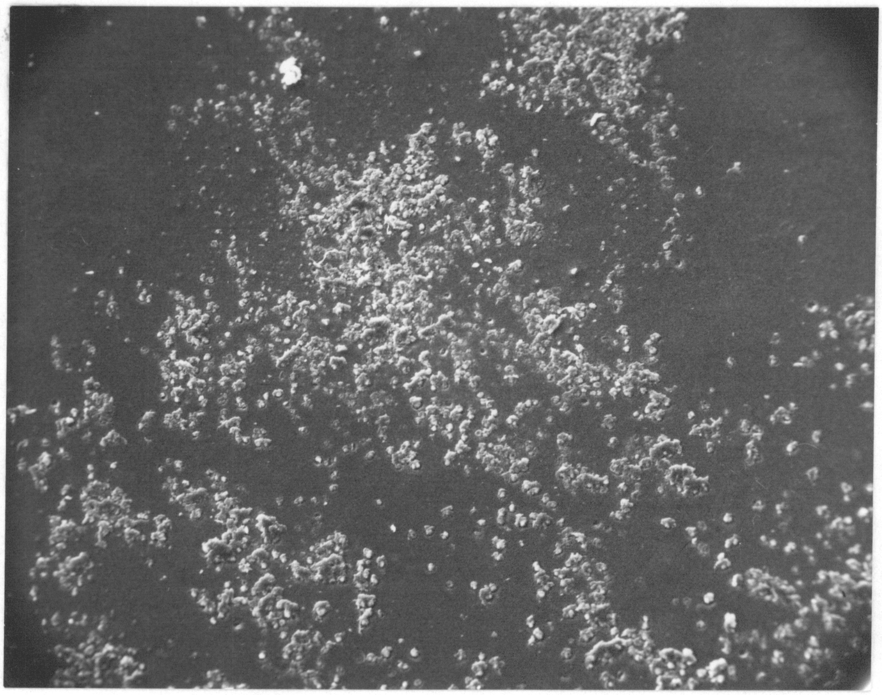

Figure 15a. SEM VO_xH_y Annealed in Oxygen (190X)

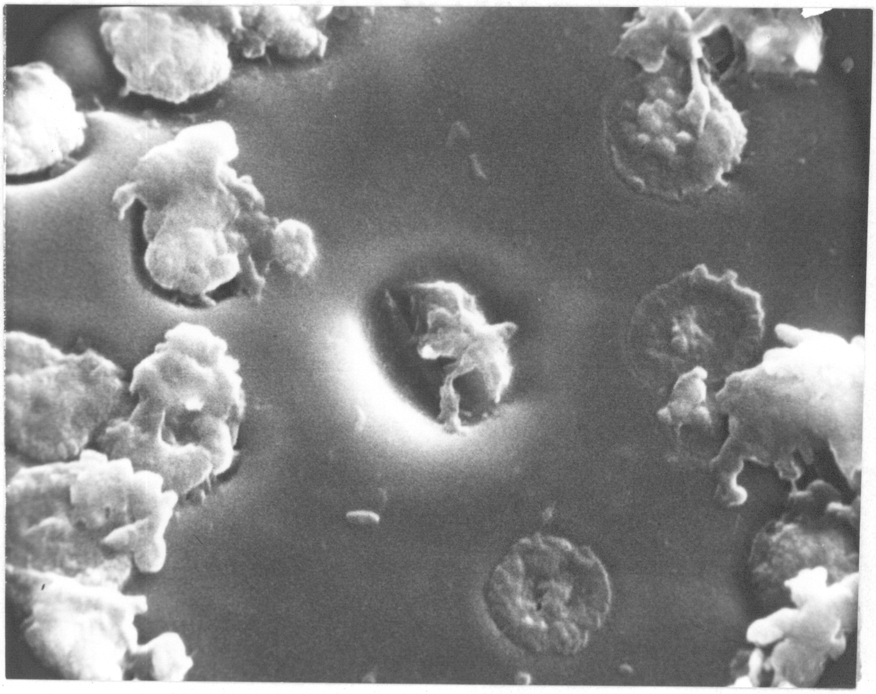

Figure 15b. SEM VO_xH_y Annealed in Oxygen (4,900X)

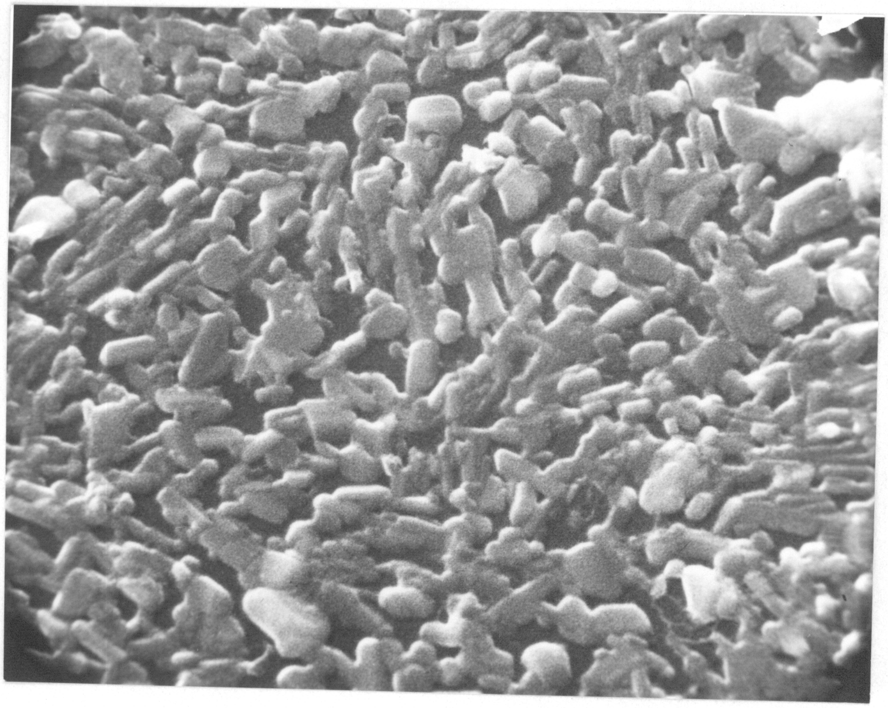

Figure 16a. SEM VO_xH_y Annealed in 95%N_2-5%H_2 (4,900X)

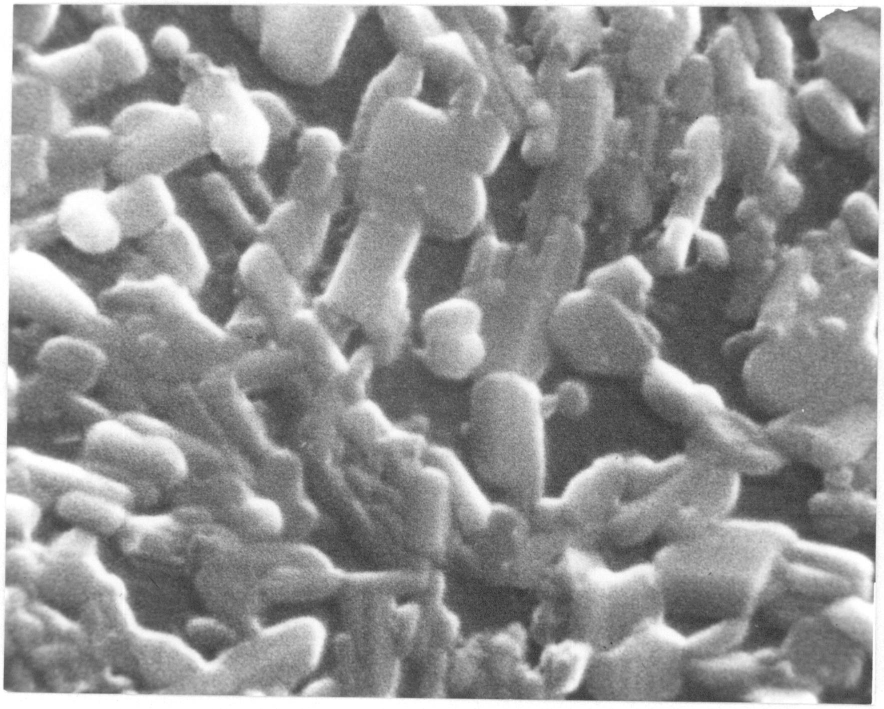

Figure 16b. SEM VO_xH_y Annealed in 95%N_2-5%H_2 (9,800)

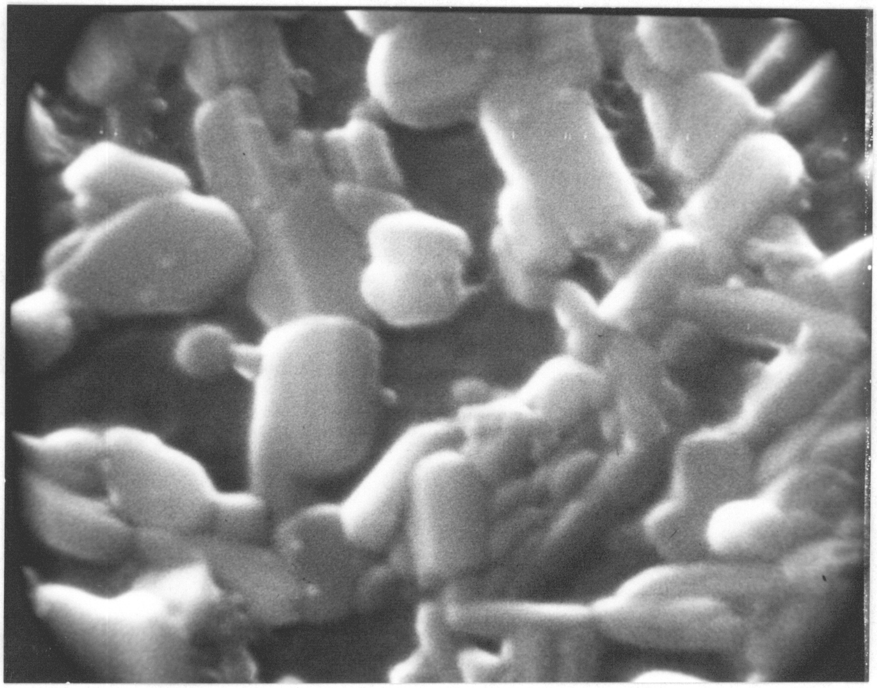

Figure 17. SEM VO_xH_y Annealed in 95%N_2-5%H_2 (19,800X)

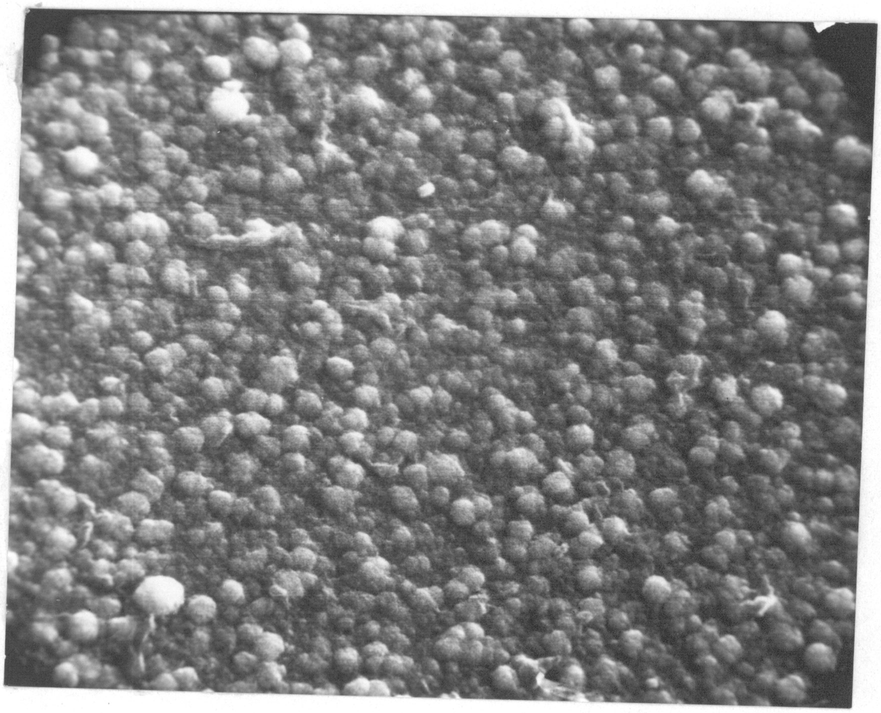

Figure 18a. SEM 60%Fe_2O_3-40%Co_3O_4 5980Å(4,900X)

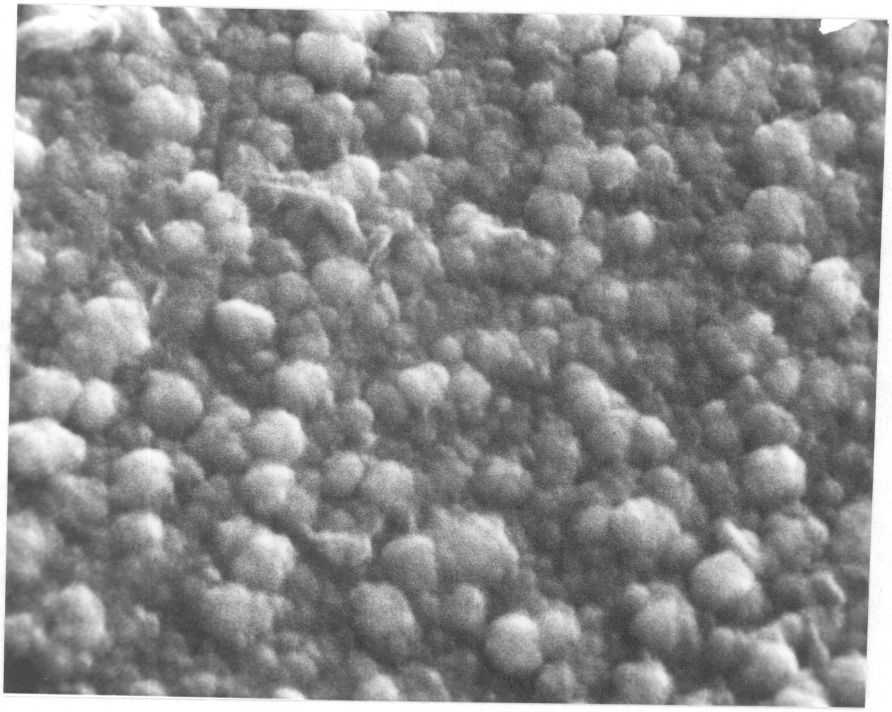

Figure 18b. SEM 60%Fe_2O_3-40%Co_3O_4 5980Å Thick(9,800X)

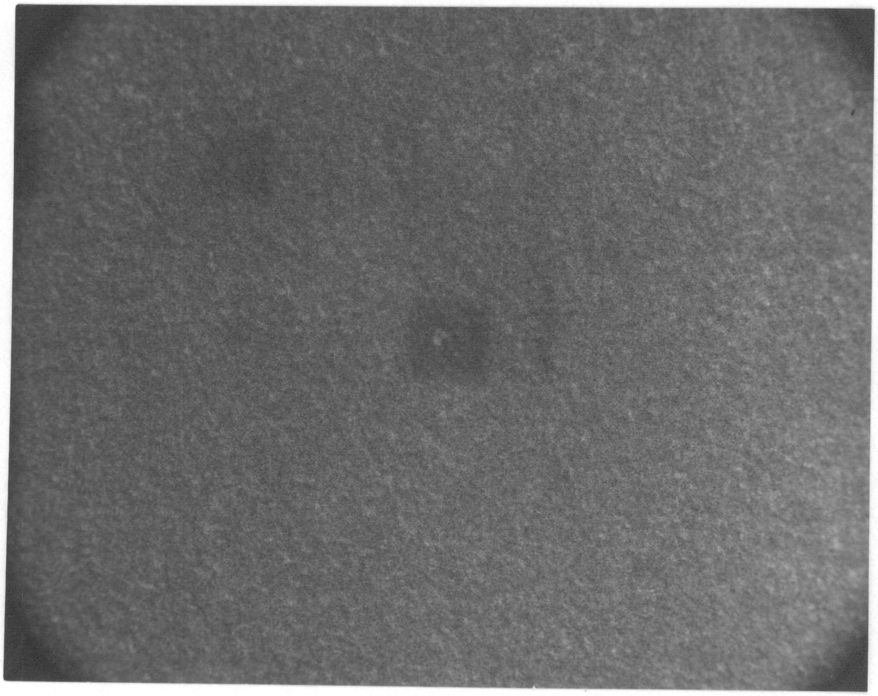

Figure 19. SEM Co_3O_4 600Å Thick (9,800X)

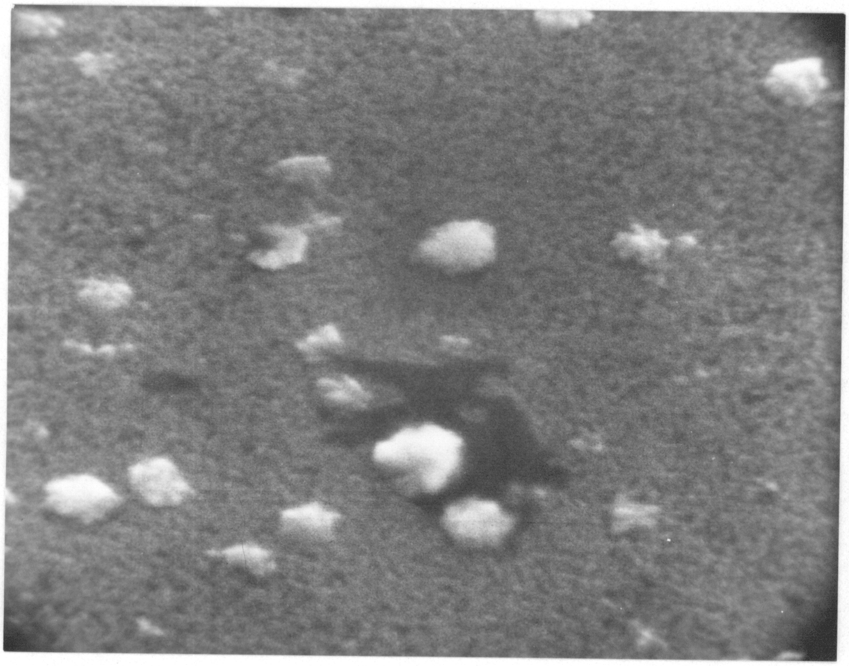

Figure 20a. SEM SnO_2 1390Å Thick(20,000X)

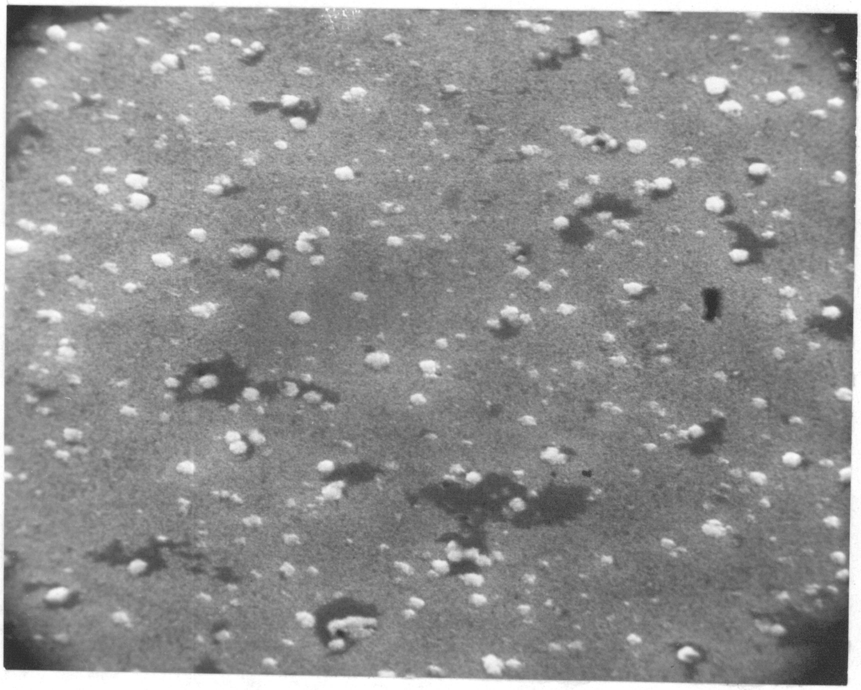

Figure 20b. SEM SnO_2 1390Å Thick(5,000X)

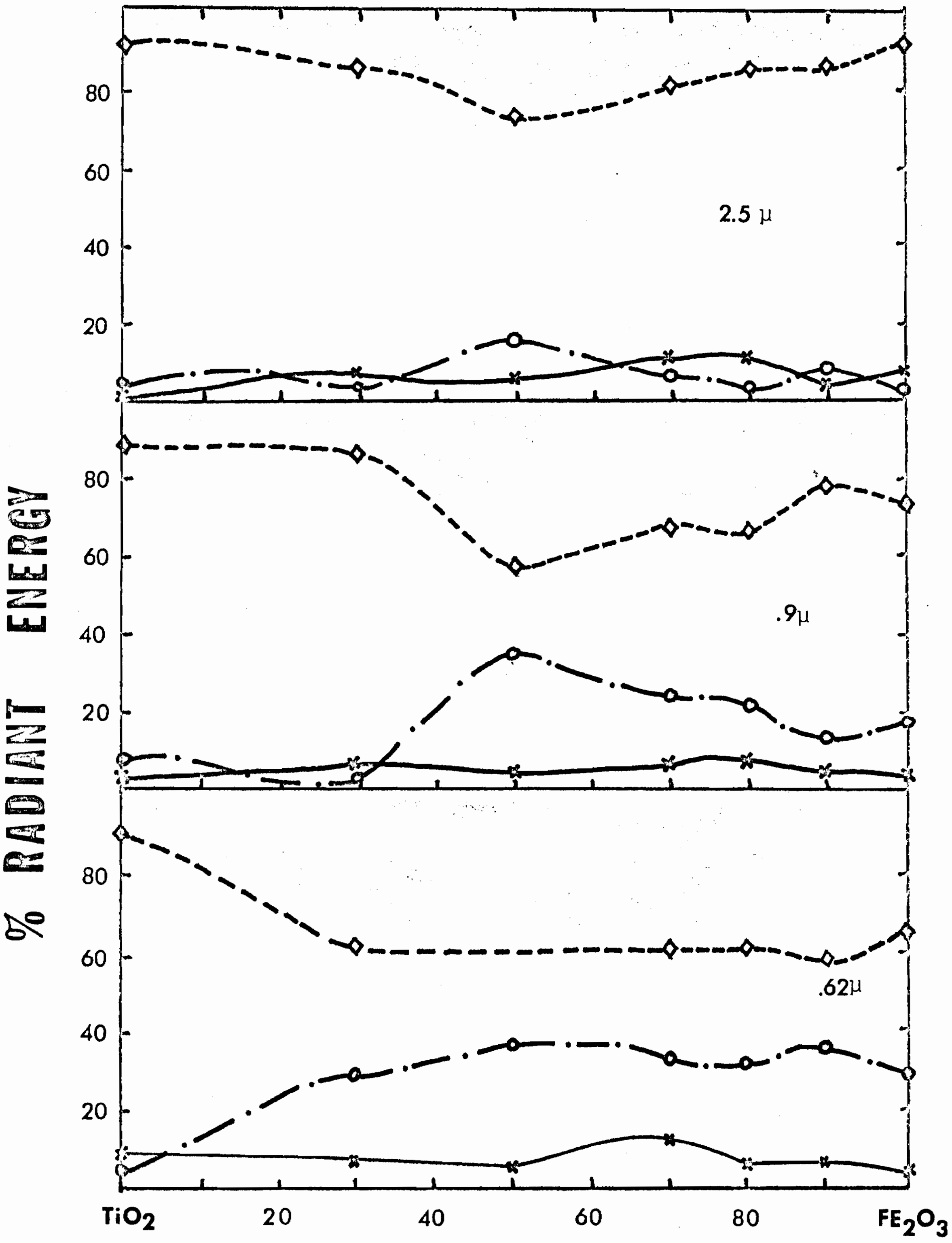

Figure 21. Transmission(◊), Absorbtion(○) and Reflection(✱) at (a). 2.5 μ, (b). 0.9μ and (c). 0.62 μ for the TiO_2 - Fe_2O_3 System.

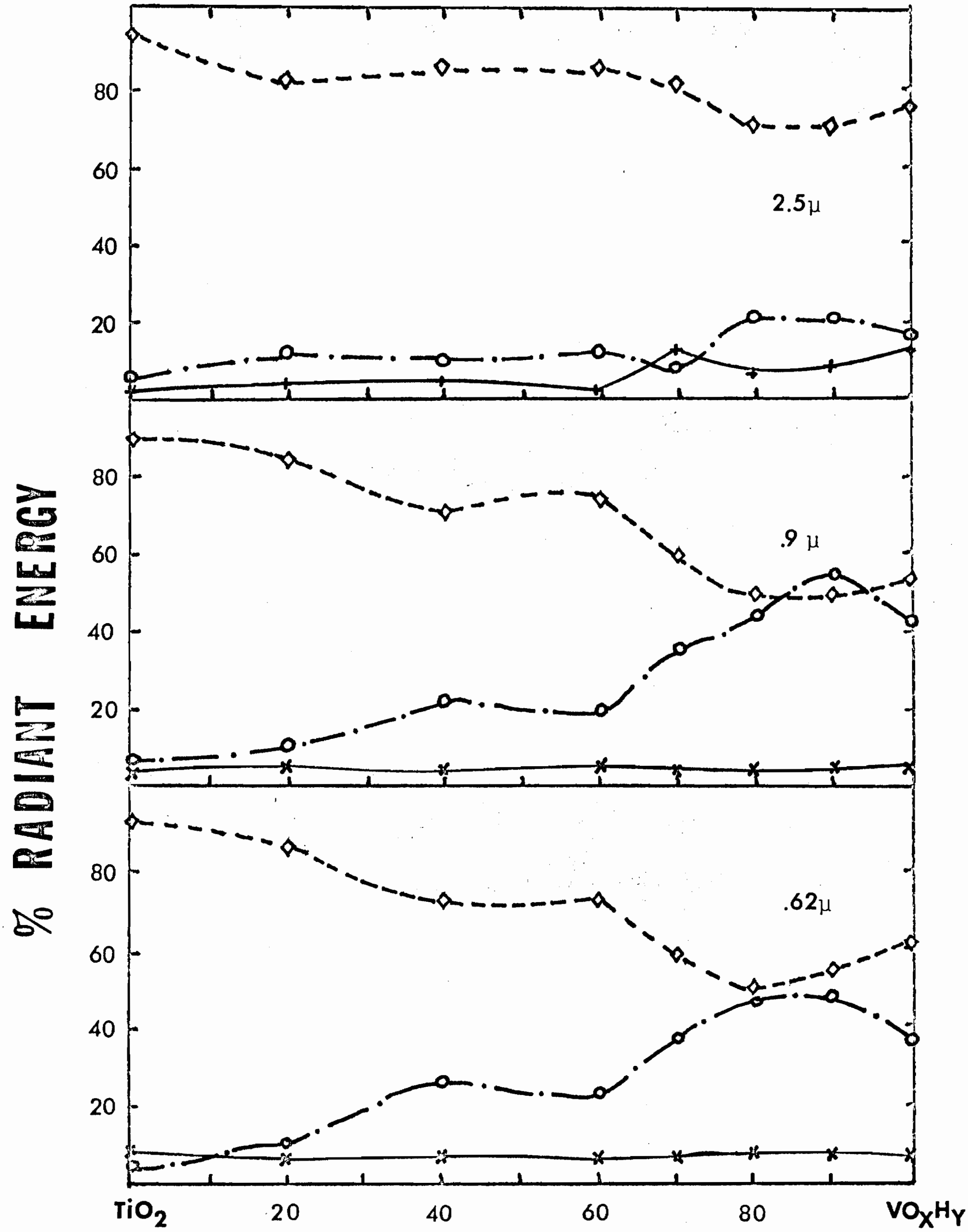

Figure 22. Transmission (◇), Absorption (○), and Reflection (×) at (a). 2.5μ, (b). 0.9μ and (c). 0.62μ for the TiO_2 - VO_xH_y System.

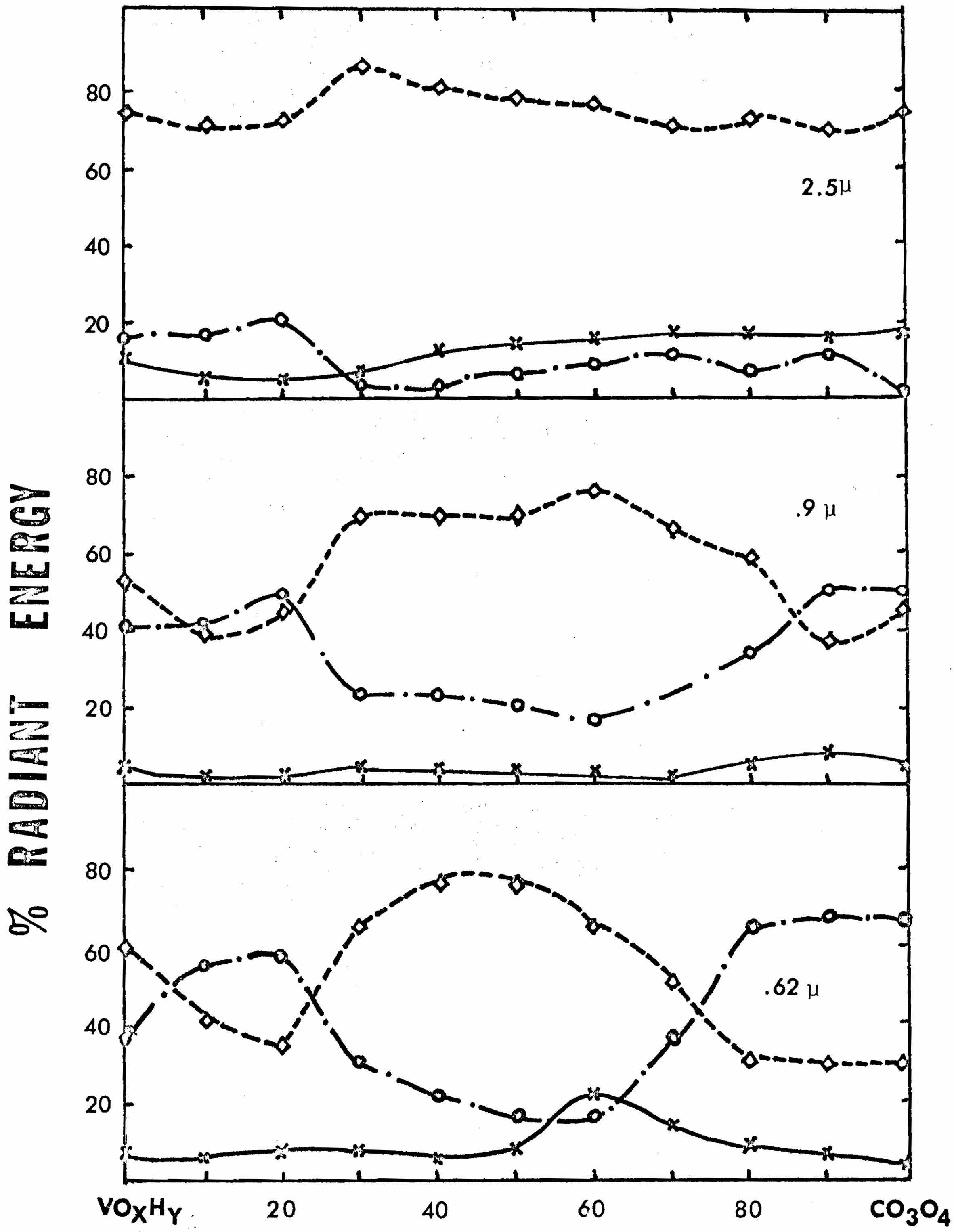

Figure 23. Transmission (◊), Absorption (○) and Reflection (✱) at (a) 2.5μ, (b) 0.9μ and (c) 0.62μ for the VO_xH_y - Co_3O_4 System.

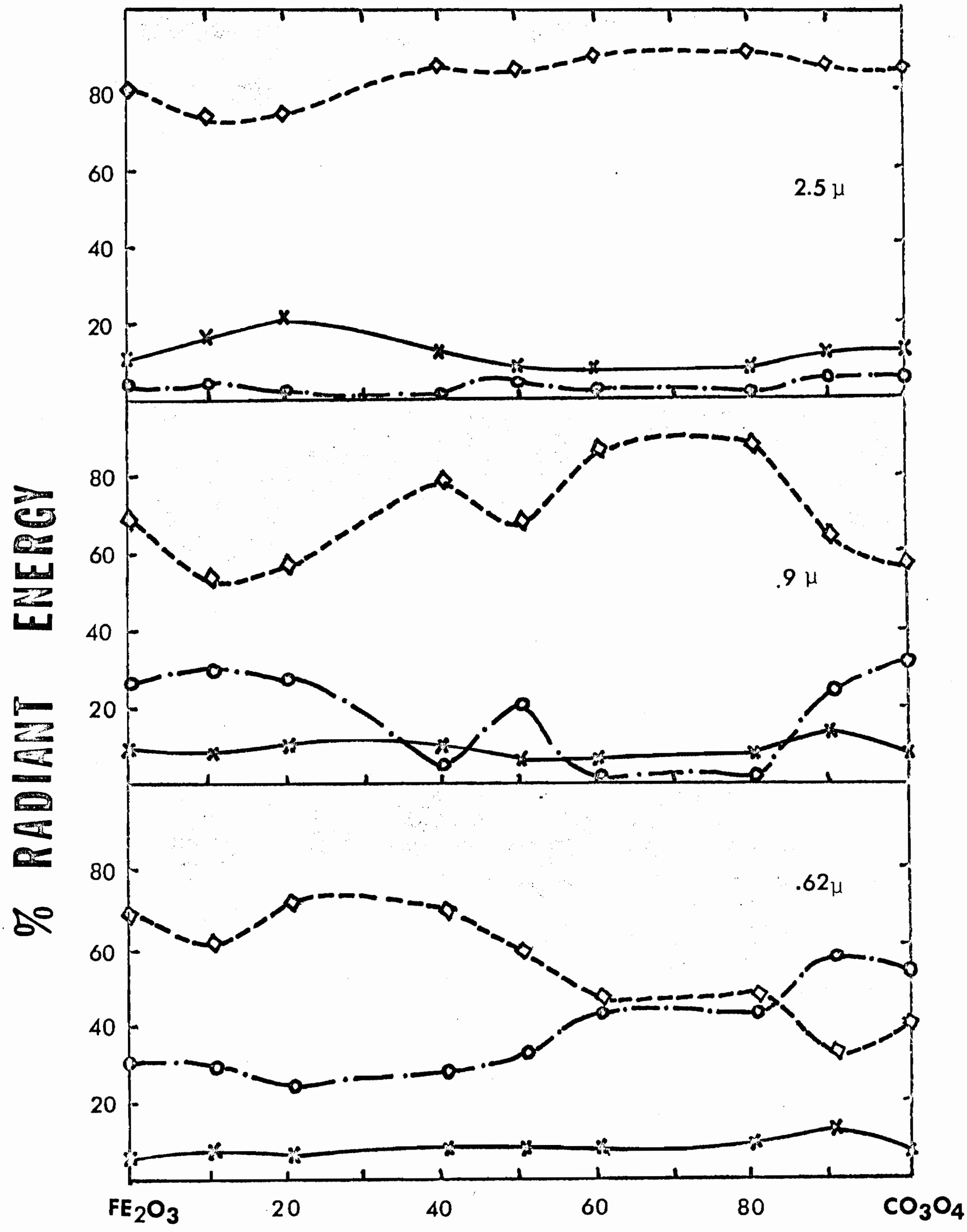

Figure 24. Transmission (◊), Absorption (○) and Reflection (×) at (a) 2.5μ, (b) 0.9μ and (c) 0.62μ for the Fe_2O_3 - Co_3O_4 System. (500-600A)

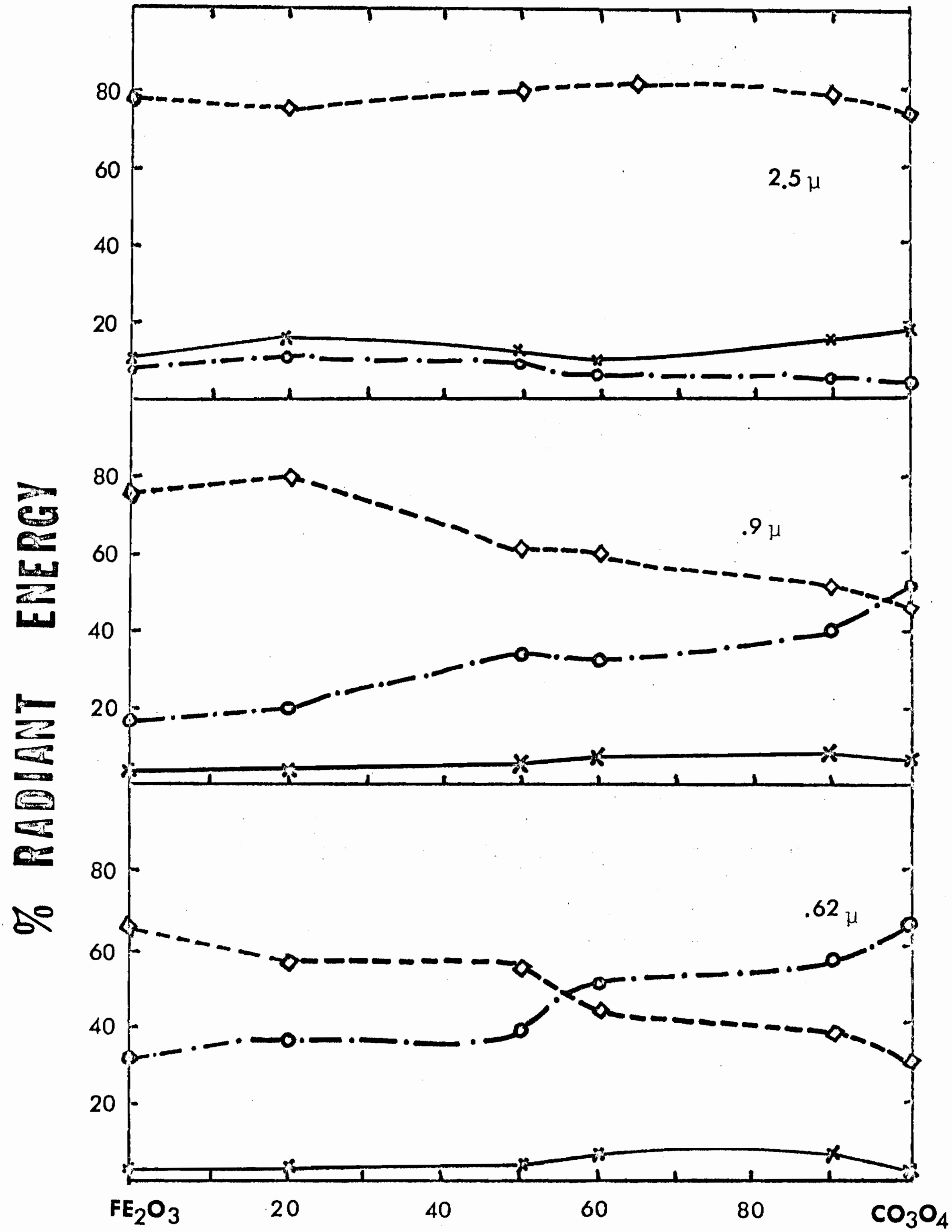

Figure 25. Transmission (◊), Absorption (○) and Reflection (×) at (a) 2.5μ, (b) 0.9μ and (c) 0.62μ for the Fe_2O_3 - Co_3O_4 System. (700-800Å)

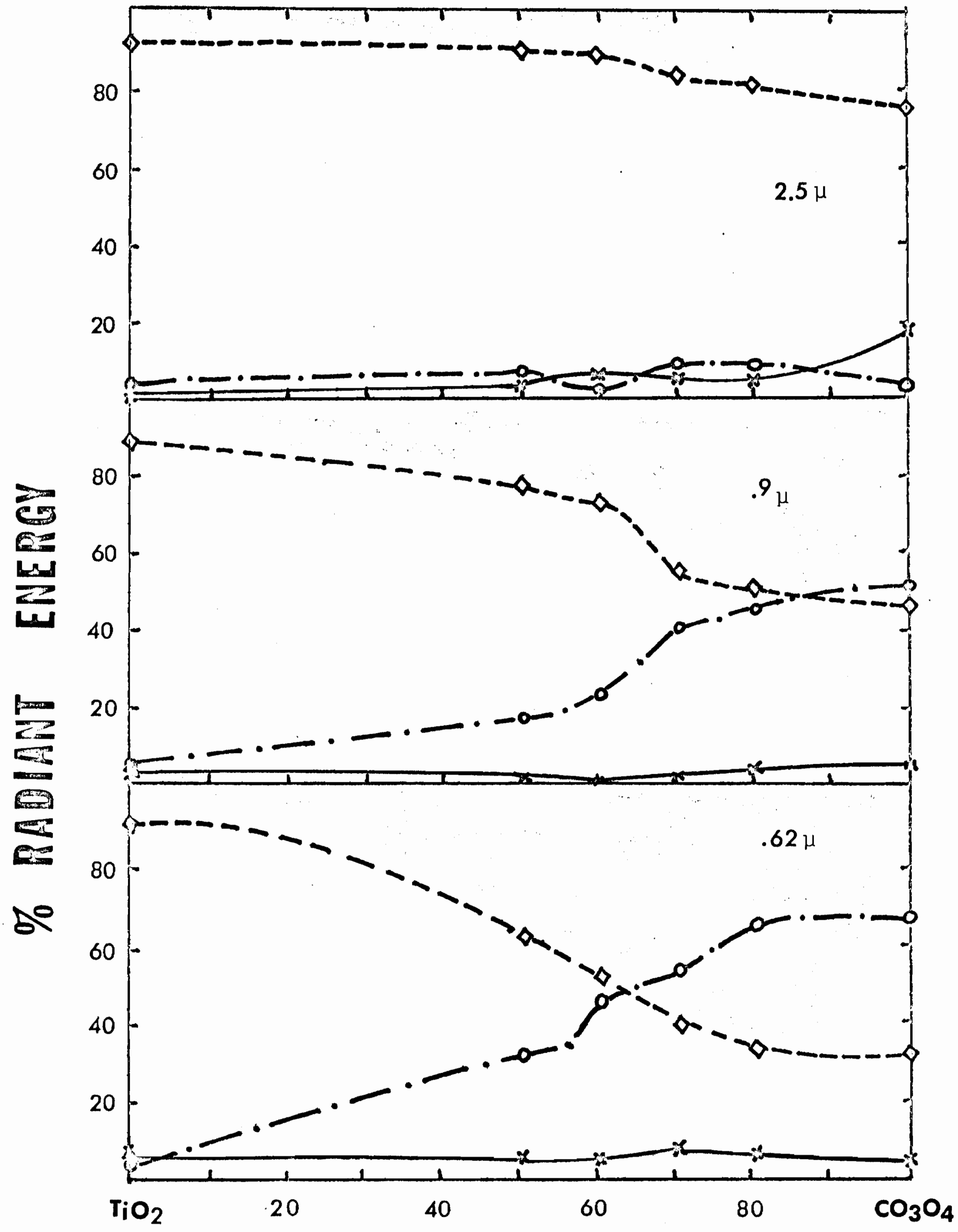

Figure 26. Transmission (◇), Absorption (○) and Reflection (✕) at (a) 2.5μ, (b) 0.9μ and (c) 0.62μ for the TiO_2 - Co_3O_4 System.

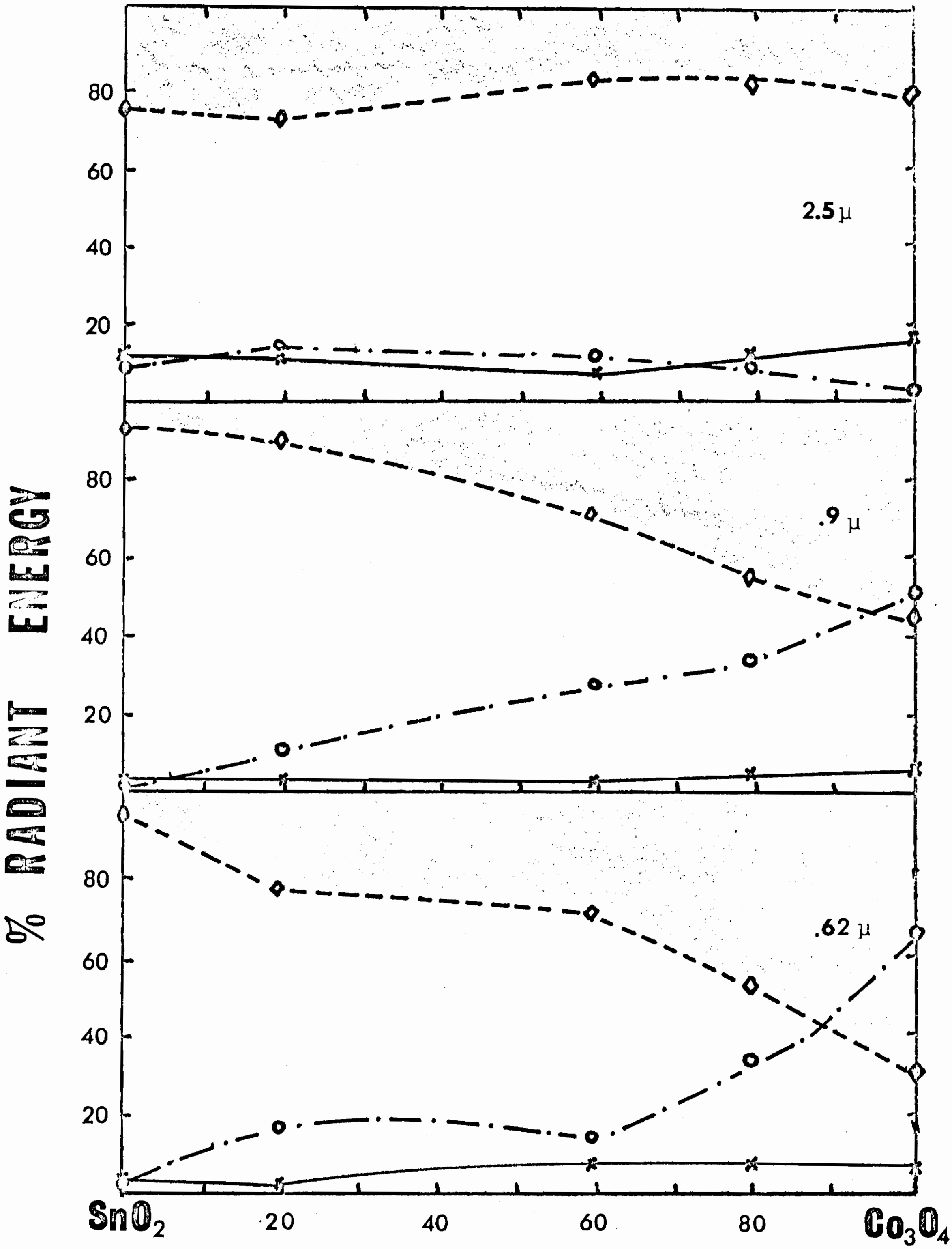

Figure 27. Transmission (◊), Absorption (o) and Reflection (x) at (a) 2.5μ, (b) 0.9μ and (c) 0.62μ for the SnO_2 - Co_3O_4 System.

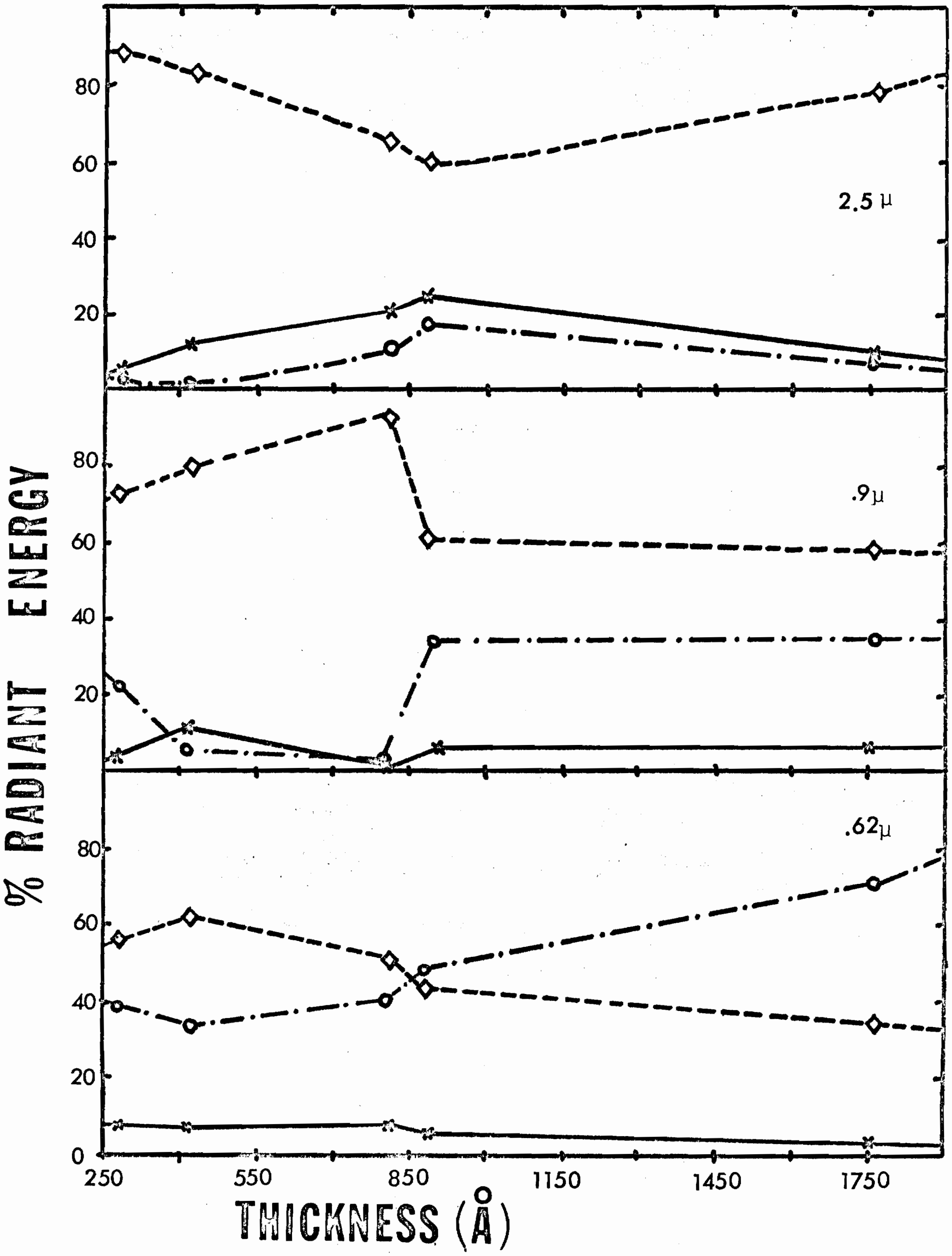

Figure 28. Relation of Optical Properties with Thickness for 60% Fe_2O_3-40% Co_3O_4, Transmission ( ), Absorption ( ), Reflection ( ).

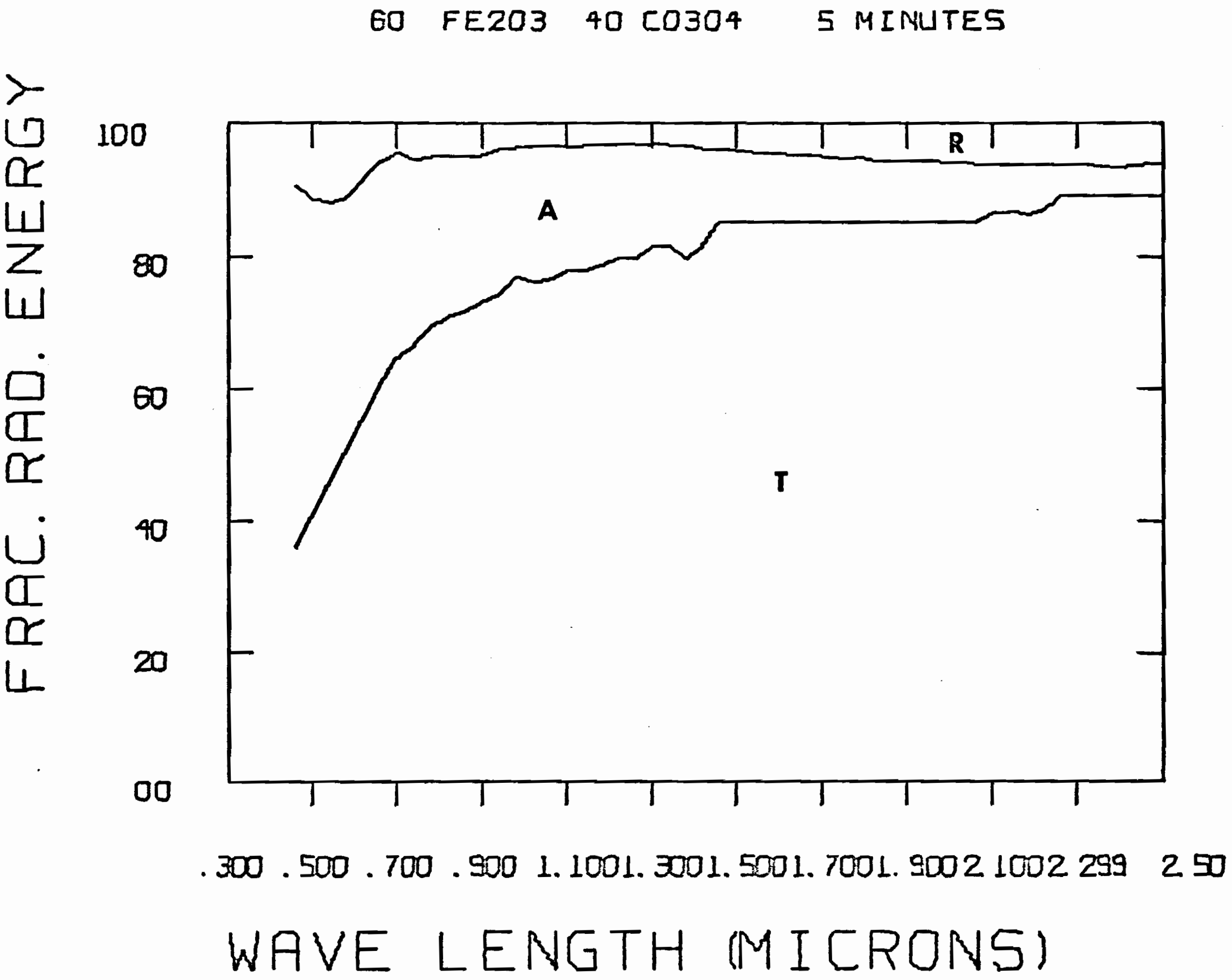

Figure 29. Optical Properties of a 60% Fe_2O_3- 40% Co_3O_4 Film 265Å Thick.

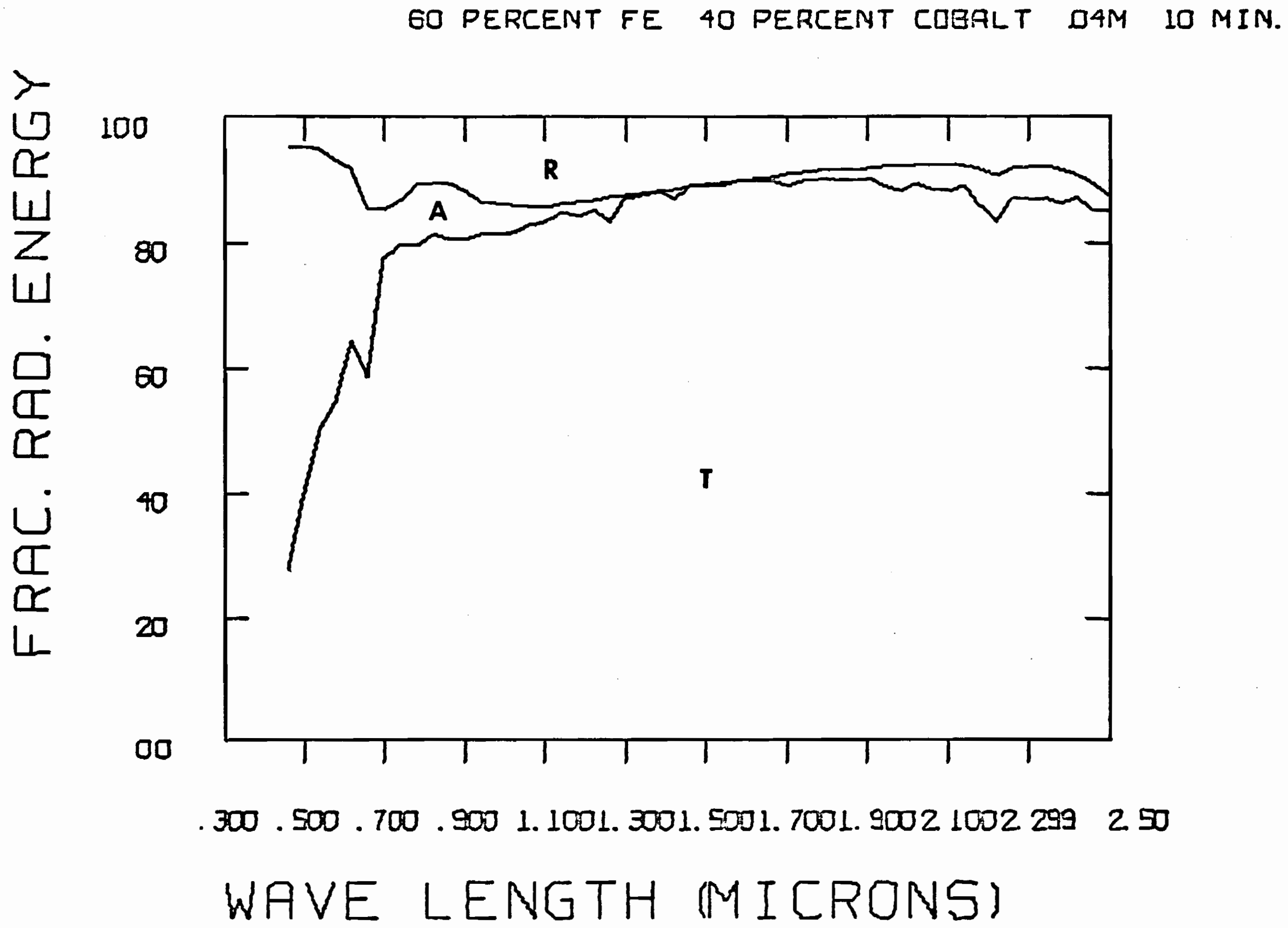

Figure 30. Optical Properties of a 60% Fe_2O_3-40%Co_3O_4 Film 441Å Thick.

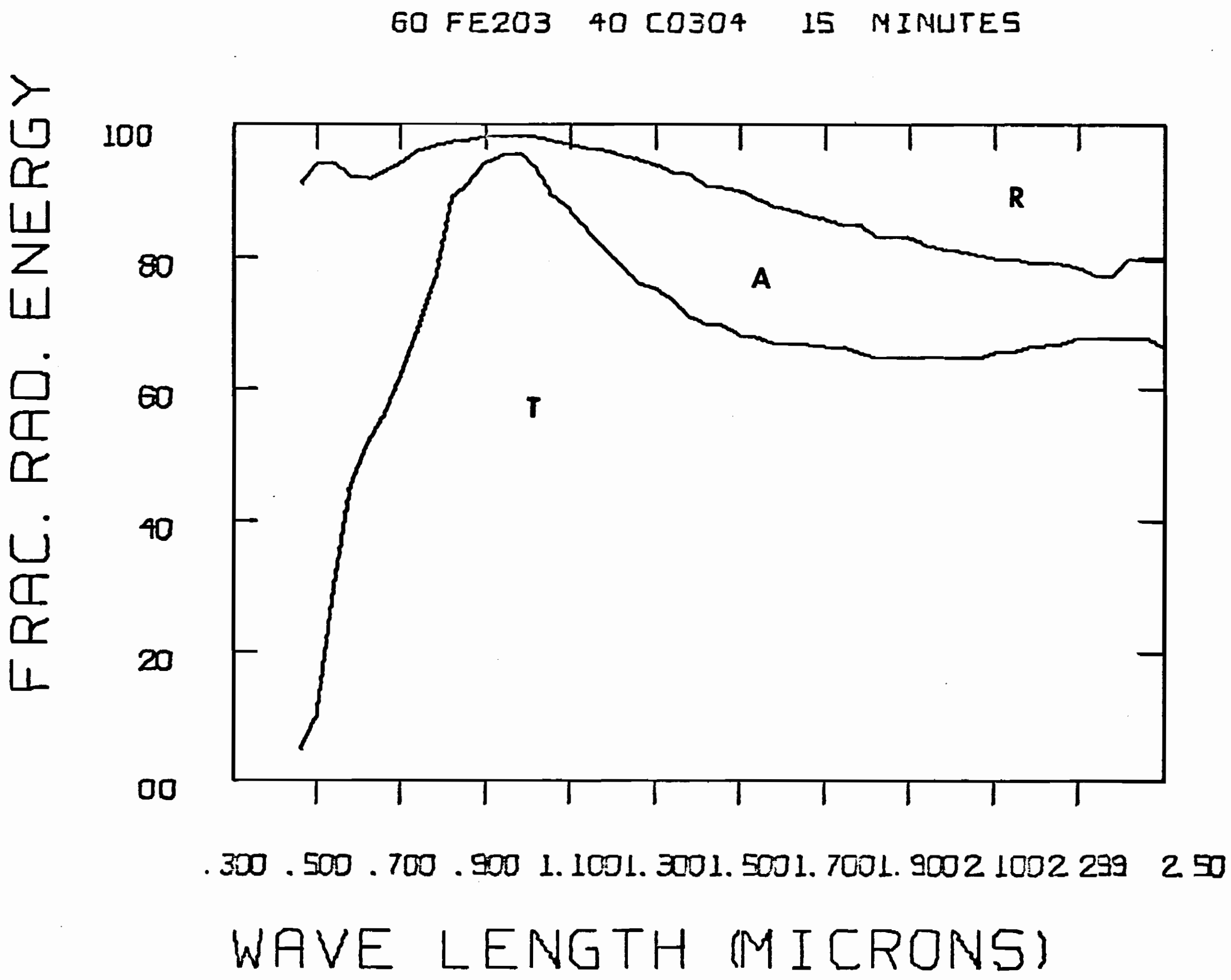

Figure 31. Optical Properties of a 60% Fe_2O_3-40% Co3O_4 Film 815Å Thick.

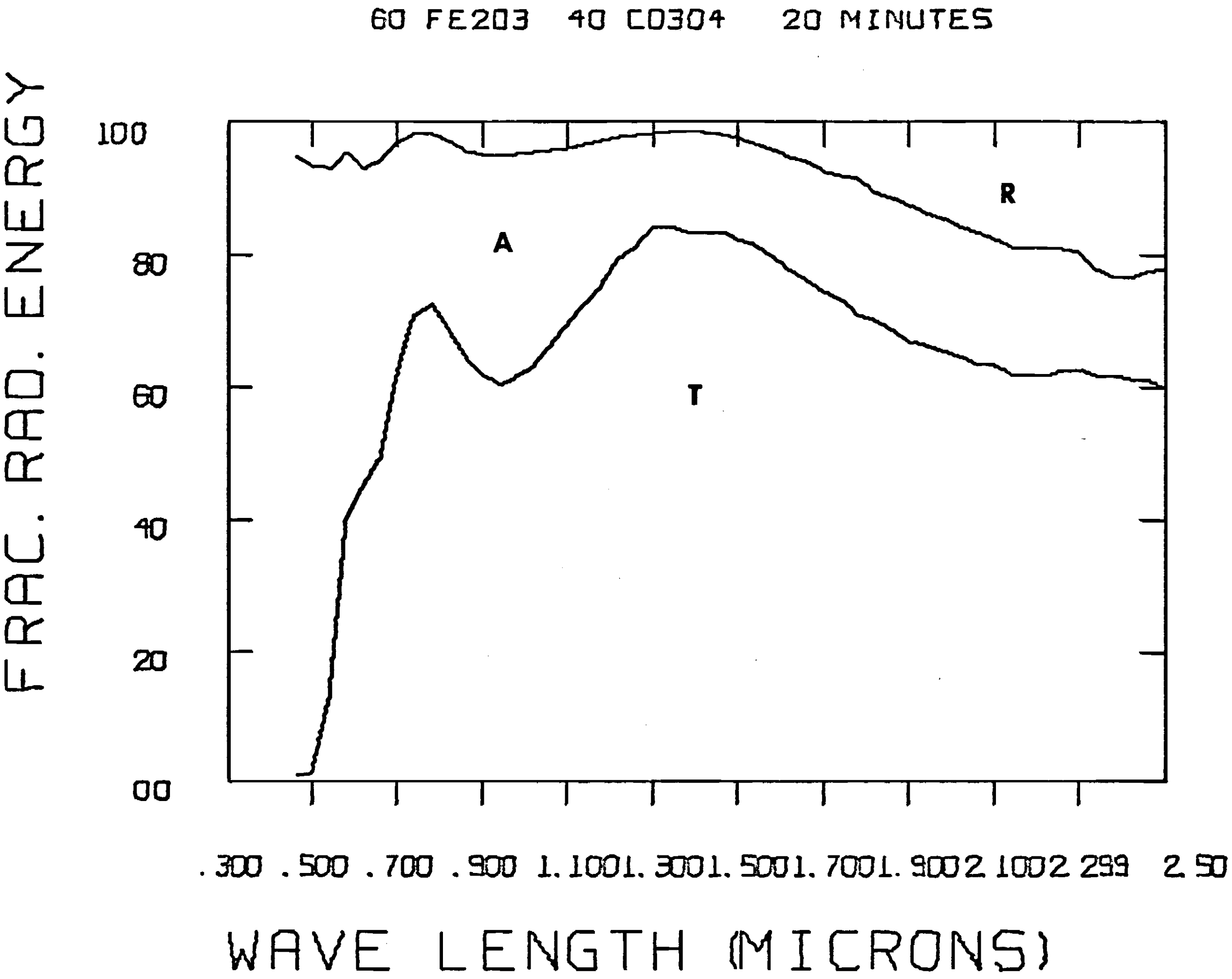

Figure 32. Optical Properties of a 60% Fe_2O_3-40% Co_3O_4 Film **907 Å** Thick.

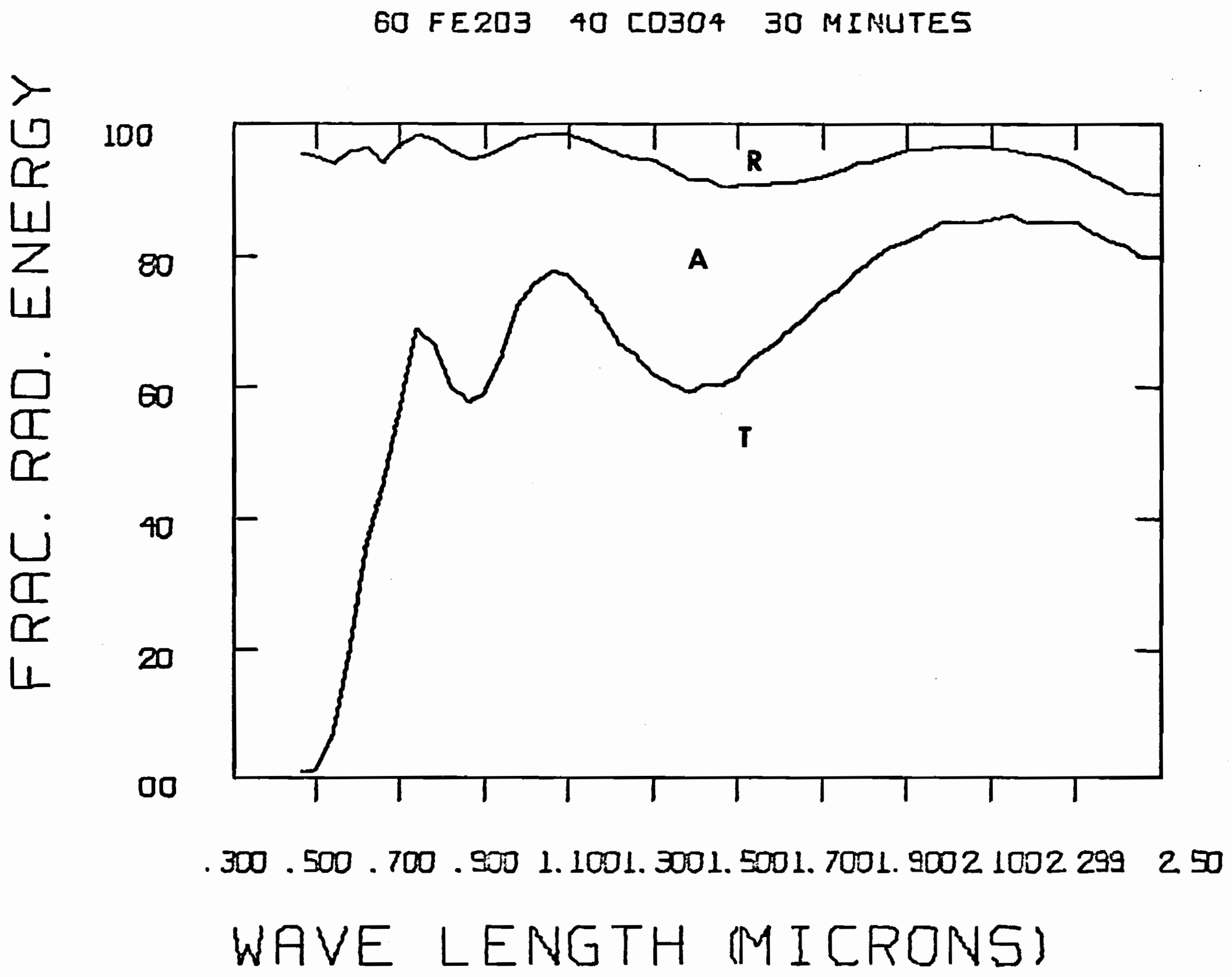

Figure 33. Optical Properties of a 60% Fe_2O_3-40% Co_3O_4 Film 1759Å Thick.

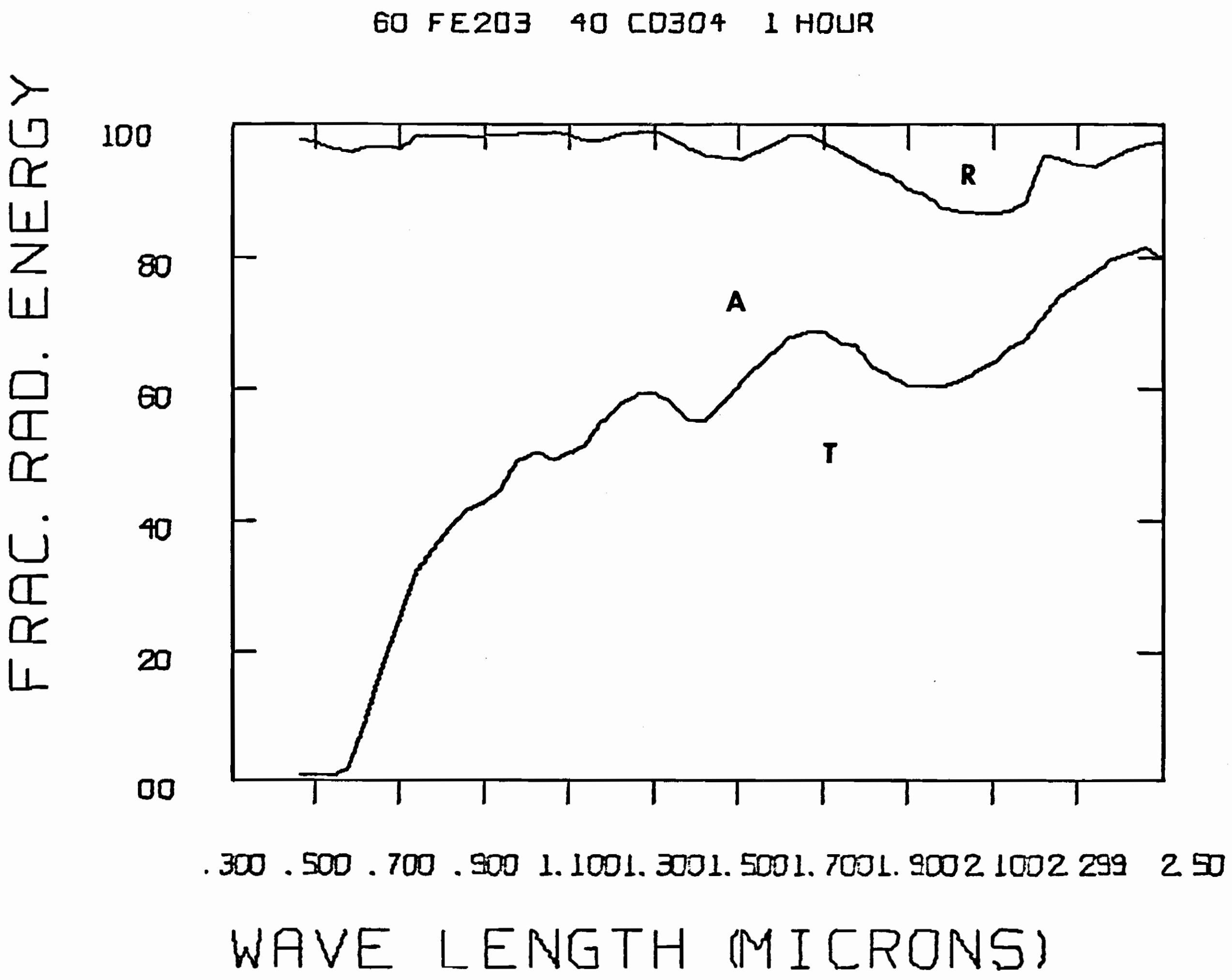

Figure 34. Optical Properties of a 60% Fe_2O_3-40% Co_3O_4 Film 5980Å Thick.

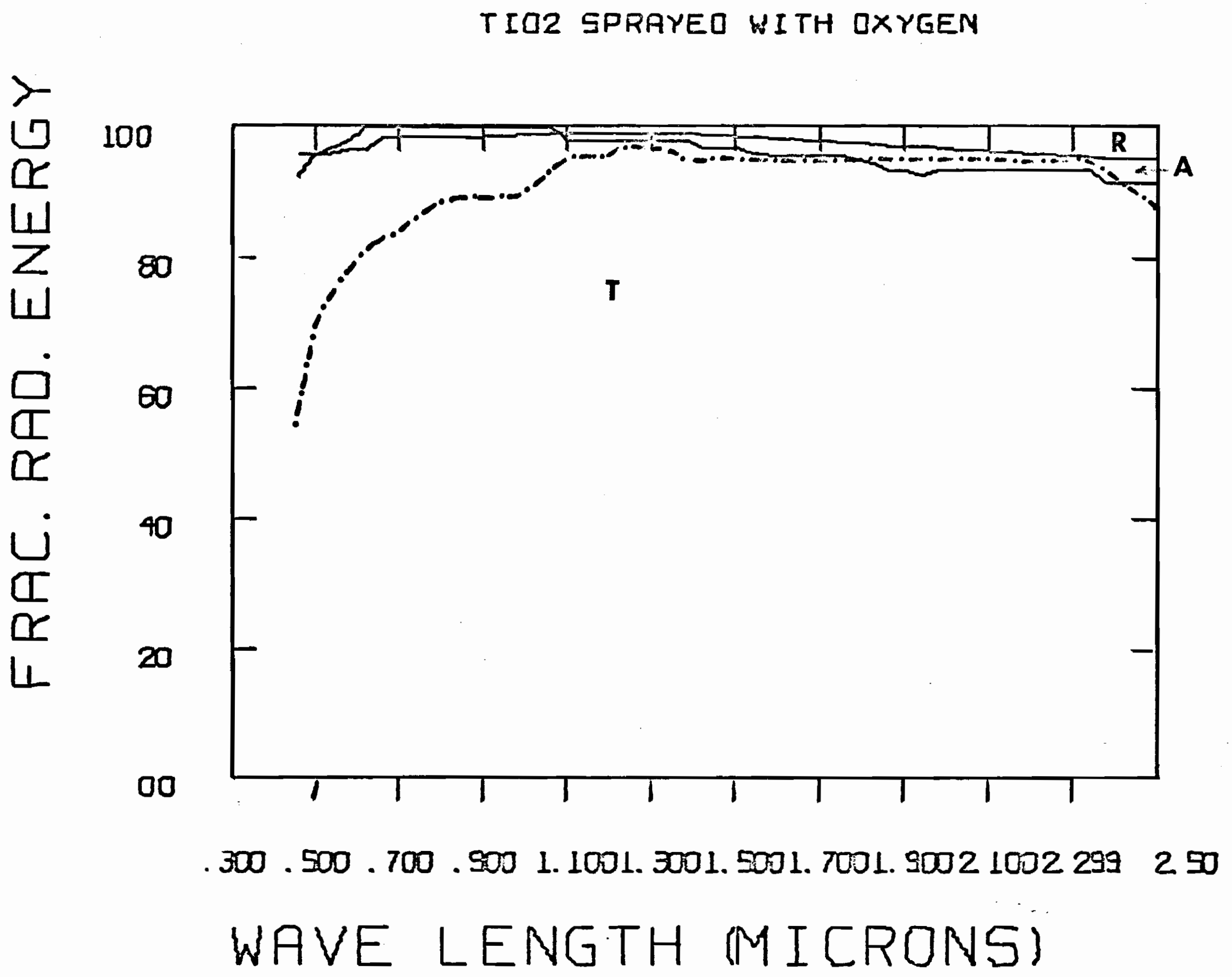

Figure 35 . Optical Properties of a TiO_2 Film Sprayed With Oxygen as Compared With an Air Reference. -·-·

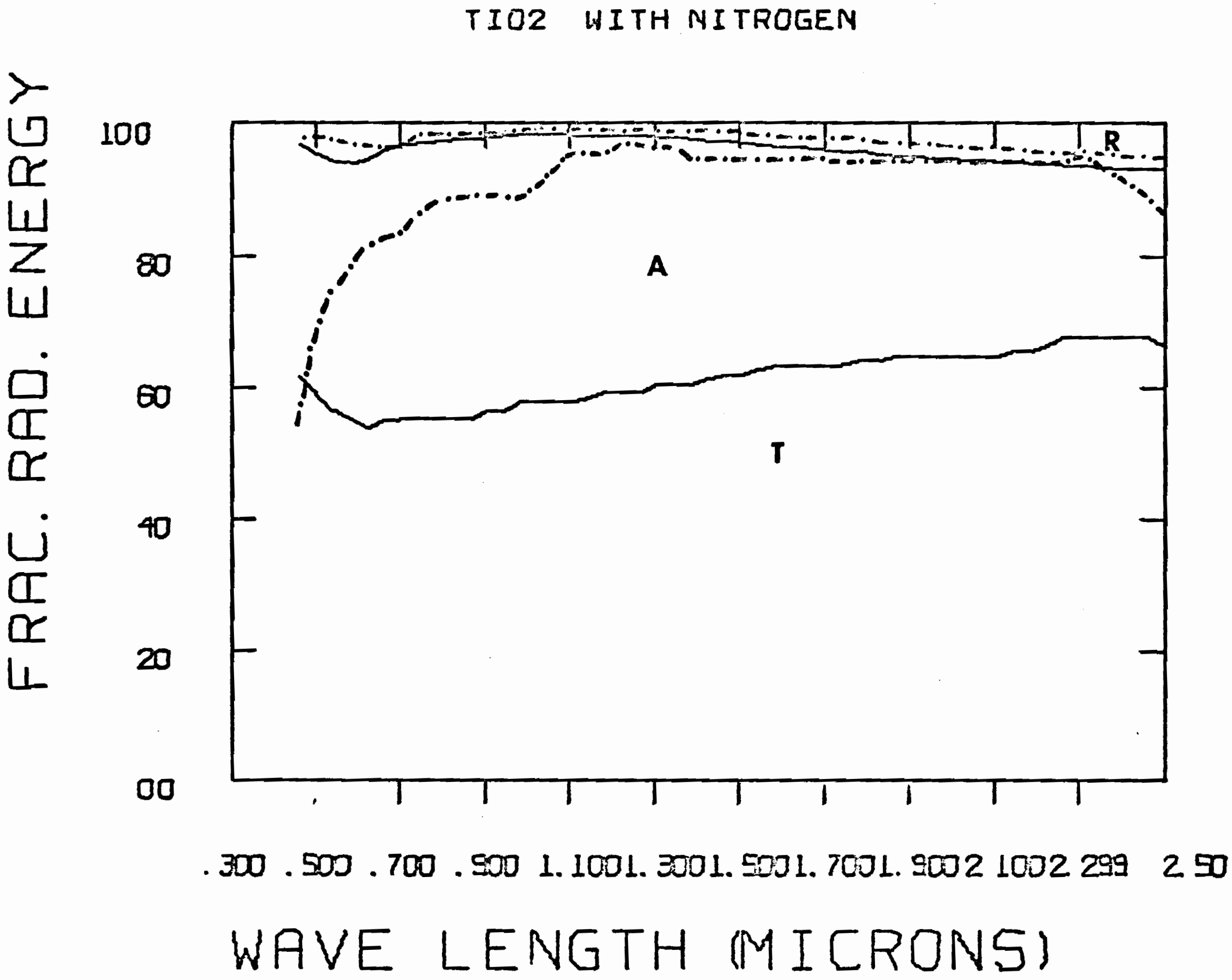

Figure 36. Optical Properties of a TiO_2 Film Spray With Nitrogen as Compared With an Air Reference ·—·—

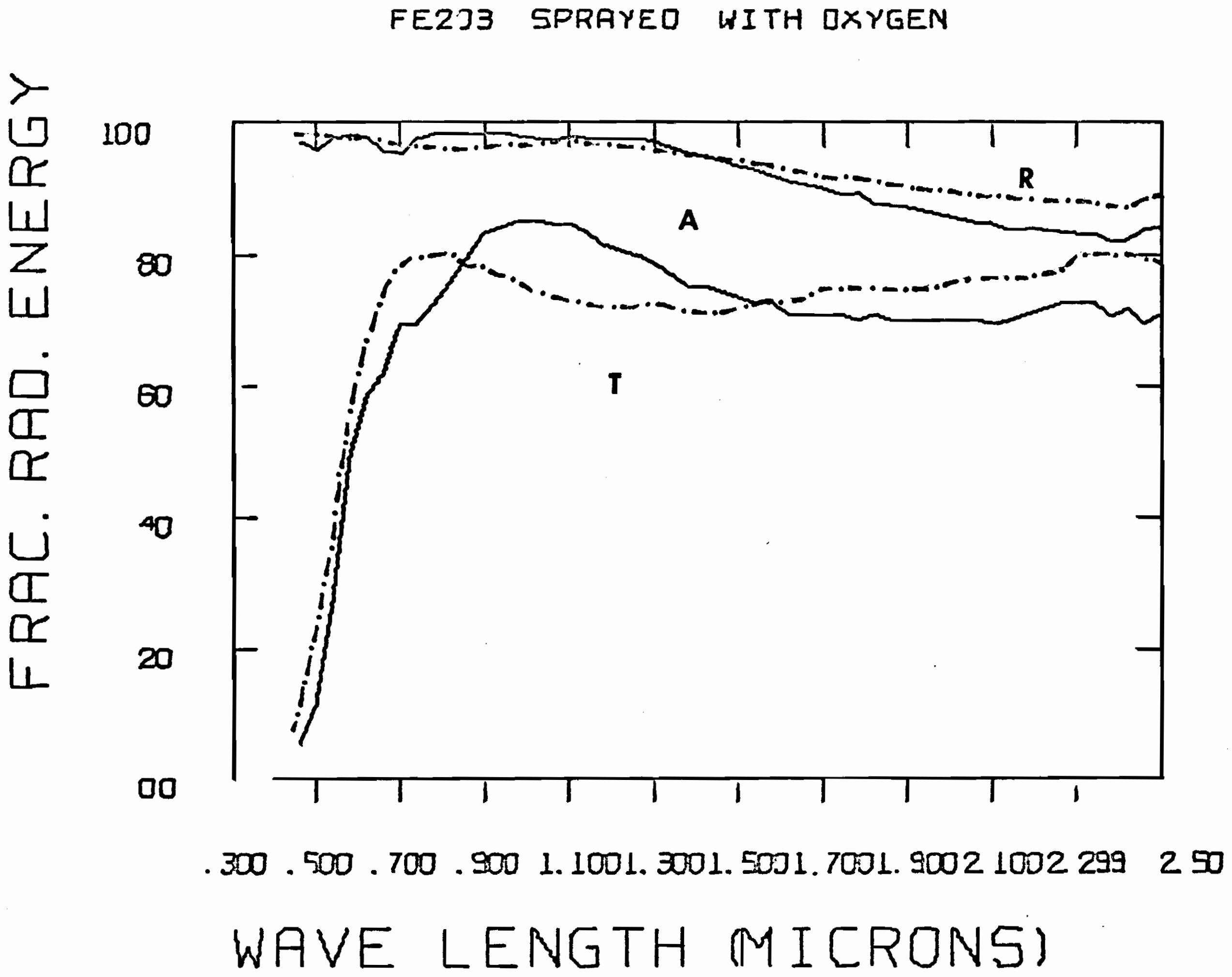

Figure 37. Optical Properties of a Fe2O3 Film Sprayed With Oxygen as Compared With an Air Reference. ·—·—

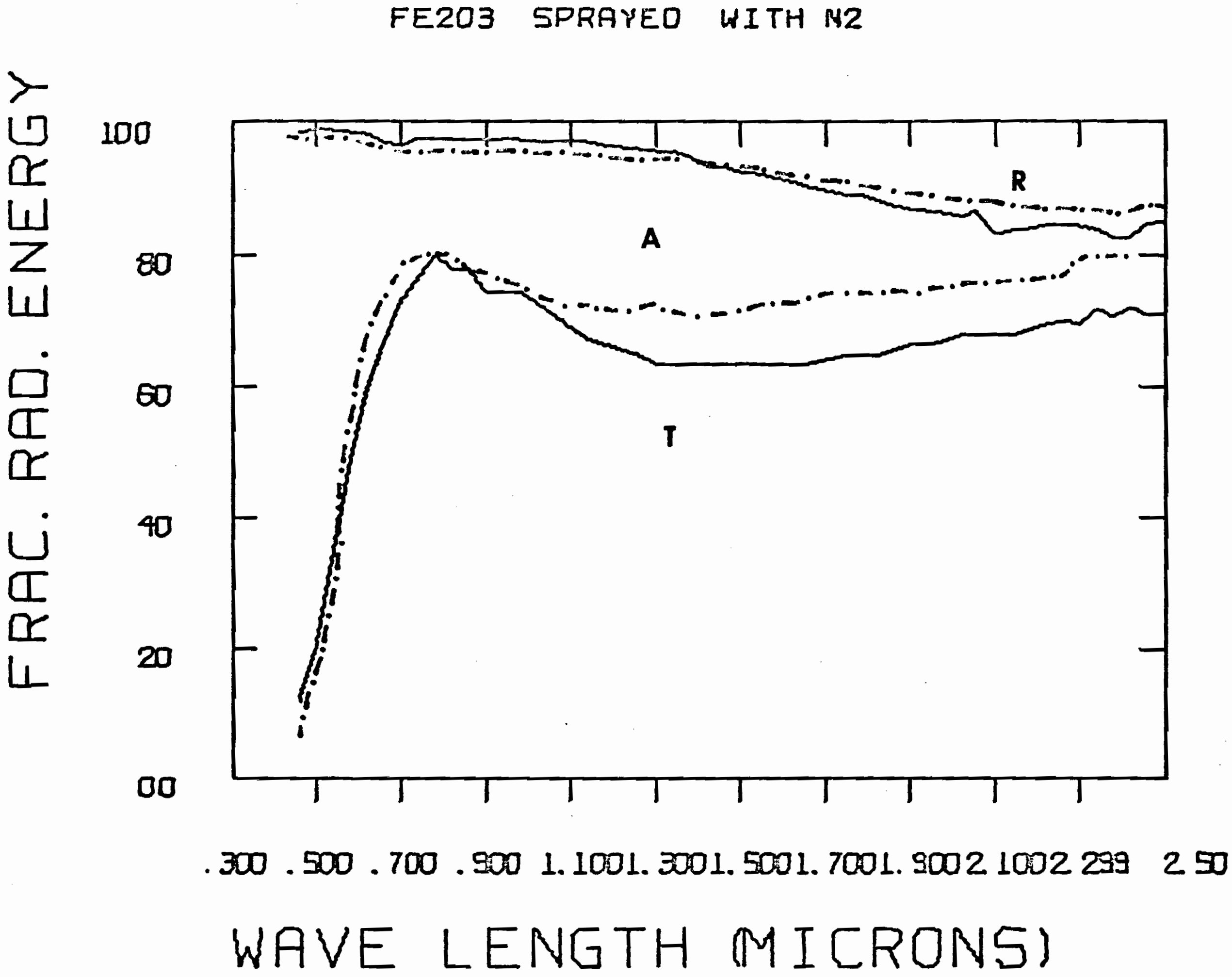

Figure 38. Optical Properties of a Fe_2O_3 Film Sprayed With Nitrogen as Compared With an Air Reference. ·—·—

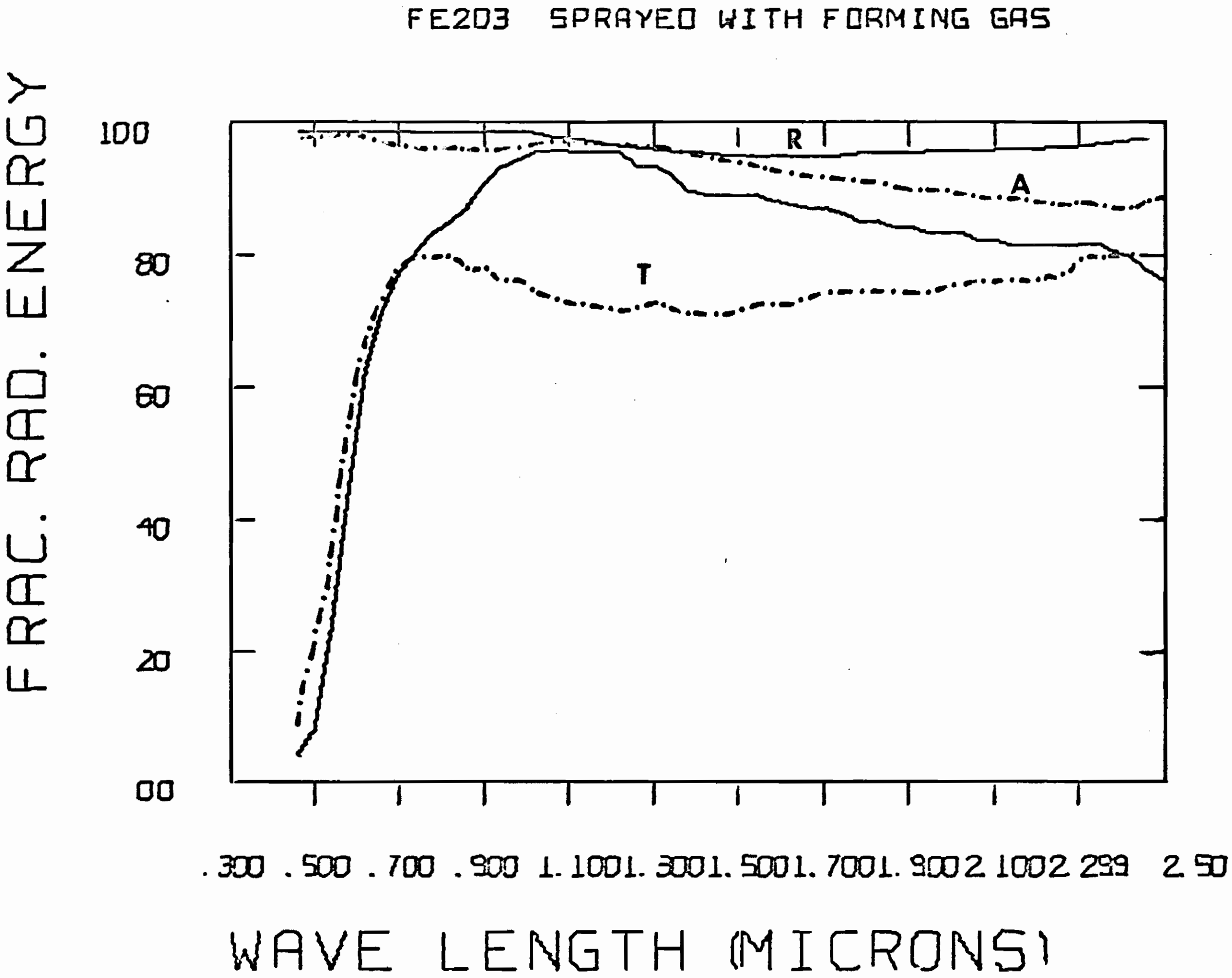

Figure 39. Optical Properties of a Fe_2O_3 Film Sprayed With Forming Gas as Compared With an Air Reference. •—•—

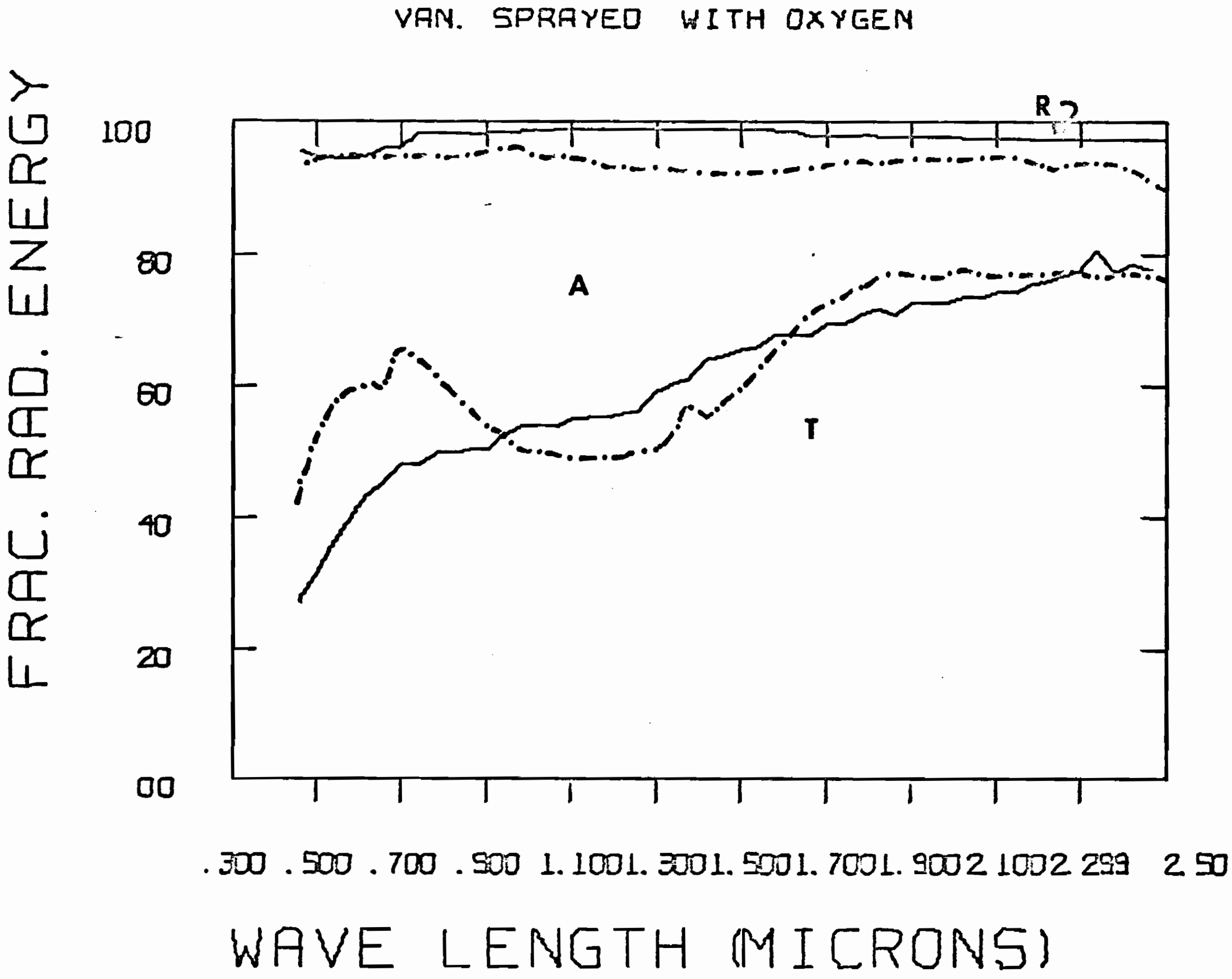

Figure 40. Optical Properties of a VO_xH_y Film Sprayed With Oxygen as Compared With an Air Reference. —·—

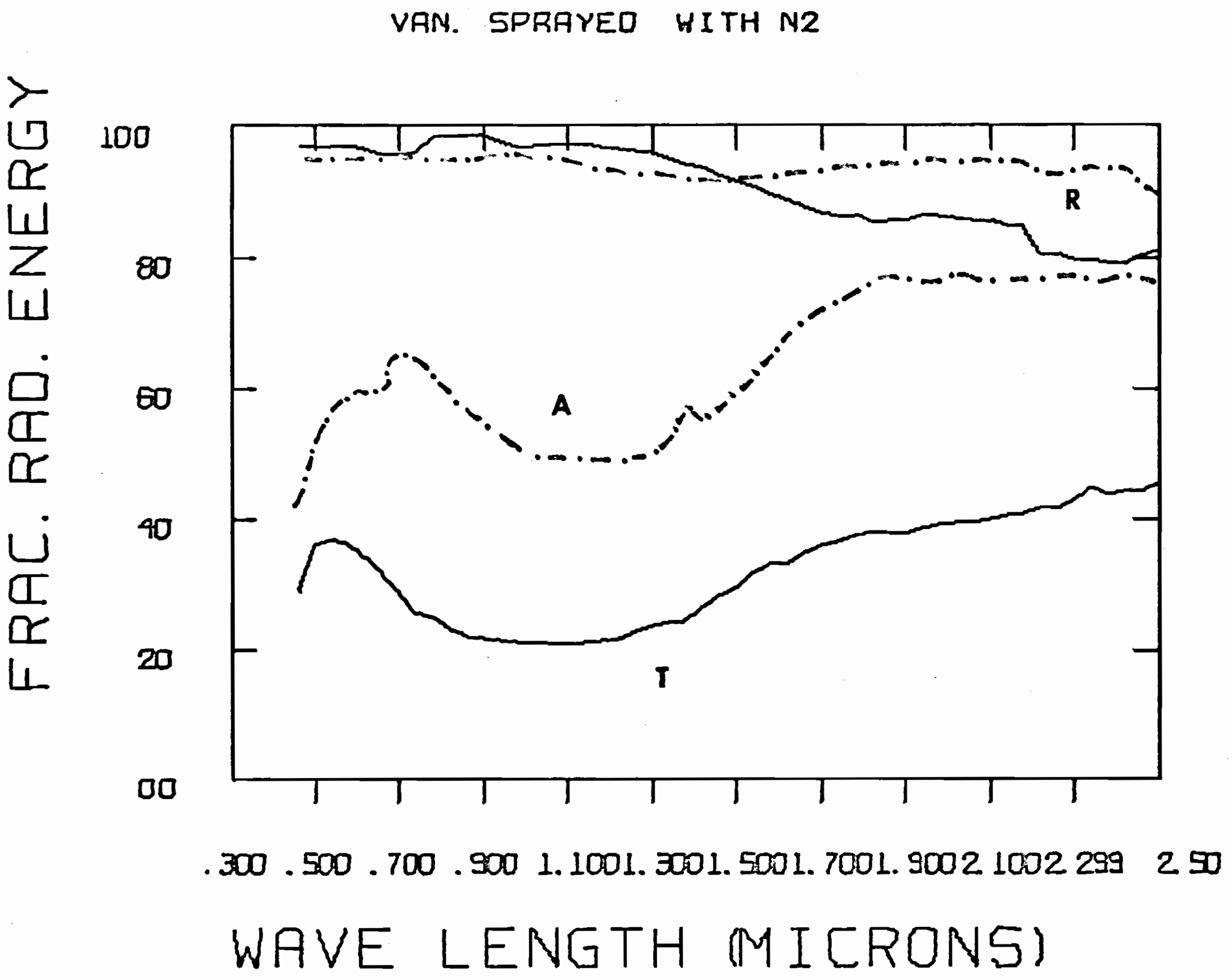

Figure 41. Optical Properties of a VO_xH_y Film Sprayed With Nitrogen as Compared With an Air Reference. ·—·—

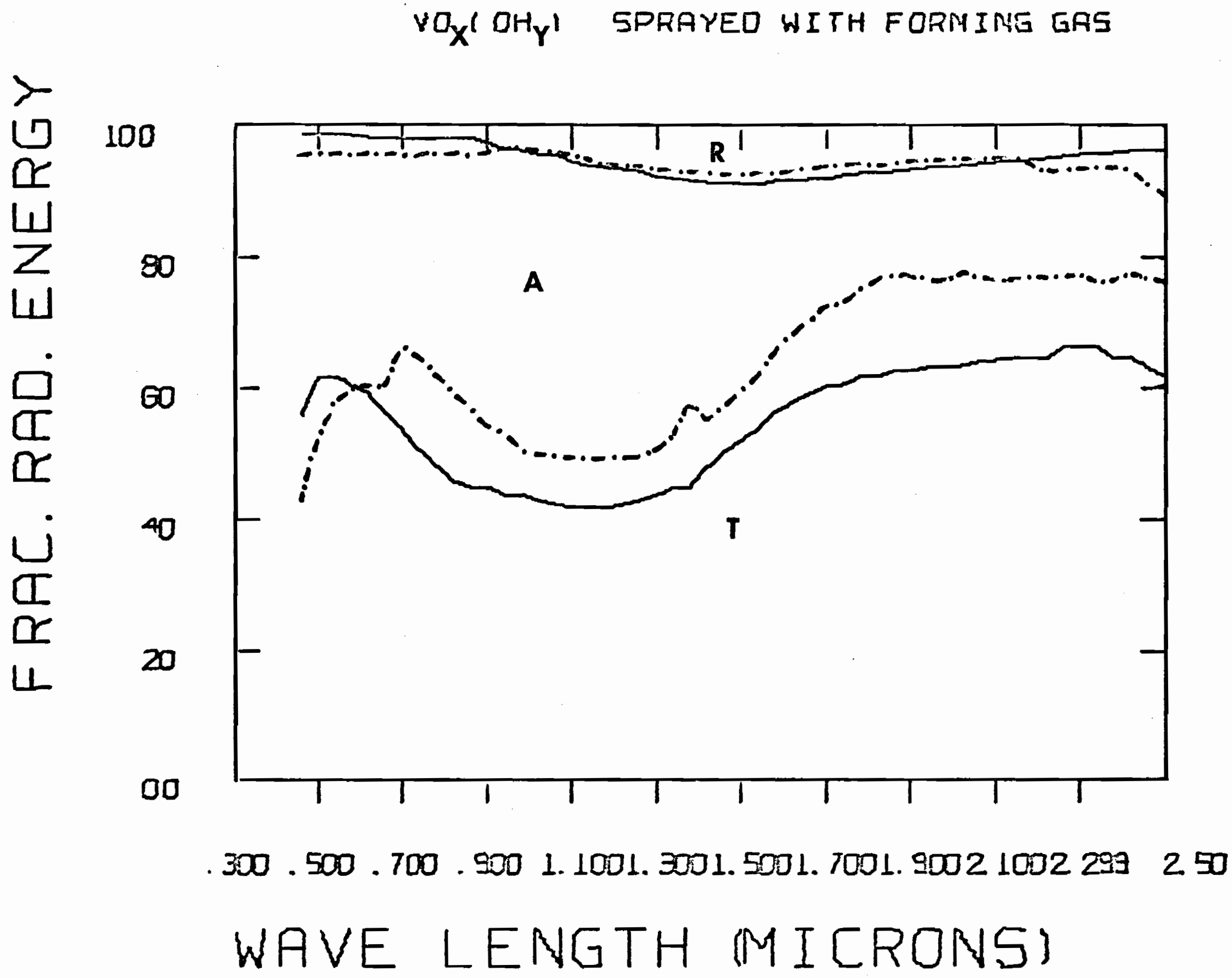

Figure 42. Optical Properties of a VO_xH_y Film Sprayed With Forming Gas as Compared With an Air Reference. ·—·—

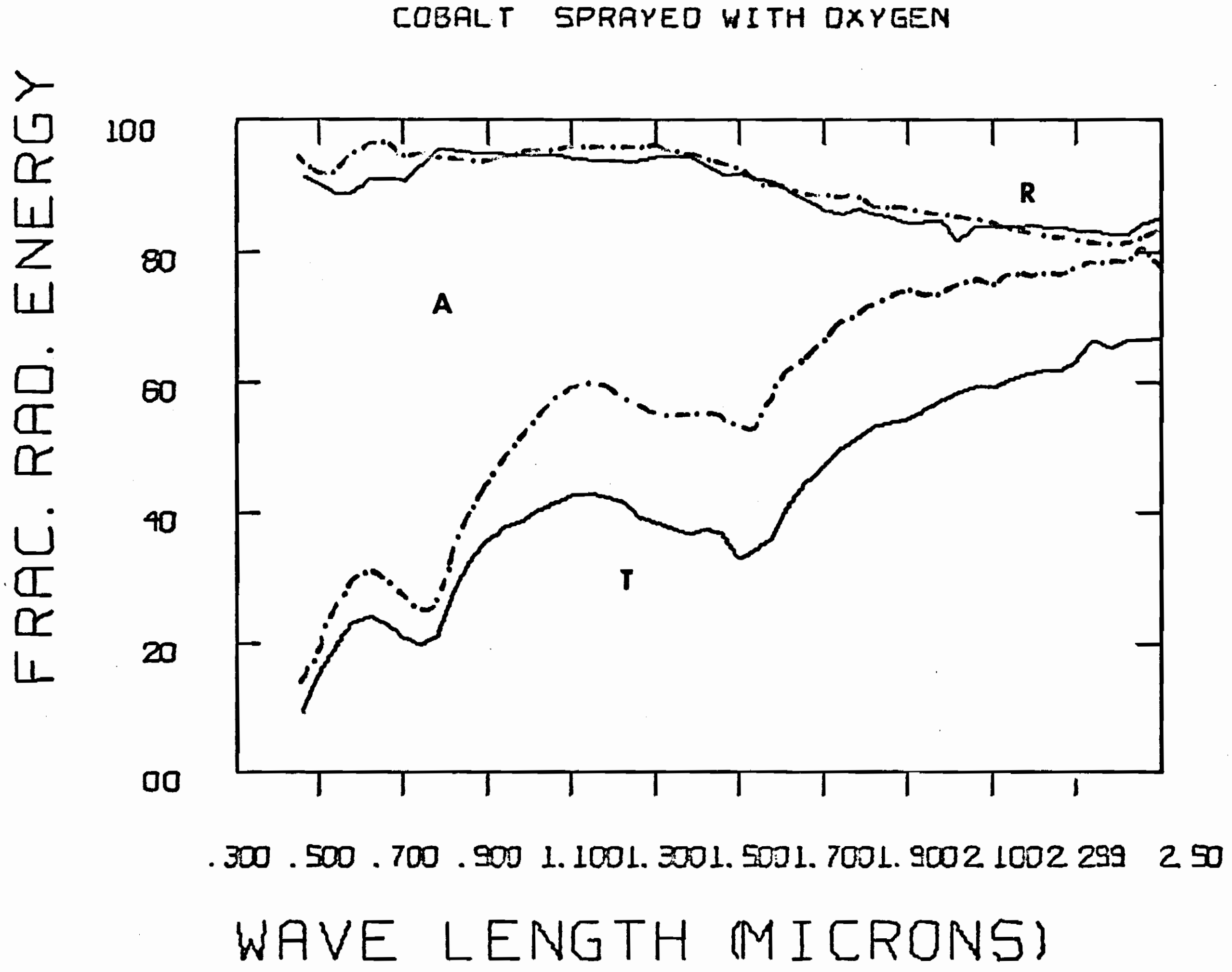

Figure 43. Optical Properties of a Co_3O_4 Film Sprayed With Oxygen as Compared With an Air Reference. ·—·—

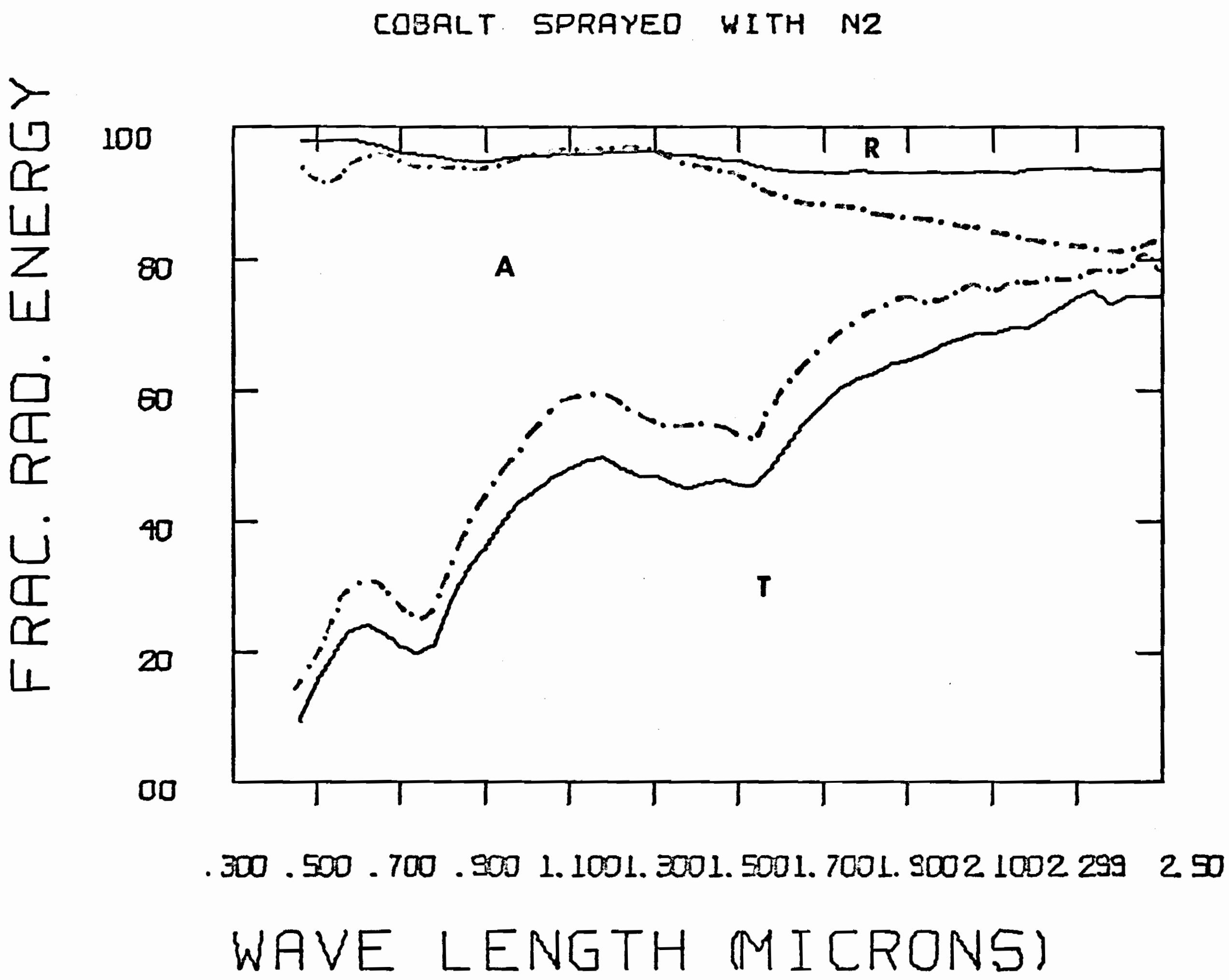

Figure 44. Optical Properties of a Co_3O_4 Film Sprayed With Nitrogen as Compared With an Air Reference.·—·—

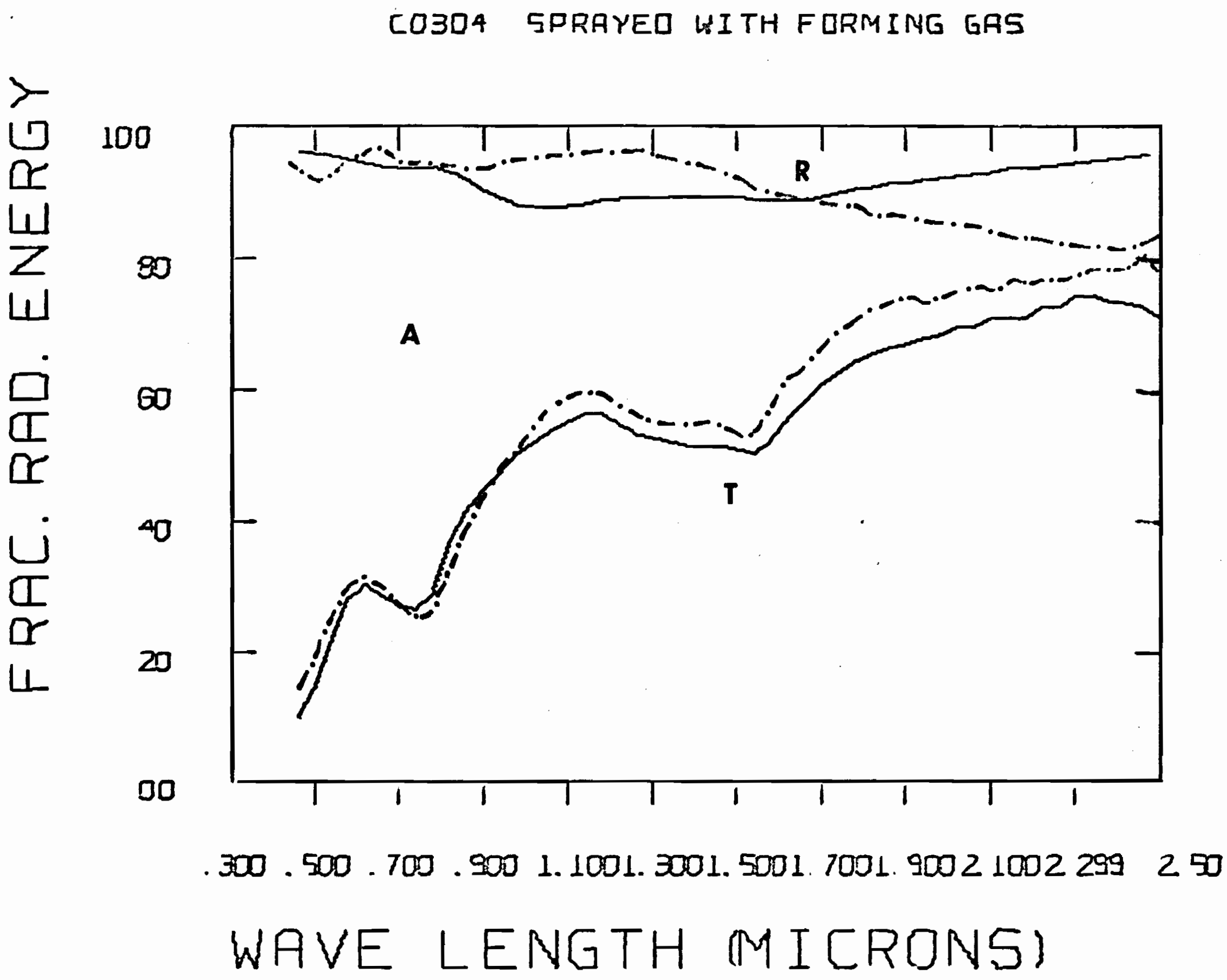

Figure 45. Optical Properties of a Co_3O_4 Film Sprayed With Forming Gas as Compared With an Air Reference.·—·—

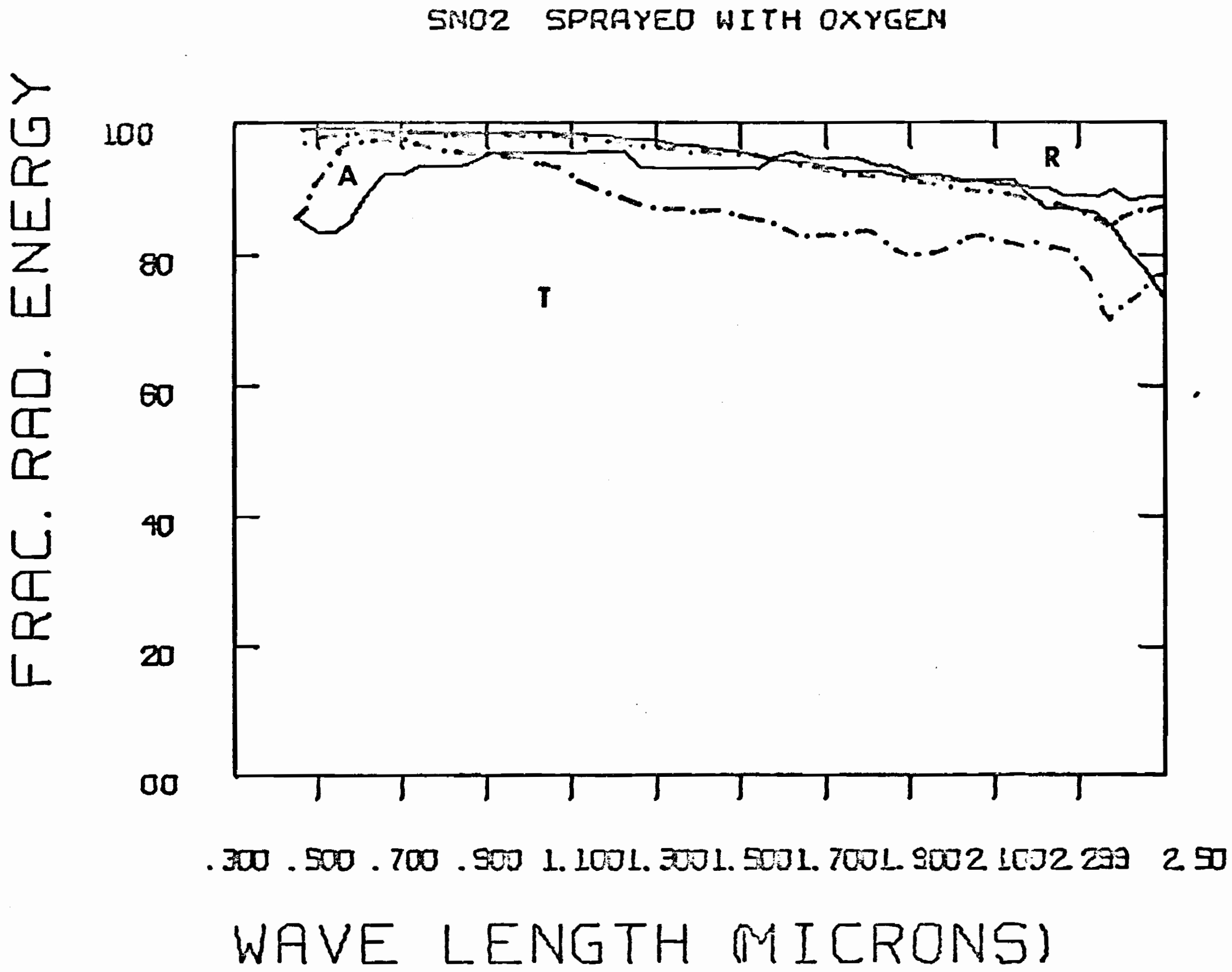

Figure 46. Optical Properties of a SnO$_2$ Film Sprayed with Oxygen as Compared with an Air Reference. ·—·—

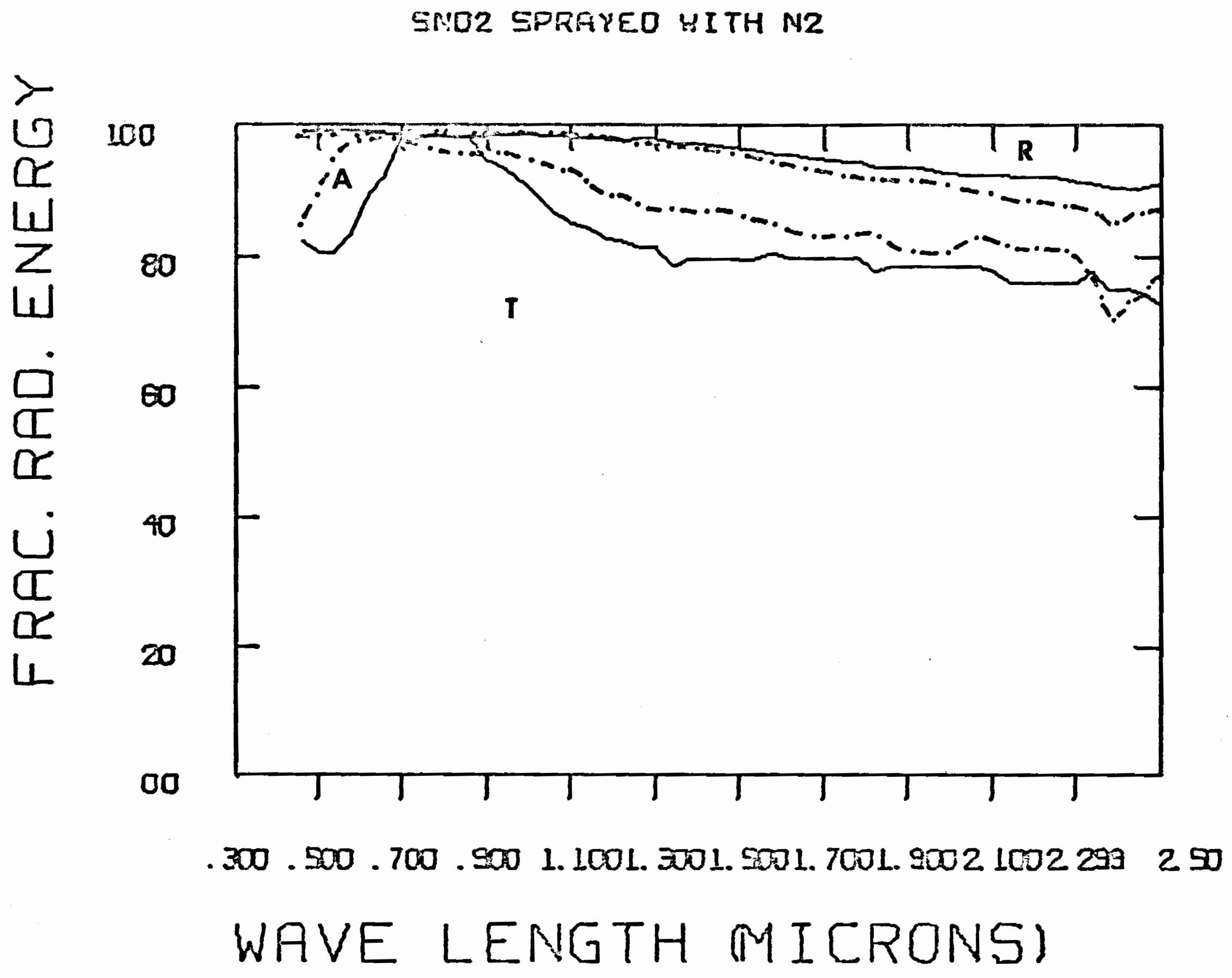

Figure 47. Optical Properties of a SnO_2 Film Sprayed with Nitrogen as Compared with an Air Reference. ·—·—·

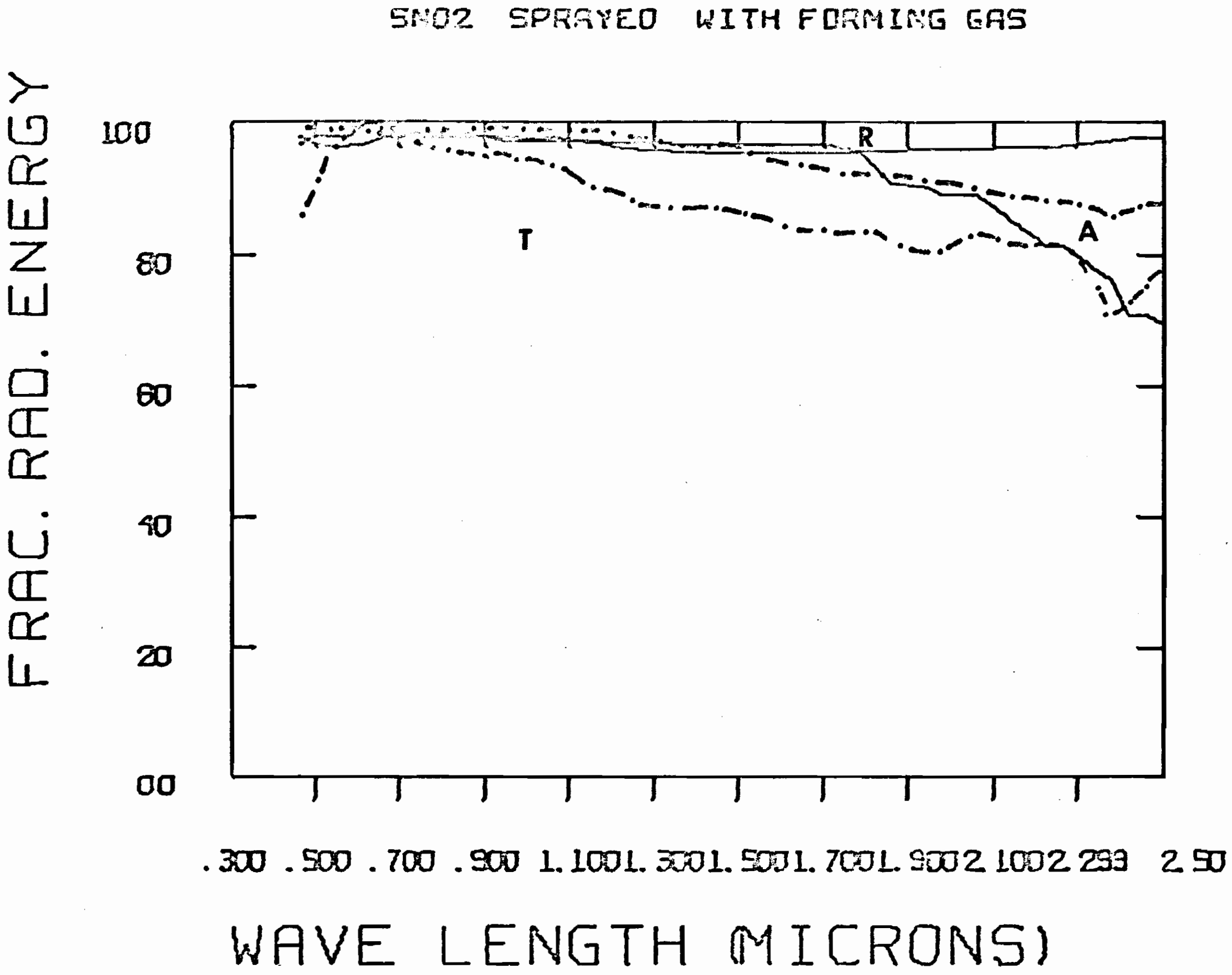

Figure 48. Optical Properties of a SnO_2 Film Sprayed with Forming Gas as Compared with an Air Reference.·—·—·

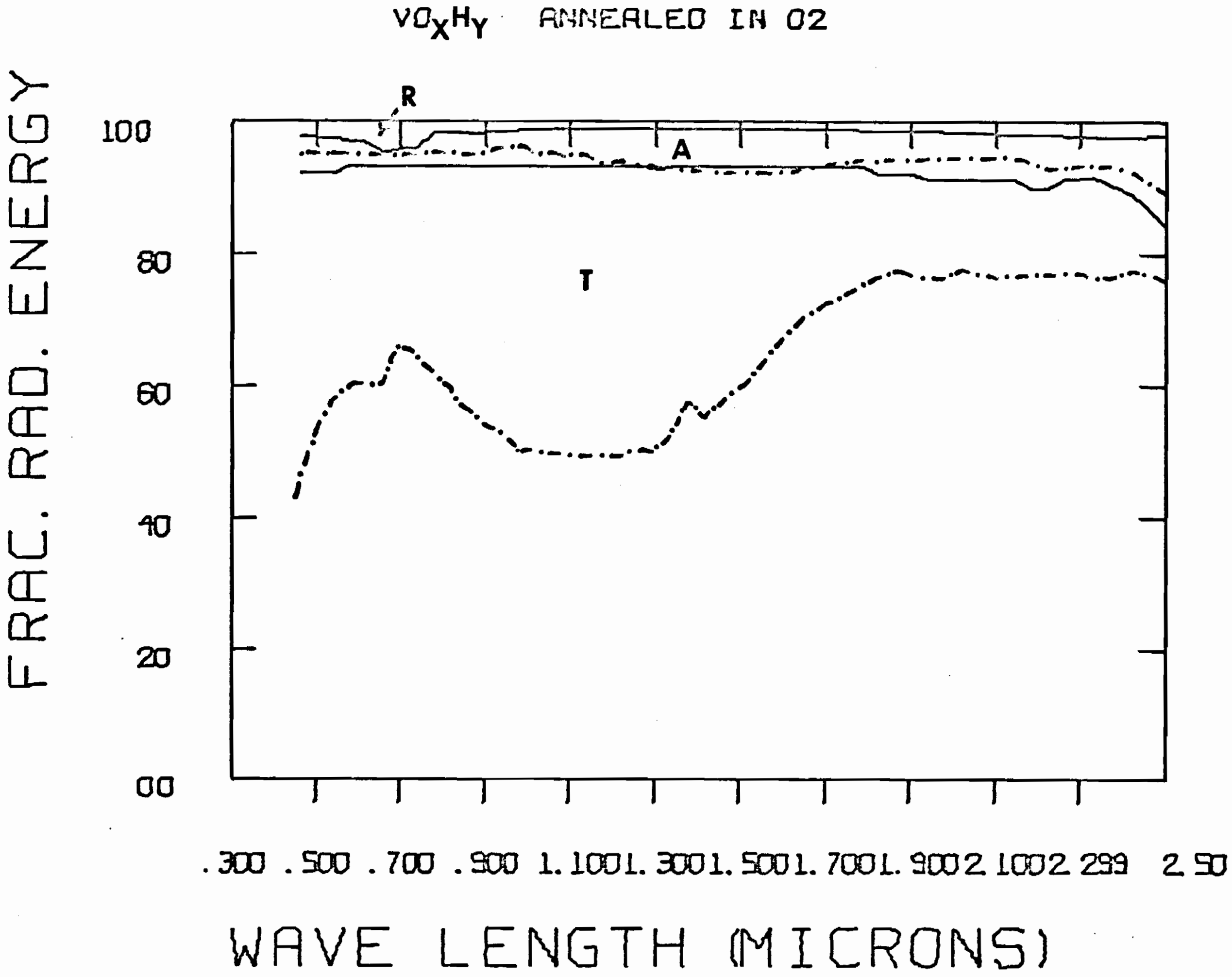

Figure 49. Optical Properties of a VO$_x$H$_y$ Film Annealed in Oxygen as Compared With an Air Reference. ·—·—

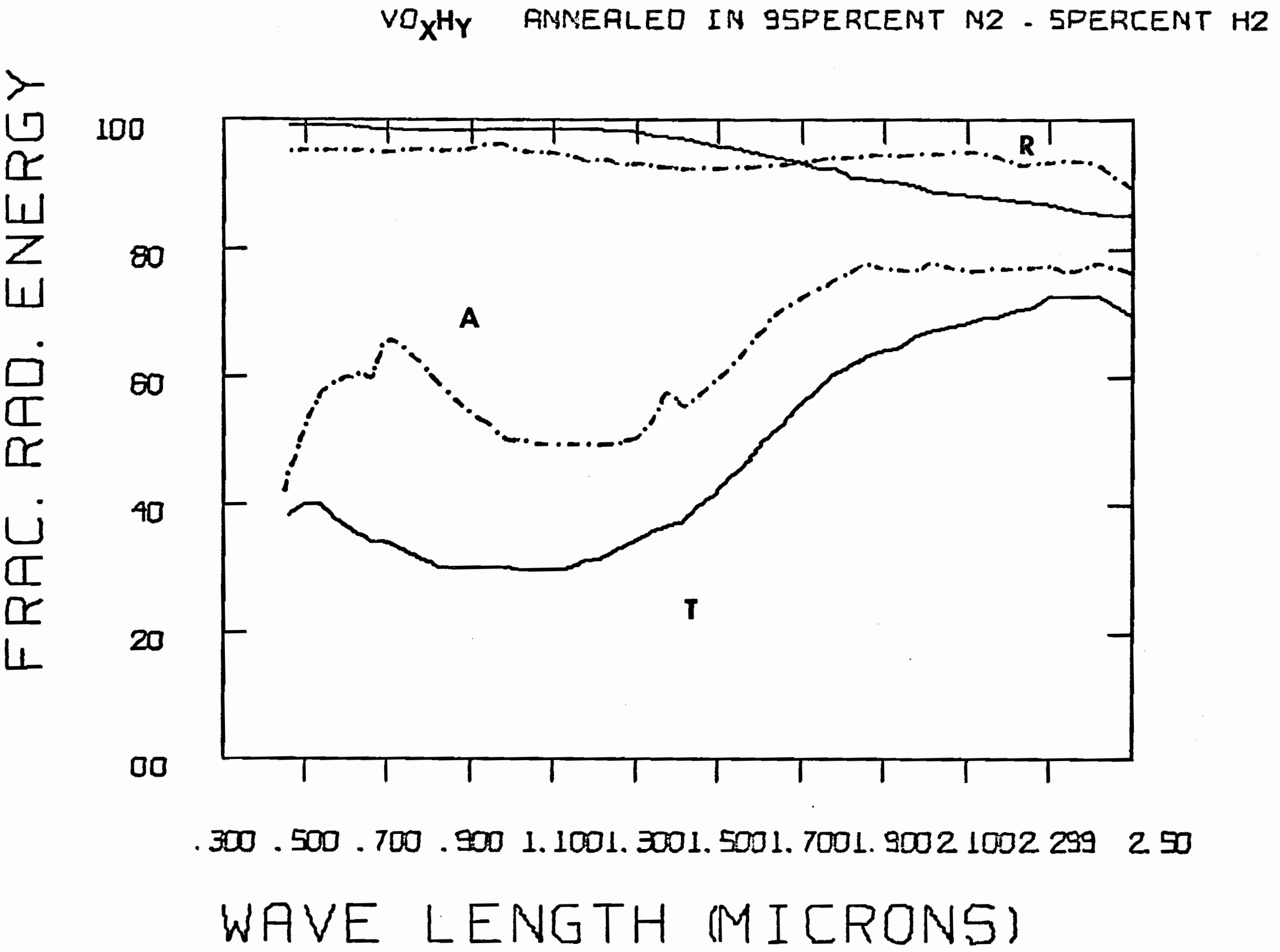

Figure 50. Optical Properties of a VO_xH_y Film Annealed in Forming Gas as Compared With an Air Reference. •—•—•

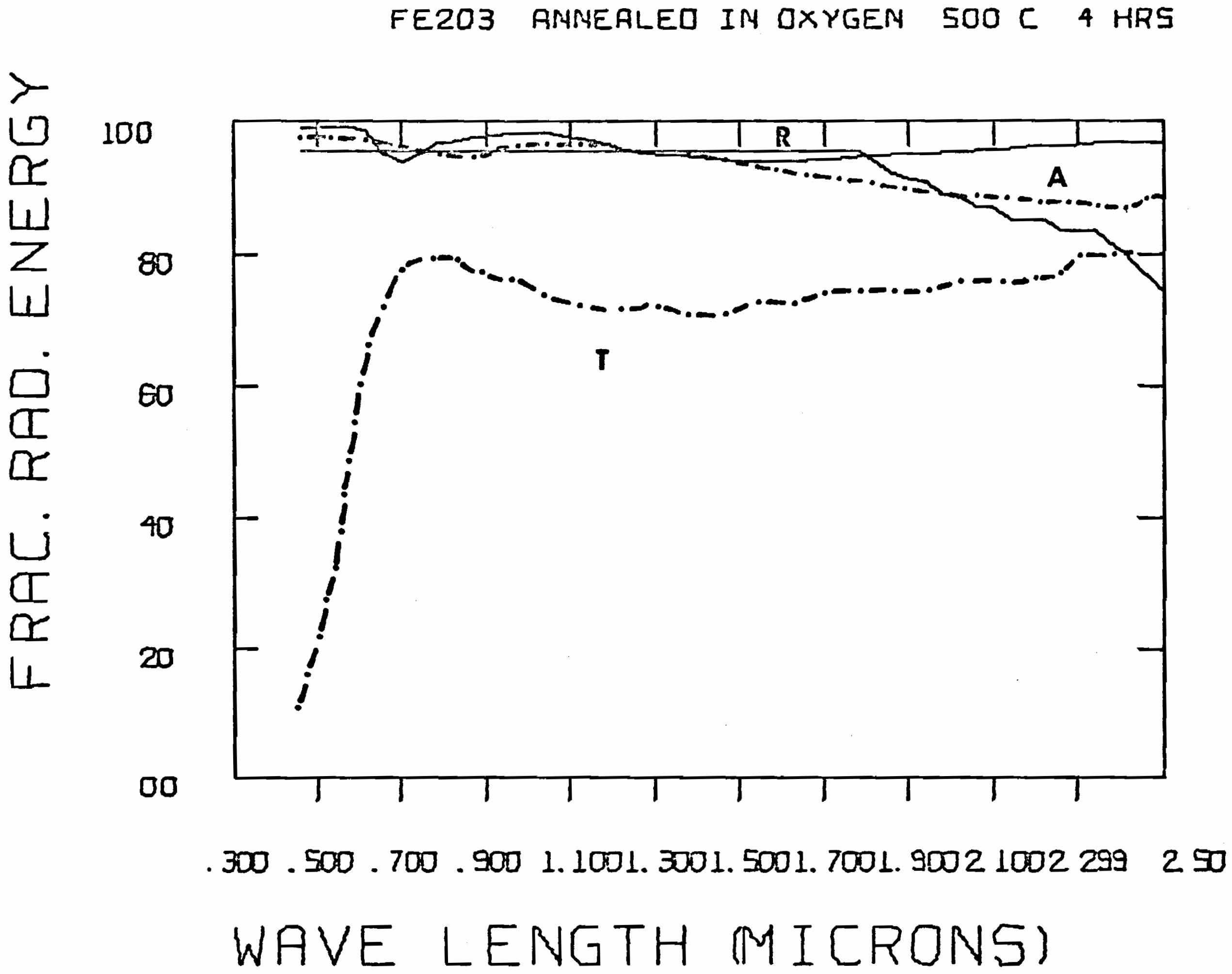

Figure 51.. Optical Properties of a Fe_2O_3 Film Annealed in Oxygen as Compared With an Air Reference. ·—·—·

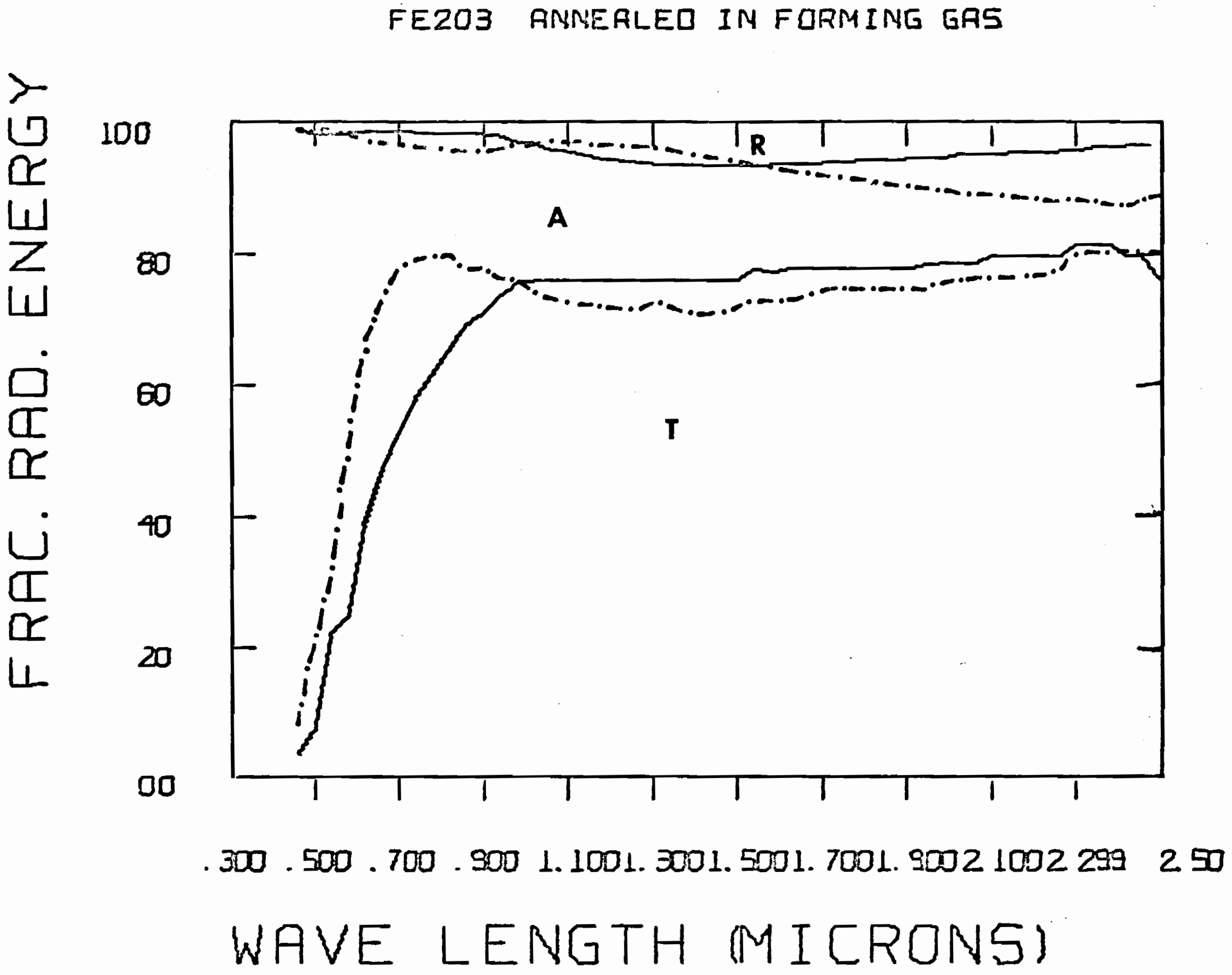

Figure 52. Optical Properties of a Fe_2O_3 Film Annealed in Forming Gas as Compared With an Air Reference. •—•—•

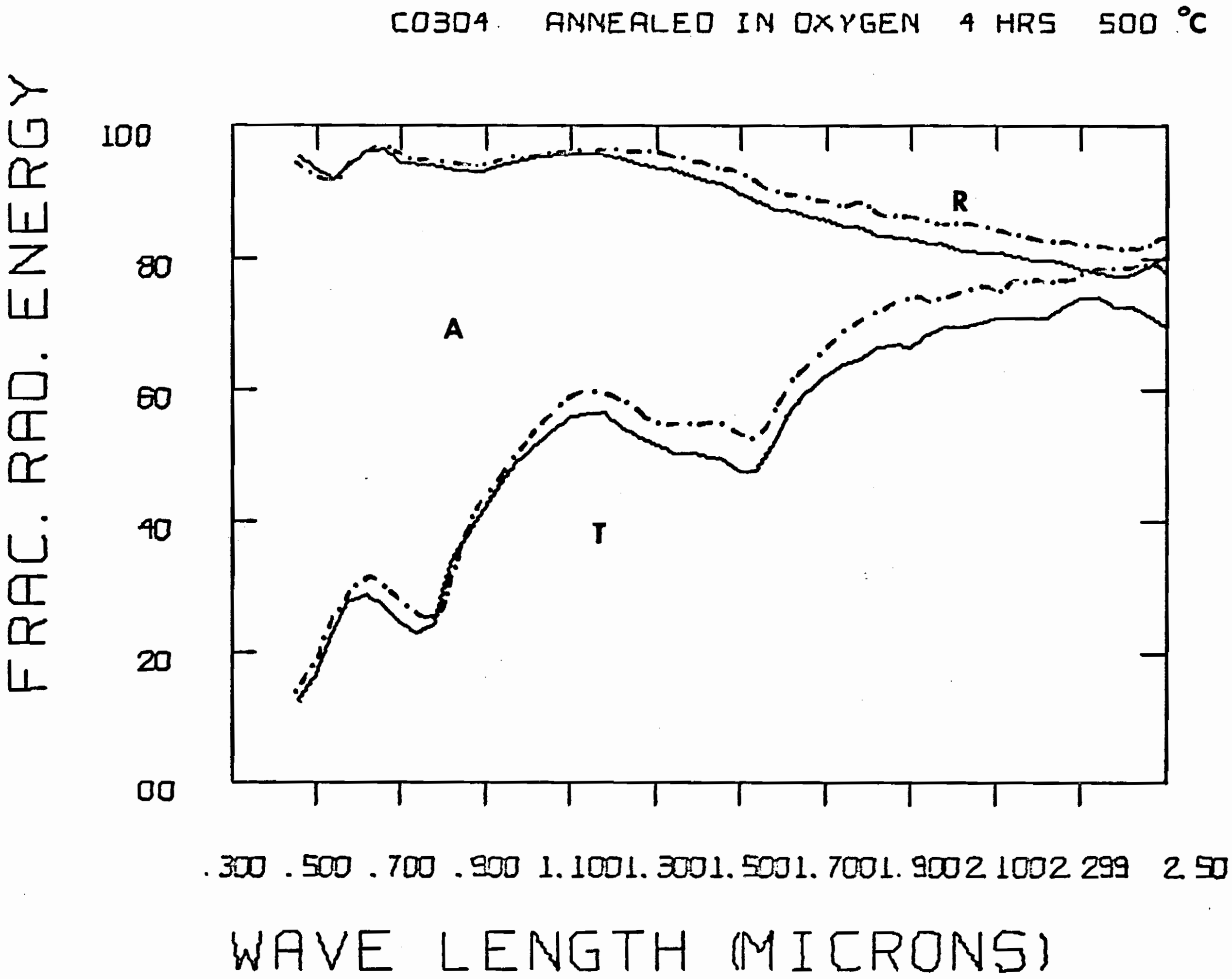

Figure 53. Optical Properties of a Co_3O_4 Film Annealed in Oxygen as Compared With an Air Reference. •—•—•

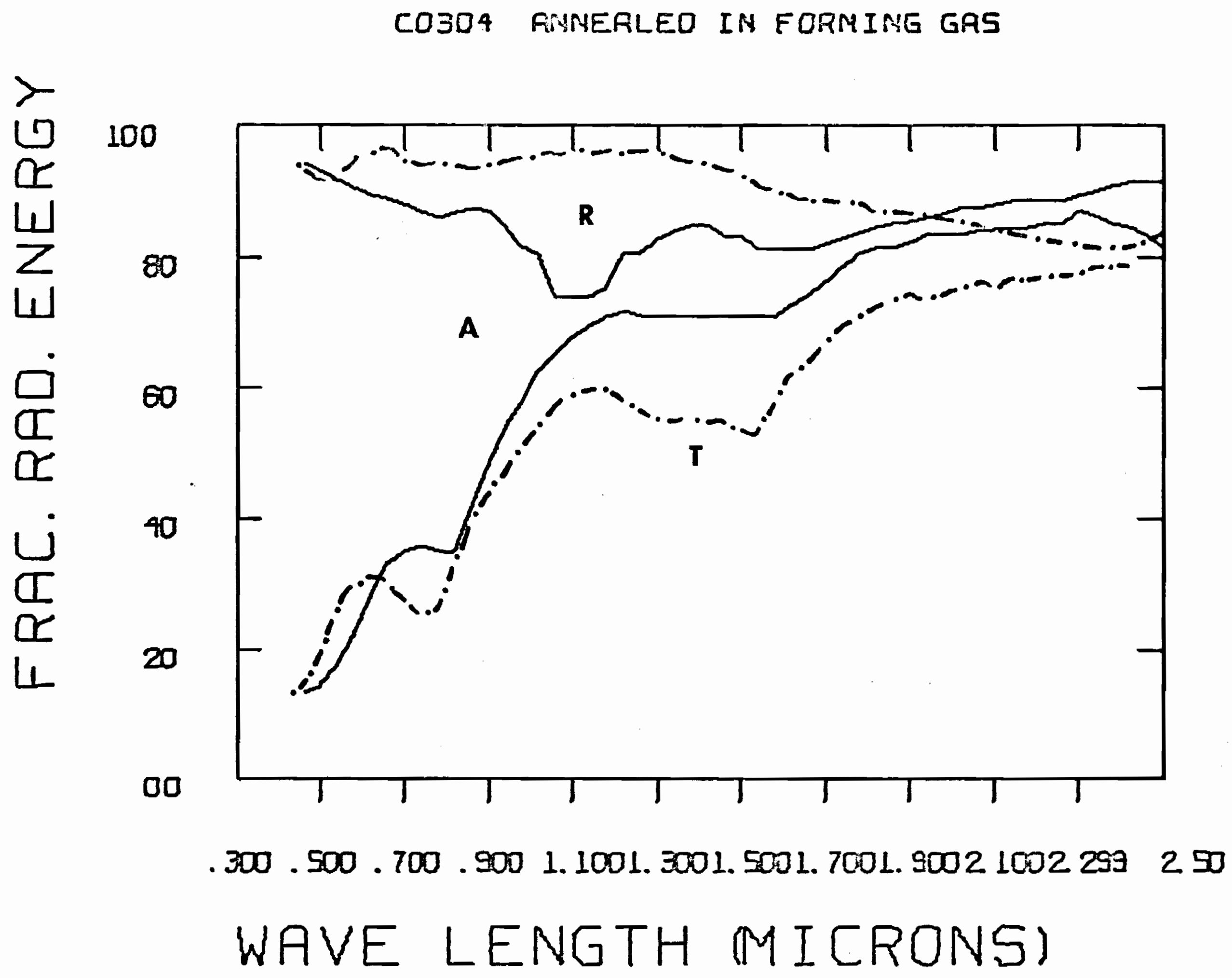

Figure 54. Optical Properties of a Co_3O_4 Film Annealed in Forming Gas as Compared With an Air Reference. ·—·—·

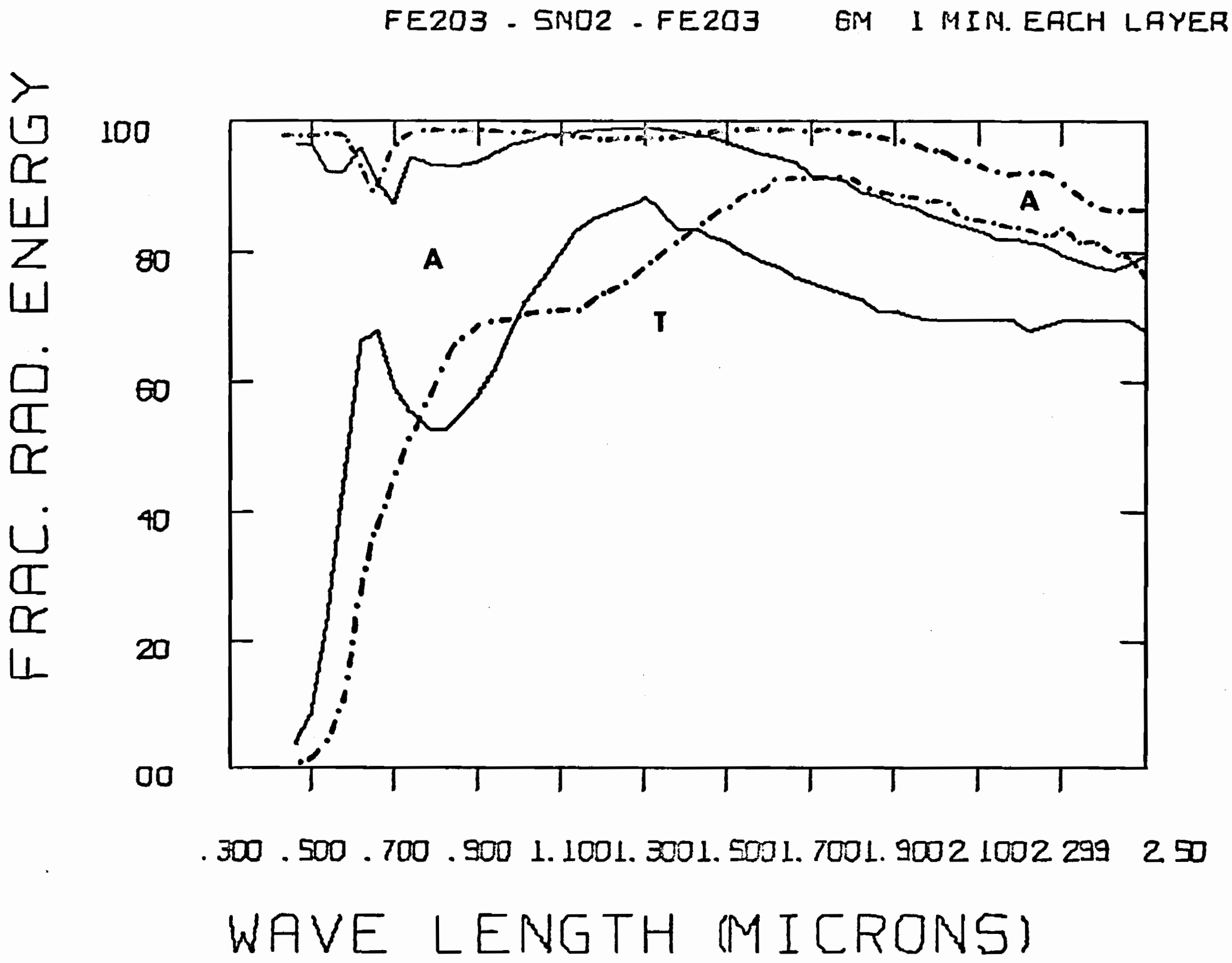

Figure 55 . Optical Properties of Fe_2O_3-SnO_2-Fe_2O_3, Each Layer 1000 Thick, Compared With Equivalent Fe_2O_3-Fe_2O_3-Fe_2O_3.

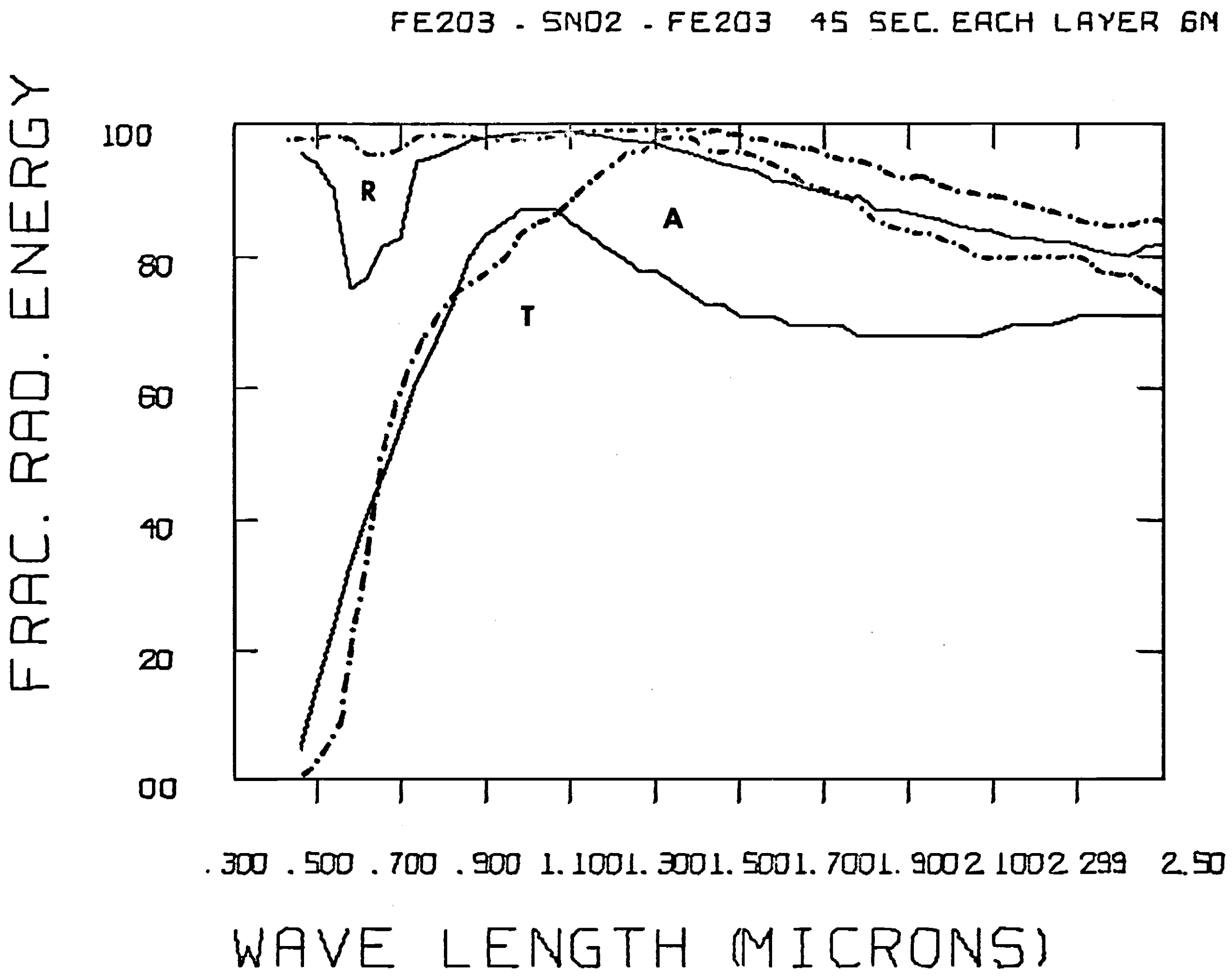

Figure 56. Optical Properties of Fe_2O_3-SnO_2-Fe_2O_3, Each Layer 500 Å Thick, Compared With Equivalent Fe_2O_3-Fe_2O_3-Fe_2O_3.

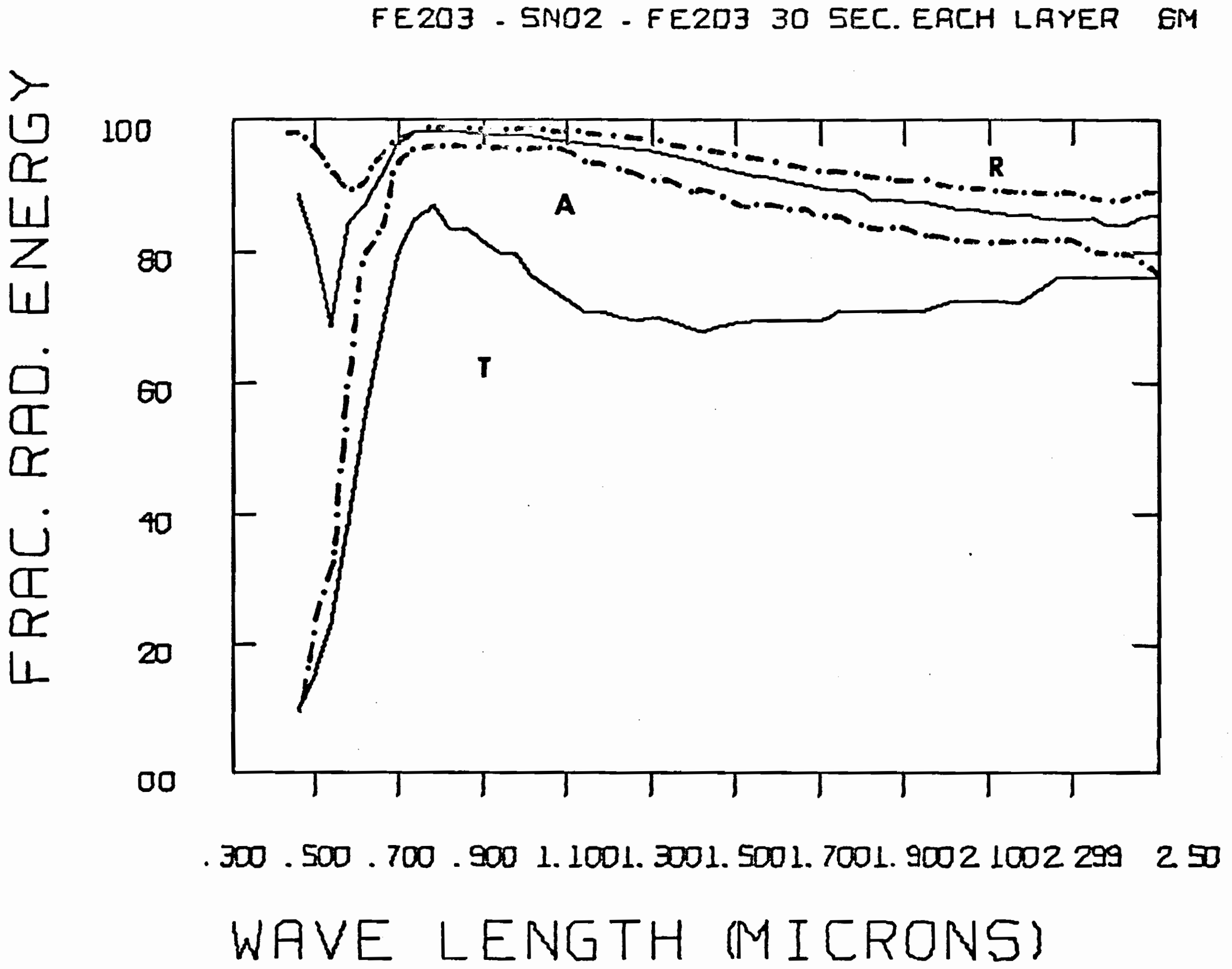

Figure 57. Optical Properties of a Fe_2O_3-SnO_2-Fe_2O_3, Each Layer 300 Å Thick, Compared With Equivalent Fe_2O_3-Fe_2O_3-Fe_2O_3.

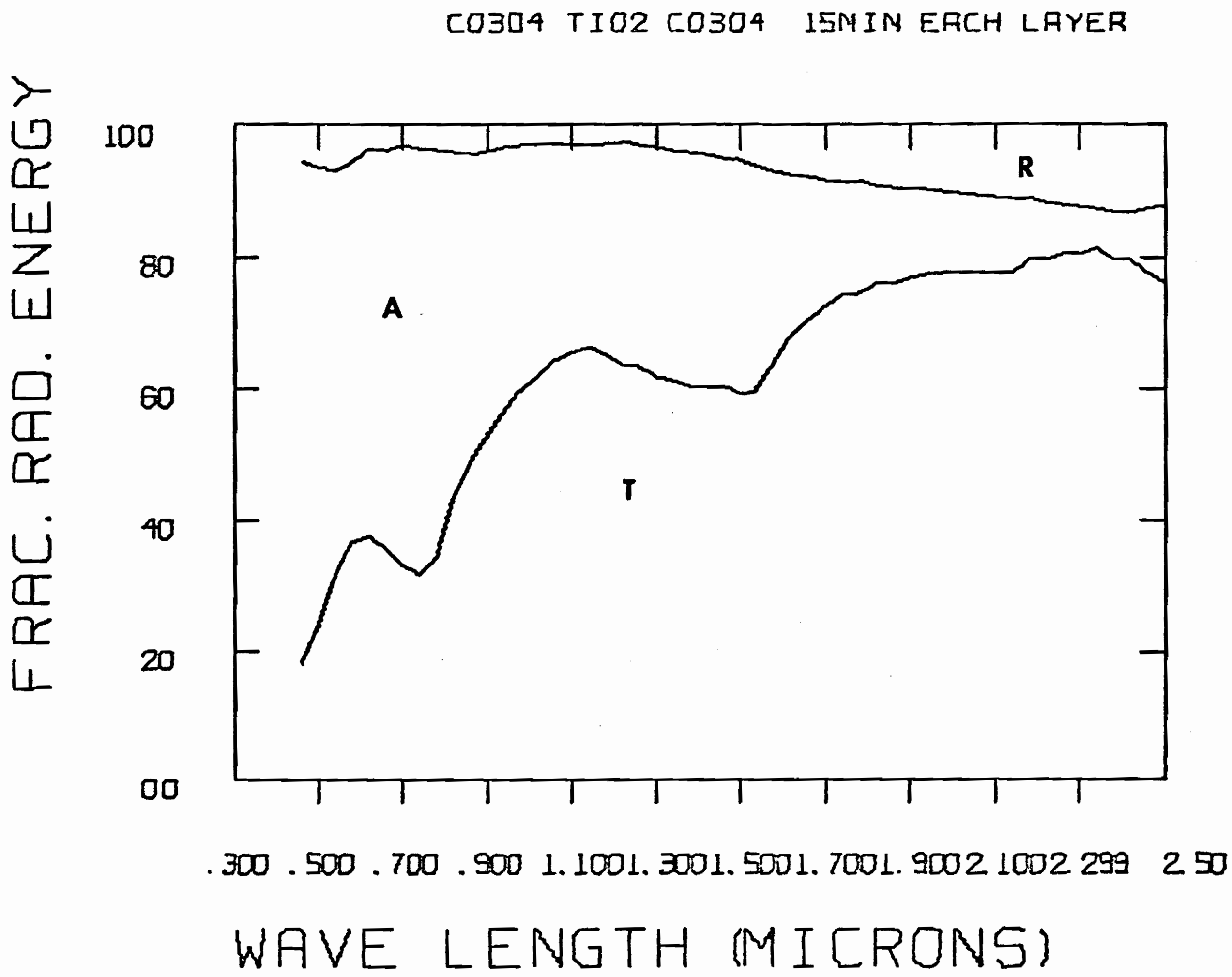

Figure 58. Optical Properties of Co_3O_4-TiO_2-Co_3O_4 Multilayered System. Each Layer 600Å Thick.

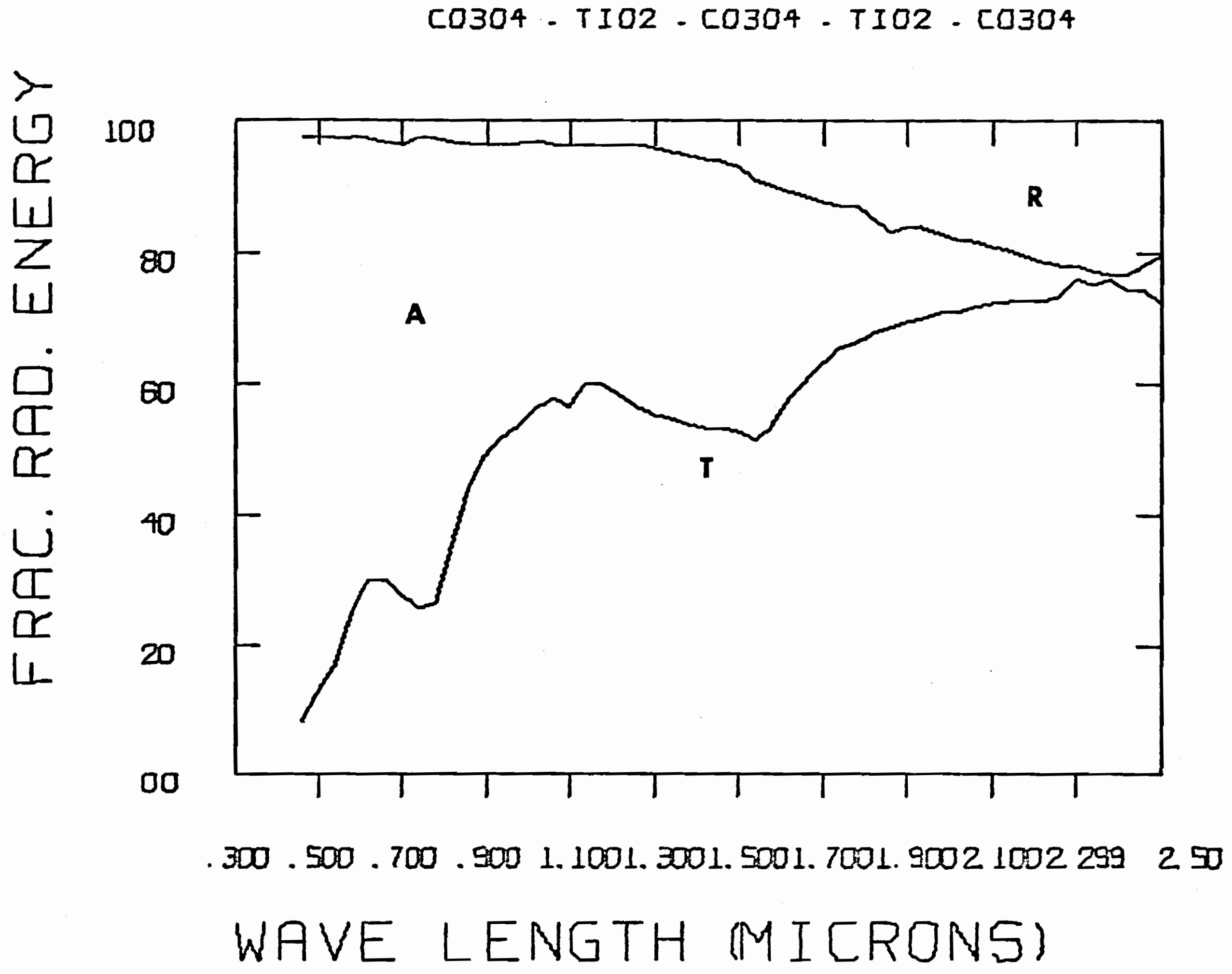

Figure 59. Optical Properties of Co_3O_4-TiO_2-Co_3O_4-TiO_2-Co_3O_4 Multilayered System. Each Layer 600A Thick.

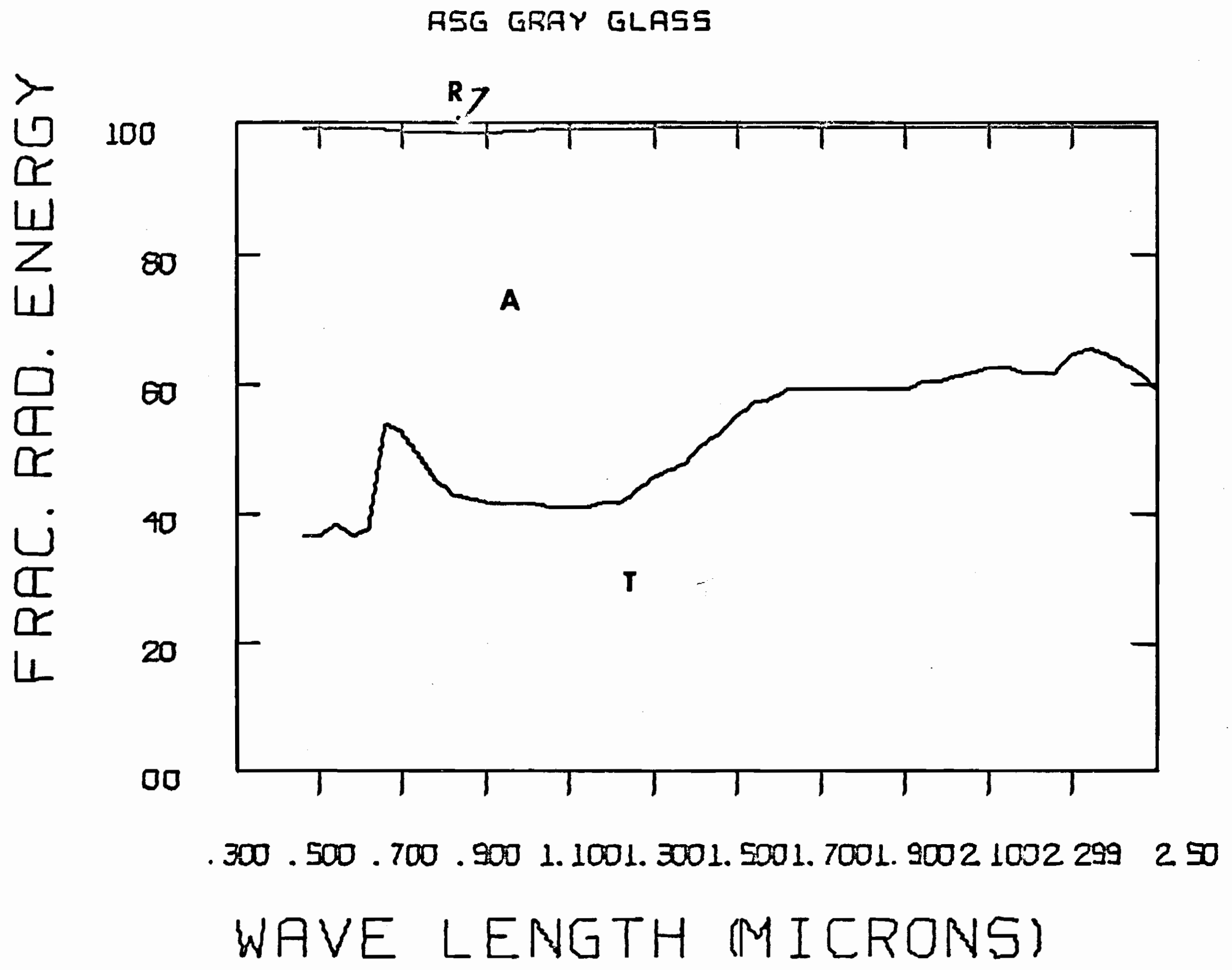

Figure 6C. Optical Properties of ASG Gray Glass.

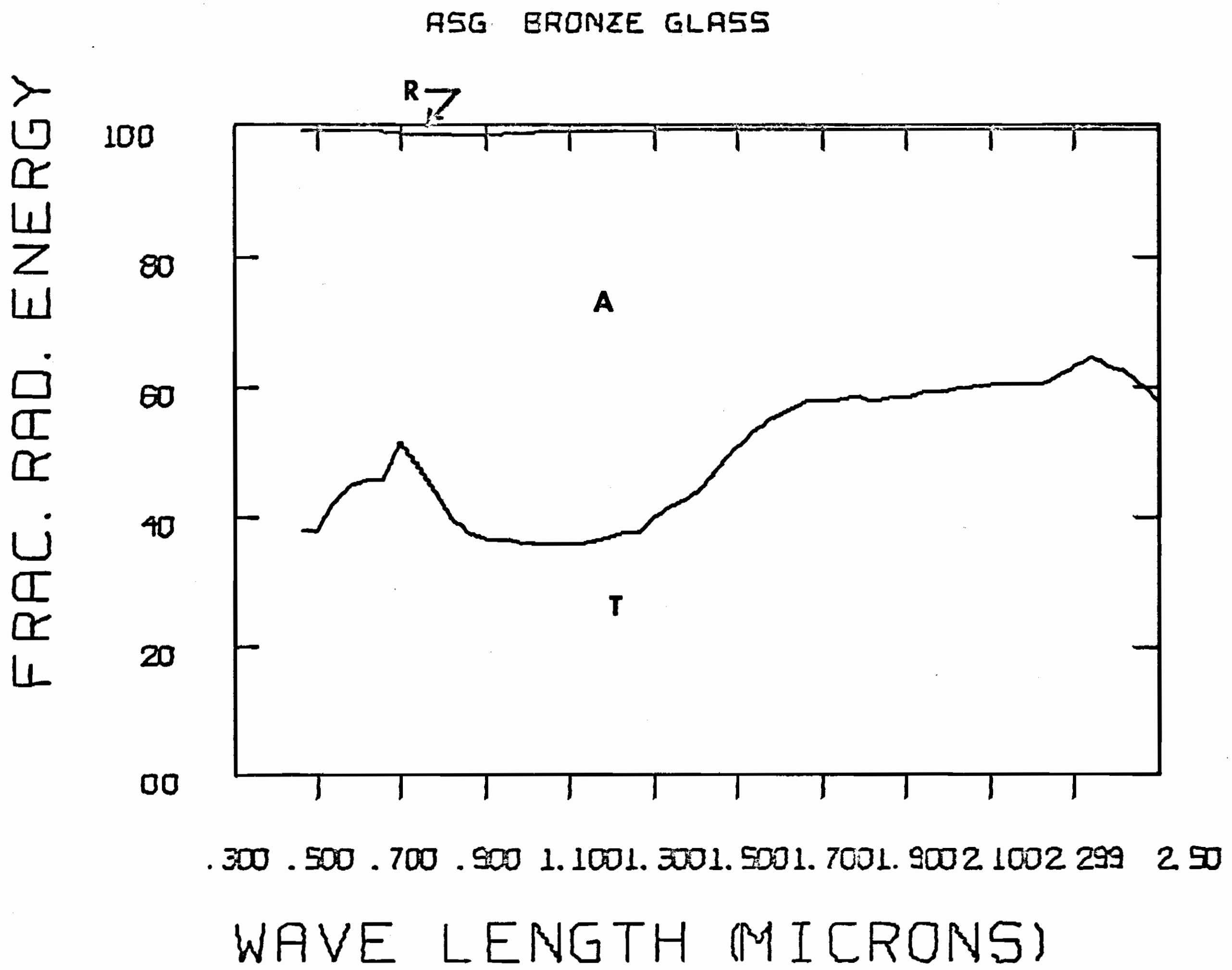

Figure 61. Optical Properties of ASG Bronze Glass.

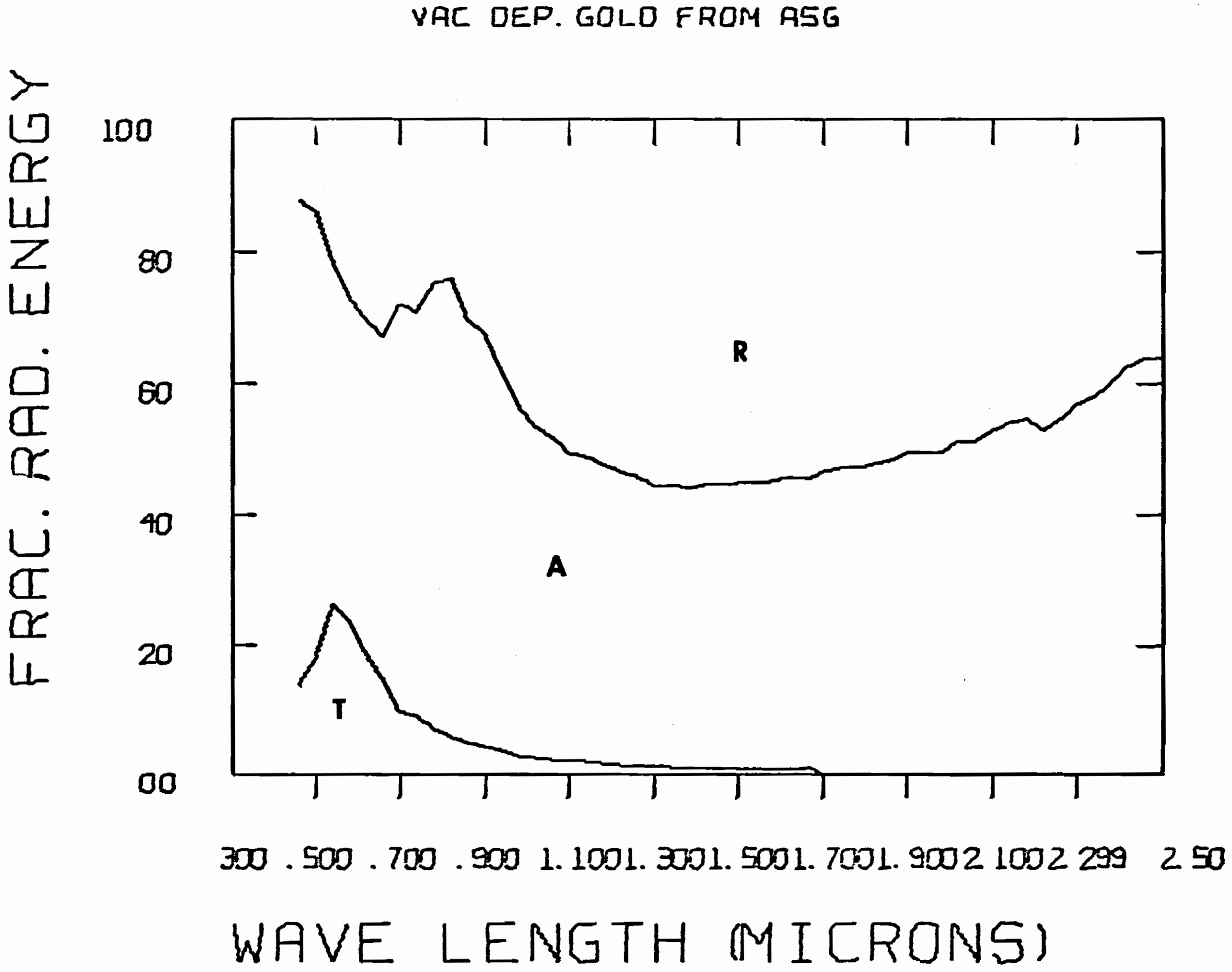

Figure 62. Optical Properties of ASG Vapor Deposited Gold.

V. DISCUSSION OF RESULTS

A. Relation of Optical Properties and Composition

Appearance. Most of the compositional systems investigated produced blends (continous, predictable variations) of colors. These include the Fe_2O_3-TiO_2 (Fig. 8B), TiO_2- VO_xH_y (Fig. 8C), Fe_2O_3-Co_3O_4 (Fig. 8E & F), TiO_2-Co_3O_4 (Fig. 8G), SnO_2-Co_3O_4 (Fig. 8H) and a portion of the Fe_2O_3-TiO_2-Co_3O_4 (Fig. 8I) systems. All of these systems had absorptions at the visible wavelengths that varied in a linear fashion. These systems merely acted like solid solutions and varied in a predictable manner, as does the lattice parameter governed by Vegard's Law.

The only system that deviated from this generalization was the VO_xH_y - Co_3O_4 system. As shown in Fig. 8-C8, VO_xH_y is green and Co_3O_4 (Fig. 8-D9) is black, but mixtures such as 50% VO_xH_y - 50% Co_3O_4 (Fig. 8-D5) and 60% VO_xH_y - 40% Co_3O_4 (Fig. 8-D4) are orange. This color change is possibly due to an altered electronic band structure, as mentioned in the introduction. A large change in the visible absorption (Fig. 23C) corresponds with this unusual color change. There is a 40% decrease in absorption for the heavily doped samples, as compared to the end members (Fig. 23). There are also corresponding increases in sheet resistance for these compositions; $10^{11}\Omega$/sq. as compared to $10^{8}\Omega$/sq. for the pure end members. This decrease in absorption along with the increase in resistance in the VO_xH_y - Co_3O_4 system may be due to a resultant structure or thickness change. Thickness though, did not vary significantly; the largest deviation was only 17Å (Table VII). The crystal structure, on the other hand, was altered. Mixtures under the 20% dopant level at either end of the composition range were crystalline, while those over this 20% limit were amorphous, according to X-ray diffraction. This is a phenomenon uncommon in bulk ceramics or very thick films. In films as thin as these and considering the fact that the entropy for these doped samples is high, disorder induced by mixing two oxides makes it difficult for the ions to organize into well formed crystalline phases. The orange colors of the intermediate films are due to changes in band structure which in turn is structure dependent. A comparison of the crystalline and amorphous semiconductors profoundly affect the band structure(s).

Interference colors often diminish the pleasing appearance of thin films. Preceding this research, it was common to consider these interference colors to be caused by Bragg diffraction of visible light, which would make these colors thickness dependent. From observations obtained in this investigation there also seems to be a great dependence on composition. The transparent coatings of SnO_2 (Fig. 8-H1) and TiO_2 (Fig. 8-G1) and a lightly colored film Fe_2O_3 (Fig. 8) display intense interference colors when viewed in specularly reflected light, while the composition Co_3O_4 does not display any interference fringes at any thickness. These interference colors could be eliminated with the increase of cobalt oxide.

For example, the composition 60% Fe_2O_3-40% Co_3O_4 (Fig. 8) demonstrated interference colors at critical thicknesses, whereas 45% Fe_2O_3-8% TiO_2-47% Co_3O_4 (Fig. 81) had no interference colors over a broader range of thicknesses.

These results indicate that interference colors can occur in two cases. First, films that are transparent, as in the case of TiO_2 and SnO_2, or secondly, when the refractive index is high as with Fe_2O_3. The results also indicate that whenever the films are strongly colored or absorbing, as with the addition of Co_3O_4, the interference colors could be eliminated. Bragg's law is going to be most operative when the refractive index changes at the film's interfaces are large. Bragg diffraction can be eliminated if the film is highly absorbing. The above observation that the 45% Fe_2O_3-8% TiO_2-47% Co_3O_4 composition had no interference colors, whereas the binary composition 60% Fe_2O_3-40% Co_3O_4 had interference colors, is due to the fact that the Bragg diffractions phenomenon was eliminated by making the film more opague (Fig. 8). This was accomplished by the addition of Co_3O_4.

This is important in production applications, where thickness control should not be critical. A film which retains its desired optical properties over a broad thickness range has an added advantage which should increase production output yields.

<u>Absorption and Transmission</u>: All of the oxide films in this investigation absorbed more in the shorter wavelengths, than in the longer wavelengths. This is logical, since the shorter wavelengths

provide greater energies to promote electron excitation and resulting energy level transitions.

Systems such as TiO_2- VO_xH_y (Fig. 22), Fe_2O_3-Co_3O_4 (Fig. 25) and TiO_2-Co_3O_4 (Fig. 26) exhibited predictable linear trends for absorption and transmission, as did appearance. The representative wavelengths of 2.5 , .9 and .62 illustrate this clearly. The absorption and transmission for these systems can therefore by predicted fairly well knowing the composition. These systems again act merely like solid solutions with continuous properties obeying a relation such as Vegard's Law.

The other systems TiO_2-Fe_2O_3 (Fig. 21) and VO_xHy-Co3O4, (Fig. 23) did not display such predictable absorption and transmission trends.

The VO_xH_y - Co_3O_4 system (Fig. 23) has a minimum in absorption between the pure end members at all wavelengths studied. This decrease in absorption, as mentioned previously, was accompanied by an increase in resistance and a decrease in crystallinity. An absorption decrease along with a decrease in conductance and crystallinity also implies that the band structure was changed.

These results indicate that in certain binary systems optical properties of the intermediate compositions can be considerably different than either of the end members.

The TiO_2-Fe_2O_3 system (Fig. 21) conversely displayed a maximum absorption of 40% (.9μ) for the composition 50% TiO_2-50% Fe_2O_3, as compared to the absorptions of pure TiO_2 and Fe_2O_3, 5 and 19%

respectively. This does not conflict with the earlier discussion concerning color, because this maximum is in the infrared, not the visible region. All of these films were amorphous insulators. The unusual changes in the optical properties, particularly at 0.9μ, is apparently due to changes in the amorphous structure as composition is changed.

Reflection. The oxide thin films studied in this research did not display the high visible - near infrared (.3 -2.5μ) reflectance as exhibited by metals. The reflectance for the oxides studied in this compositional investigation were rarely over 20%. Unlike absorption and transmission, reflection did not relate to composition in such a predictable manner. There were no observed structure dependencies. Many of the films, crystalline and amorphous, had the same reflectance . The reflection, though, was generally higher in the infrared (2.5μ), rather than in the visible or near infrared.

Visible reflection depended primarily on refractive index. For example, pure TiO_2 had the highest reflectance of 10% and Fe_2O_3 and Co_3O_4 also having high indices of refraction had reflections equal in magnitude. The lower index oxides SnO_2 and VO_xH_y displayed the lowest visible reflectance . On the other hand, reflectance in the infrared measured at 2.5 did not correlate well with refractive index, but was rather related to the phenomena of of coloration of the film. For example cobalt oxide, a higher colored film had an infrared reflectance of 19%. Fe_2O_3, somewhat less colored, had a reflectance of 12%. VO_xH_y, also less colored than cobalt oxide, had a reflectance of 13%. The two transparent films TiO_2 and SnO_2 had negligible reflectances of 2%.

It can be summarized that visible reflectance obeys the simple optic principle that reflection of a surface is directly proportional to the difference in index of refraction between the medium in which the light is traveling and the reflecting medium. In the infrared, though, it is evident that whatever is causing the films to be highly colored and absorbing, is also causing them to be highly reflecting. The phenomenon of coloration is related to the optical excitation of electrons from energy traps into the conduction band. Reflection is also known to be associated with the concentration and mobility of electrons in a materials surface. In the extreme case metals are highly reflective because their surface is saturated with many highly mobile electrons. This reasoning suggests that the highly colored oxide films, such as Co_3O_4 have a greater number of electrons present in the surface to participate in the reflection. This concept is reinforced by the electrical measurements. Co_3O_4, the most reflecting oxide film, had the lowest resistance ($10^7\Omega$/sq), whereas Fe_2O_3 and VO_xH_y had lower resistivities equal to $10^{11}\Omega$/sq and $10^8\Omega$/sq, respectively. TiO_2 with its minimal infrared reflectance was an insulator.

The exception to this trend was SnO_2. SnO_2 is known to be conducting even though it is not colored. However, SnO_2 becomes almost totally reflective in the very far infrared as mentioned in the introduction.

B. Variation of Pyrolytic Deposition Atmospheres as Related to the Film's Optical Properties

In general the effect of oxidizing and reducing pyrolytic deposition atmospheres on the optical properties of oxide thin films was very dependent upon the compound formed. The effect of deposition atmospheres will now be discussed for each individual film; then generalities concerning the behavior of the films will be presented.

The TiO_2 films' absorbance was affected greatly when sprayed with oxygen and nitrogen. The TiO_2 film sprayed with oxygen (Fig. 93) displayed a transmittance that was practically like that of plain glass and the absorption edge at .4μ was completely eliminated. This TiO_2 film was also very resistive ($10^{12}\Omega/sq$). These optical and electrical results suggest that oxygen promoted the formation of stoichiometric TiO_2 which is an insulator.

Conversely, the TiO_2 film sprayed with nitrogen had an increased absorbance of 40% throughout the visible - near infrared spectrum. (Fig. 94) The resistance of this film ($10^{10}\Omega/sq$) was less than the TiO_2 film sprayed with air ($10^{11}\Omega/sq$). Therefore, it is probable that these spraying conditions promoted the formation of TiO_{2-x}. Bulk TiO_{2-x} (29) has a blue color just as this thin film does (Fig. 9-03). The effect of thickness is relevant in this case. The film sprayed with nitrogen was 300Å greater than its counterparts sprayed with oxygen and air. It is possible that the spraying pressure of the nitrogen was slightly different than the pressure of air. A TiO_2 film did not deposit when sprayed with the reducing 95% N_2 - 5% H_2 gas.

There may not have been sufficient oxygen at the glass surface to form a significant TiO_2 film in the time sprayed. All of the TiO_2 films in this experiment were amorphous, therefore no correlation could be drawn with the degree of crystallinity.

The effect of deposition atmospheres on the formation of Fe_2O_3 was not as pronounced when Fe_2O_3 was deposited with oxygen; the transmission maximum normally at .65 shifted to 1.0μ Many authors have reported the transmission maximum at .65(13). The exact cause for this shift is uncertain. The resistance of this film was high (10^{11} Ω/sq), just as is Fe_2O_3 sprayed with air. There was though, a difference in the degree of crystallinity. The Fe_2O_3 film deposited with air was slightly crystalline, whereas the Fe_2O_3 film deposited with oxygen was amorphous. This is a possible explanation for the absorption decrease in the latter film. Reflection was enhanced slightly out in the infrared (1.7-2.5) in the Fe_2O_3 film sprayed with oxygen (Fig. 37).

The Fe_2O_3 film sprayed with nitrogen did display an absorption increase; approximately 10% between 1.0μ to 2.5μ. The absorption was accompanied by a decrease in resistance; 10^9Ω/sq as compared to 10^{11} Ω/sq. The Fe_2O_3 film sprayed with nitrogen was amorphous, so the increased absorption was probably due totally to oxygen deficiency. Reflection was enhanced a few percent out in the infrared (2.5μ).

One would now think that Fe_2O_3 deposited with 95% N_2 - 5% H_2 should drive the Fe_2O_3 far from stoichiometry and really increase absorption. On the contrary, there was a totally different occurrence.

The specimen was fairly transmitting, as high as 95% at 1.1μ. This is due to a sharp decrease in thickness. Apparently forming gas is so oxygen deficient that it is a detriment for iron oxide film formation.

Due to the multivalency and reactivity of vanadium, X-ray diffraction did not clearly identify what compounds were formed from the pyrolytic reaction of $VO(C_5H_2O_2)_2$ and alcohol. The X-ray pattern did not correspond to any vanadium oxide listed in the ASTM files. However, several of the peaks did correspond to those of the vanadium oxyhydroxides. It appears that the pyrolytic vanadium film has the general formula VO_xH_y, where most of the films displayed the major (001) peak of Häggite ($H_6V_4O_{10}$). This phase is fibrous in character as shown in the SEM (Fig. 13), and as reported by Evans and Mrose (47).

This film was as stable in air and as adhesive as the other films studied, so its optical properties were also investigated. This oxyhydroxide of vanadium reacted greatly when sprayed with different atmospheres. The vanadium film sprayed with oxygen was about half the thickness of the oxide films. This is logical, since oxygen does not promote the formation of a hydroxide. Its absorption, which is approximately 40% (Fig. 49), did not vary much from the sample sprayed with air. The reflectance decreased to 2%, compared to the sample sprayed with air. X-ray diffraction analysis indicated that this film was amorphous. This film had a very high resistance, greater than $10^{11}\Omega$/sq.

Spraying this vanadium oxyhydroxide with nitrogen, on the other hand, enhanced the absorbance and reflectance at most wavelengths. Absorbance increased to approximately 60% and the film became a dark green. The resistance decreased two orders of magnitude ($10^6\Omega$/sq as opposed to $10^8\Omega$/sq) and the x-ray crystal peaks were enhanced, indicating an increased crystal size. From these results the increase in absorption could very well be due to both oxygen deficiency and increased crystallinity. Reflection increased 12% out in the infrared (2.5μ). This may be associated with an increased concentration of conduction electrons associated with the oxygen vacancies.

Once again the film sprayed with forming gas did not follow normal expectations. This vanadium oxyhydroxide film had an absorbance increase of 5% relative to the sample sprayed with air (Fig.42), whereas the absorbance of the film sprayed with nitrogen increased 30%. The crystallinity, conductance and absorbance were all greater than those of the reference air sample, but were less than the vanadium oxyhydroxide film sprayed with nitrogen (Table VII and Fig.41). These effects again are probably associated with the thickness, which was 600Å as compared with 650Å for the vanadium oxyhydroxide sprayed with air. (Table VII)

Co_3O_4 acted in a different manner than TiO_2, Fe_2O_3 and VO_xH_y in that it absorbed more when it was sprayed with oxygen (Fig. 40). The Co_3O_4 film sprayed with air did not have an absorbance in between the films sprayed with oxygen and nitrogen, as noted in the other oxides. A decrease in absorbance, accompanied with an increase in resistance occurred when the Co_3O_4 films were deposited with reducing atmospheres. The Co_3O_4 film sprayed with oxygen, on the other hand, was the most conducting (Table VII). This is completely opposite the conductance of the previous oxides. Semiconducting Co_3O_4 is amphoteric and it is very possible that this thin film is behaving as an oxygen excess semiconductor. TiO_2, Fe_2O_3 and VO_xH_y were all accompanied by a resistance increase when sprayed with oxygen. This behavior is typical for n-type semiconductors such as these(5). Stoichiometric insulating compounds form when these n-type oxides are exposed to oxidizing conditions. Co_3O_4, on the other hand, behaves as a p-type semiconductor(5) that conducts more when exposed to oxidizing conditions. This type of semiconductor becomes metal deficient or oxygen excess, which has an electron hole associated with each defect, promotes conductance and absorbance.

C. Annealing in Oxidizing and Reducing Atmospheres as Related to the Films' Optical Properties

Annealing in oxidizing and reducing atmospheres had some pronounced effects on the optical properties of oxide thin films, similar to those discussed in the previous section.

Appearance was especially altered. The green vanadium oxyhydroxide film (Fig. 9K) annealed in oxygen became transparent (Fig. 9K), whereas it became blue when annealed in forming gas. The Fe_2O_3 film turned a bright red-orange when it was annealed in oxygen (Fig. 9L), but became very dull and mottled when annealed in forming gas (Fig. 9L). The Co_3O_4 film became darker when annealed in oxygen and became slightly hazy when annealed in forming gas (Fig. 9M).

The n and p-type semiconducting oxides again displayed opposite absorption and conduction trends. N-type or insulating Fe_2O_3 completely lost all absorption when annealed in oxygen (Fig.51). It also became very resistive. X-ray analysis determined this film to be crystalline Fe_2O_3. The Fe_2O_3 film annealed in 95% N_2-5% H_2 (Fig.52), on the other hand, absorbed slightly more than the reference air sample. This film also displayed a decrease in resistance of $10^9\Omega$/sq as opposed to $10^{11}\Omega$/sq. This film also proved to be Fe_2O_3 by x-ray analysis. It can therefore be concluded from this experiment that absorption in hematite films is mainly due to electron excitations which promote energy level transitions and not to structural changes.

The VO_xH_y film annealed in oxygen also lost all its absorption. (Fig.49) Resistance increased to a value greater than

$10^{12}\Omega$/sq. Scanning electron microscopy assisted in understanding the observed results. As shown in Fig. 14 and the X-ray analysis (Fig.10), oxygen completely destroyed the VO_xH_y film. It appears as though the film shrank and rolled up into a "donut" morphology. The SEM micrographs 15a and b show that oxygen also promoted a reaction of the film with the microscope glass surface. It is very possible that a low melting vanadium silicate formed,although it was not detected by X-ray diffraction.

The vanadium oxyhydroxide film annealed in forming gas on the other hand, had an absorption increase at all wavelengths. This film though, was not oxygen deficient, as evidenced by a resistance increase from $10^8\Omega$/sq to $10^{11}\Omega$/sq. The absorption increase can be explained by an increase in crystallinity.

X-ray diffraction revealed that annealing in 95% N_2-5% H_2 produced three phases. Häggite ($H_6V_4O_{10}$) which was present before annealing (Fig. 10), underwent crystal growth as shown in the SEM Micrographs 13a and b and the X-ray diffraction pattern (Fig. 10). Two other phases appeared after this annealing, $VO(OH)_2$ and $V_3O_5(OH)_4$, as shown in Fig.10. According to Evans et al.(48) it is common for these oxyhydroxides to exist together. These phases may have been present before annealing, but could not be detected with X-ray diffraction analysis until grown to a significant size. Annealing in forming gas definitely promoted crystal growth in all three phases, whereas annealing in water vapor only promoted the growth of Häggite.

This is further evidence that crystallinity is directly related to absorption, at least with this composition. Reflection again was enhanced in the far infrared. P-type Co_3O_4, on the other hand, was most absorbing when annealed in oxygen (Fig.43). This absorption was expected, since the cobalt oxide film sprayed with oxygen displayed an increased absorption. Both of these films were metal deficient having enhanced conductances (Table VII). The annealing of Co_3O_4 in 95% N_2-5% H_2 (Fig.45) produced the desired effect of maximum reflectance with minimum absorbance in the near infrared region. This effect seems to be only possible with p-type oxides that are exposed to reducing conditions. P-type semiconductors become less metal deficient (more stoichiometric) when exposed to reducing atmospheres. The reduction in positive hole concentration reduces conduction and absorption.

The cobalt oxide film annealed in forming gas was the most reflecting of the films in this investigation. The reflection reached a maximum of 35% in the near infrared region (Fig.45). This film was amorphous (Fig.12), whereas the Co_3O_4 films sprayed with air and annealed in oxygen were crystalline.

Reflectivity does not seem to be related directly to crystallinity or conduction. Rather, it seems to be a function of the composition chosen. For example, cobalt oxide, especially when annealed in a reducing atmosphere, has the greatest reflectance. This suggests that high reflectance in oxides can be attained by using p-type semiconducting oxides, and then perhaps annealing them in a reducing atmosphere.

D. Effect of Thickness on the Optical Properties of Oxide Films

Thickness is a parameter that influences the optical properties of thin films considerably. Figure 9J displays the effect of thickness on the appearance of a film. As a film with the composition 60% Fe_2O_3 - 40% Co_3O_4 becomes progressively thicker, it becomes opaque.

The reflection, absorption and transmission as a function of thickness for the single composition 60% Fe_2O_3 - 40% Co_3O_4 at the representative wavelengths 2.5μ, .9μ and .62μ is shown in Figure 28. It is immediately evident that the exact dependence of thickness varies with wavelength. Figures 29 through 34 progressively indicate the effect over the entire .3μ - 2.5μ spectrum. The maximums and minimums in the transmission curves are possibly due to interference fringes.

In the visible region (Figure 28c) absorption increases as the film becomes thicker. This is expected, since there is more material available to interact with the light. Reflection did not vary significantly. In the near infrared region (Figure 28b) there was a sharp increase in absorption with the film that was 907 Å thick. This deviation may possibly be a result of the interference of light at this .9μ wavelength. A maximum in reflection occurred when the film was 907 Å at 2.5μ. It is unknown why this maximum occurred at this particular thickness. It has been reported that maximum reflectance in a Co_3O_4 film occurs when it is approximately 1200 Å thick.(13) They suggest that it may be due to the amount of film.

A film thicker than 1200 Å produces an excess that scatters and absorbs light, instead of reflecting it. As expected the thickest film (5980Å) absorbed the most in all wavelength regions (Figure 34).

There seemed to be a critical thickness for identification by X-ray diffraction. X-ray diffraction identified the 60% Fe_2O_3 - 40% Co_3O_4 as having the αFe_2O_3 structure at a thickness approximately equal to 815 Å. Utilizing EDAX with scanning electron microscopy, both iron and cobalt were identified. This is evidence that cobalt oxide is in solid solution with iron oxide, but takes on the αFe_2O_3 lattice structure. The thickness to achieve X-ray diffraction analysis may be due to the longer time that the sample has to be heated to obtain this thickness. The crystal growth in oxide thin films is very dependent on both time and temperature, just as in bulk ceramics. The crystalline surface of the thickest 60% Fe_2O_3 - 40% Co_3O_4 film (5980 Å) is shown in Figure 18. This can be compared to the micrograph of Co_3O_4 that was 600 Å thick (Figure 19).

E. The Sequential Stacking of Oxide Layers of Alternating Index of Refraction as Related to Optical Properties

The successive stacking of alternate layers having high and low index of refraction, as mentioned in the literature review, geometrically enhances reflection. This enhancement was accomplished especially in the visible wavelengths. Absorption also increased since light does become trapped between the high index layers and eventually gets absorbed in the layers.

The alternate layers of Fe_2O_3-SnO_2-Fe_2O_3, having the refractive index sequence H(3.2) L (2.0) H(3.2), increased reflection that varied with the thickness of each layer. The thicker layers increased reflection out in the far infrared region, while the thinner stacking schemes enhanced reflection in the shorter wavelengths. On the average layers .2μ thick enhanced reflection the most at the visible wavelengths.

Figures 56 and 59 illustrate the effect of stacking more than three layers of Co_3O_4 and TiO_2. Reflectance again increased in the far infrared region, while absorbance increased slightly (5-10%) in the visible and near infrared region.

The major disadvantage with the multilayered oxide film systems was that they appeared cloudy and often had interference colors. There is also a disadvantage in the production of such a system on large scale. It may be a costly operation to deposit these individual layers. If these engineering and economic problems could be solved then oxide multilayered systems may have a great potential for solar reflectance by architectural glass.

F. Morphology of Oxide Thin Films

Scanning electron microscopy shows that oxide films have morphologies that vary widely. Four different compositions were investigated and, as shown in the SEM micrographs (Figures 13 through 20), all four had a unique crystalline morphology. The Co_3O_4 film (600 Å thick) exhibits a very fine texture (Fig. 19), whereas 60% Fe_2O_3 - 40% Co_3O_4 (5980 Å thick) displays a mushroom like structure (Fig. 18). The vanadium oxyhydroxide crystals, on the other hand, are elongated and are randomly distributed on the glass surface (Fig. 13). SnO_2 is unusual in that it has a fine textured matrix with distinct white crystallites superimposed on it (Fig. 20). These results indicate that the morphologies of these oxides are unique and that they are dependent on composition.

G. Applications for Reflecting and Absorbing Thin Films

It was determined in this investigation that oxide thin films have many different optical properties. Co_3O_4, for example, absorbs in the visible and near infrared where most of the sun's energy is concentrated, but transmitts the far infrared wavelengths (thermal energy), Figure 45. In contrast tin oxide, transmits the visible and near infrared, and reflects the far infrared radiation (Figure 3). Utilizing these films in conjunction with each other produces a solar insulating window (Figure 63). As the Co_3O_4 film absorbs the sun's radiation, it will activate thermal phonons, heat, and then will emit thermal energy. This thermal energy will then be reflected by the SnO_2 film which is on the front surface of the second window. This thermal energy will not become entrapped between the glass and the films, since Co_3O_4 transmitts the thermal energy. The air space between the two window panes is probably necessary to avoid heating by conduction. The SnO_2 film acts as an insulator of thermal radiant energy. This system should be tested for feasibility by fabricating a prototype that utilizes a lamp source which has the same energy spectrum as the sun. Theoretically, this system should function efficiently, as shown in the analysis (Fig. 64).

In the winter, this system could be reversed by simply turning the window around (Fig. 63). The SnO_2 film, now on the back surface of the first window, will transmit the solar radiation that will eventually heat up the Co_3O_4 film. This Co_3O_4 film will eventually emit heat into the room. The air space plus the SnO_2 film will effectively keep the heat in the room. The major advantage of the solar insulating window is that it employs the inexpensive stable oxides.

An oxide thin film solar collector can be fabricated using Co_3O_4 and SnO_2 (Figure 65). As the Co_3O_4 film heats, it will become trapped and heat the air space between the windows. This hot air can then be circulated for storage or for energy consumption.

The thermal reflecting film SnO_2 has numerous applications. One such application is to coat the fiber burner pad which is under the new glass ceramic stove tops. This would reduce thermal losses by directing the heat through the stove top. This should result in an increase in efficiency.

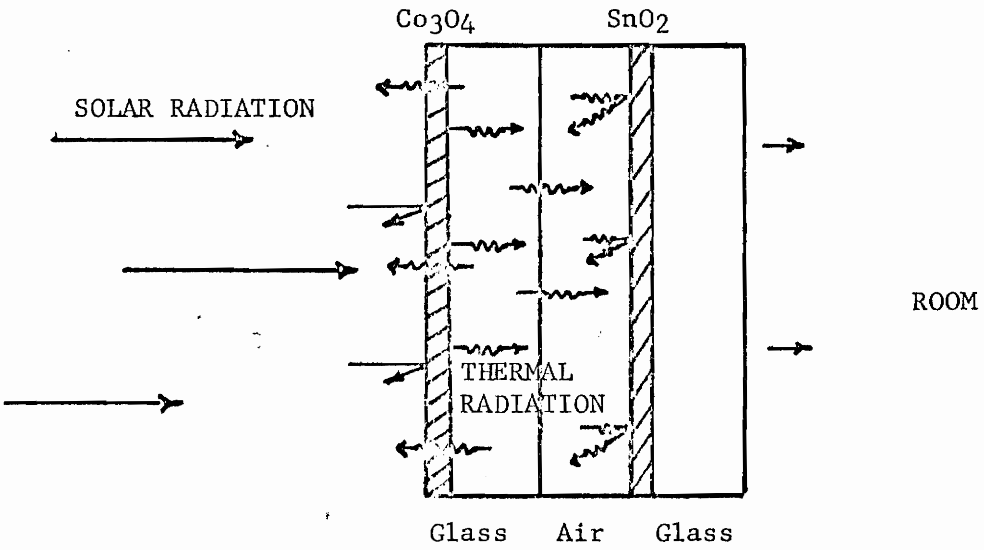

(a) Solar-Thermal Insulating Window·

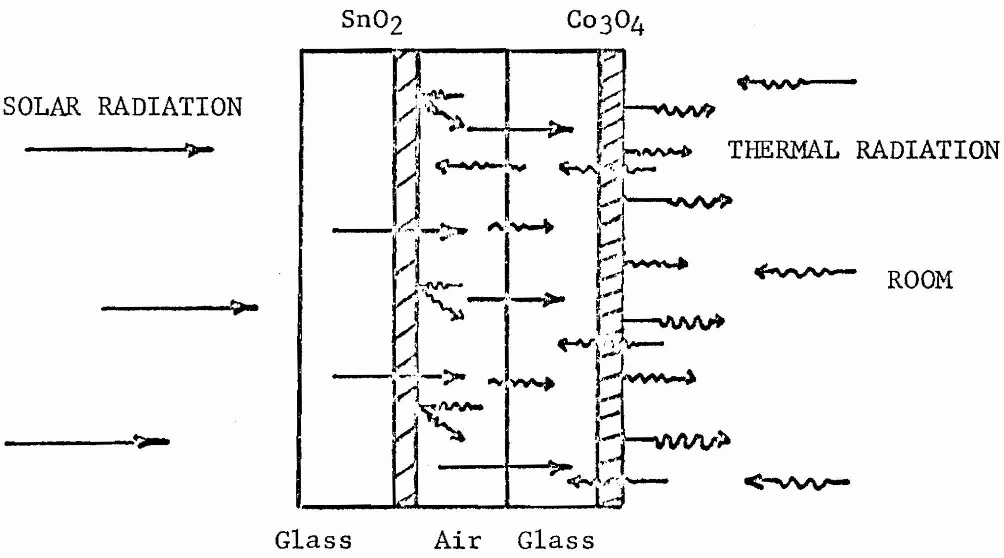

(b) Thermal Emitting Window.

Figure 63. Applications for Oxide Coatings on Glass.

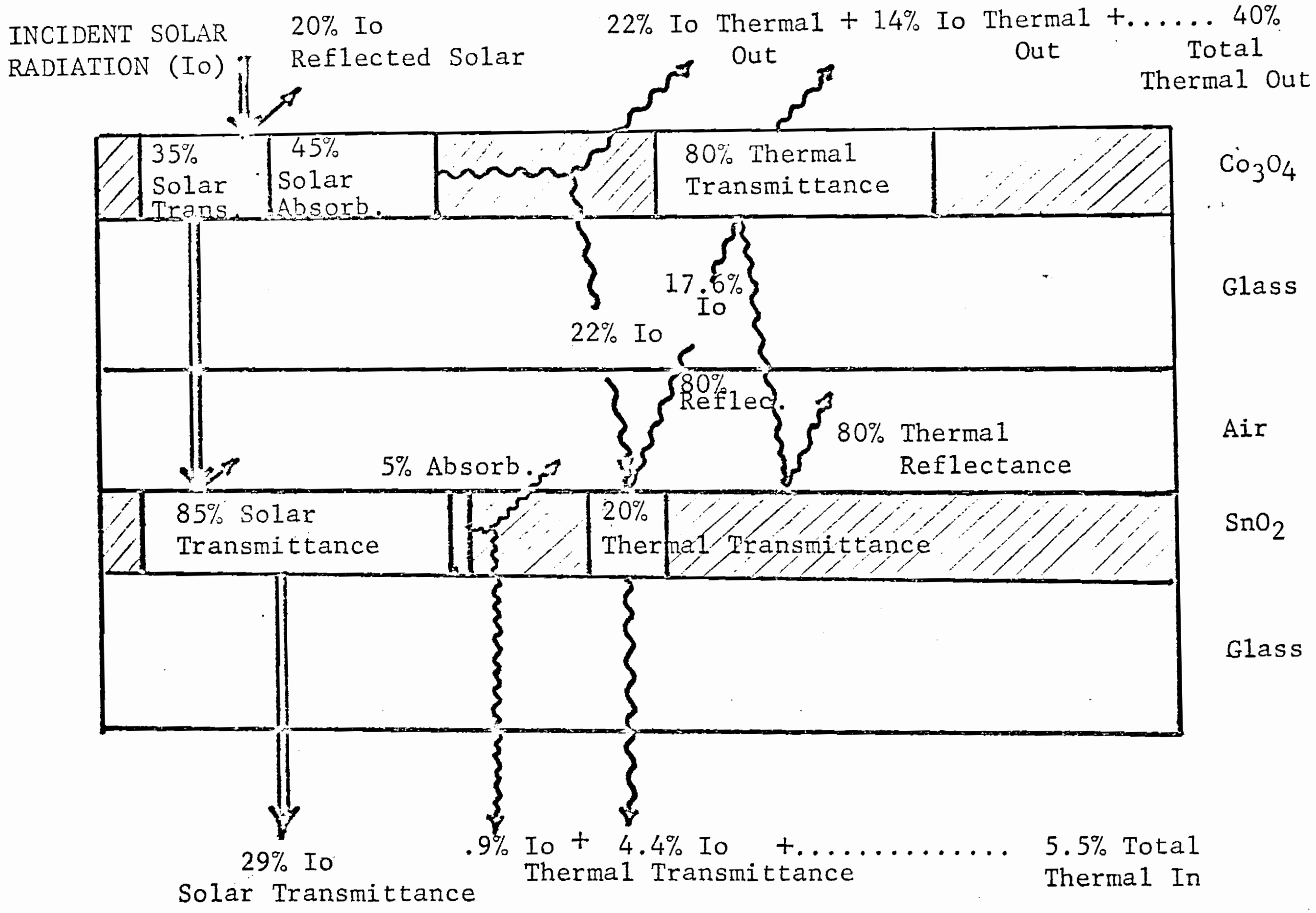

Figure 64. Analysis of the Solar-Thermal Insulating Window.

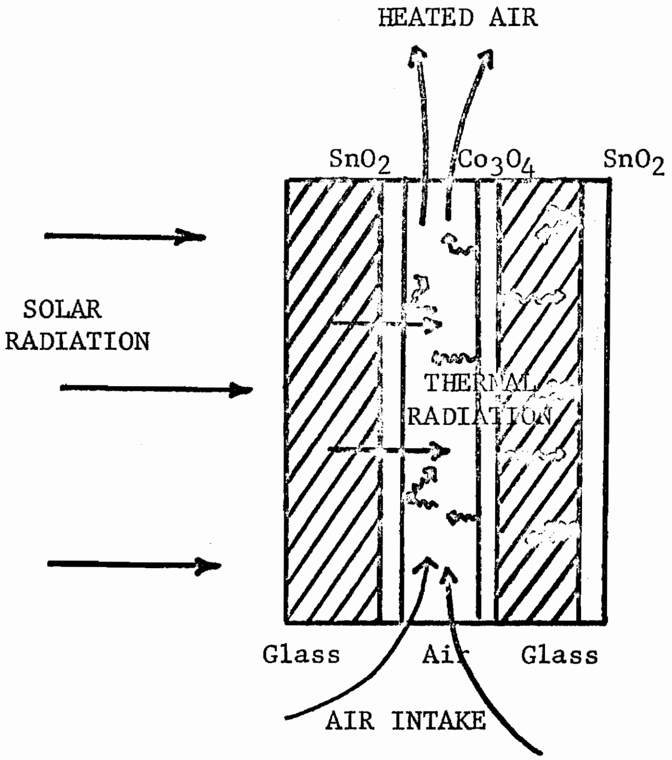

Figure 65. An Oxide Coated Glass Solar Collector.

VI. CONCLUSIONS

The following can be concluded from observations and results of this investigation:

(1) Most oxide compositional systems produce coatings that display predictable color blends. These films have absorbances and resistances that vary in a linear fashion.

(2) Ternary compositions tended to produce more uniform and consistent optical properties over a broad thickness range.

(3) Interference color fringes are most evident in transparent films in which Bragg diffraction can occur. The interference fringes are eliminated by using absorbing films which prevent Bragg diffraction. Lightly colored films (Fe_2O_3) exhibit interference colors especially if they have high indices of refraction which enhance interface reflection and encourage Bragg diffraction.

(4) Scanning electron microscopy revealed that the crystalline morphology of oxide films is unique for each composition.

(5) The pyrolytic decomposition of the vanadium organic ($VO(C_7H_5O_2)_2$) contrasted with the other salts, in that it formed a oxyhydroxide instead of an oxide. This oxyhydroxide was stable and adhesive and displayed high visible through infrared absorbances. This suggests that there are other materials that could be utilized besides oxides.

(6) Absorbance in oxide thin films occurs by two basic mechanisms. One is an electronic mechanism, such as electron excitation that is evidenced by a decrease in resistance. The other is a structural

mechanism. For the same composition a film that is highly crystalline absorbs more than one that is less crystalline or amorphous.

(7) Whenever pure pyrolytic thin films are crystalline, mixtures tend to be noncrystalline. This is probably due to the induced disorder which is a result of a high entropy of mixing.

(8) Absorbance is enhanced in n-type semiconducting oxide thin films by spraying with or annealing in reducing atmospheres, which induce oxygen dificiency.

(9) Absorbance is enhanced in p-type semiconducting oxide thin films by spraying with, or annealing in oxidizing atmospheres. Oxidizing conditions cause these oxygen excess semiconductors to become more oxygen excess.

(10) Reflectance in both n and p-type semiconducting oxide thin films is enhanced in specific, but not consistent wavelength regions, by spraying with or annealing in reducing atmospheres. The far infrared reflectance increased for the n-type, while the near infrared reflectance increased for the p-type.

(11) In multilayered systems, alternating high and low indices of refraction increases reflection, especially in the visible regions. absorption also increased, since the light energy apparently becomes entrapped between the high index layers.

(12) Oxide films do not display high solar reflectances as do metals, such as gold. However, judicious configurations of oxide coated windows can selectively screen solar and thermal energy.

VII. PROPOSED FUTURE RESEARCH

The research described in this thesis answers a few questions and raises more. The following are proposed topics that deserve attention:

(1) To gain a deeper understanding of the optical properties of oxide thin films as related to crystal size. This can be accomplished by annealing in conducive atmospheres at various times and temperatures followed by examination with the scanning electron microscope.

(2) Investigate the rare earth oxides as candidates for oxide films exhibiting with solar reflectance, if they could be fabricated. The rare earths are noted for their high concentration of outer electrons and intense colors.

(3) Convert the vanadium oxyhydroxide film into a vanadium oxide film such as VO_2 or V_2O_3. At the present time a simple method of preparation of these films is not available. These films have interesting electrical properties and optical properties.

(4) Design a feasibility test for the applications suggested in this thesis, utilizing a solar lamp source and temperature monitors.

(5) Measure optical properties out in the far infrared, greater than 2.5μ, to gain further insight into the thermal properties of oxide thin films.

(6) Continue more research on multilayered systems. It may be necessary to stack as many as nine layers to obtain metallic reflectances. Problems must be solved with appearance, production and cost in these multilayered systems.

REFERENCES

1. Vorob'eva and Bessonova, "Solar Heat Protective Glass Based on Iron Oxide Films", Institute of Glass, Translated from Stekloikeramika Vol. 21, (9), 1964.

2. F. D. Bloss, Crystallography and Crystal Chemistry , Holt, Rinehart and Winston Inc., 1971 pp 432.

3. T. Takada, Y. Bando, N. Yamomoty, K. Nagasawa, "Growth of Co_3O_4 Single Crystals and It's Reaction Mechanism", JAP. J. Appl. Phys. 8 [5] 619 1969.

4. J. B. Goodenough, "Influence of Atomic Vacancies on the Properties of Transition Metal oxides I. TiO_x and VO_x", Phys. Rev. 5 [8] 1972.

5. W. D. Kingery, Introduction to Ceramics , John Wiley & Sons, Inc. 1960.

6. Brekhovskikh and Borisova, "The Resistance of Oxide - Metallic Films on Glass to the Action of Ionizing Radiation", Translated from Steklo iKeramika (1) Jan 1962 pp 4-6.

7. V. A. Ryabov, Naiman and Borisova et al Information Bulletin GIS, "Steklo", (1) 1960.

8. Brekhovskikh, Symposium, "The Glassy State" Academy Sciences, USSR, 1960.

9. Botvinkin and Borisova, "New Type of Sun Protective Building Glass", Translated from Steklo i Keramiika, Vol. 21, (5) 1964 pp 7-10.

10. Vavilov, "Eyes and Sun", Izd.Academy Science (1961); I. M. Naiman, "Protecting the Eyes in Industry Profizdat" (1961).

11. Borisova and Botvinkin, "Investigating the Conditions for the Formation of Cobalt Oxide Coatings on Glass", Institute of Glass, Translated from Steklo i Keramika, Vol. 22 (5) 1965 pp 15-19.

12. Rekant and Borisova, "Optical and Energy Parameters of Cobalt Oxide-Coated Glass", Geliotekhnika, Vol. 3 (2) 1966 pp 42-47.

13. Rekant et al, "Selective Films on Glass and Their Characteristics", Semiconductor Solar Energy Converters, Edited by V. A. Baum Avail. NTIS # A7010766 Oct. 31, 1972.

14. Vorob'eva and Bessonova, "Solar Heat Protective Glasses Based on Iron Oxide Films", Institute of Glass, Translated from Steklo i Keramika Vol. 21 (9) Sept. 1964 pp 9-13.

15. Tannhauser, D. S., "Conductivity in Iron Oxides", Journal of Physical Chemistry, Solids, 23, p. 25-39, 1962.

16. Gardner, R. G. G., Sweet, F., and Tanner, D. W., "The Electrical Properties of Alpha Ferric Oxide - II. Ferric Oxide of High Purity", Journal of Physical Chemistry, Solids, 24, p. 1183-1196, 1963.

17. Verwey, E. J. W., Hoaijman, P. W., Romeijn, F. C., and Van Oosterhout, G. W., "Controlled Valency Semiconductors," Phillips Res. Rep., 5, p. 173-187, 1950.

18. Hackler, C., M.S. Thesis, "Reactive Radio Frequency Sputtering of Iron Oxide Thin Films for Electrical Resistivity Characterization", Virginia Polytechnic Institute and State University, May, 1974.

19. American Institute of Physics Handbook, Second Edition, McGraw-Hill, 1963.

20. G. Haas, "Thin Films of Titanium Oxide", Vacuum, 2(1952) 331.

21. S. Sakurai and M. Watanabe, Rev. Elect. Comm. Lab., 11[178] 1963.

22. Hollander, "Aniosotropic Conduction in Nonstoichiometric Rutile (TiO_2)", Phys. Rev. 119(1960) 1882.

23. W. S. Baer, J. Phys. Chem. Solids, 28(1967) 677.

24. F. A. Grant, Rev. Mod. Phys., 31[646] 1959.

25. H. P. R. Frederikse, "Recent Studies on Rutile (TiO_2)", J. Appl. Phys., 32(1961) 2211.

26. R. N. Blumenthal, J. Bankus, and W. M. Hirthe, "Studies of the Defect Structure of Nonstoichiometric Rutile, TiO_{2-x}", J. Electro Chem. Soc. 114[2] 1967.

27. T. Hurden, "On the Defect Structure of Rutile", Acta. Chem. Scand. 13(1959) 365.

28. D. S. Tannhauser, Solid Commun., 1[223] 1963.

29. Blumenthal, J. Coburn, J. Bankus and W. M. Hirthe, J. Phys. Chem. Solids, 27[643] 1966.

30. Y. Katsuta, R. Akahane, and K. Yahagi, "Electrical Properties of Rutile (TiO_2) Thin Films", Jap. J. of Applied Phys. 10[8] 1971.

31. D. C. Crunemeyer, "Electrical and Optical Properties of Rutile Single Crystals", Phys. Rev. 87(1952) 876.

32. Yokuzawa, Iwasa, Teramoto, "Vapor Deposition of TiO_2," Jap. J. App. Phys. 7(1968) 96-97.

33. Fitzgibbons, K. J. Sladek, Hartwig, "TiO_2 Film Properties as a Function of Processing Temperature", J. Electrochem. Soc. 119[6] 1972.

34. A. E. Feursanger, Proc. IEEE 52 (1964) p. 1463.

35. J. Maserjian, "Conduction Through Thin Titanium Dioxide Films", Avail NTIS N66-39934, 9[1] 1966.

36. L. D. Loch, "The Semiconducting Nature of Stannic Oxide", J. Electrochem. Soc. Vol. 110 (10) Oct. 1963, pp. 1081-1083.

37. E. E. Kohnke, "Electrical and Optical Properties of Natural Stannic Oxide Crystals", Phys. Chem. Solids, 23, 1557-62 (1962).

38. Rohatgi, Viverito and Slack, "Electrical and Optical Properties of Tin Oxide Films", J. Am. Cer. Society Vol. 57 (6) June 1974.

39. (a) C. A. Vincent, "Nature of Semiconductivity in Polycrystalline Tin Oxide", J. Electrochem. Soc. Vol. 119 (4) 515-18 (1972).

    (b) C. A. Vincent and D. G. C. Weston, "Preparation and Properties of Semiconducting Polycrystalline Tin Oxide", ibid, pp. 519-21.

40. Giani & Kelly, "A Study of SnO_2 Thin Films by Sputtering and by Anodizing", J. Electrochem. Soc. Vol. 121 (3) March 1974 394-399.

41. Muto and Furwichi, "Electrical Properties of Tin Oxide Films Prepared by Chemical Vapor Deposition", Reports Res. Lab, Asahi Glass Co., Ltd., 25[1] (1973).

42. J. C. C. Fan, "Preparation and Optical Properties of Crystals and Films of Vanadium Oxides", Ph.D. Thesis Harvard University avail through NASA 1972.

43. Powder Diffraction File, Joint Committee on Powder Diffraction Standards, Swarthmore, Pa.

44. A. Rohatgi, "Semiconducting Thin Films on Glass", M.S. Thesis, VPI & SU, 1972.

45. T. R. Viverito, E. W. Rilee, L. H. Slack, "Oxide Film Deposition by an Improved Pyrolytic Decomposition Process".

46. G. A. Rozgonyi and W. J. Polito, "Preparation of Thin Films of Vanadium (Di, Sesgoi-, and Pent-) Oxide", J. Electrochem. Soc. 115[1] 1968.

47. M. A. Gisin and E. A. Nesmelov, Optika i Spektroskopiya 14 (3), 395-400 (1963) (Russ).

48. M. V. Vijayalaxmi and M. Ramakrishna Rao, "Performance Evaluation of Thin Film Multilayer Systems Using Electronic Digital Computer", Indian Journal of Pure and Applied Physics, Vol. 10, Jan. 1972, 43-47.

49. A. E. Ennos, "Stresses Developed in Optical Film Coatings", Appl. Opt. 5(1969) 51.

50. P. B. Clapham, "Progress in the Production of Optical Multilayered Films", Thin Solid Films, 4(1969) 291-305.

51. P. Bousquet, Opt. Acta, 3 (1966) 153.

52. M. Bourg, Ann. Phys. 7 (1962) 623.

53. R. J. King and M. J. Downs, "Ellipsometery Applied to Films on Dielectric Surfaces", Surface Sci., 16(1969) 288.

54. M. Laikin, "Optical Coatings for Laser Use", Appl. Opt., 4(1965) 1032.

55. D. L. Evans and G. R. Fisher, "X-ray Determination of Film Thickness Using the Glassy Halo", Bull. Am. Cer. Soc. 52[6] 1973.

56. H. T. Evans and M. E. Mrose, "A Crystal Chemical Study of Vanadium Oxide Minerals, Häggite and Do loresite", The Am. Mineral, 45[9] 1960.

APPENDIX A

Oxide Film Deposition by an Improved Pyrolytic Decomposition Process

T. R. Viverito, E. W. Rilee and L. H. Slack

With the proliferation of oxide thin films for optical and electrical applications, the controlled pyrolytic deposition of oxides is of wide spread interest, especially in cases where vacuum deposition is impractical or uneconomical. The conventional pyrolytic process consists of spraying a salt solution onto a heated substrate on which the solvent evaporates, the salt decomposes and the salt's cation combines with atmospheric oxygen to form the oxide film on the substrate. When the salt decomposition and subsequent oxidation provides a negative free energy change, the oxide film is formed.

The conventional pyrolytic deposition of oxide films(1-4) consists of spraying a dilute solution of a metal salt from a corrosion resistant spray gun onto the heated substrate. The improved method disperses the solution into micron sized droplets to form a fog, using the glass apparatus shown schematically in Fig. 1. The solution is pumped, using a conventional circulating tubing pump, to the sprayer where it flows over a hollow glass sphere (A). The sphere has a 0.006 in. wide slit through which air is blown. This flow of air causes the thin sheet of solution flowing over the sphere to be ruptured and dispersed into a fog(5). Two obstructions, a glass impactor (B) and a trap in the tube (C), capture the larger droplets and return them to be recycled with the excess solution. The fog is directed by a tube to the heated substrate, where pyrolytic decomposition and oxide formation occurs.

TABLE I

Comparison of the New and Conventional Processes Spraying a 2.85 M $SnSl_4 \cdot 5H_2O$ Alcohol Solution to Provide a SnO_2 Film

	Substrate	Air Flow	Spray	Cooling After	
	Temp.(°C)	Rate (cfm)	Time(sec)	10 sec.	60 sec.
New	350	0.60	240	57°C	65°C
Conventional	650	5.00	15	95°C	163°C

	Thickness Å	Resistivity (cm)
New	1034	0.05
Conventional	1391	0.05

Any oxide deposited by conventional spraying can also be deposited by this new technique. Thus far, oxides of tin, iron, cobalt, vanadium and titanium have been deposited by the new method. A comparison of the conventional and new process has been made using a 2.85 M $SnCl_4 \cdot 5H_2O$ solution to deposit SnO_2 films. Some results are summarized in Table I. Both films were identified by X-ray diffraction as crystalline SnO_2 with identical diffraction patterns. The electrical sheet resistance of the tin oxide films were essentially the same. The optical properties were similar except that the film deposited with the fog generator was slightly more yellow even though it was thinner. These films had a broad weak absorption band between 0.8 and 1.4 μm not evident in the film formed by the conventional method.

The most striking difference between the conventional sprayer and the fog generator is the difference in the lowest substrate temperature used to provide a good quality tin oxide film. The very high flow rate required by the conventional sprayer causes considerable substrate surface cooling during the first seconds of spraying. Therefore, the substrates must be heated $\approx$ 300°C above the temperature used with the fog generator to maintain the substrate above the minimum deposition temperature throughout the entire spraying cycle. Spraying times can be varied by changing the solution concentration.

The low air flow rate used with the fog generator leads to other advantages. The spray is easily contained and guided to the substrate. There is little waste of material and the operator and equipment are not exposed to the fog. The film thickness can be precisely controlled by presetting the time the solution is circulated. Film uniformity was also improved using the fog generator in these laboratory experiments. Furthermore, the glass construction facilitates cleanup and eliminates corrosion problems sometimes encountered when using metal sprayers.

This work was supported by the U. S. Army Research Office in Durham, Grant No. DA HCO4 74G 0081, and ASG Industries, Kingsport, Tennessee.

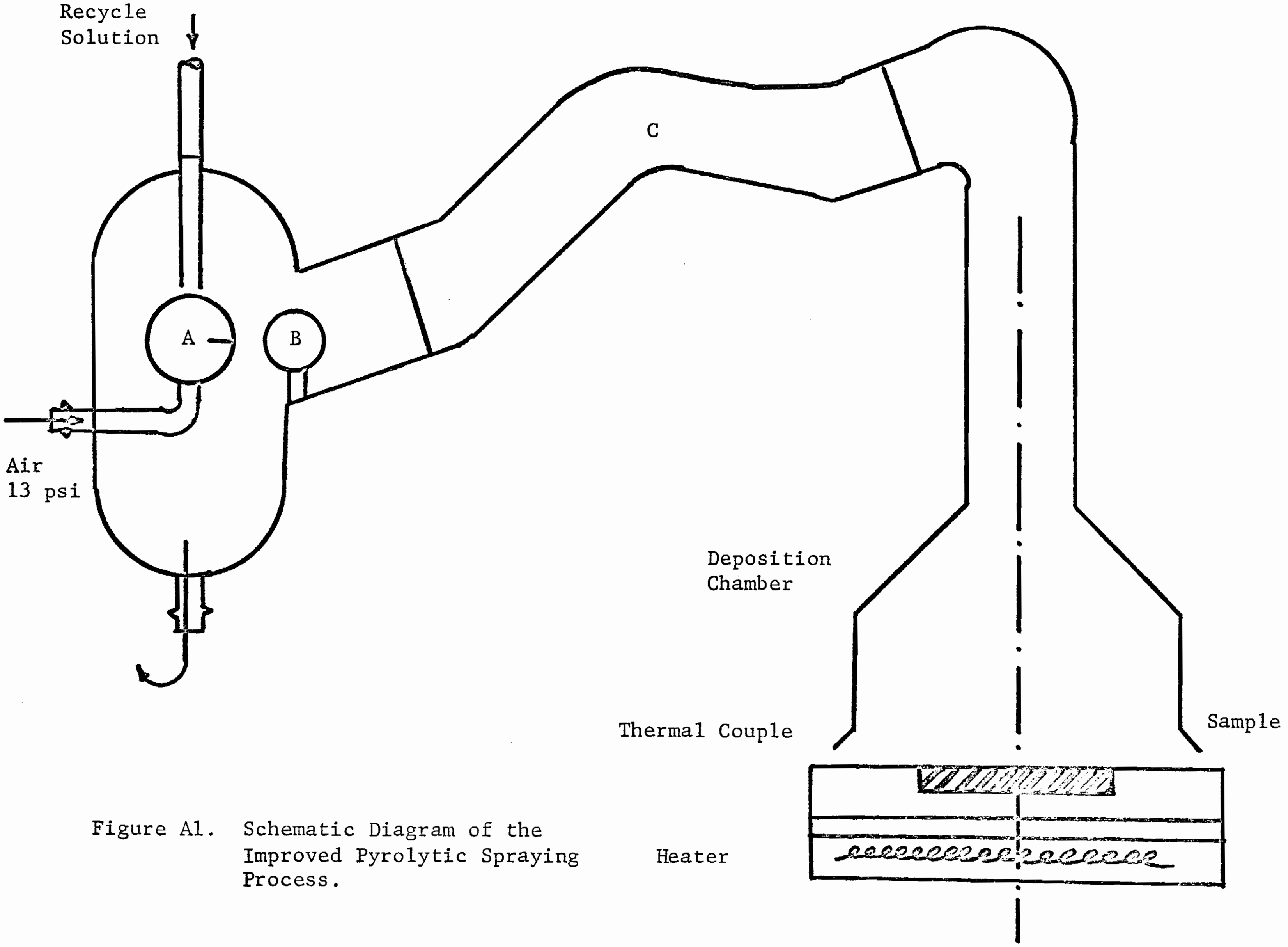

Figure A1. Schematic Diagram of the Improved Pyrolytic Spraying Process.

References

1. A. Rohatgi, T. R. Viverito and L. H. Slack, "Electrical and Optical Properties of Tin Oxide Films," J. Amer. Ceram. Soc., 57 [ ] 00-000 (1974).

2. R. Gomer, "Preparation and Some Properties of Conducting Transparent Glass," Rev. Sci. Instrum., 24, 993 (1953).

3. V. K. Moloslavskii, "Infrared Absorption of Thin Films of Tin Dioxide," Opt. Spectrosc. (USSR), 1, 154 (1959).

4. C. A. Vincent and D. G. C. Weston, "Preparation and Properties of Semiconducting Polycrystalline Tin Oxide," J. Electrochem. Soc., 119 [4] 518-21 (1972).

5. S. Dresner, "It's Superspray," Popular Science, 1973, [5] p. 102.

APPENDIX B

Computer Plot Routine

```
C PROGRAM TO COMPUTE AND PLOT REFLECTANCE AND TRANSMITTANCE
C FROM REFLECTANCE AND ABSORBANCE DATA.
C REFLECTANCE USES TWO CALIBRATION CURVES AND THE RELATIONS
C          A(1) - A(2) = 2 LOG RM
C          A(1) - A(3) = LOG RM + LOG RS
C A(1) = REFLECTIVITY OF SYSTEM MIRROR.
C A(2) = REFLECTIVITY OF THE CALIBRATION MIRROR.
C A(3) = REFLFCTIVITY OF THE UNKNOWN SAMPLE.
C RM = REFLECTANCE OF THE CALIBRATION SAMPLE
C RS = REFLECTANCE OF UNKNOWN SAMPLE.
C FIRST DATA CARD CONTAINS:
C          COLUMNS 1-4 NUMBER OF DATA POINTS. RIGHT JUSTIFIED.
C          COLUMNS 5-8 NUMBER OF DATA SETS. RIGHT JUSTIFIED.
C          COLUMNS 9-18 BEGINNING VALUE OF WAVELENGTH WITH DECIMAL.
C          COLUMNS 19-29 WAVE LENGTH INCREMENTAL VALUE.
C          COLUMNS 29-38 SCAN SPEED ANG./TIME
C          COLUMNS 39-48 CHART SPEED TIME/DIVISION     Y
C          COLUMNS 49-80 PUNCH ONLY "(10F10.2)"
C     SECOND DATA CARD CONTAINS THE NUMBER
C     ONE IN COLUMN TWO FOR AN 8"X5" PLOT.  ANY
C     OTHER DIGIT YIELDS 5"X3.5" PLOT.
C THIRD  GROUP OF DATA CARDS CONTAIN VALUES OF A(1) PUNCHED, WITH DECIMAL,
C IN SUCCESSIVE 10 COLUMN GROUPS
C FOURTH GROUP OF DATA CARDS CONTAIN VALUES OF A2 PUNCHED WITH DECIMAL
C FIFTH  GROUP OF DATA CARDS CONTAINS VALUES OF A(3) PUNCHED, WITH DECIMAL,
C IN SUCCESSIVE 10 COLUMN GROUP.
C FOR ADDITIONAL DATA SETS PUNCH ONLY A(3) DATA CARDS.
C PROGRAM HANDLES UP TO 100 DATA POINTS AND ANY NUMBER OF DATA SETS
      DIMENSION A1(100), A2(100), A3(100), X(10), LABLE(20), LAMDA(100),
     CALAMDA(100), RS(100),ABS(100),TRANS(100)
      REAL*4LAMDA,INTER,LENGTH,MULT
      INTEGER*4SIZE
```

```
      READ(5,1) INDEX, NOSETS, BLAMDA, SCNSPD, CHTSPD, (X(I), I=1,10)
    1 FORMAT(2I4,3F10.2,10A4)
      XMAX=BLAMDA
      READ(5,300)SIZE
  300 FORMAT(I2)
      DLAMDA=SCNSPD*CHTSPD
C      COMPUTE VALUES OF WAVELENGTH
      DO 20 KI=1,INDEX
      ACNT=KI-1
      LAMDA(KI)=BLAMDA-ACNT*DLAMDA
   20 CONTINUE
C     ESTABLISH SCALE LENGTHS
      LENGTH=LAMDA(1)-LAMDA(INDEX)
      MULT=10.
      INTER=LENGTH/MULT
      DIGIT=ALOG10 (INTER)
      IDIGIT=DIGIT
      DIGIT=IDIGIT
      AINTER=INTER/10.**DIGIT
      IINTE=AINTER
      AINTER=IINTE
      INTER=AINTER*(10.**DIGIT)
  111 CHECK=INTER*MULT
      IF(CHECK.GE.LENGTH)GO TO 110
      MULT=MULT+1.0
      GO TO 111
  110 CONTINUE
      LENGTH=CHECK
      XMIN=LAMDA(1)-LENGTH
C     SELECT PLOT SIZE.  TWO OPTIONS SIZE=1 YIELDS
C     A SINGLE PAGE PLOT X=8 INCH Y=5INCH SIZE DIFFERENT
C     FROM ONE YIELDS PLOTS TWO FOR A PAGE X=5 INCH
```

```
C      Y = 3.5 INCH
       IF(SIZE.EQ.1) GO TO 200
       XSCALE=5.
       YSCALE=3.5
       GO TO 201
  200 CONTINUE
       XSCALE=8.
       YSCALE=5.
  201 CONTINUE
C   SCALE VARIABLE FOR X-AXIS
       DO 204 K2=1,INDEX
       ALAMDA(K2)=((LAMDA(K2)-XMIN)/LENGTH)*XSCALE
  204 CONTINUE
       COLAM=BLAMDA/10.**4
C      ESTABLISH ORIGIN
       CALL PLOT(3.,3.,-3)
       NODONE=0
       READ(5,X) (A1(N), N=1,INDEX)
       READ(5,X) (A2(N), N=1,INDEX)
    6 READ(5,100) LABLE
  100 FORMAT (20A4)
       WRITE(6,80)
   80 FORMAT ('1')
       WRITE(6,100) LABLE
       WRITE(6,10)
   10 FORMAT ('0',4X,'A(1)',12X,'A(2)',12X,'A(3)',13X,'RM',14X,'RS',
      C12X,'LAMBDA',10X,'ABS',11X,'TRANS')
       READ (5,X) (A3(N), N=1,INDEX)
       READ(5,X) (ABS(N), N=1,INDEX)
       DO 3 J=1,INDEX
       RMLOG = (A1(J)-A2(4))/2.
       RSLOG = A1(J)-A3(J)-RMLOG
```

```
      RS(J) = 10.**RSLOG
      RM=10.**RMLOG
      TRANS(J)=(10.**(2.-ABS(J)))/100.
      FACTOR=J-1
      WRITE(6,2) A1(J),A2(J),A3(J),RM,RS(J),LAMDA(J),ABS(J),TRANS(J)
    2 FORMAT (' ',E12.5,3X,E12.5,3X,E12.5,3X,E12.5,3X,E12.5,3X,E12.5,3X,
     CE12.5,3X,E12.5)
      RS(J)=1.00-RS(J)
    3  CONTINUE
C   SCALE VARIABLE FOR Y-AXIS
      DO 310 KJ=1,INDEX
      RS(KJ)=RS(KJ)*YSCALE
      TRANS(KJ)=YSCALE*TRANS(KJ)
  310 CONTINUE
C     PLOTTING ROUTINES
C     DRAW MARGINS
      CALL PLOT(XSCALE,0.,2)
      CALL PLOT(XSCALE,YSCALE,2)
      CALL PLOT(0.0,YSCALE,2)
      CALL PLOT(0.0,0.0,2)
C     PLACE TIC MARKS ON X-AXIS AND SCALE VALUES
      DIST=XSCALE/MULT
      KSTOP=MULT-1.0
      YLEN=YSCALE-0.125
      CALL NUMBER(ALAMDA(1),-0.5,0.1,CDLAM,0.0,+2)
      DO 210 K3=1,KSTOP
      ANUM=K3
      XTIC=ANUM*DIST
      CALL PLOT(XTIC,0.0,3)
      CALL PLOT(XTIC,-0.125,2)
      XV=XTIC-0.15
      XVAL=(XMIN+(INTER*ANUM))/10.**4
```

```
      CALL NUMBER(XV,-0.5,0.1,XVAL,0.0,3)
      CALL PLOT(XTIC,YSCALE,3)
      CALL PLOT(XTIC,YLEN,2)
  210 CONTINUE
      CXMI=XMIN/10.**4
      CALL NUMBER(-0.15,-0.5,0.1,CXMI,0.0,3)
C     PLACE TIC MARKS AND SCALES ON Y-AXIS
      CALL SYMBOL(-0.5,-0.1,0.1,'00',0.0,2)
      YDIST=YSCALE/5.
      XLEN=XSCALE-0.125
      VALY=0
      DO 220 K4=1,4
      YINT=K4
      VALY=VALY+20.
      YTIC=YDIST*YINT
      Y=YTIC-0.1
      CALL PLOT(0.0,YTIC,3)
      CALL PLOT(0.125,YTIC,2)
      CALL NUMBER(-0.5,Y,0.1,VALY,0.0,-1)
      CALL PLOT(XSCALE,YTIC,3)
      CALL PLOT(XLEN,YTIC,2)
  220 CONTINUE
      Y2=YSCALE-0.1
      CALL SYMBOL(-0.7,Y2,0.1,'100',0.0,3)
C     AXIS LABLES, X-AXIS
      CALL SYMBOL(0.0,-1.0,0.2,'WAVE LENGTH (MICRONS)',0.0,21)
C     AXIS LABLES, Y-AXIS
      CALL SYMBOL(-1.0,0.5,0.2,'FRAC. RAD. ENERGY',90.,18)
C     IDENTIFY PLOT
      YDEF=YSCALE+0.5
      CALL SYMBOL(0.0,YDEF,0.1,LABLE,0.0,80)
C     PLOT DATA CURVE
```

```
      CALL PLOT(ALAMDA(1),RS(1),3)
      DO 500 KP=1,INDEX
      CALL PLOT(ALAMDA(KP),RS(KP),2)
  500 CONTINUE
      CALL PLOT(ALAMDA(1),TRANS(1),3)
      DO 610 KSP=1,INDEX
      CALL PLOT(ALAMDA(KSP),TRANS(KSP),2)
  610 CONTINUE
  230 CONTINUE
C     INDICATE DATA SCALES ON DATA SHEETS
      WRITE(6,250)XMAX
  250 FORMAT('0',5X,'MAXIMUM VALUE OF X-AXIS=',F10.2)
      WRITE(6,251)XMIN
  251 FORMAT(' ',5X,'MINIMUM VALUE OF X-AXIS=',F10.2)
      WRITE(6,252)INTER
  252 FORMAT(' ',5X,'INTERVAL BETWEEN X-AXIS TIC MARKS=',F10.2)
      CALL PLOT(XSCALE+5.,0.0,-3)
      NODONE =NODONE + 1
      IF(NOSETS - NODONE) 4,4,5
    5  GO TO 6
    4  CONTINUE
      CALL PLOT(0.,0.,-4)
      STOP
      END
```

APPENDIX C

Salt Solutions and Organo-Metallics

(1)	Ferric Chloride	$FeCl_3 \cdot 6H_2O$
(2)	Vanadium Oxyacetylacetonate	$VO(C_5H_7O_2)_2$
(3)	Cobalt Acetylacetonate	$Co(C_5H_7O_2)_2$
(4)	Titanium Tetrachloride	$TiCl_4$
(5)	Stannic Chloride	$SnCl_4 \cdot 5H_2O$
(6)	Stannous Chloride	$SnCl_2 \cdot 2H_2O$
(7)	Cobalt(ous) Acetate	$Co(CH_3COO)_2 \cdot 4H_2O$
(8)	Antimony Trichloride	$SbCl_5$
(9)	Cobalt Chloride	$CoCl_2 \cdot 6H_2O$
(10)	Vanadium Trichloride	VCl_3
(11)	Manganese Chloride	$MnCl_2$
(12)	Nickelous Chloride	$NiCl_2 \cdot 6H_2O$
(13)	Praseodymium Chloride	
(14)	Cerous Chloride	$CeCl_3 \cdot XH_2O$
(15)	Magnesium Chloride	$MgCl_2 \cdot 6H_2O$
(16)	Lanthanum Chloride	$LaCl_3 \cdot 6H_2O$
(17)	Phosphorus Pentachloride	PCl_5
(18)	Cupric Chloride	$CuCl_2 \cdot 2H_2O$
(19)	Zinc Chloride	$ZnCl_2$
(20)	Indium Trichloride	$InCl_3 \cdot 4H_2O$
(21)	Chromium Chloride	$CrCl_3 \cdot 6H_2O$
(22)	Bismuth Trichloride	
(23)	Barium Chloride	$BaCl_2 \cdot 2H_2O$

(24)	Aluminum Chloride	$AlCl_3$
(25)	Copper Oxalate	
*(26)	Copper Acetylacetonate	$Cu(C_5H_7O_2)_2$
(27)	Barium Acetylacetonate	
(28)	Cerous Acetylacetonate	$Ce(C_5H_7O_2)_3$
(29)	Chromium Acetylacetonate	$Cr(C_5H_7O_2)_3$
		$CoC_2O_4 \cdot 2FeC_2O_4 \cdot 6H_2O$
(31)	Molybdenum Pentachloride	$MOCl_3$
(32)	Cadmium Formate	

APPENDIX D

Optical Properties as a Function of Wavelength for the Oxide Thin Film Compositions

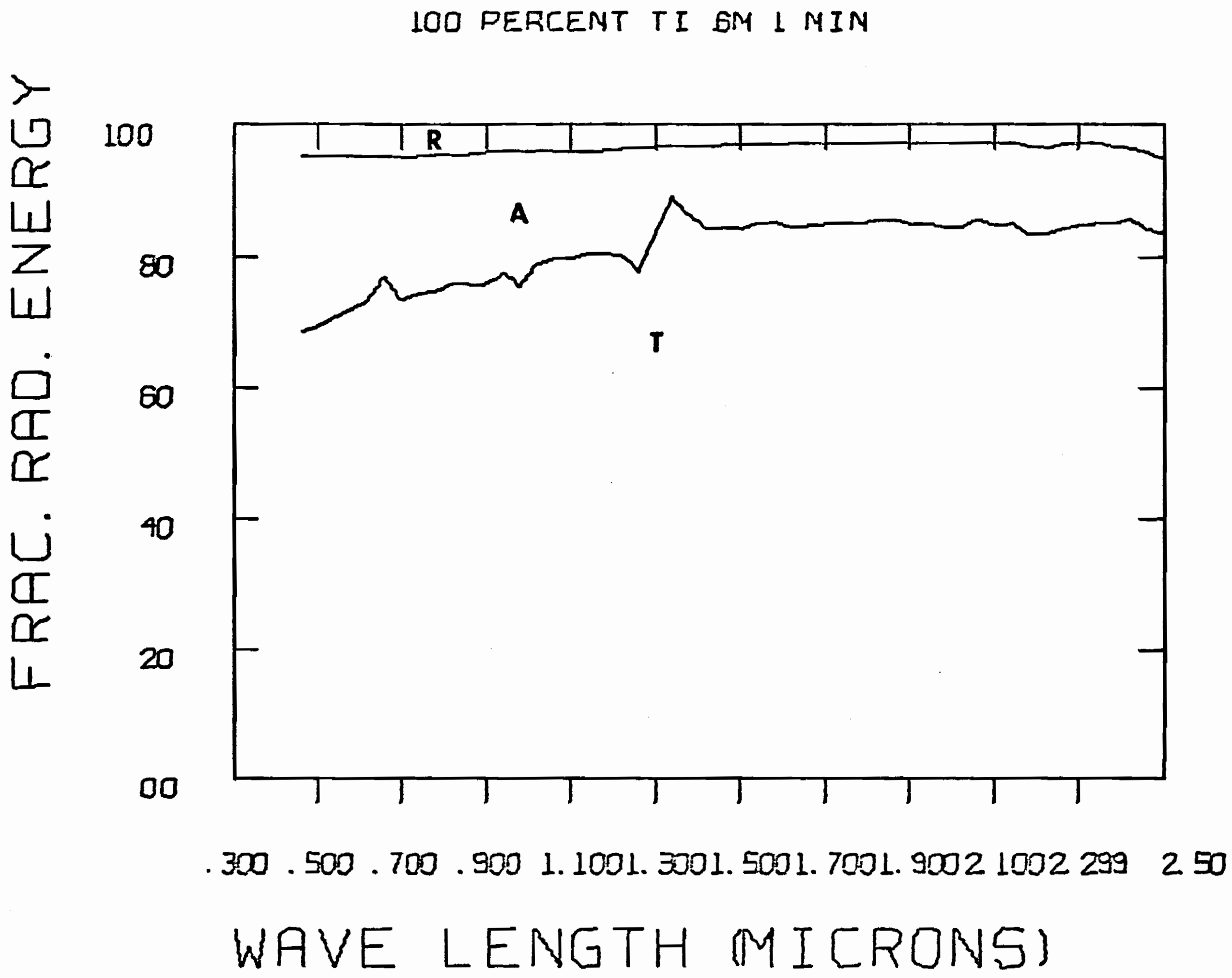

Figure D-1. Optical Properties of 100% TiO2.

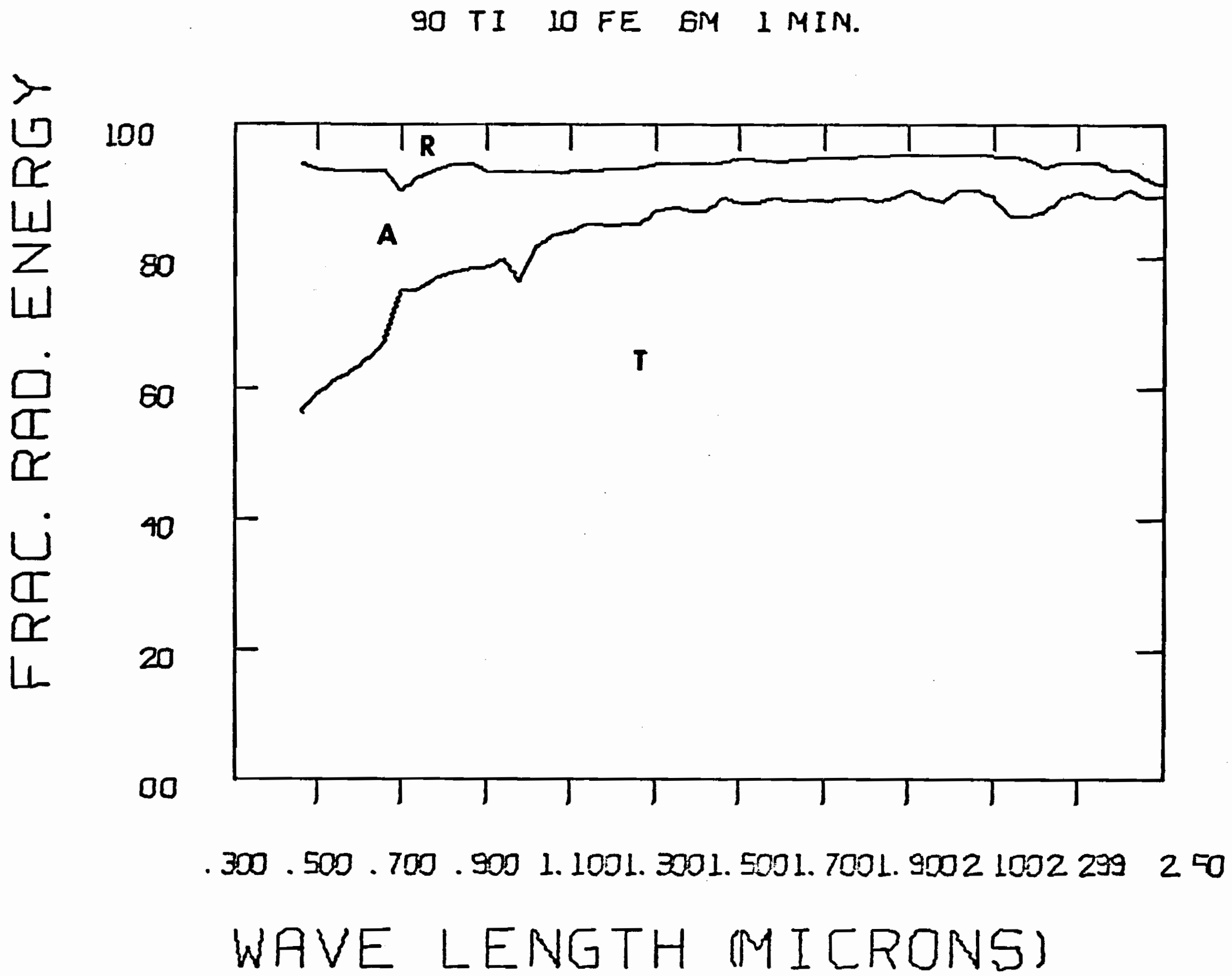

Figure D-2. Optical Properties of 90%TiO_2-10%Fe_2O_3

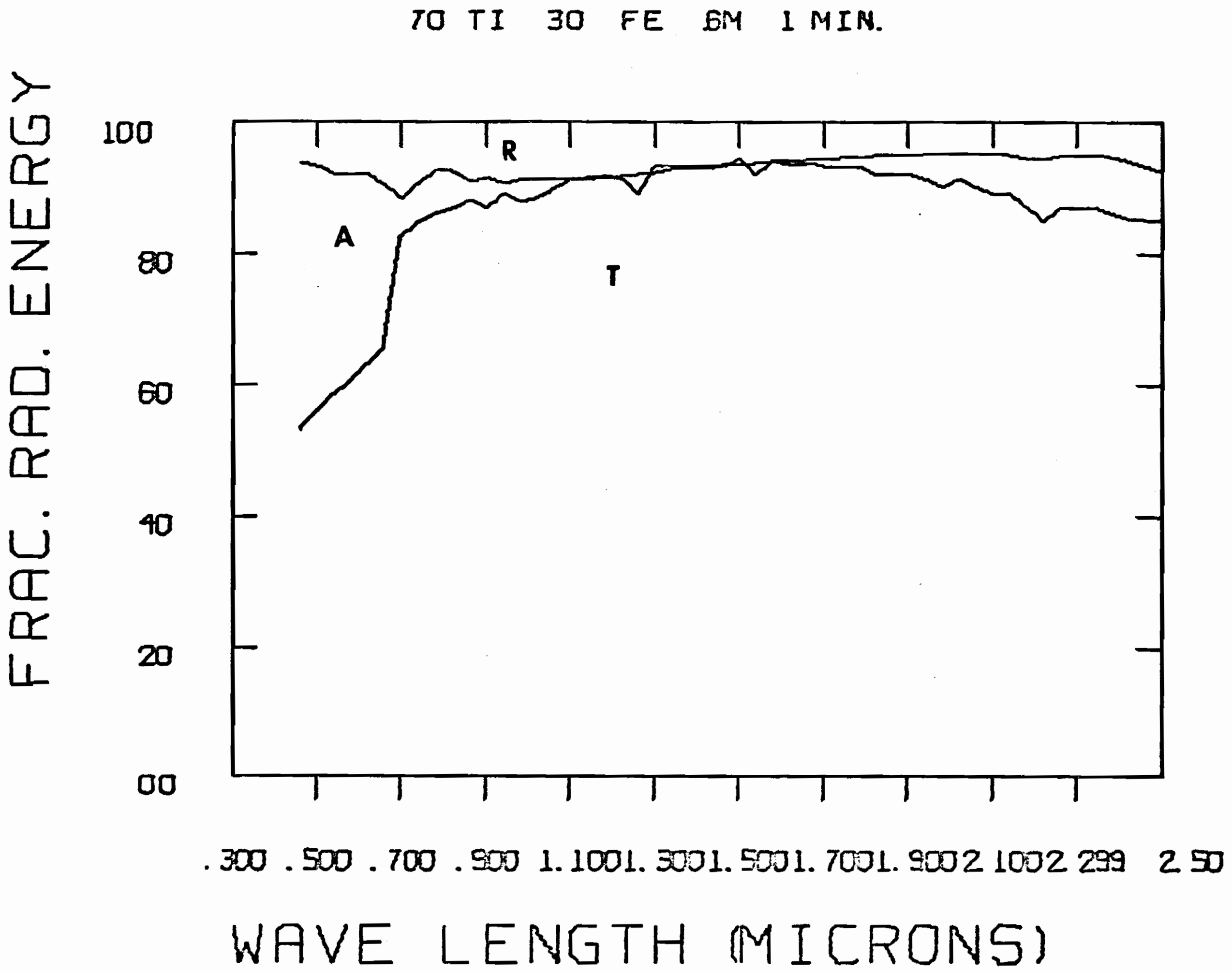

Figure D-2. Optical Properties of $70\%TiO_2-30\%Fe_2O_3$

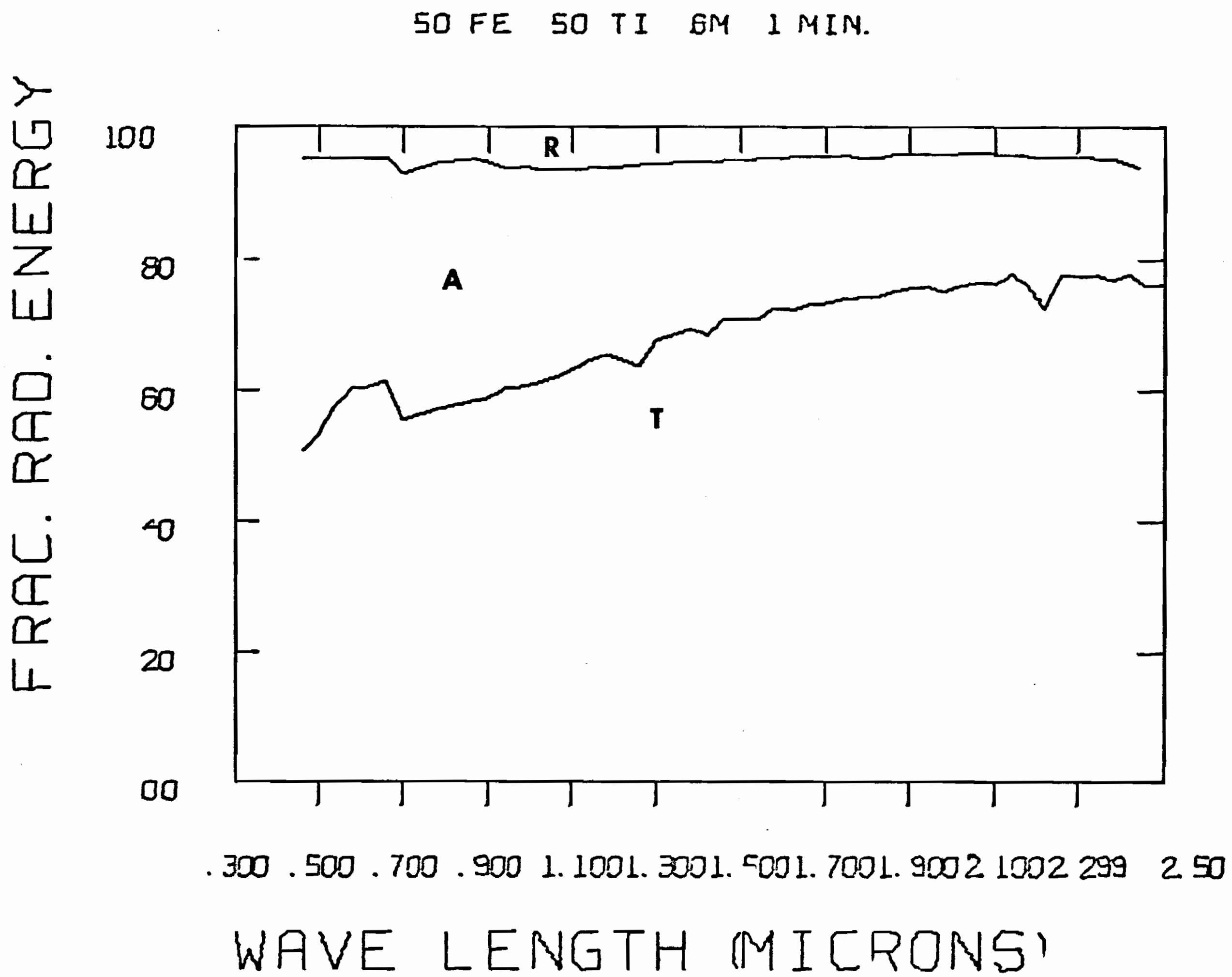

Figure D-4. Optical Properties of 50%TiO_2-50%Fe_2O_3

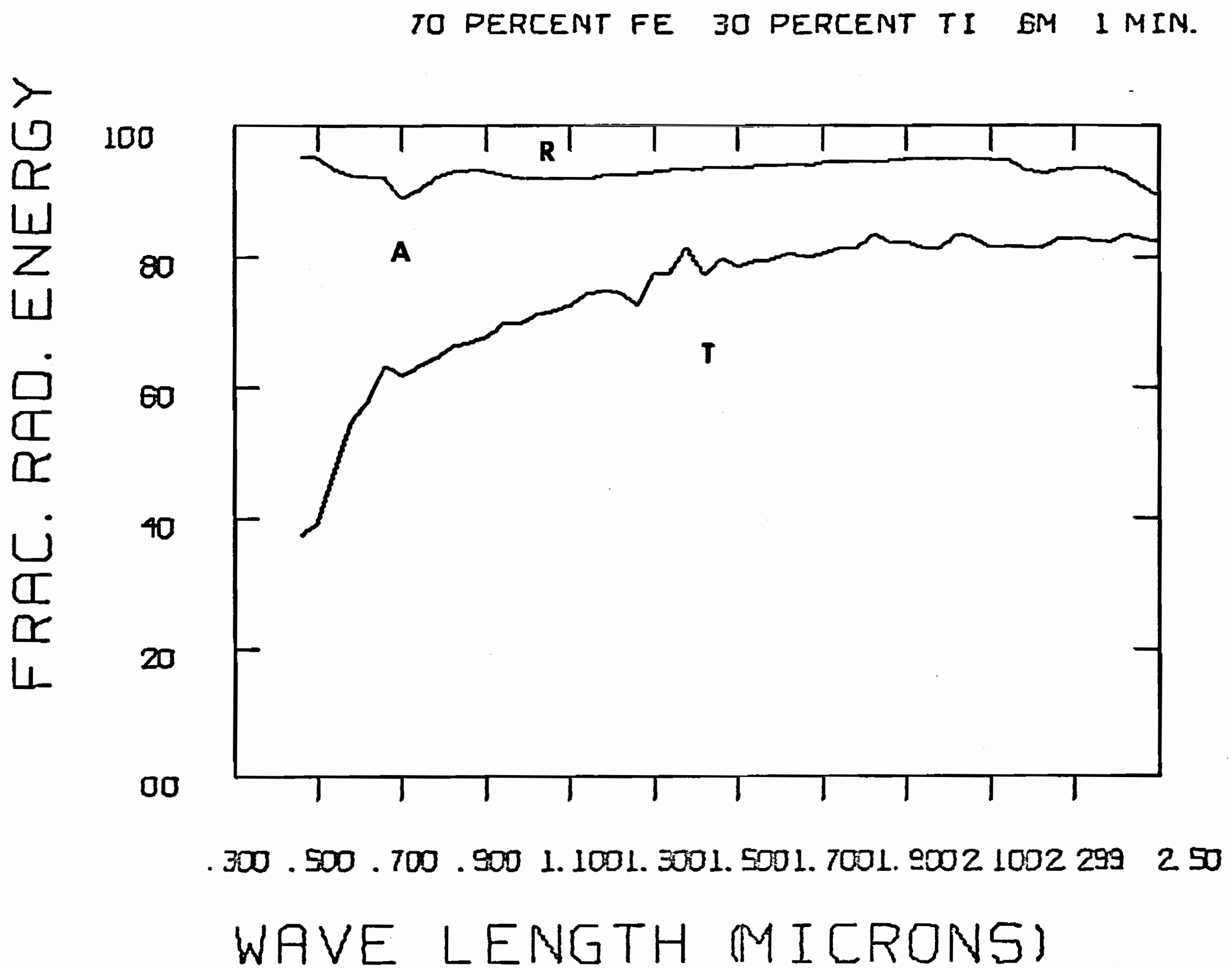

Figure D-5. Optical Properties of $30\%TiO_2-70\%Fe_2O_3$

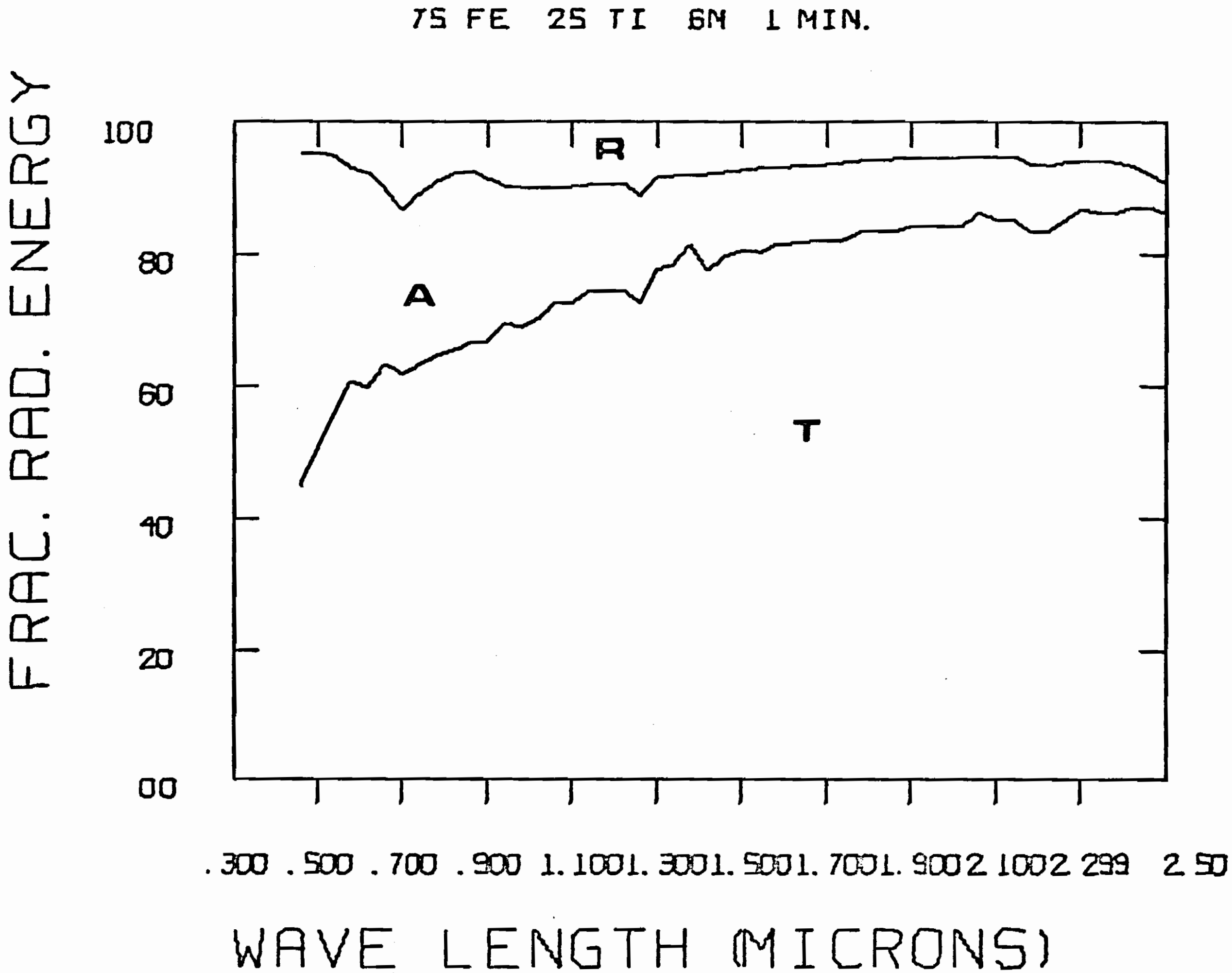

Figure D-6. Optical Properties of 75%Fe_2O_3-25%TiO_2.

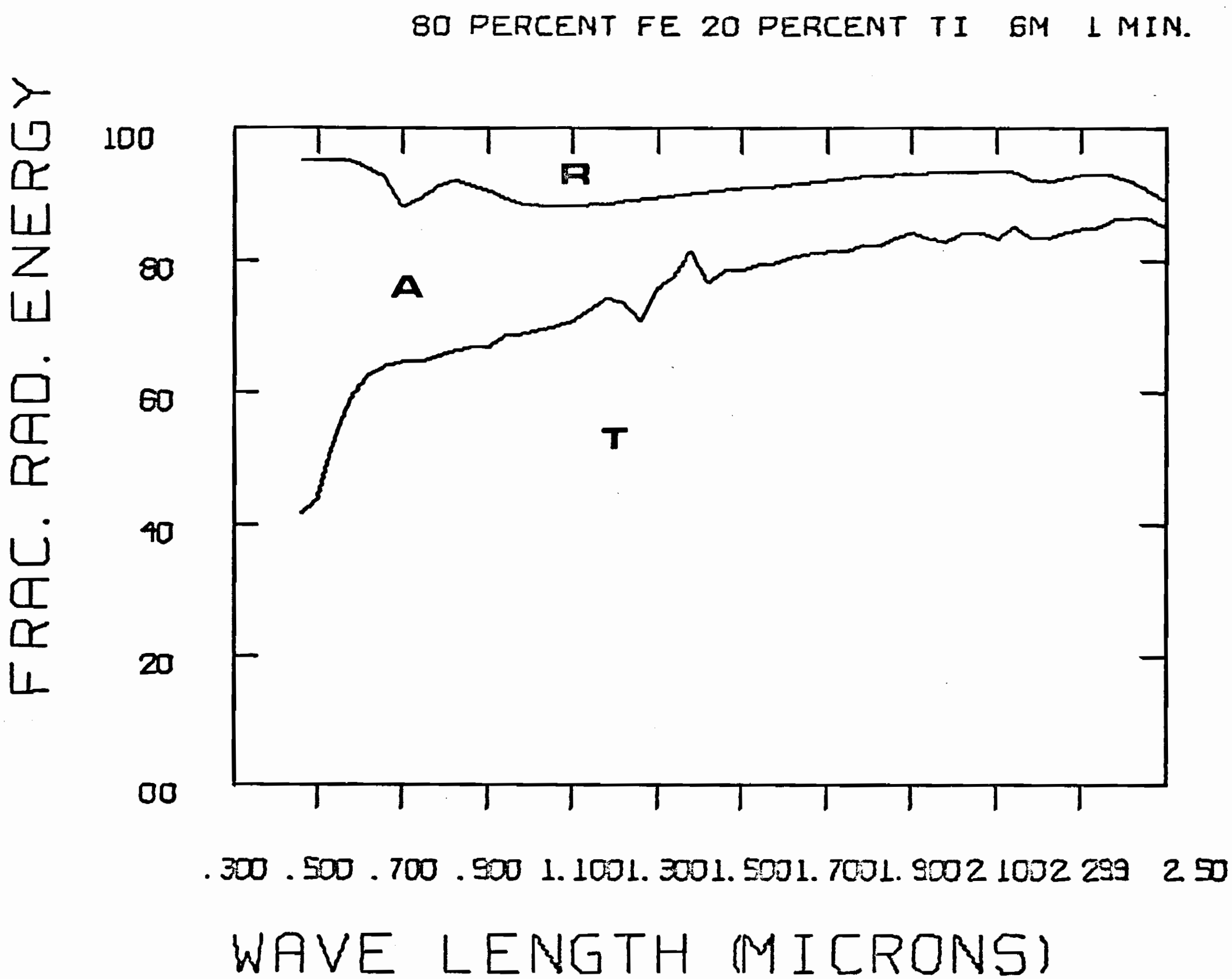

Figure D-7. Optical Properties of $80\%Fe_2O_3$-$20\%TiO_2$

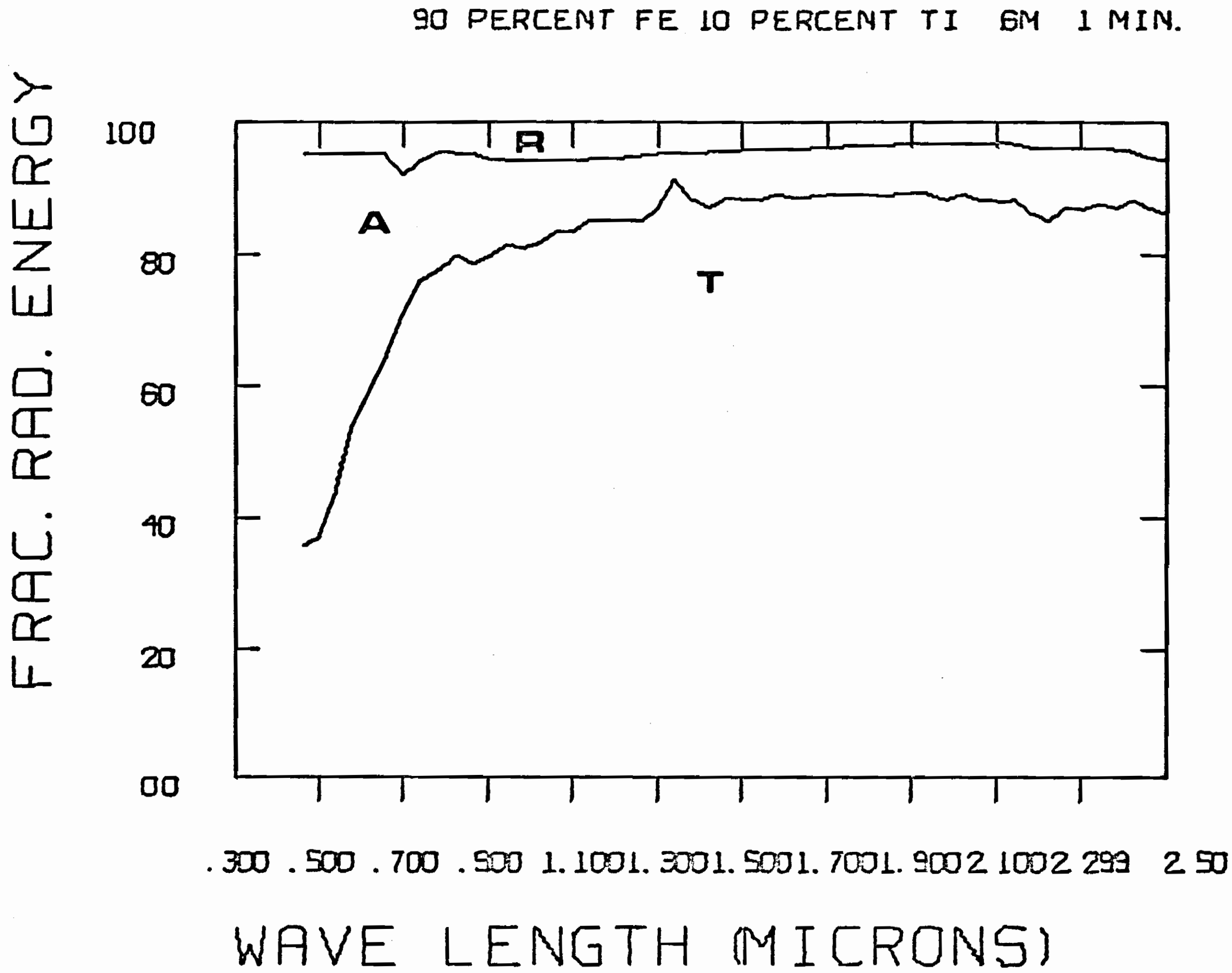

Figure D-8. Optical Properties of $90\%Fe_2O_3$-$10\%TiO_2$

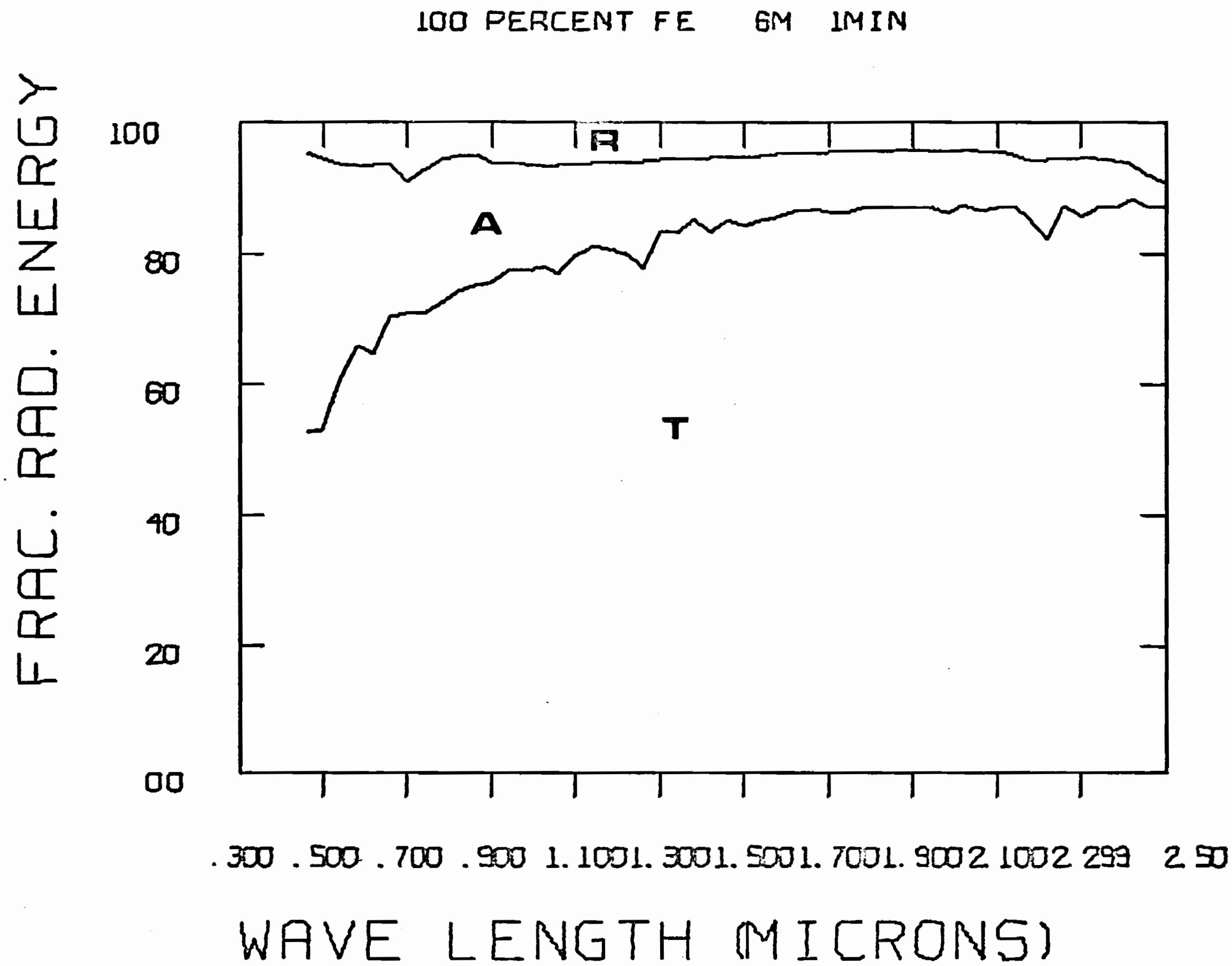

Figure D-9. Optical Properties of 100%Fe_2O_3

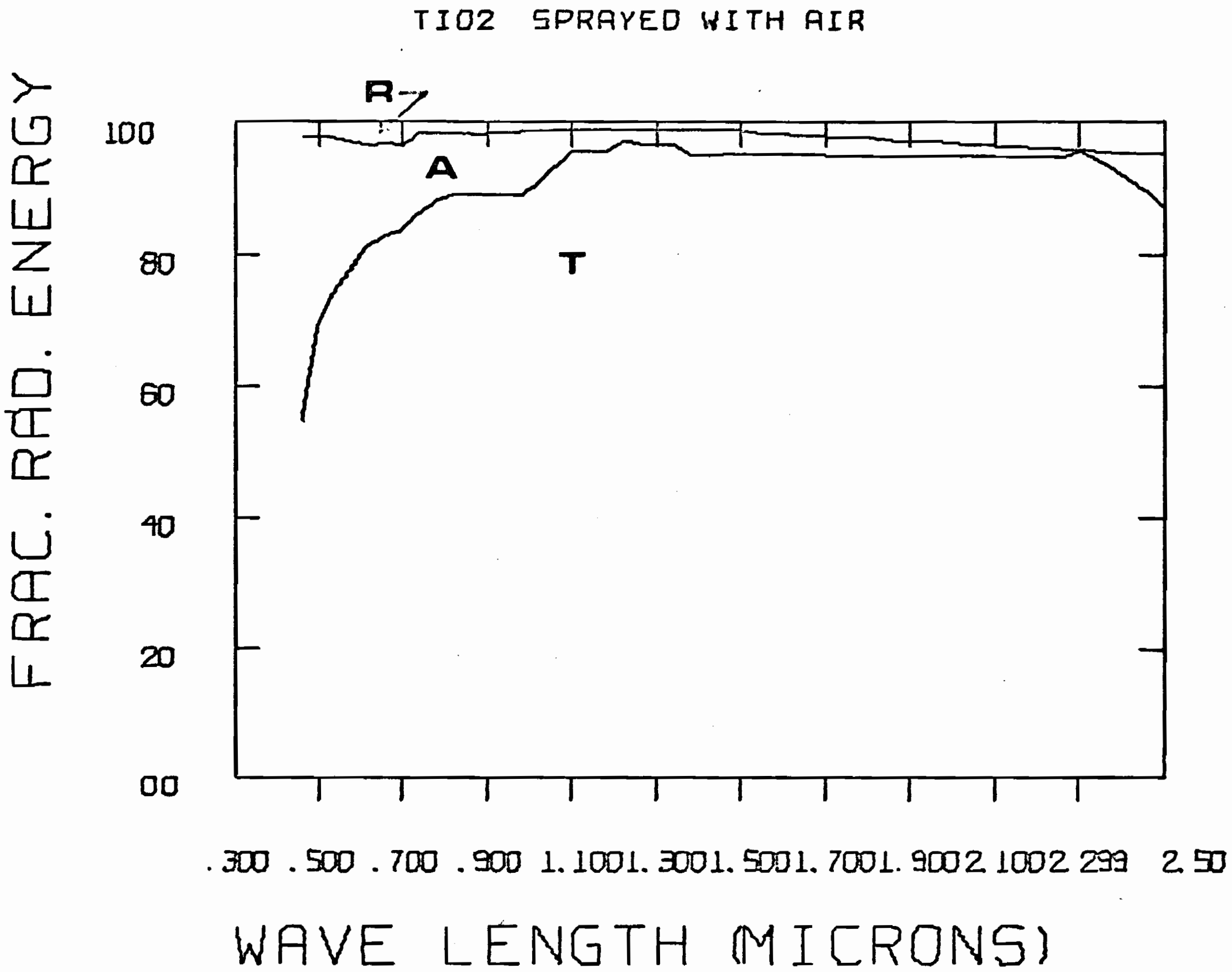

Figure D-10. Optical Properties of TiO_2 Sprayed with Air.

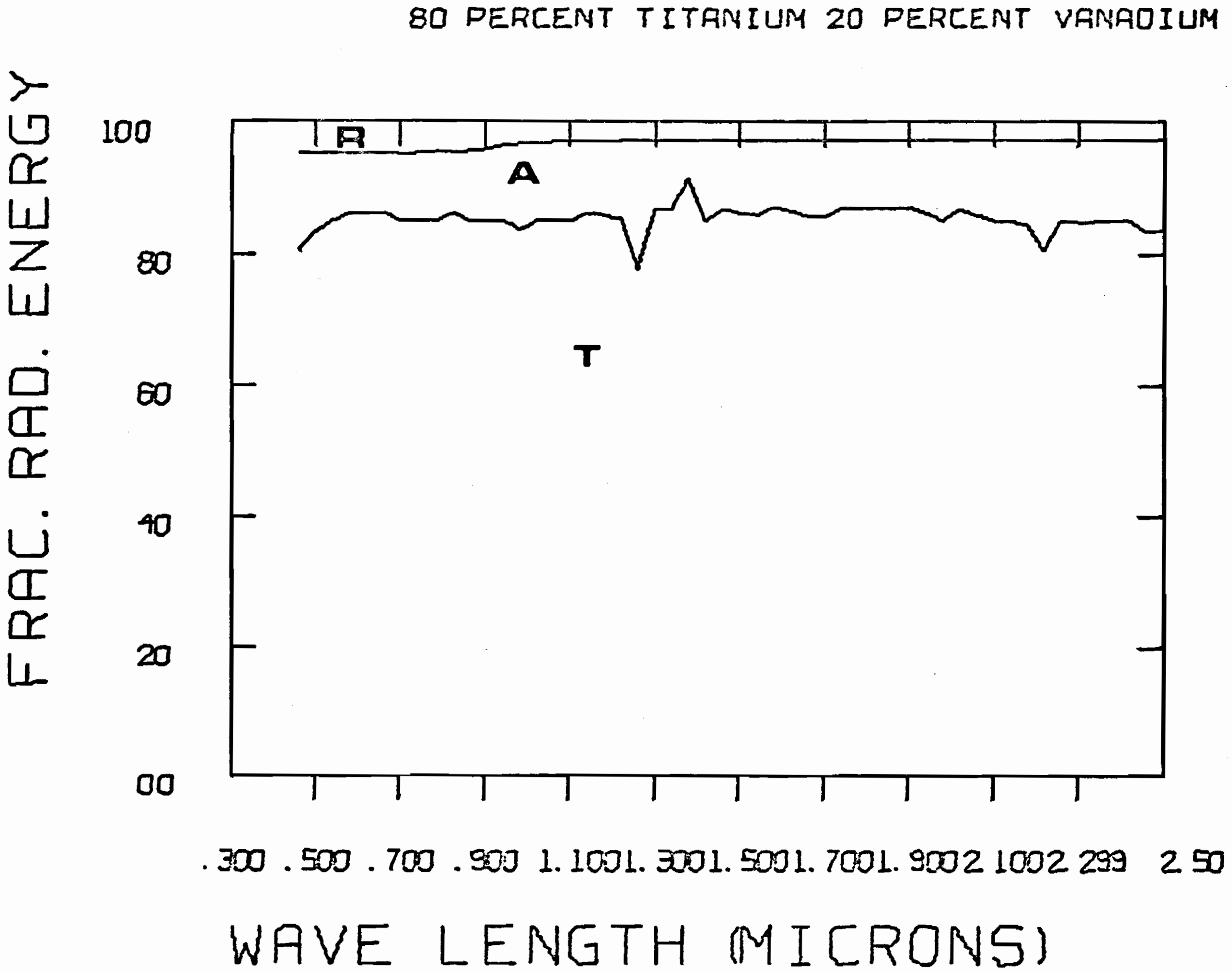

Figure D-11. Optical Properties of 80%TiO_2-20% VO_xH_y

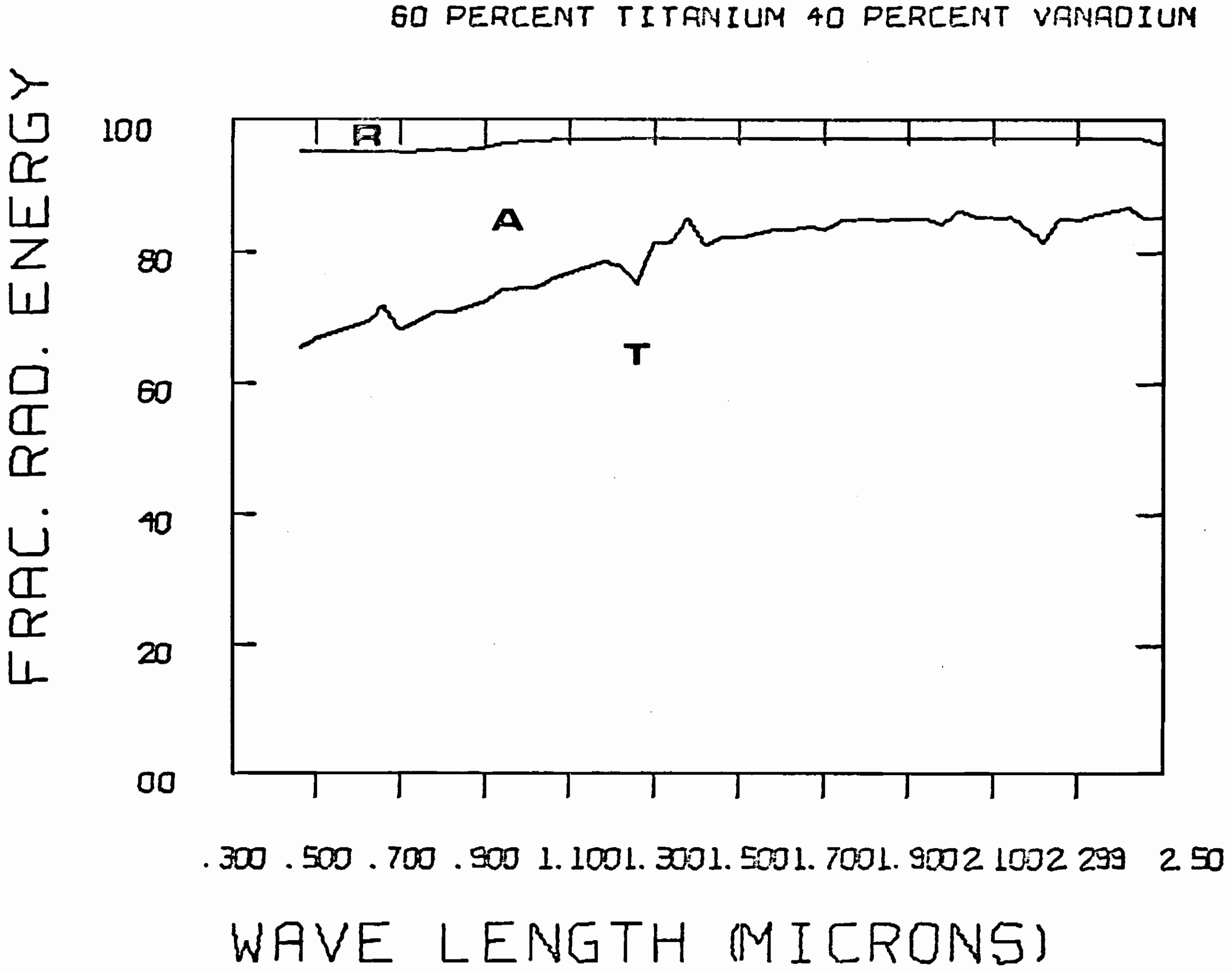

Figure D-12. Optical Properties of 60%TiO_2-40% VO_xH_y

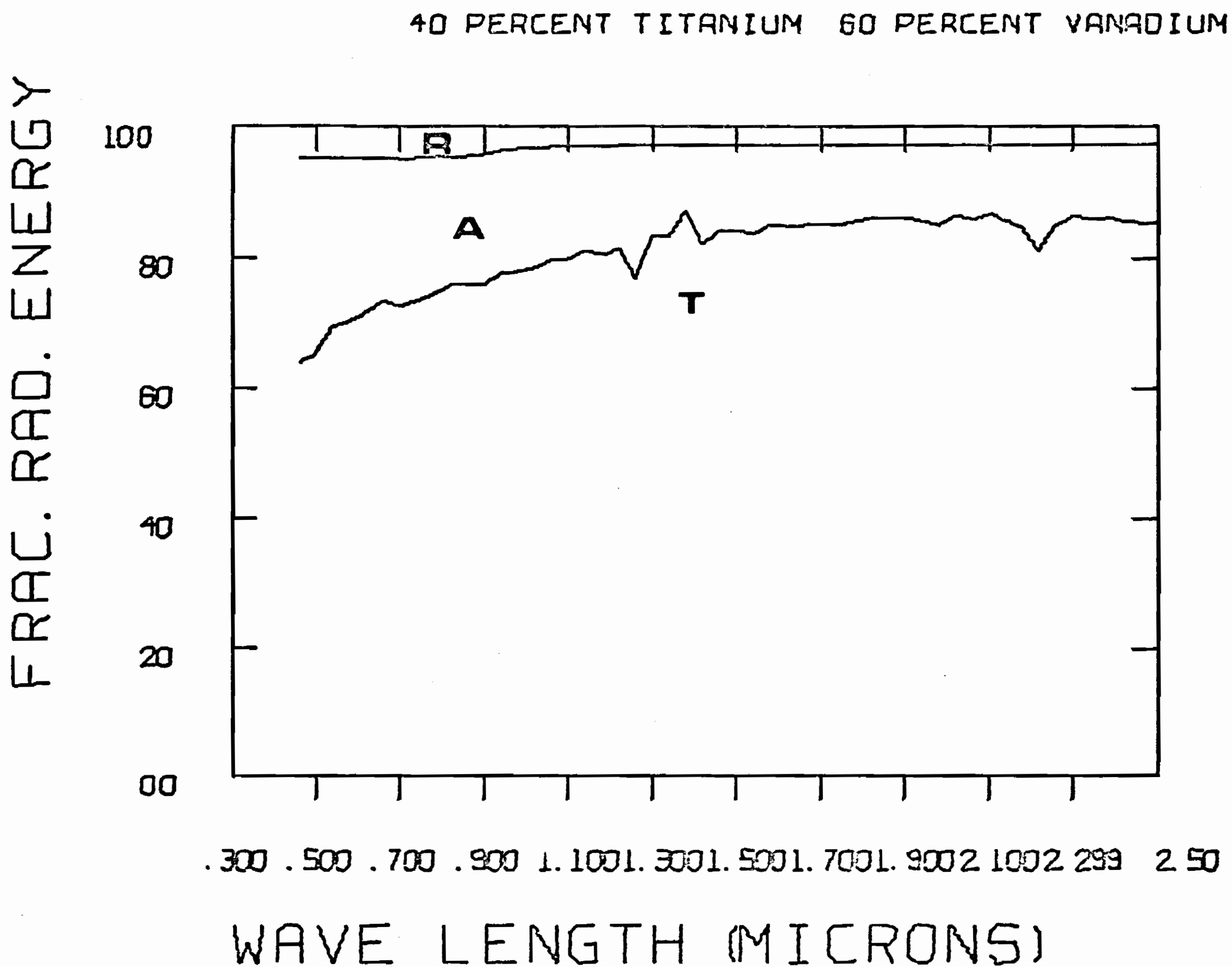

Figure D-13. Optical Properties of 40%TiO_2-60% VO_xH_y

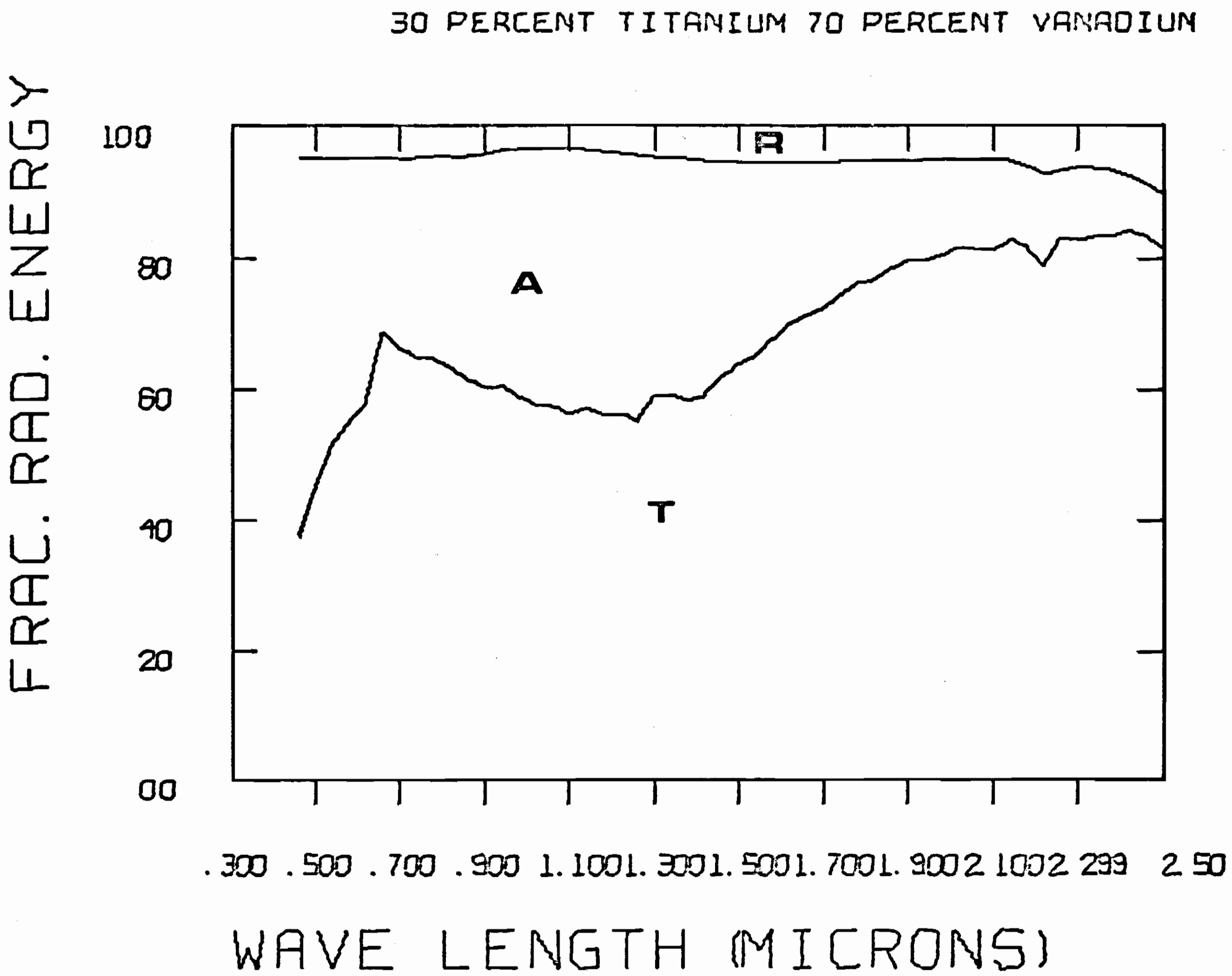
30 PERCENT TITANIUM 70 PERCENT VANADIUM

Figure D-14. Optical Properties of 30%TiO_2-70% VO_xH_y

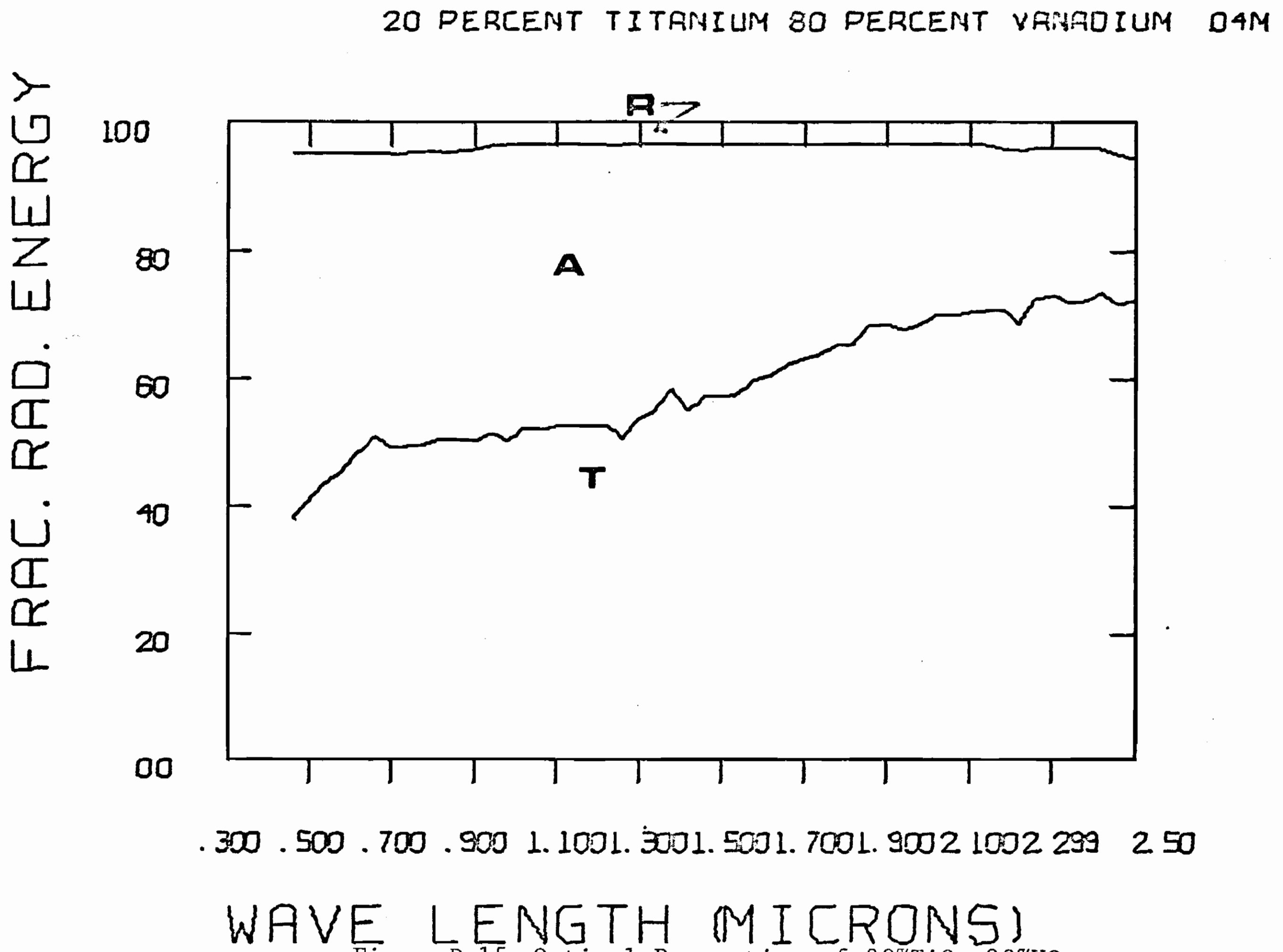

Figure D-15. Optical Properties of $20\%TiO_2-80\%VO_xH_y$

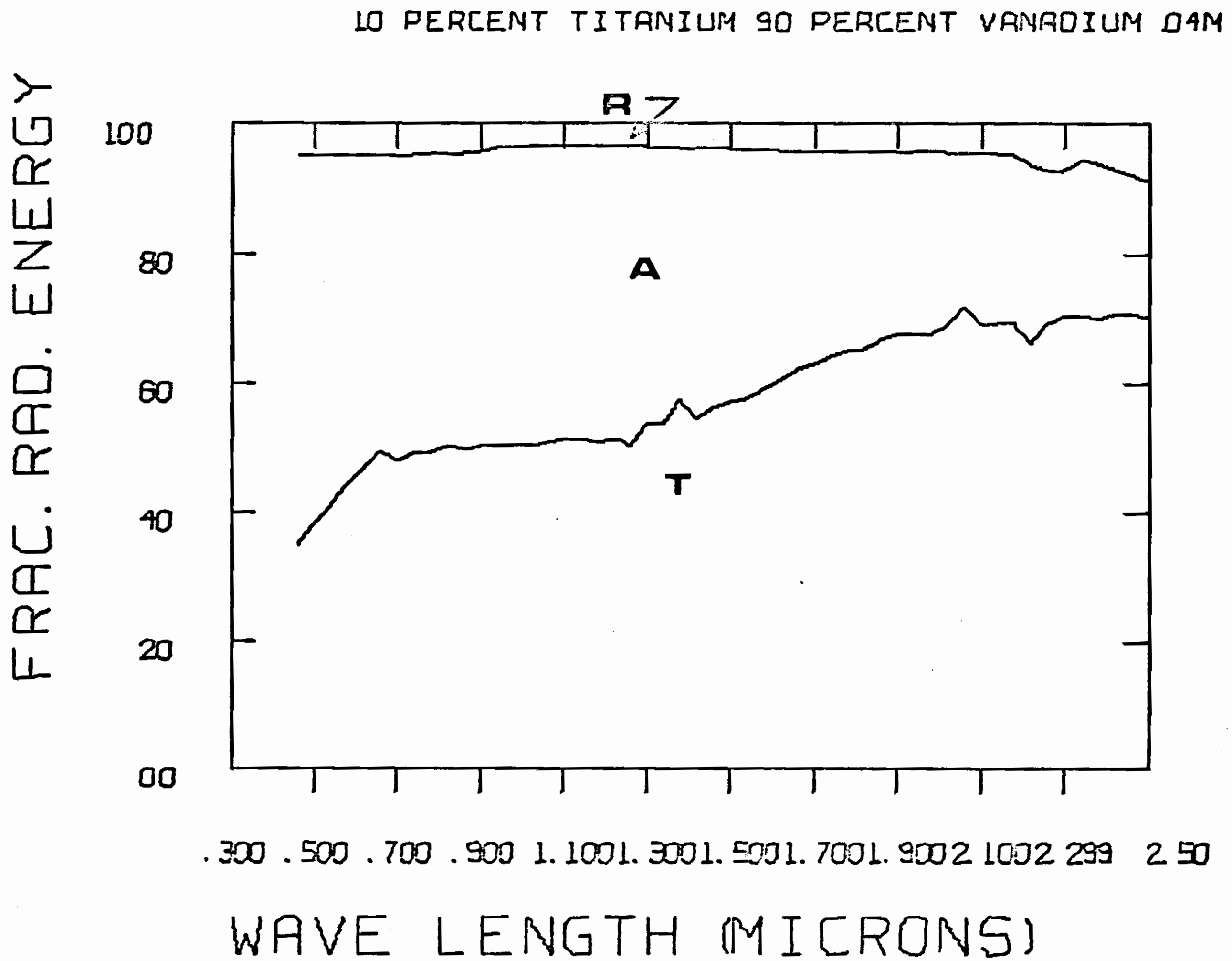

Figure D-16. Optical Properties of $10\%TiO_2-90\% VO_xH_y$

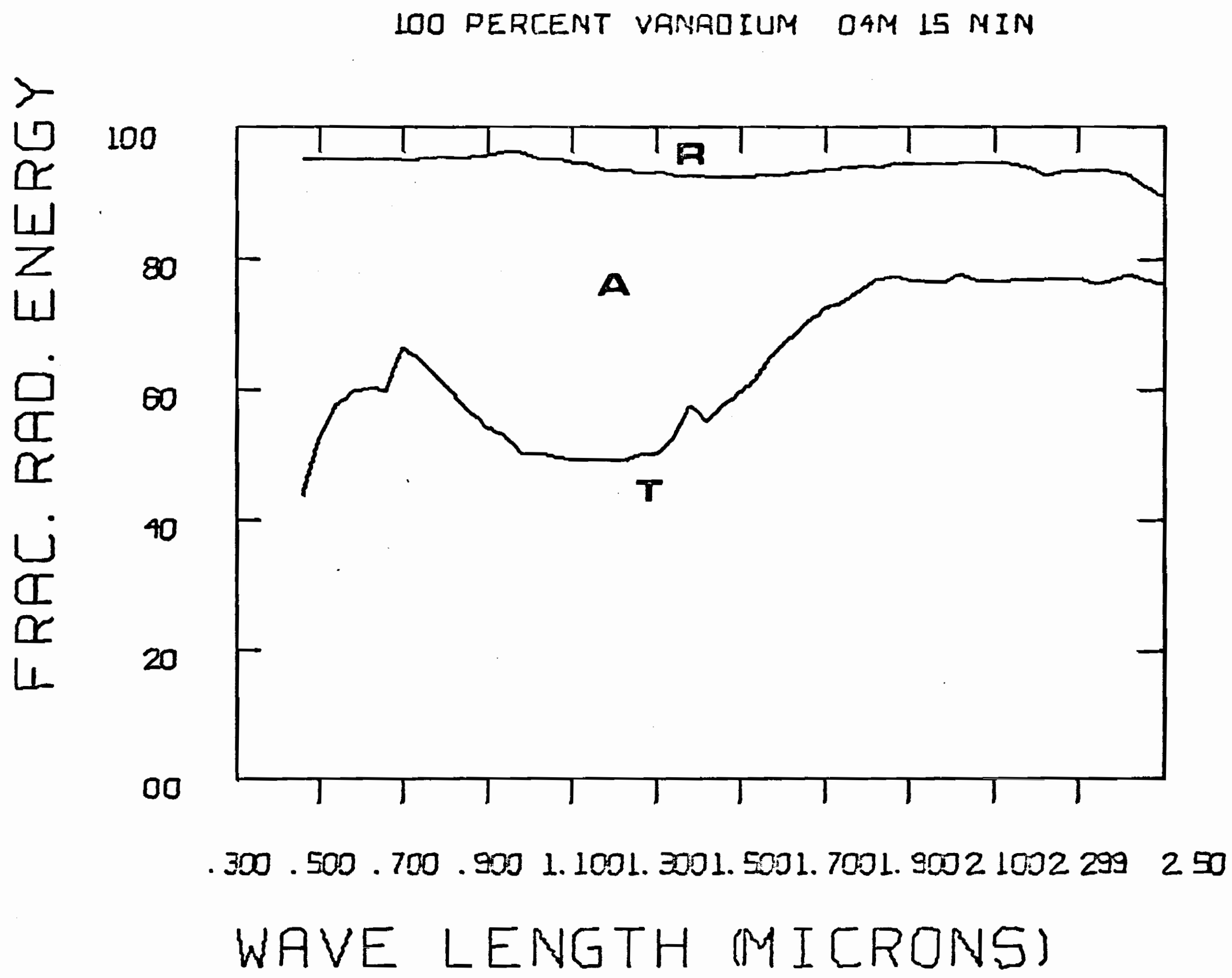

Figure D-17. Optical Properties of 100% VO_xH_y.

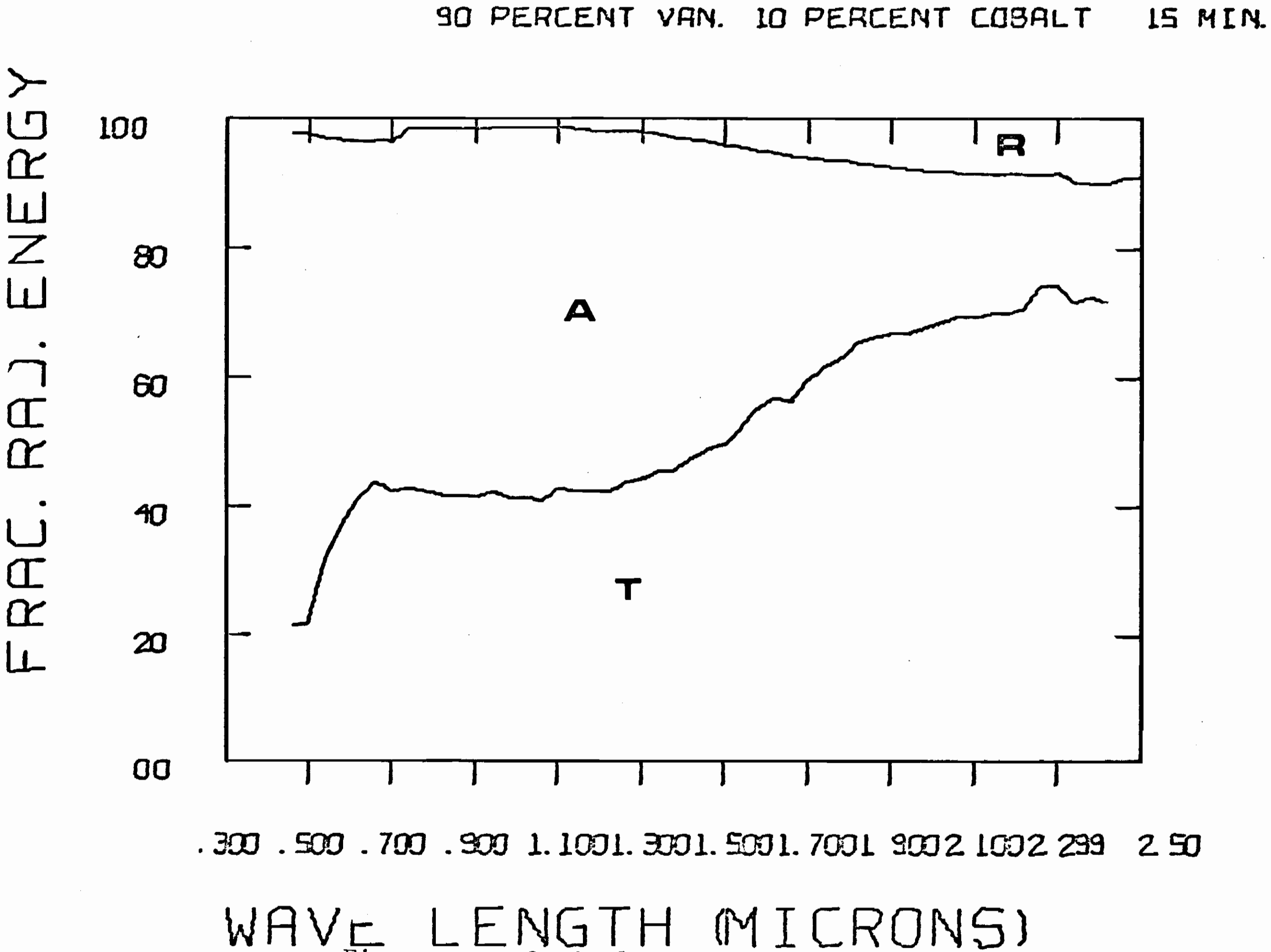

Figure D-18. Optical Properties of 90%VO_xH_y -10%Co_3O_4

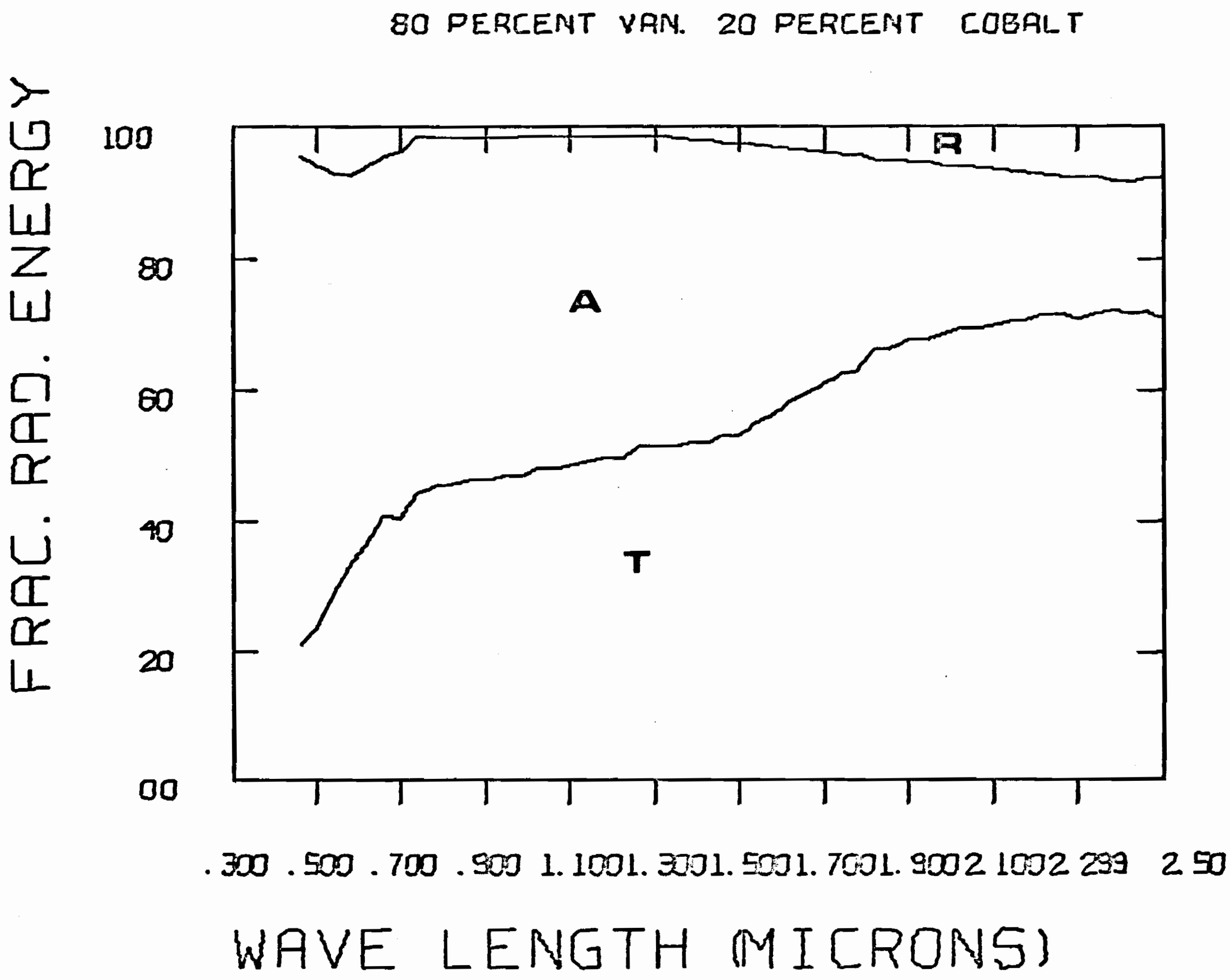

Figure D-19.Optical Properties of 80%VO_xHy -20%Co_3O_4

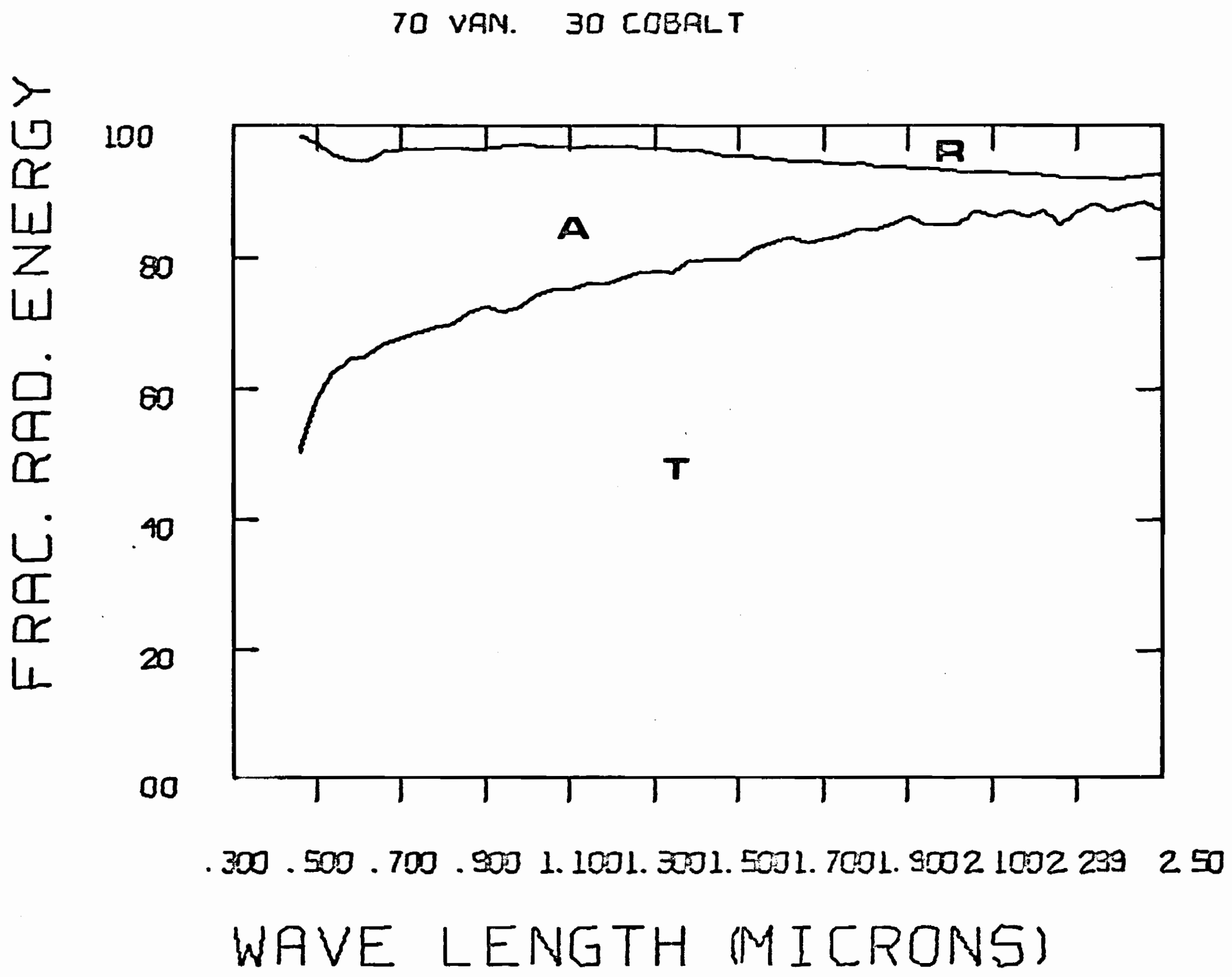

Figure D-20. Optical Properties of 70% VO_xH_y -30% Co_3O_4

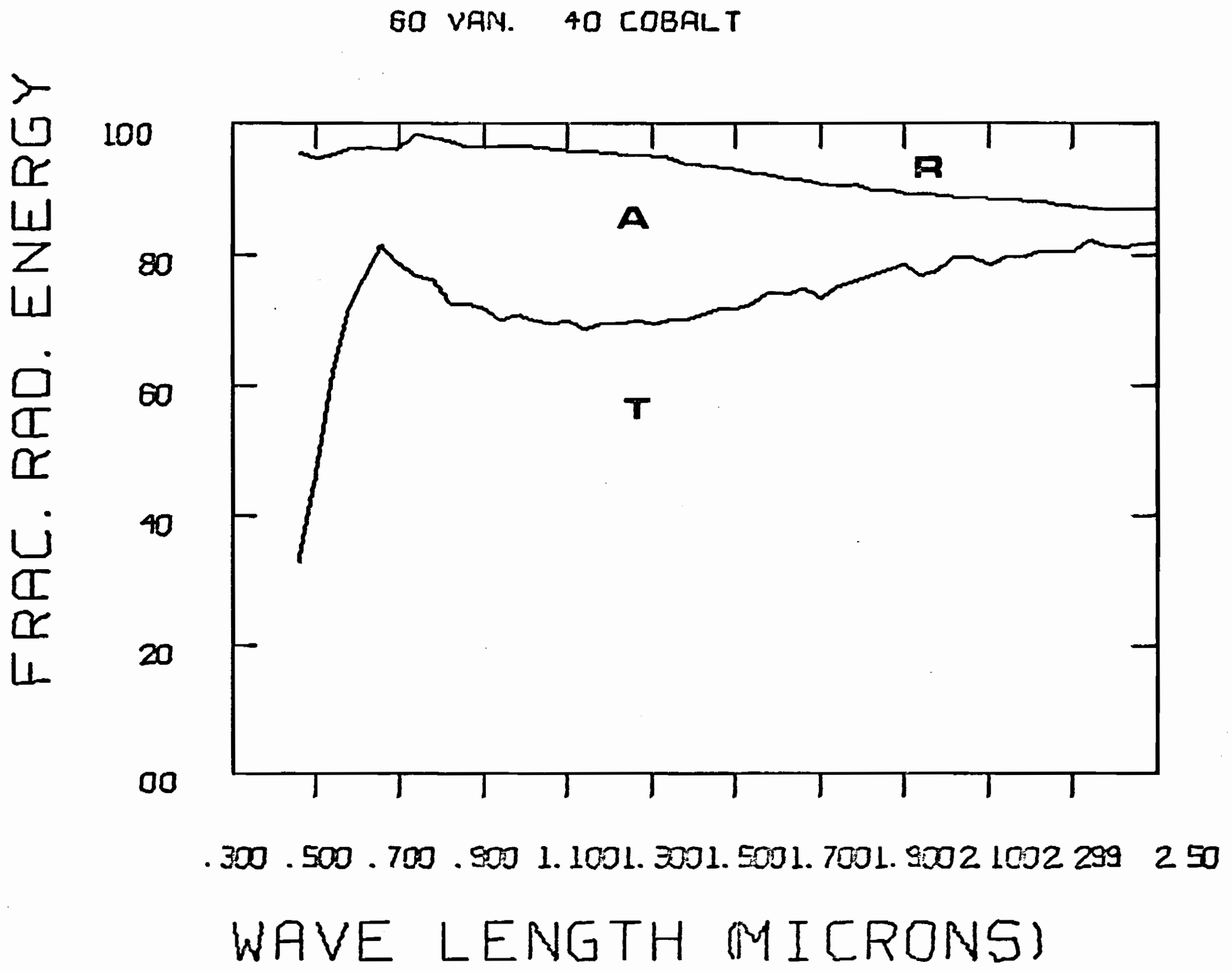

Figure D-21. Optical Properties of 60% VO_xH_y -40%Co_3O_4

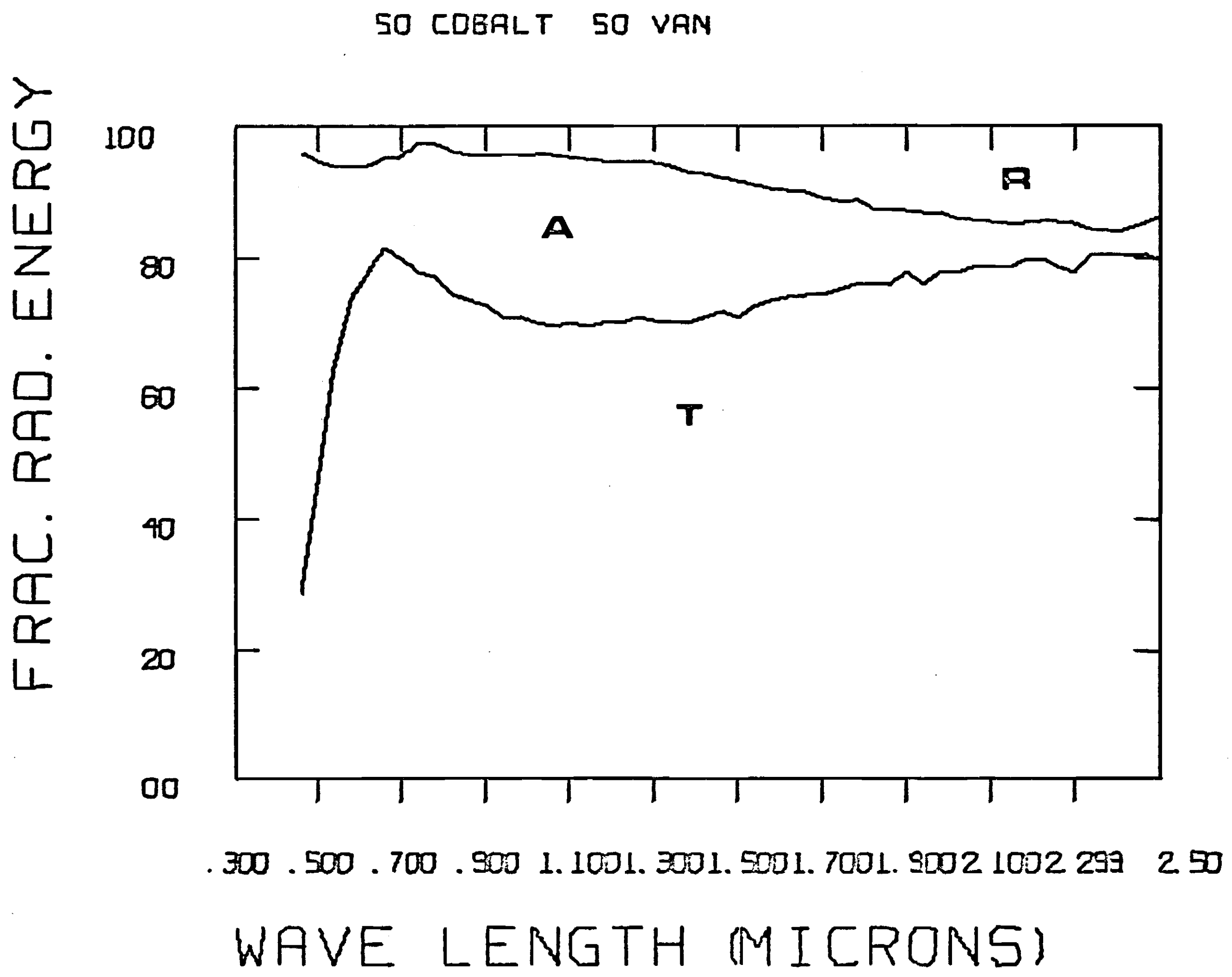

Figure D-22. Optical Properties of 50% VO_xH_y -50%Co_3O_4

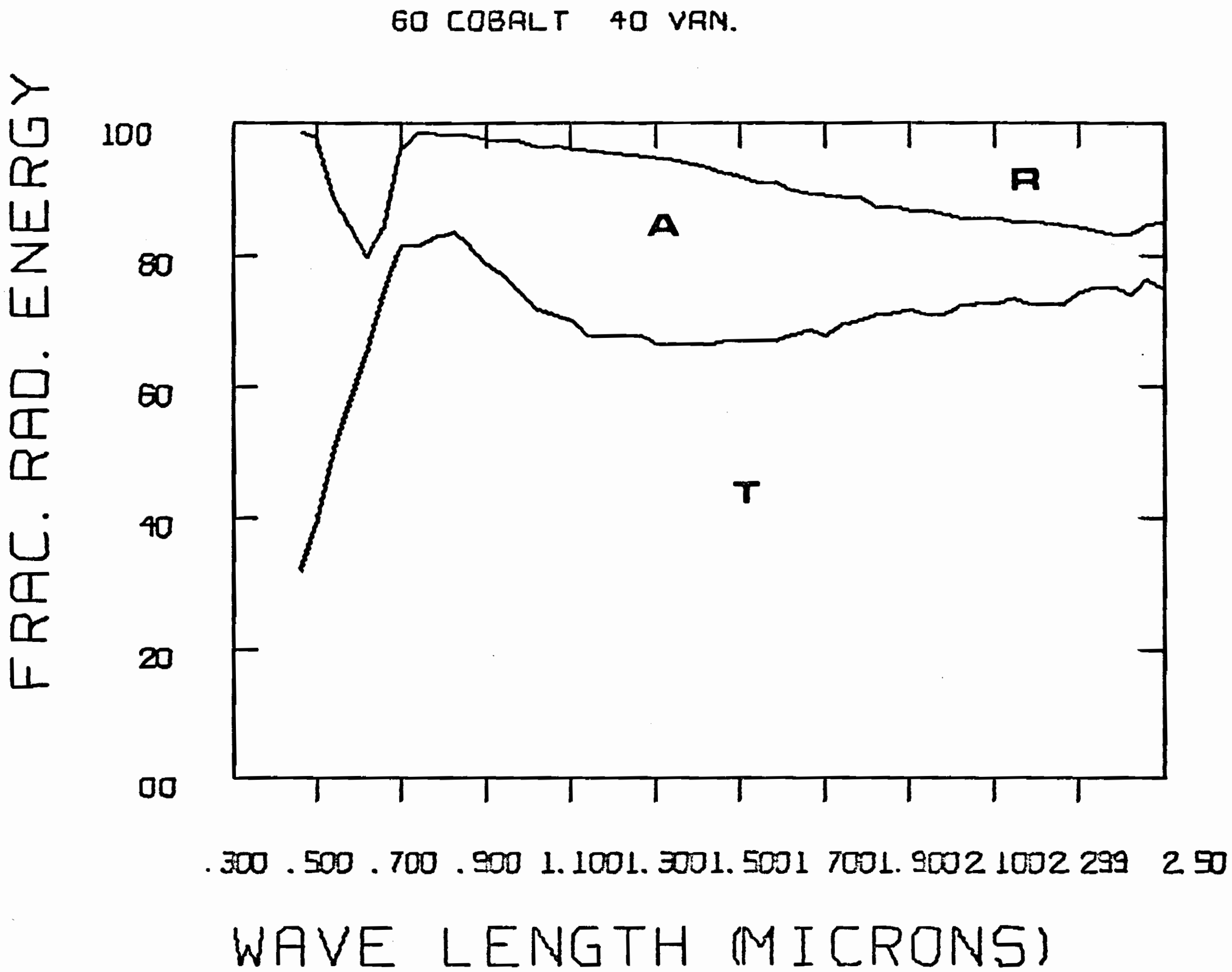

Figure D-23. Optical Properties of 40% VO_xH_y -60%Co_3O_4

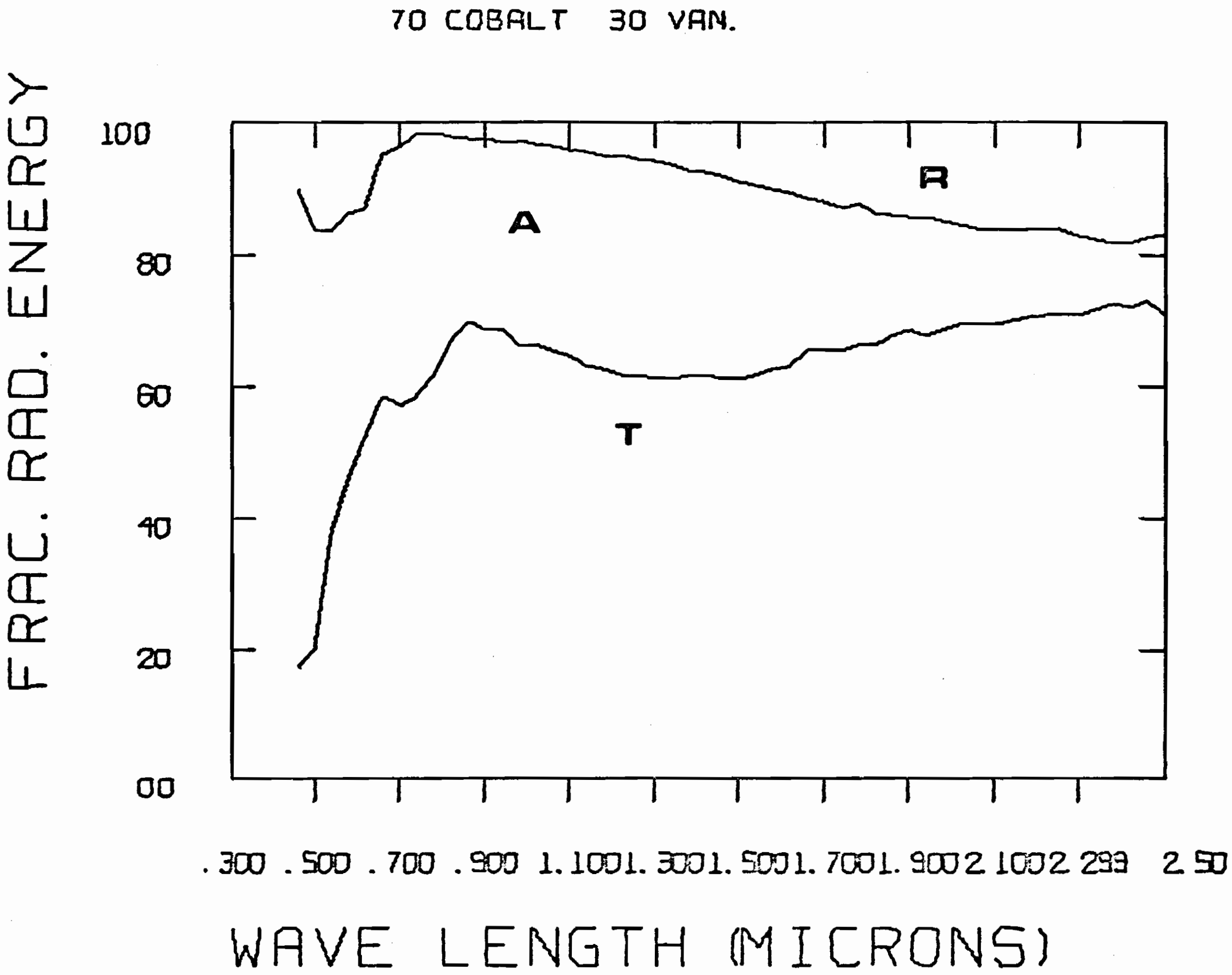

Figure D-24. Optical Properties of 30% VO_xH_y -70% Co_3O_4

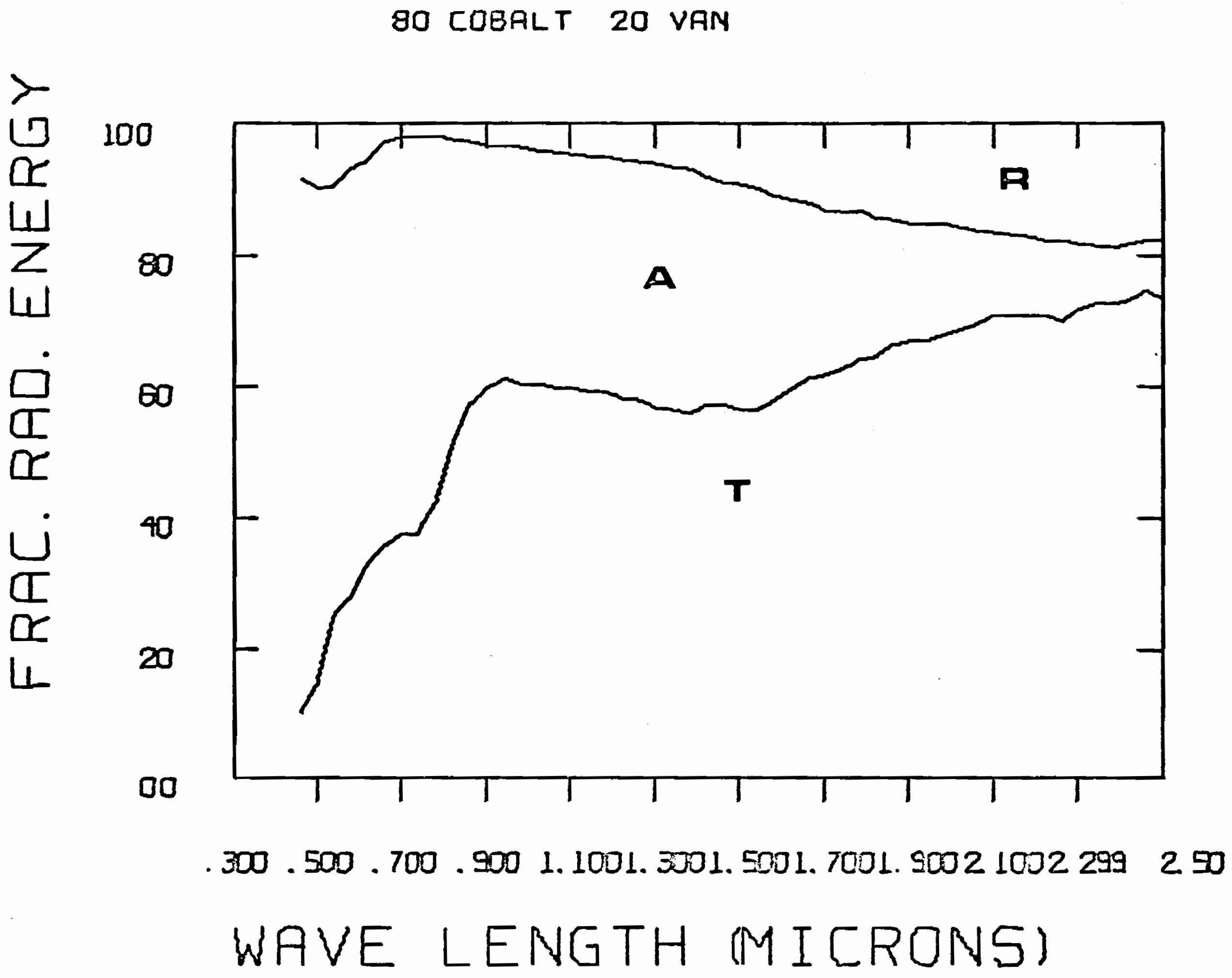

Figure D-25. Optical Properties of 20% VO_xH_y-80% Co_3O_4

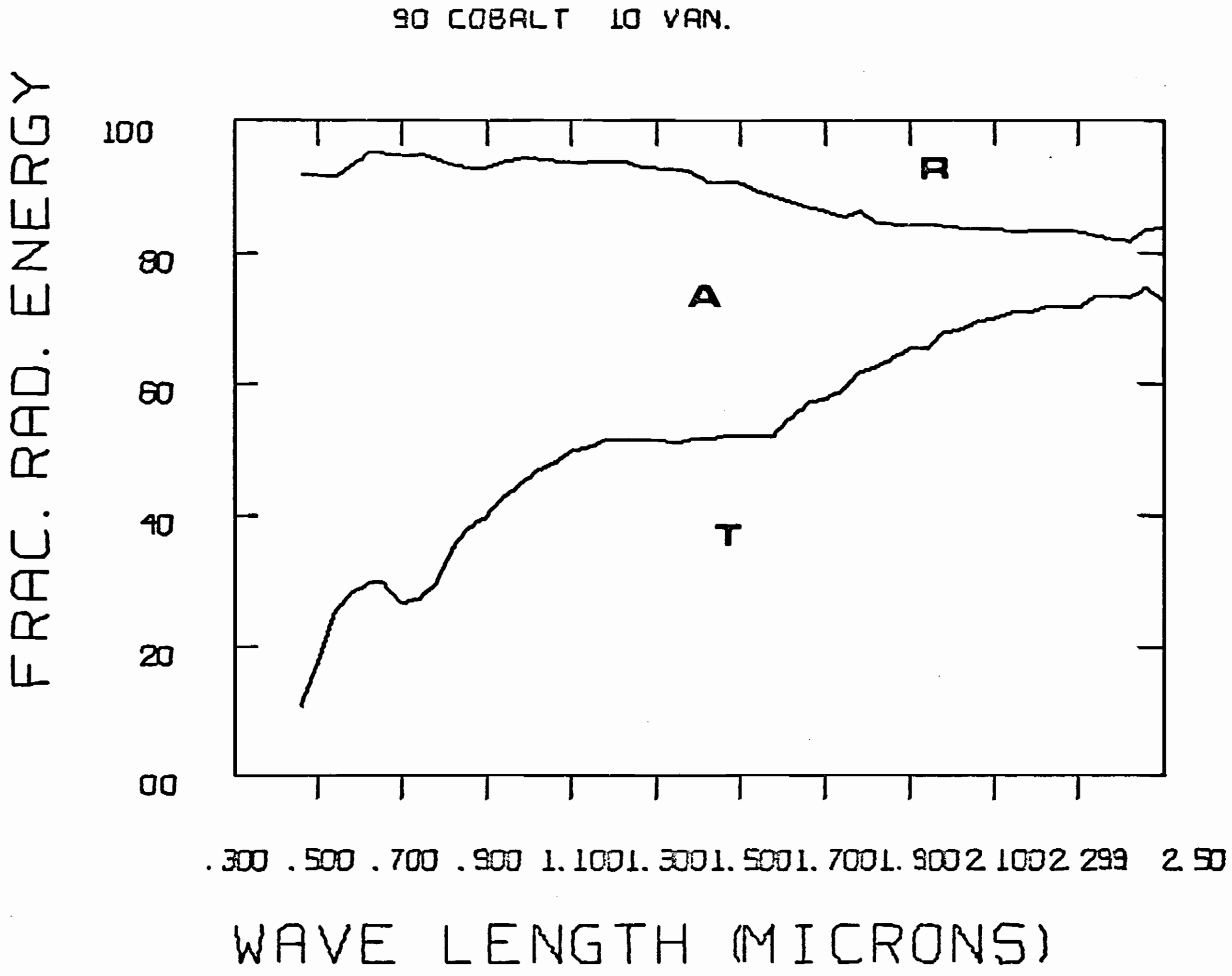

Figure D-26. Optical Properties of 10% VO_xH_y -90%Co_3O_4

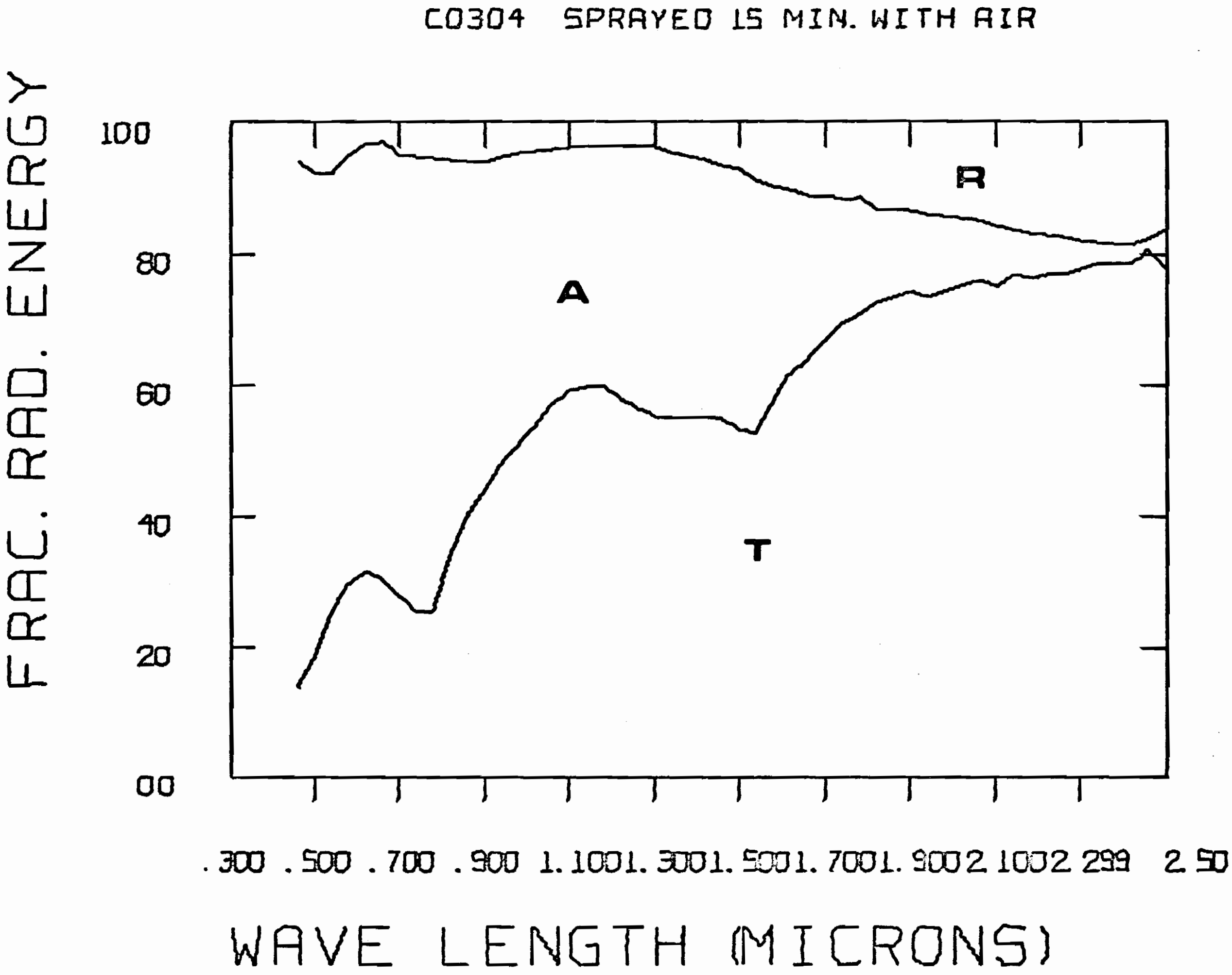

Figure D-27. Optical Properties of 100% Co_3O_4 Sprayed with Air.

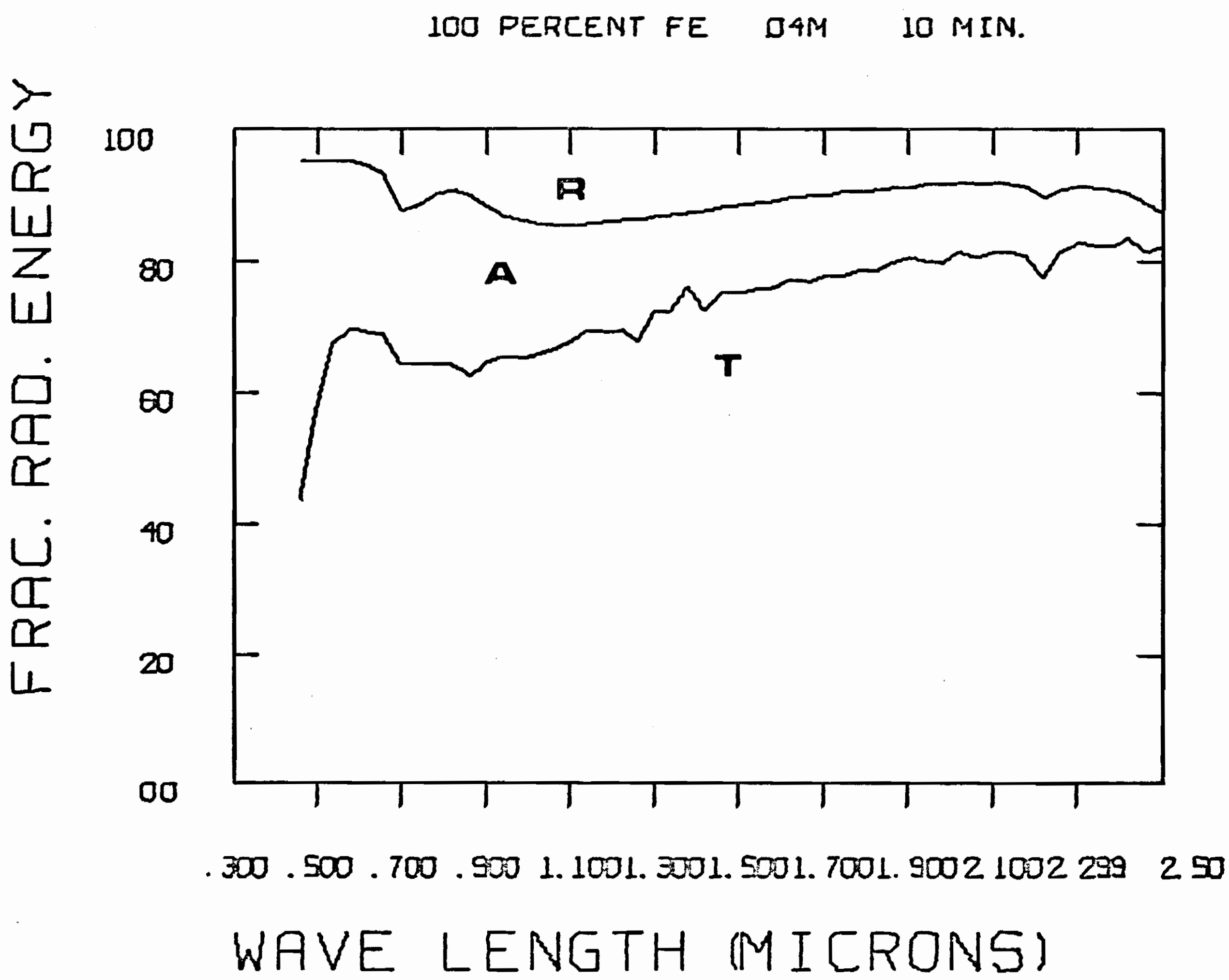

Figure D-28. Optical Properties of 100% Fe_2O_3 Sprayed with Air.

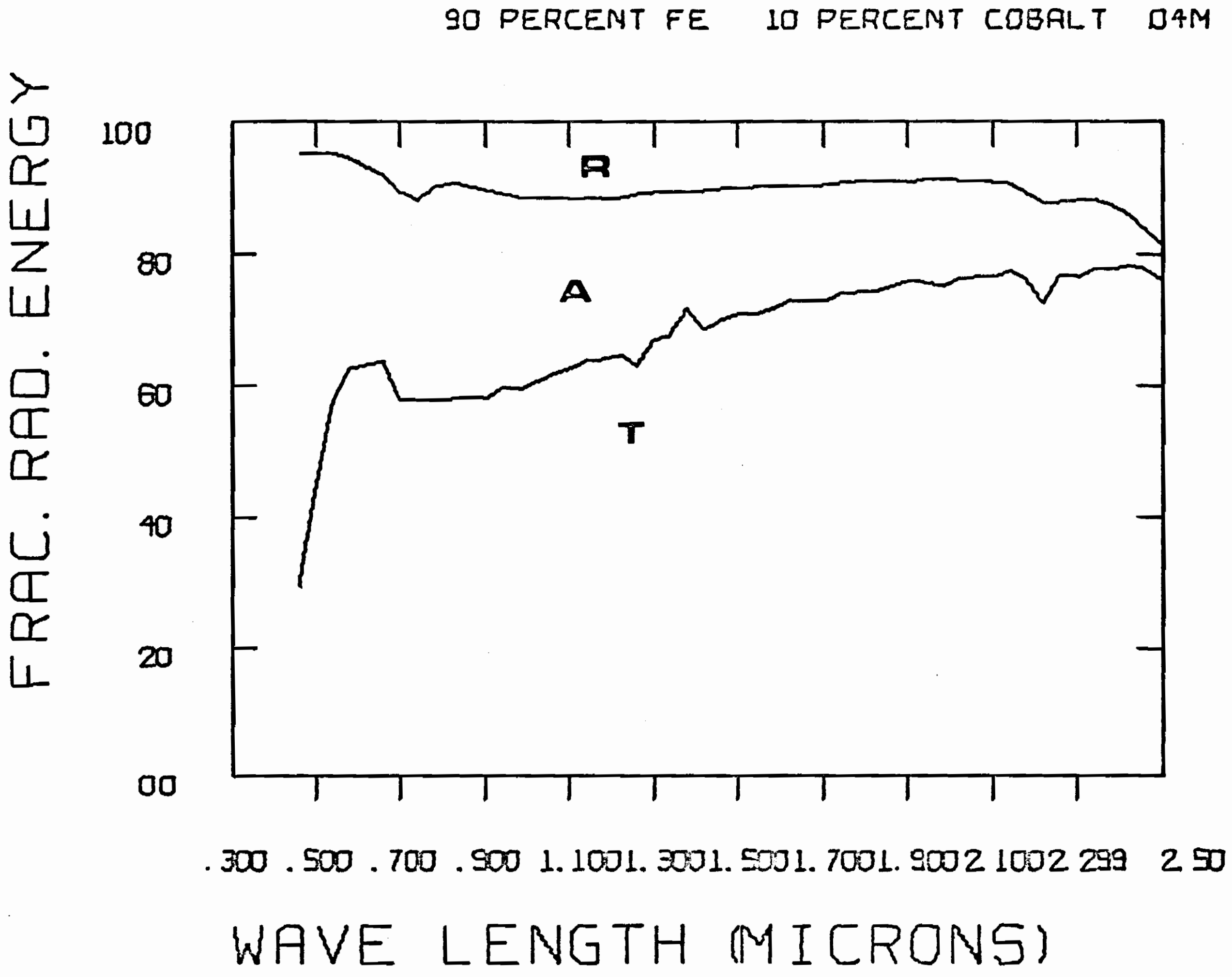

Figure D-29. Optical Properties of 90% Fe_2O_3-10% Co_3O_4.

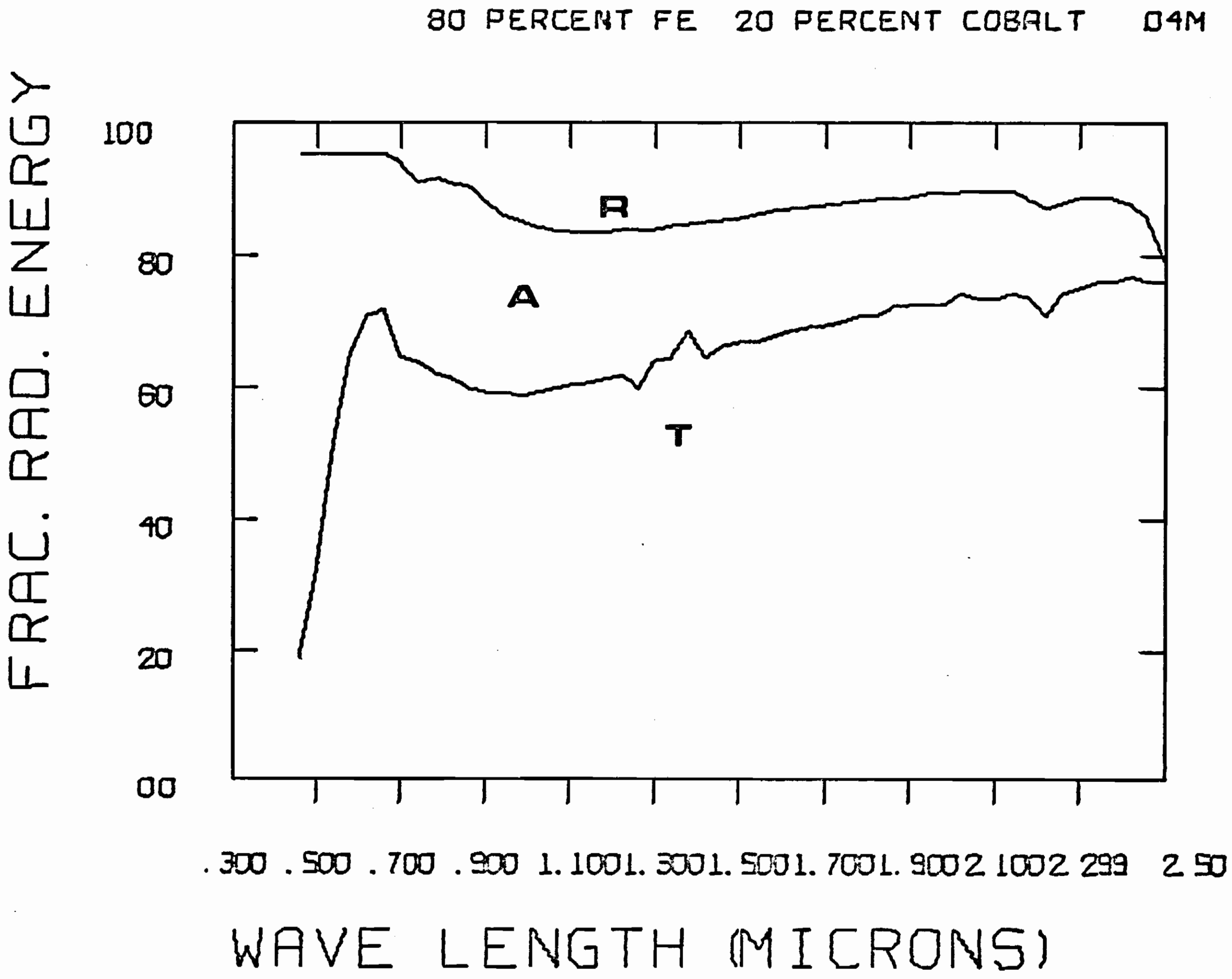

Figure D-30. Optical Properties of 80% Fe_2O_3-20% Co_3O_4.

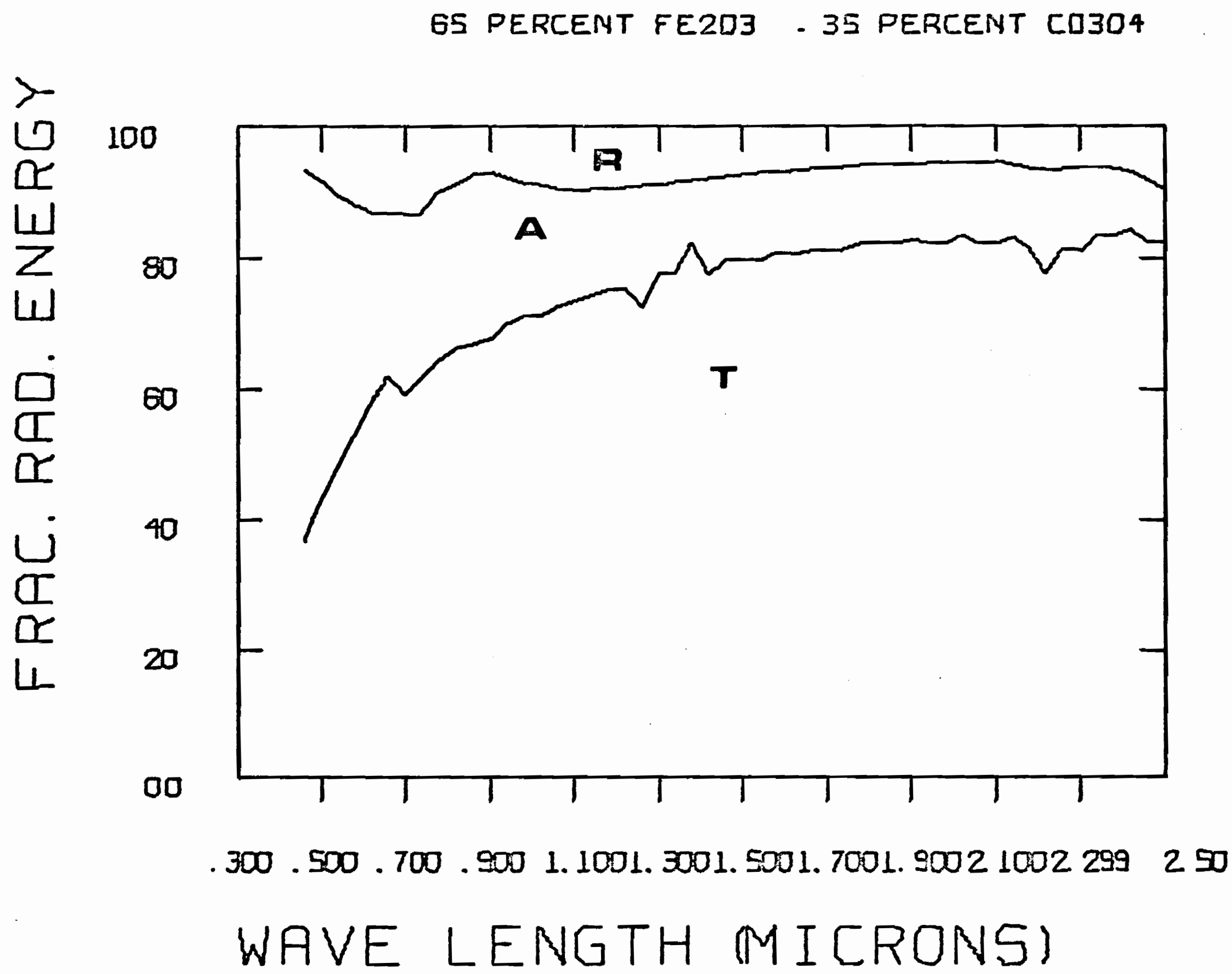

Figure D-31. Optical Properties of 65% Fe_2O_3-35% Co_3O_4.

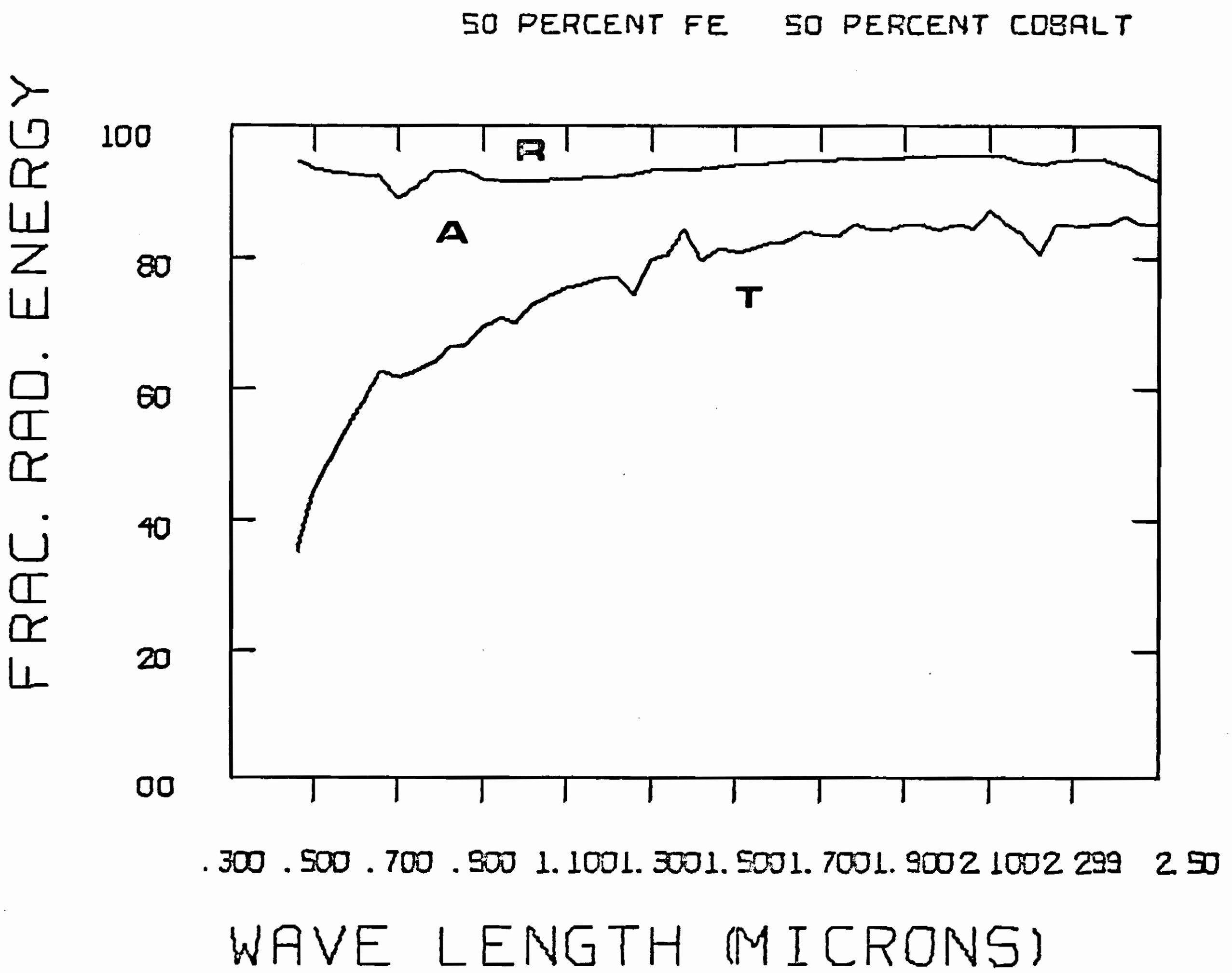

Figure D-32. Optical Properties of 50% Fe_2O_3-50% Co_3O_4.

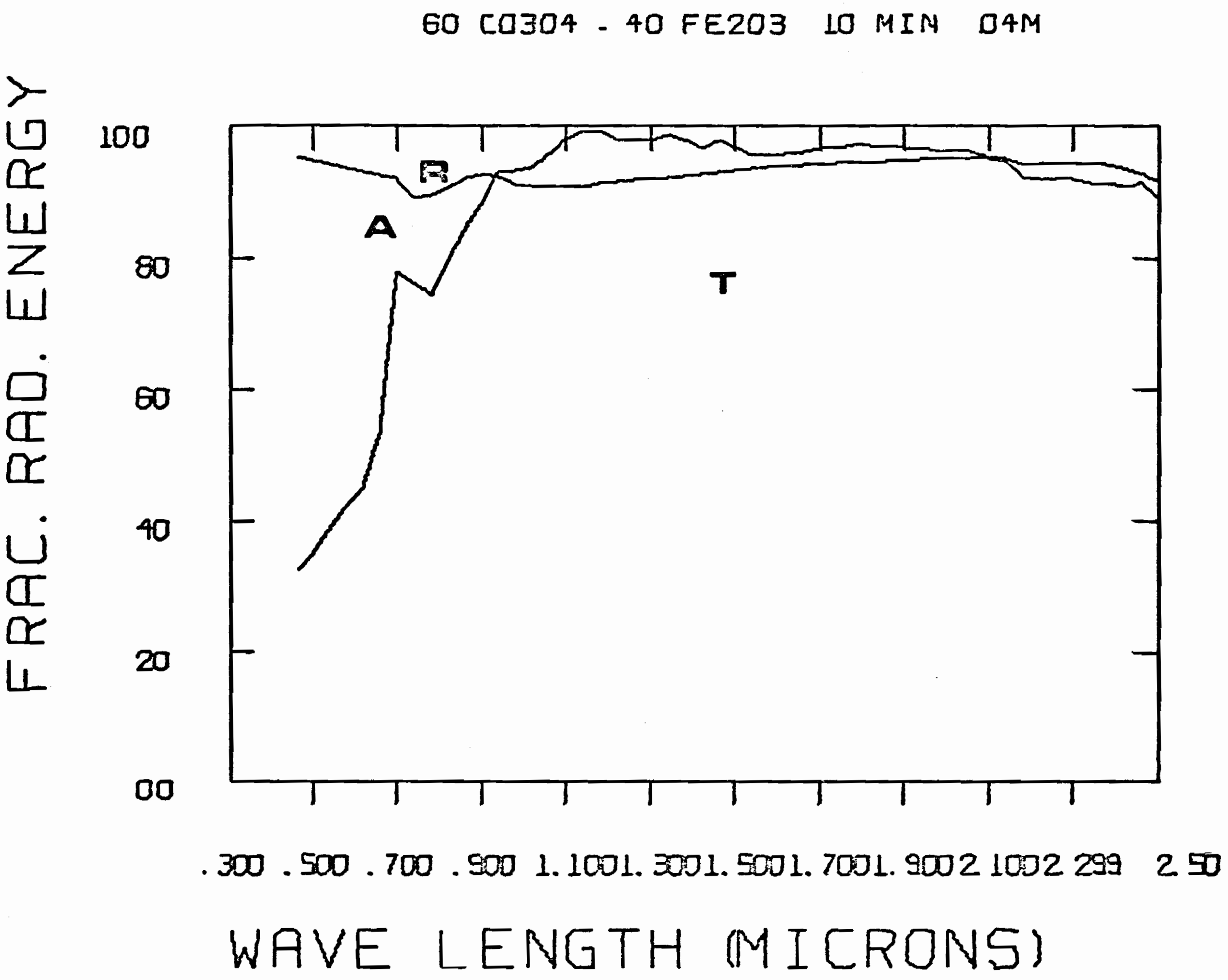

Figure D-33. Optical Properties of 60% Co_3O_4-40% Fe_2O_3.

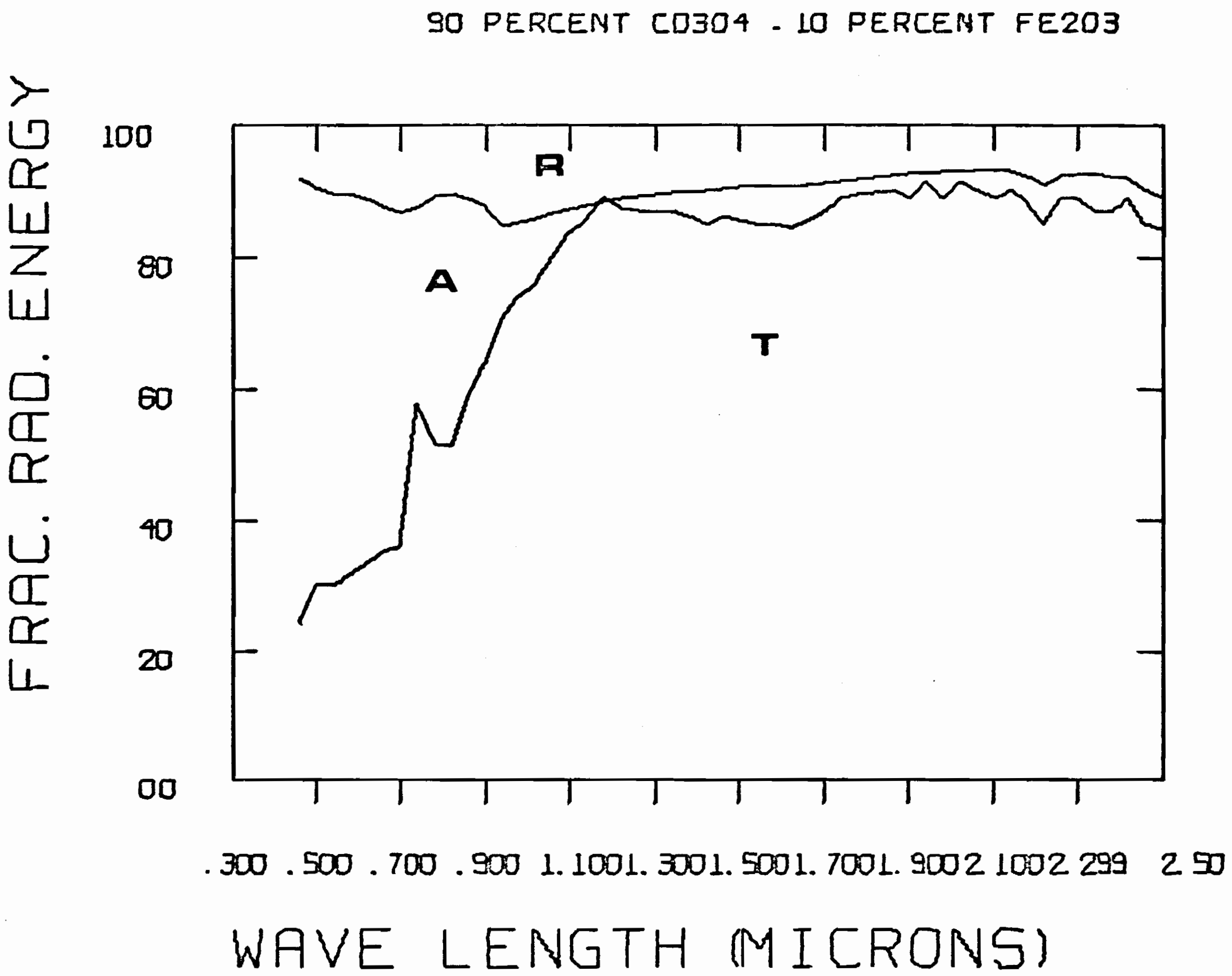

Figure D-34. Optical Properties of 90% Co_3O_4-10% Fe_2O_3.

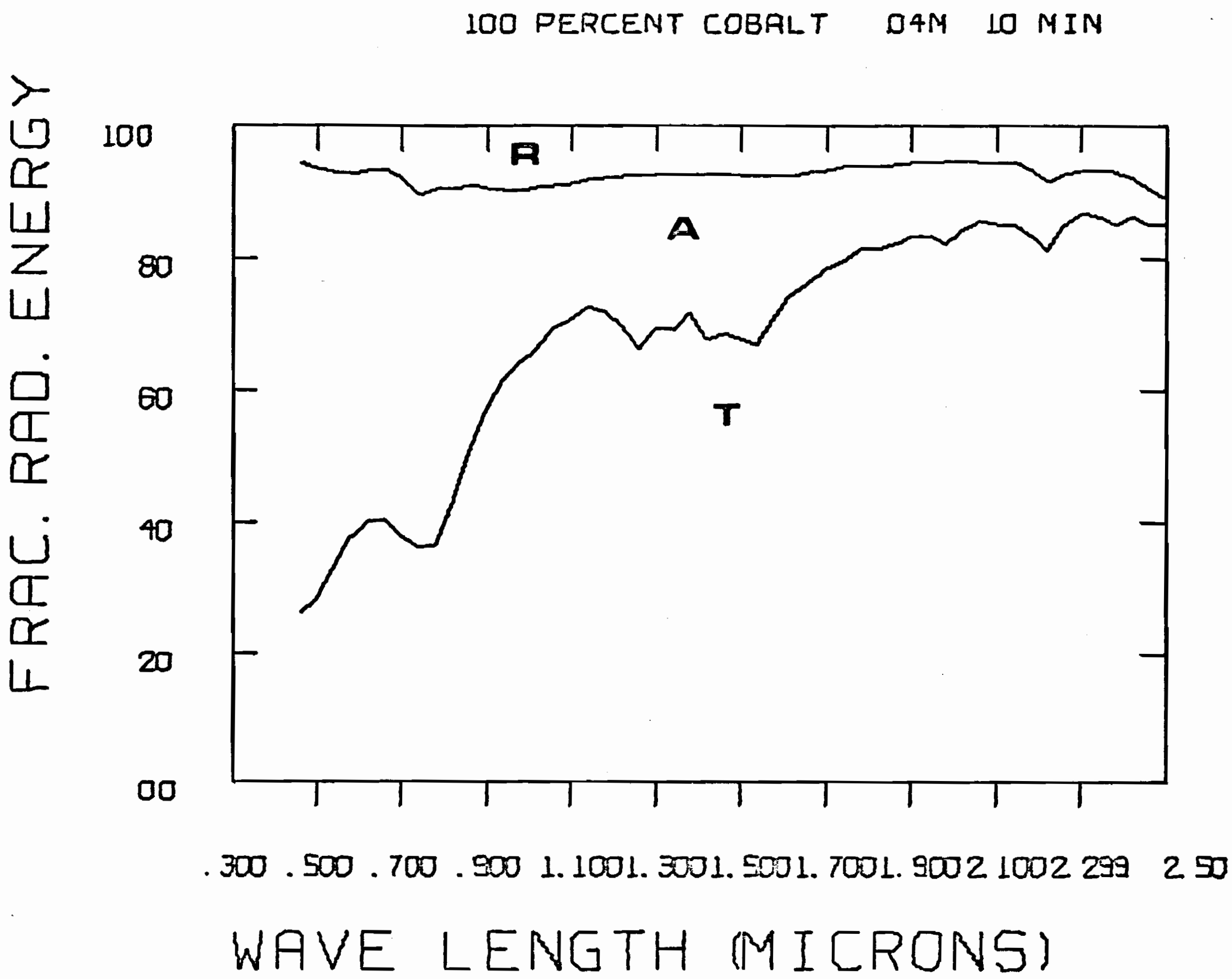

Figure D-35. Optical Properties of 100% Co_3O_4 Sprayed with Air 10 Min.

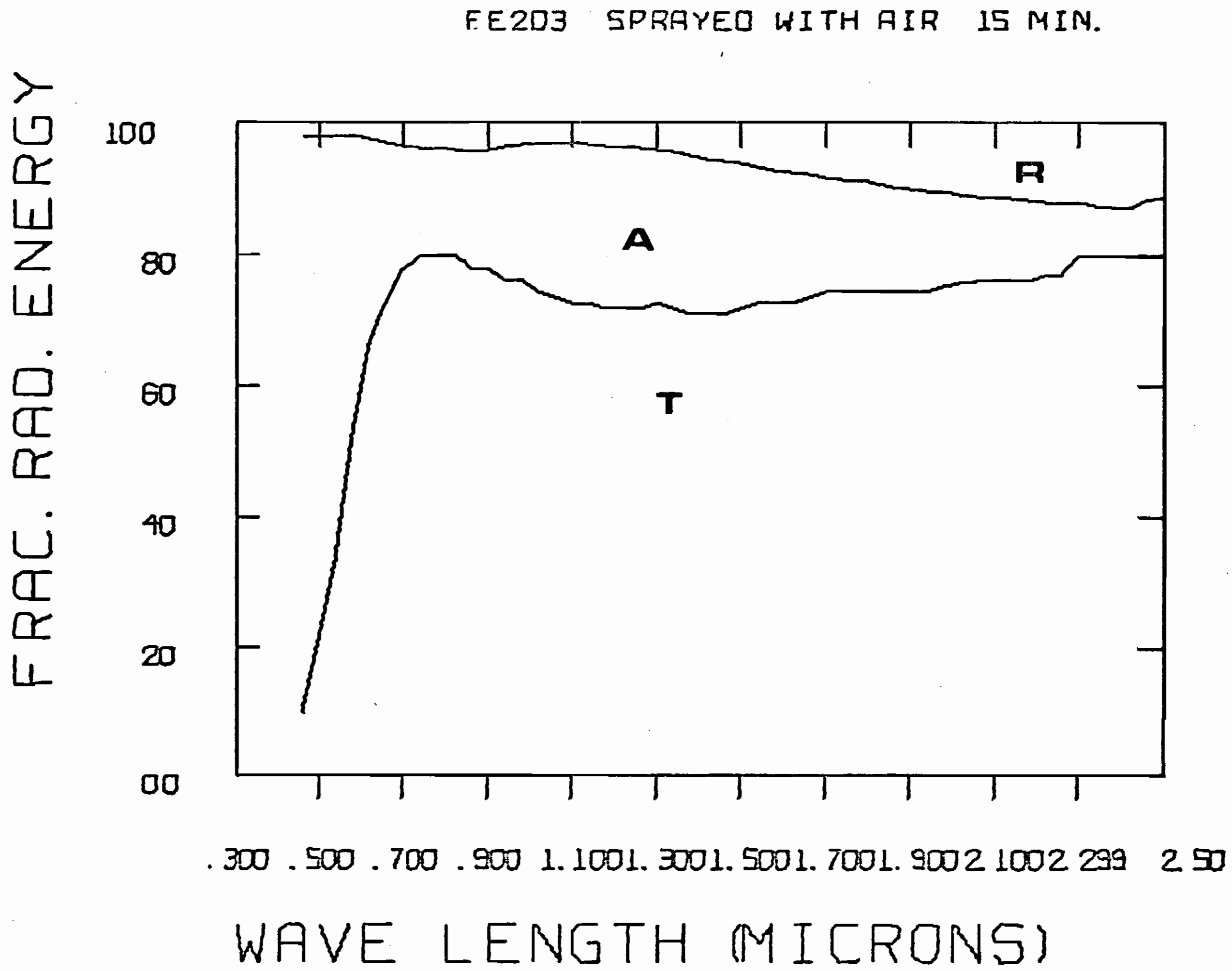

Figure D-36. Optical Properties of 100% Fe_2O_3 Sprayed with Air 15 Min.

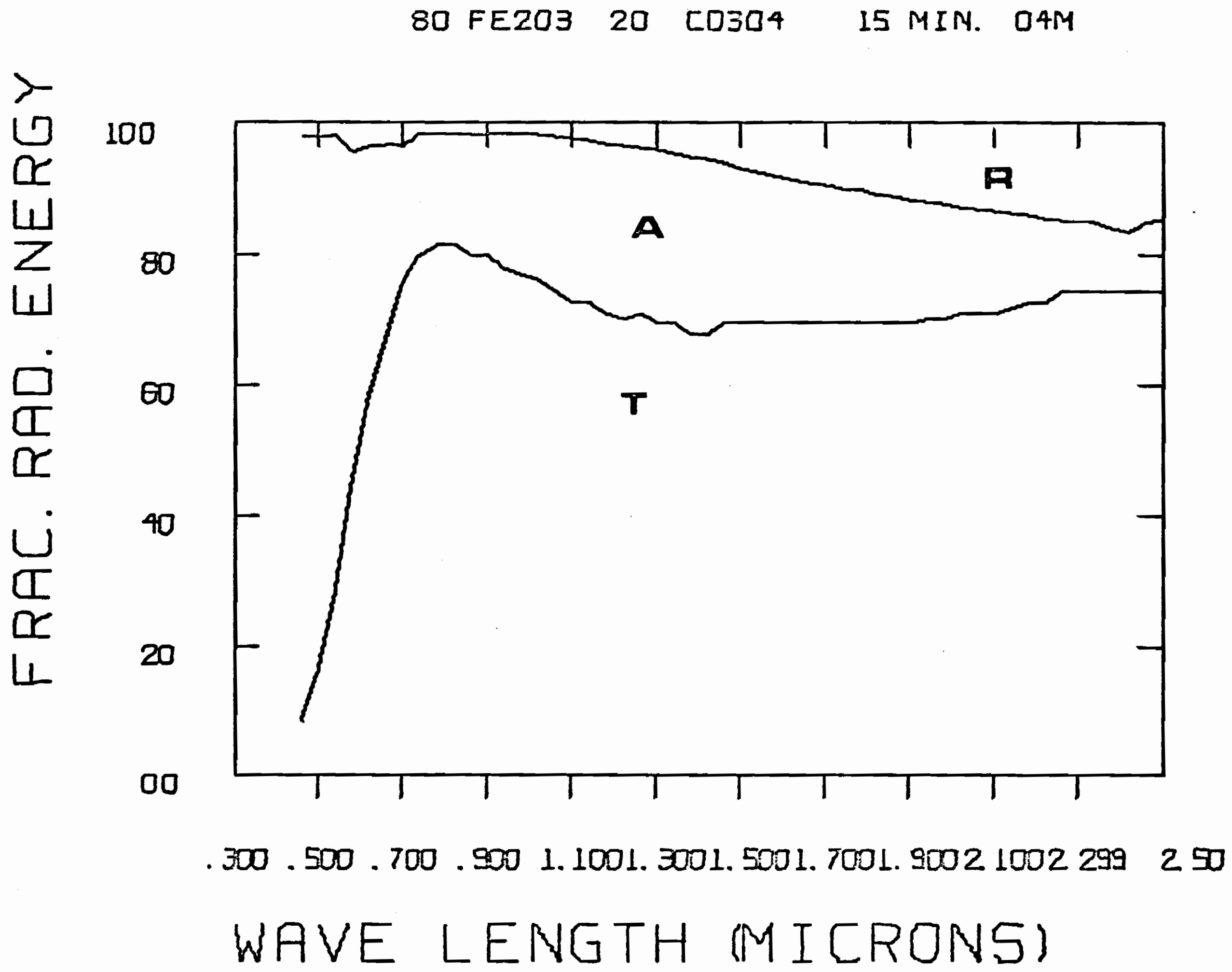

Figure D-37. Optical Properties of 80% Fe_2O_3-20% Co_3O_4 Sprayed with Air 15 Min.

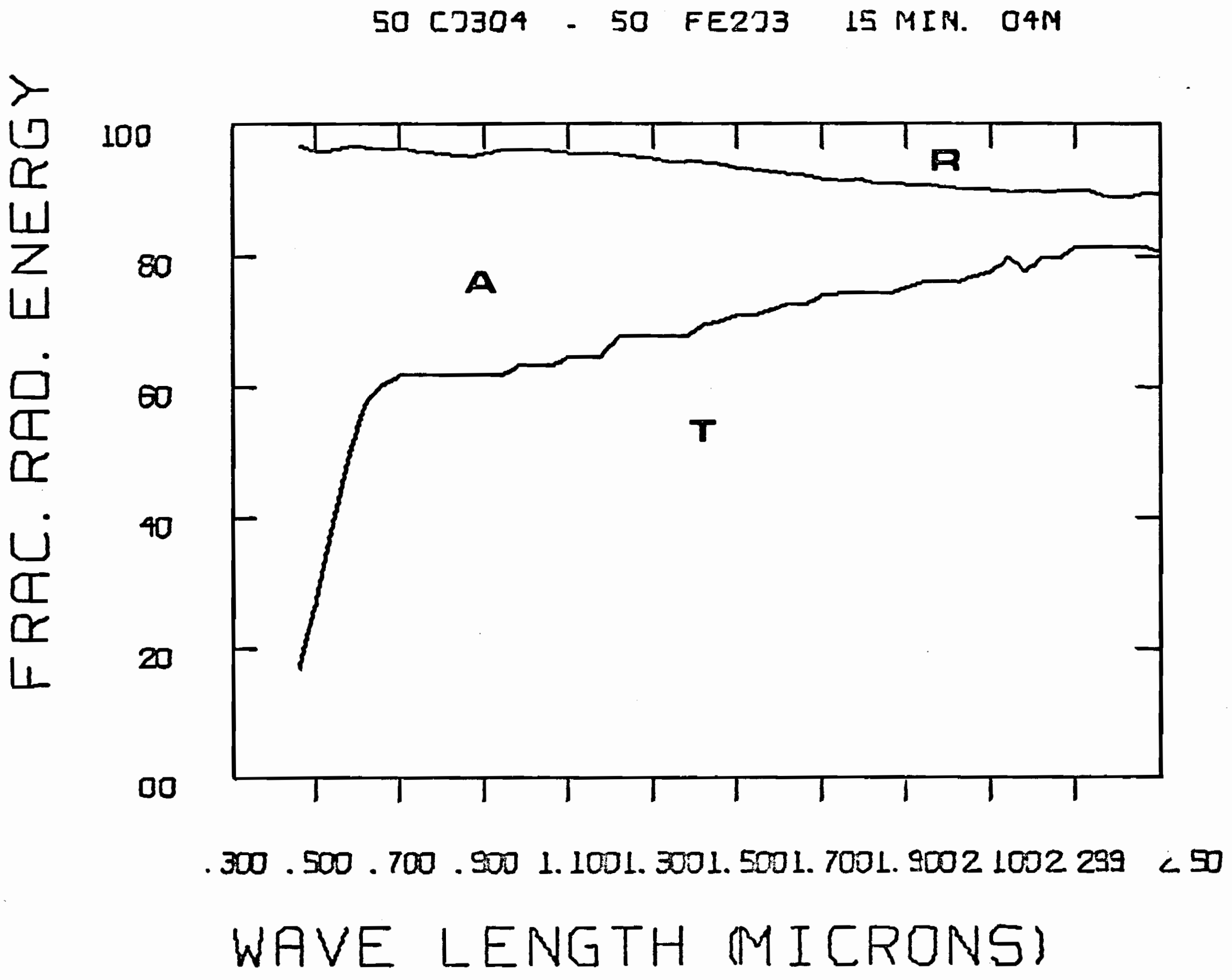

Figure D-38. Optical Properties of 50% Co_3O_4-50% Fe_2O_3.

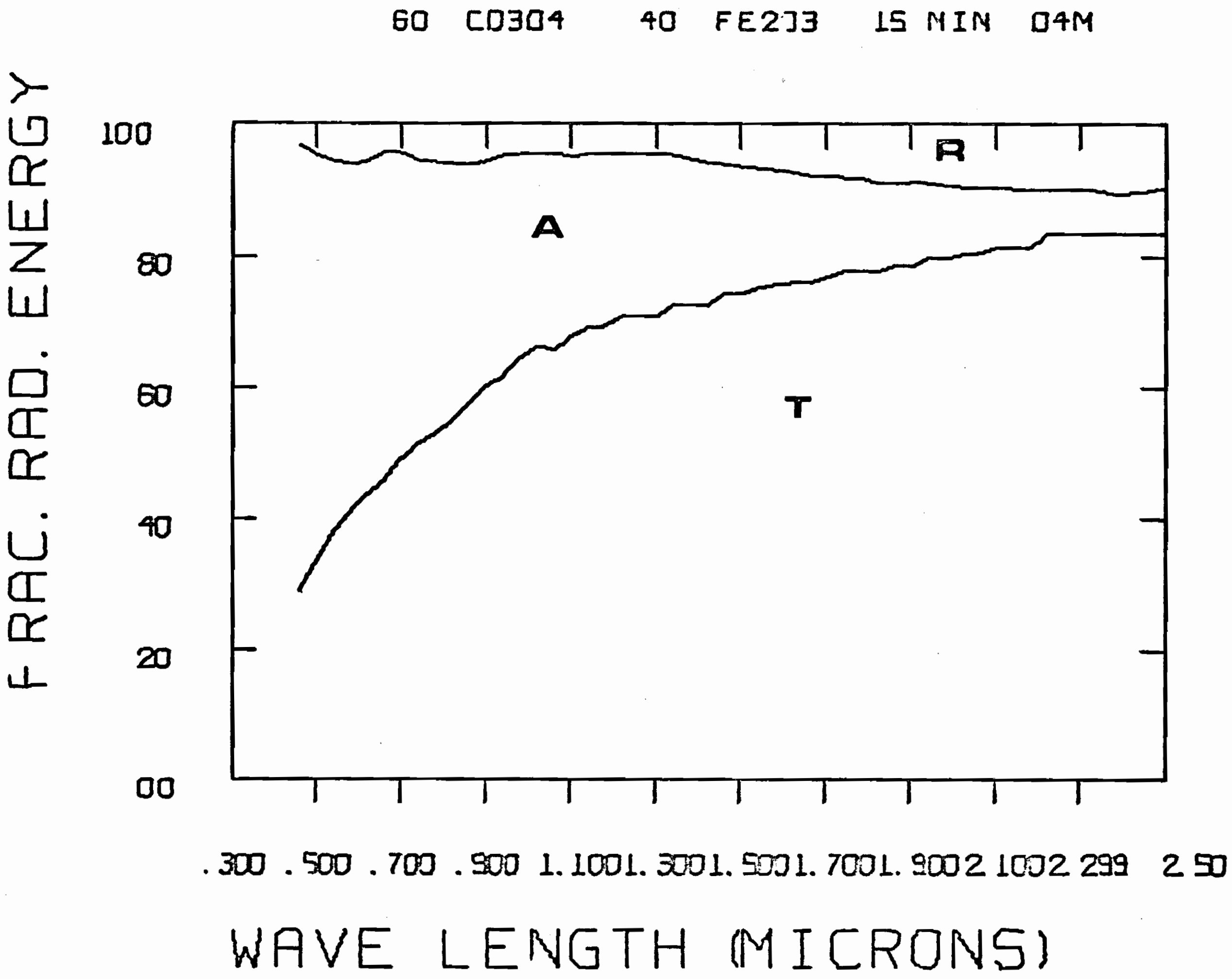

Figure D-39. Optical Properties of 60% Co_3O_4-40% Fe_2O_3.

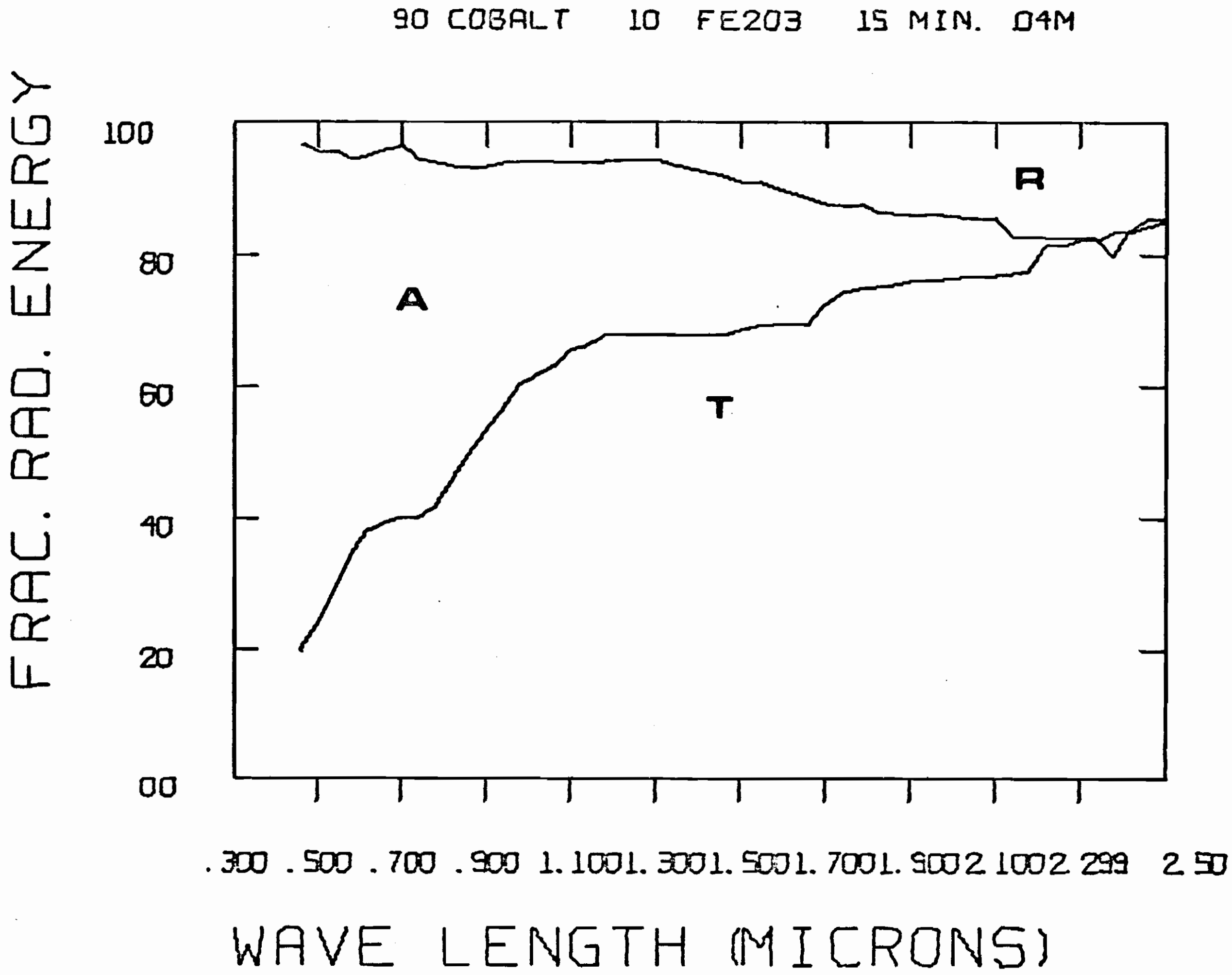

Figure D-40. Optical Properties of 90% Co_3O_4-10% Fe_2O_3.

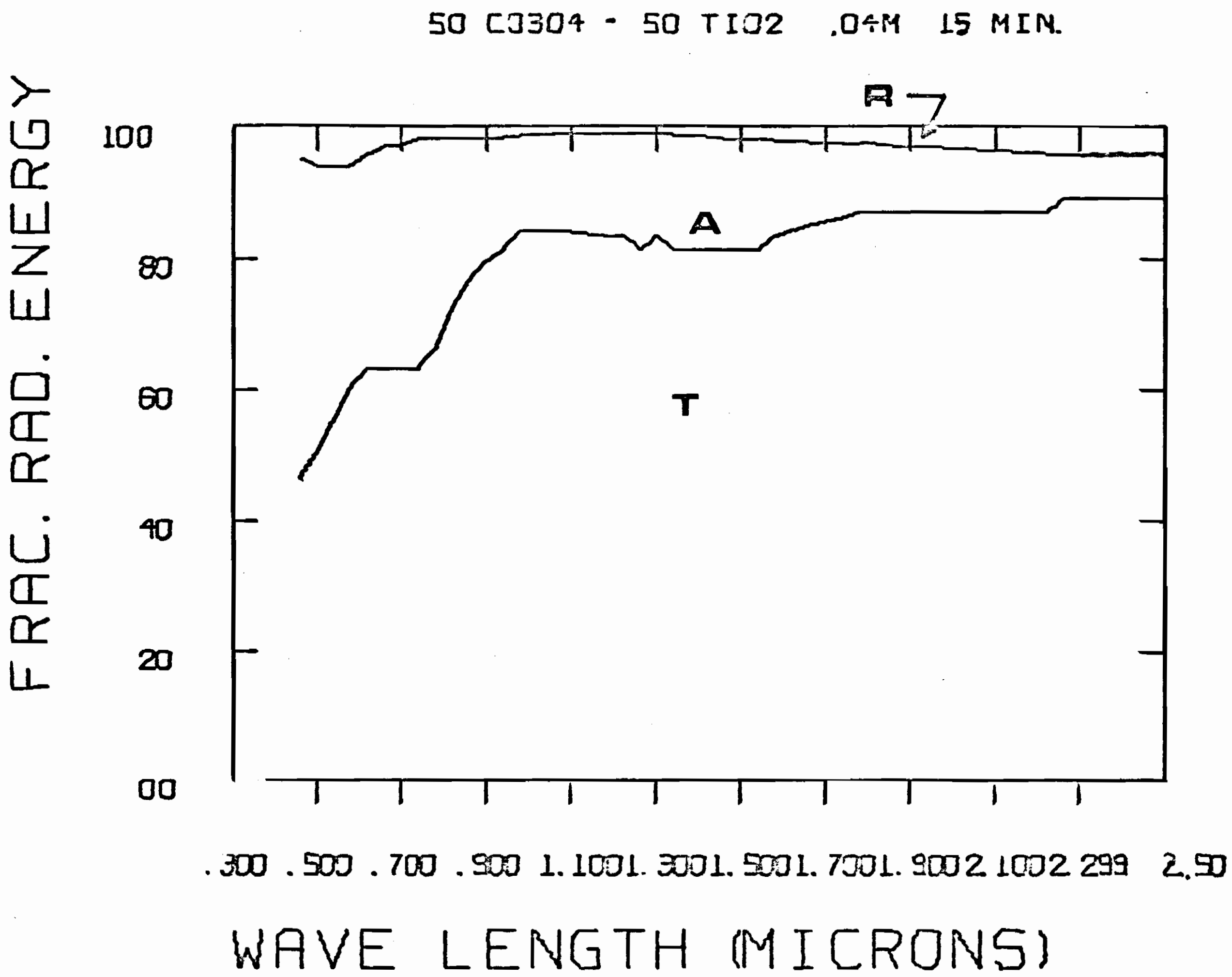

Figure D-42. Optical Properties of 50% Co_3O_4-50% TiO_2.

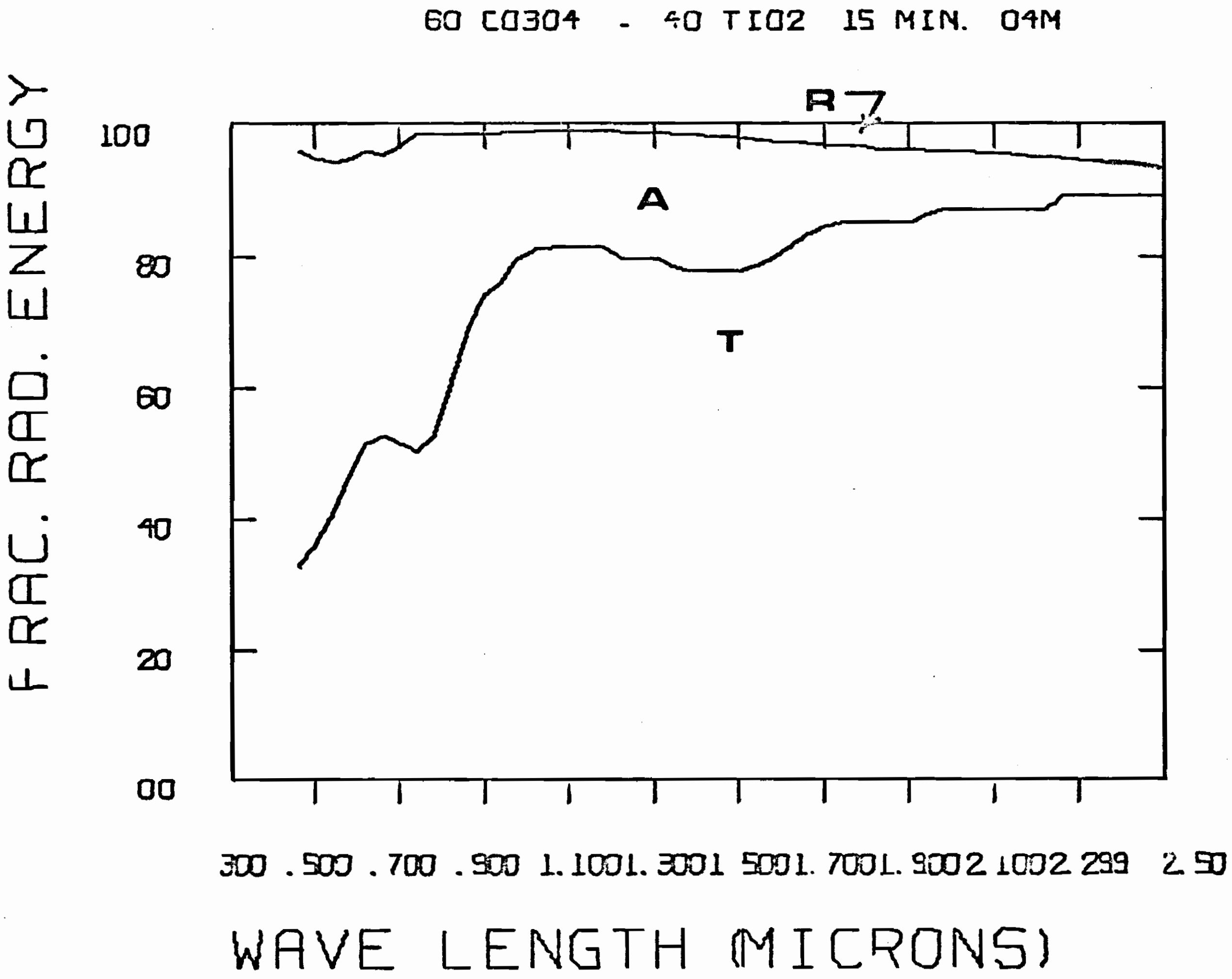

Figure D-43. Optical Properties of 60% Co_3O_4-40% TiO_2.

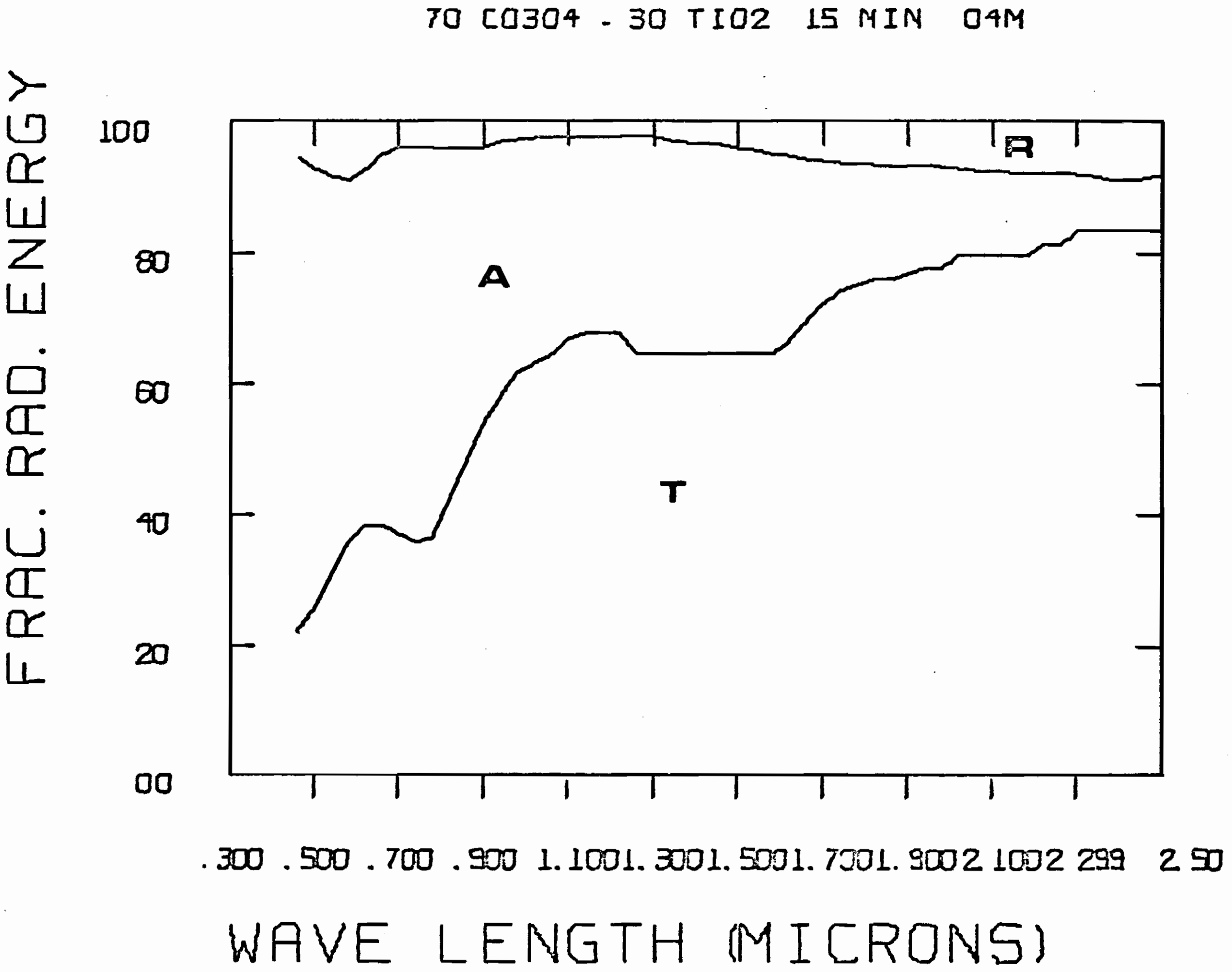

Figure D-44. Optical Properties of 70% Co_3O_4-30% TiO_2.

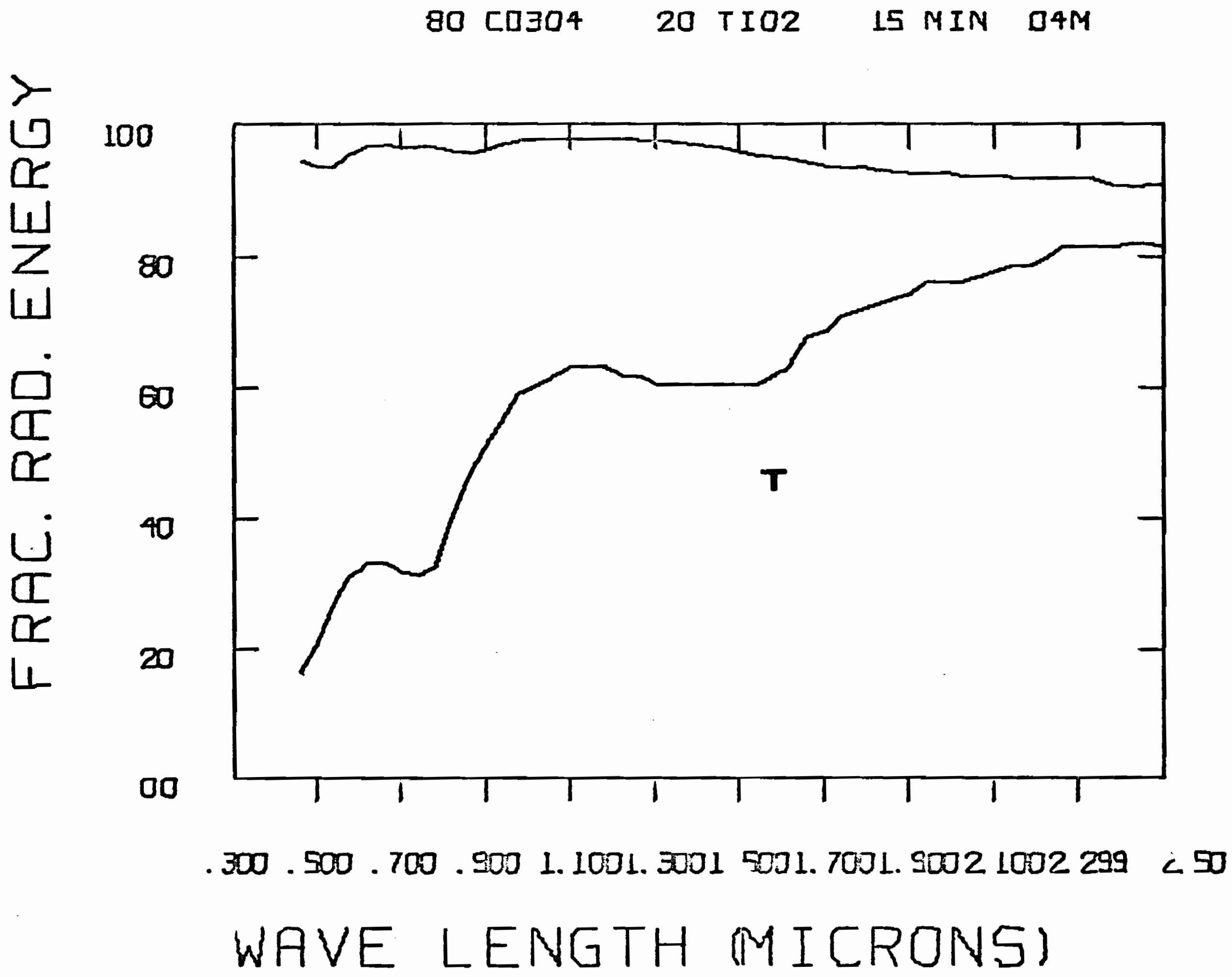

Figure D-45. Optical Properties of 80% Co_3O_4-20% TiO_2.

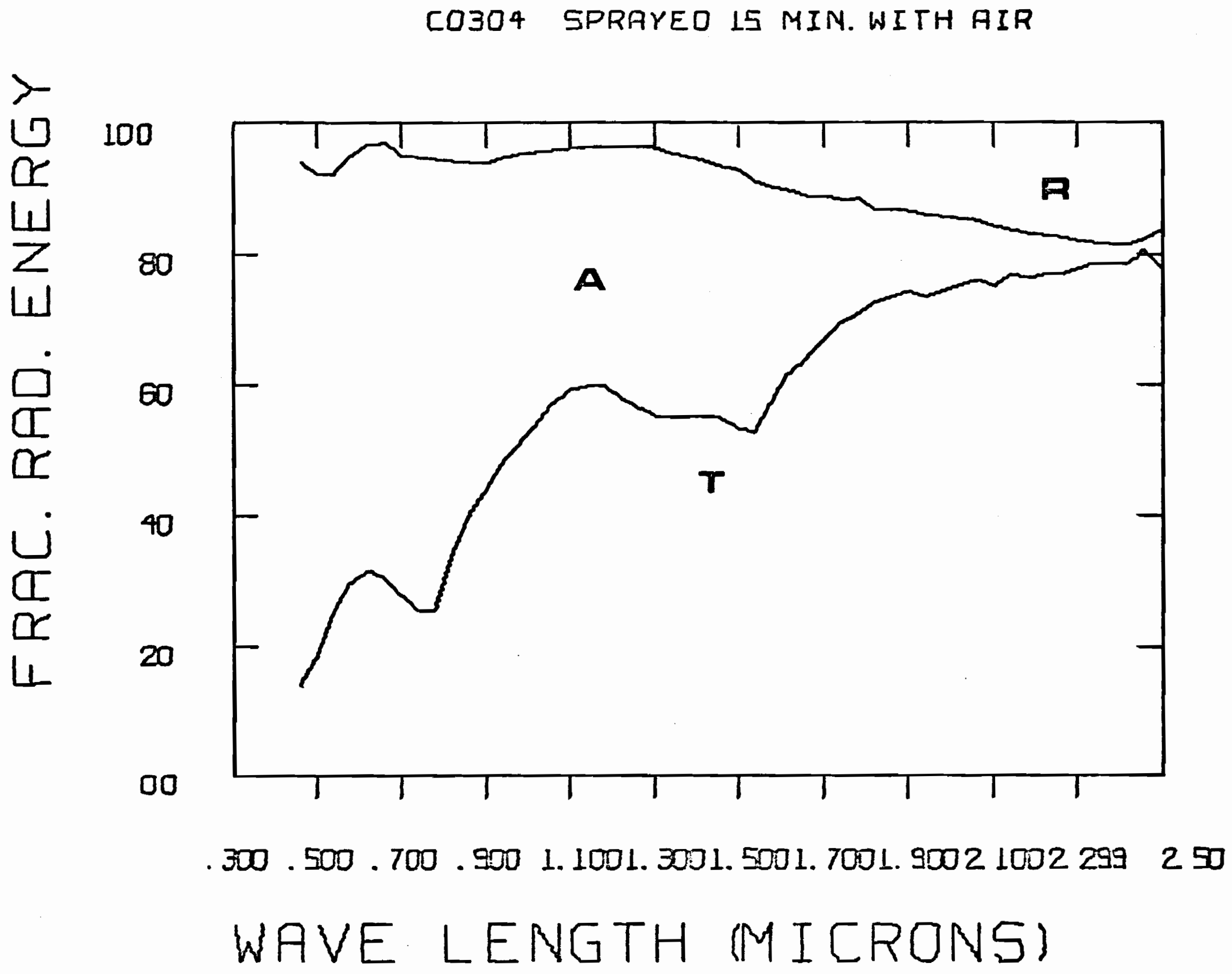

Figure D-46. Optical Properties of 100% Co_3O_4 Sprayed with Air 15 Min.

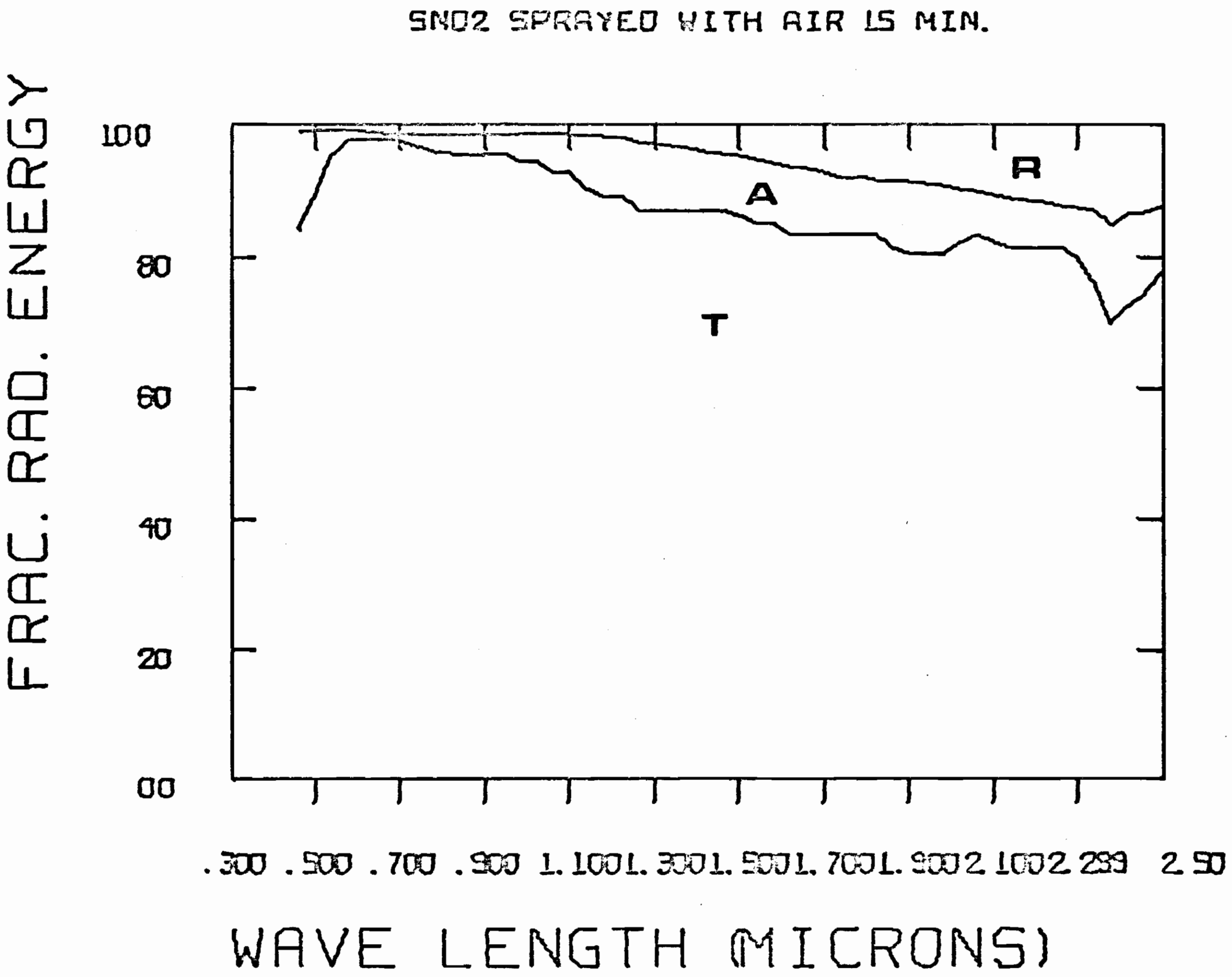

Figure D-47. Optical Properties of 100% SnO_2 Sprayed with Air 15 Min.

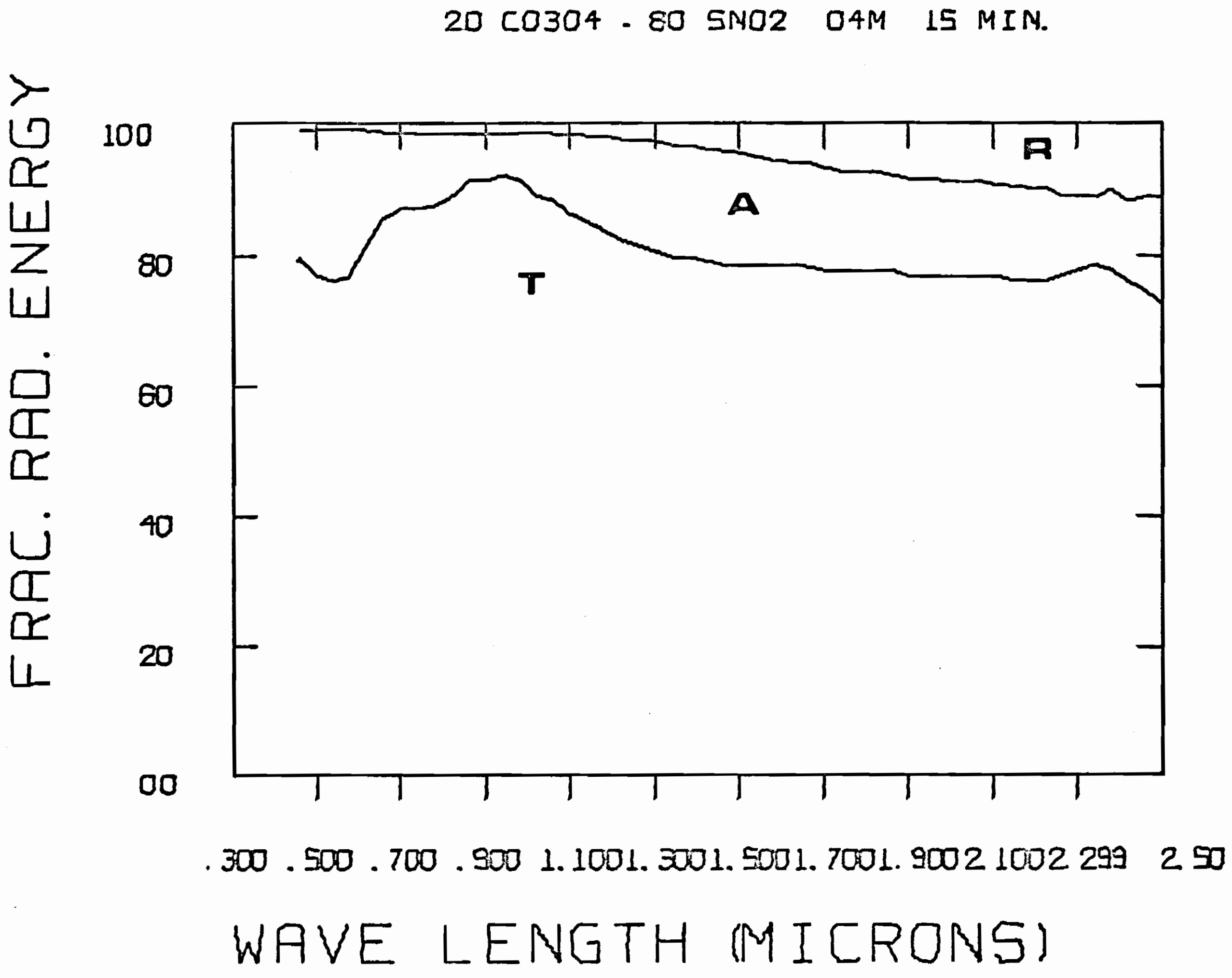

Figure D-48. Optical Properties of 20% Co_3O_4-80% SnO_2.

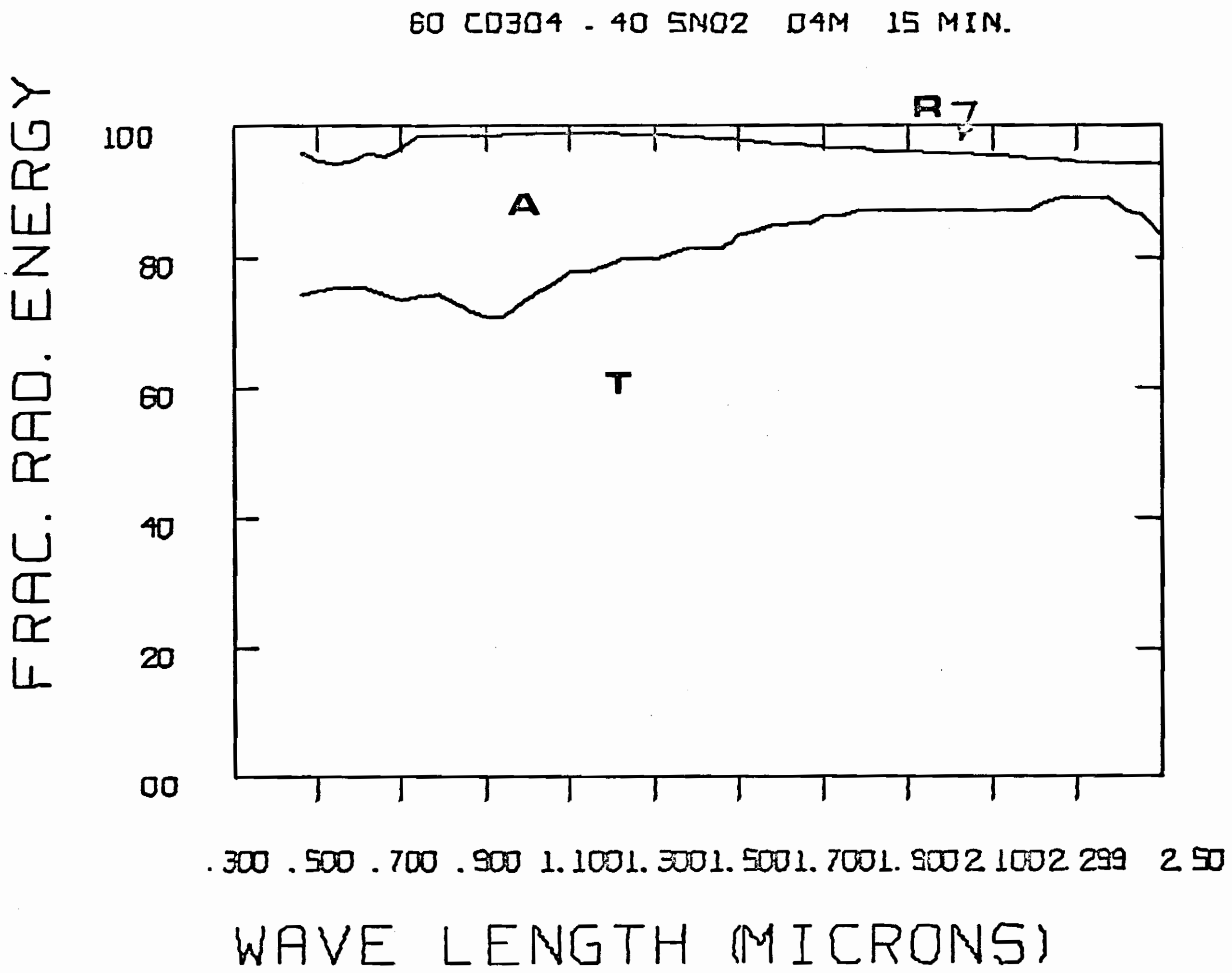

Figure D-49. Optical Properties of 60% Co_3O_4-40% SnO_2.

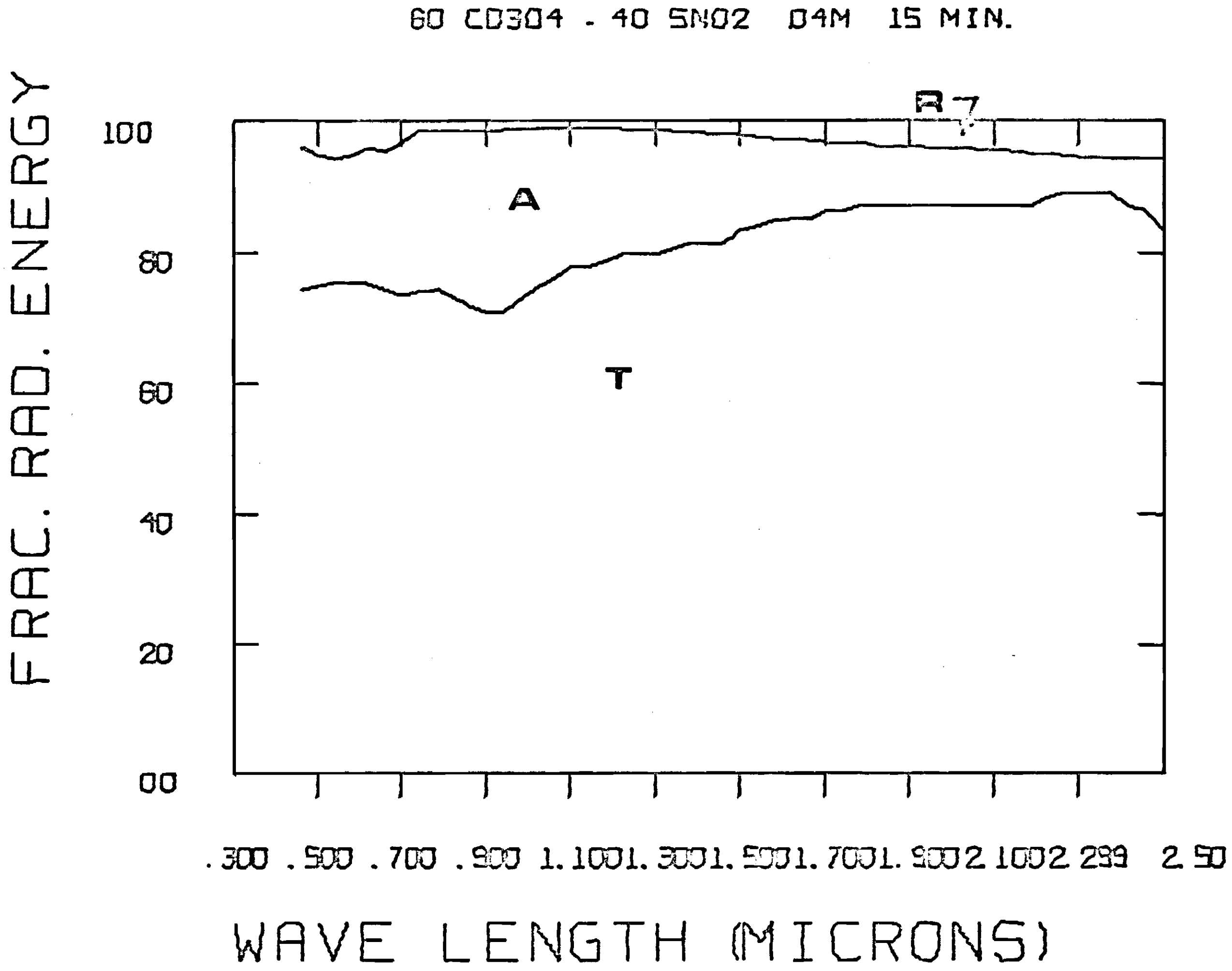

Figure D-49. Optical Properties of 60% Co_3O_4-40% SnO_2.

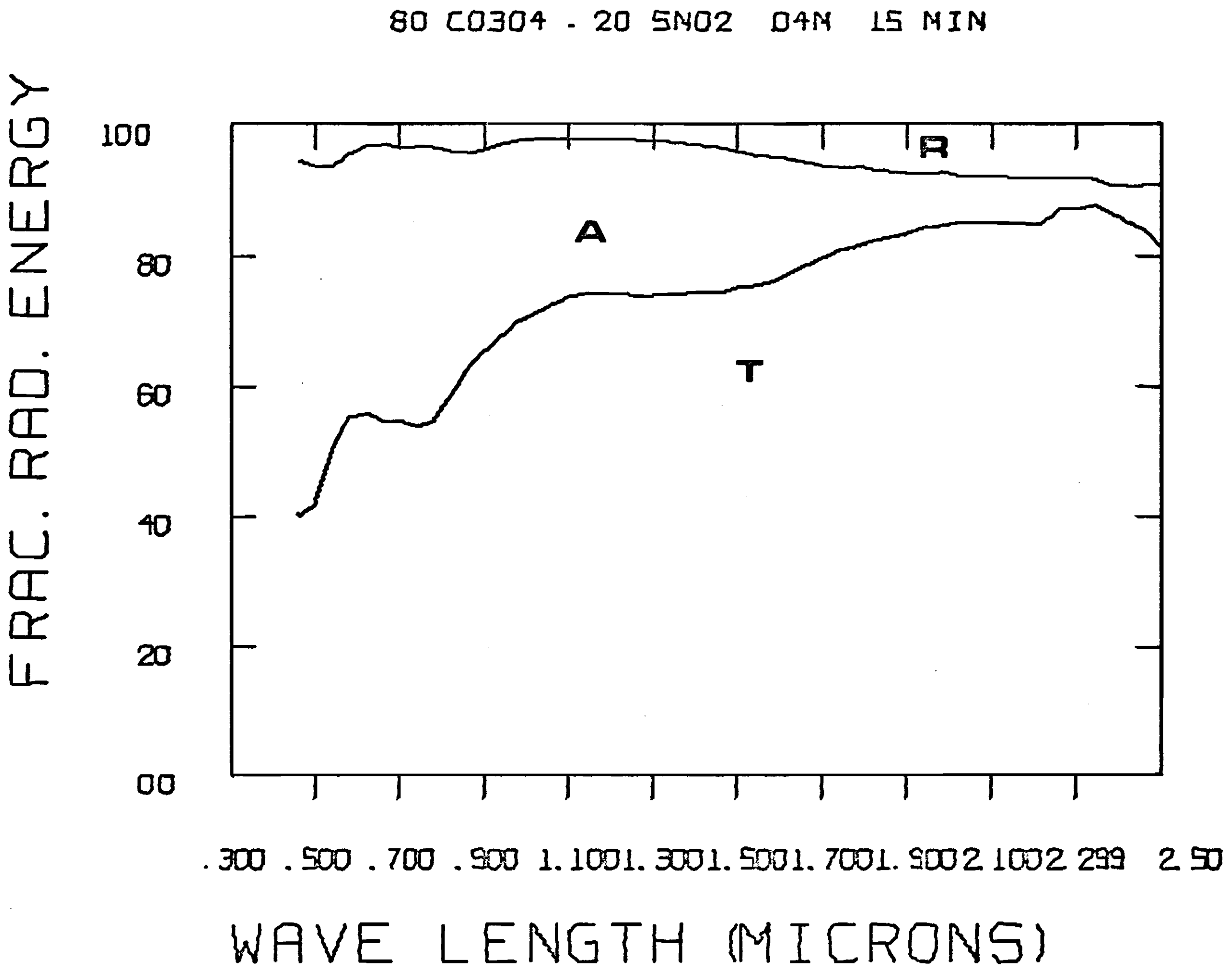

Figure D-50. Optical Properties of 80% Co_3O_4-20% SnO_2.

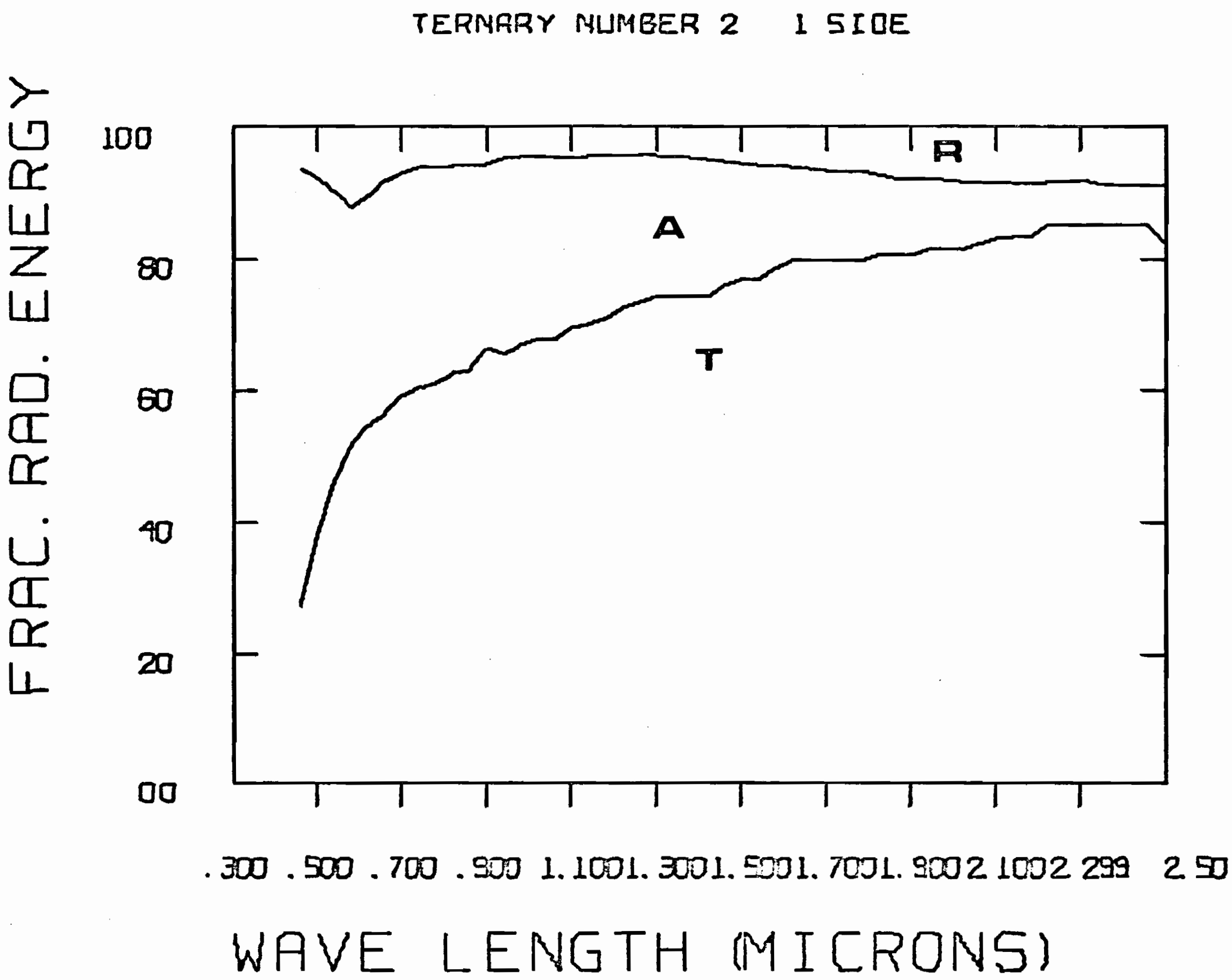

Figure D-51. Optical Properties of 45% Fe_2O_3-48%Co_3O_4-7% TiO_2.

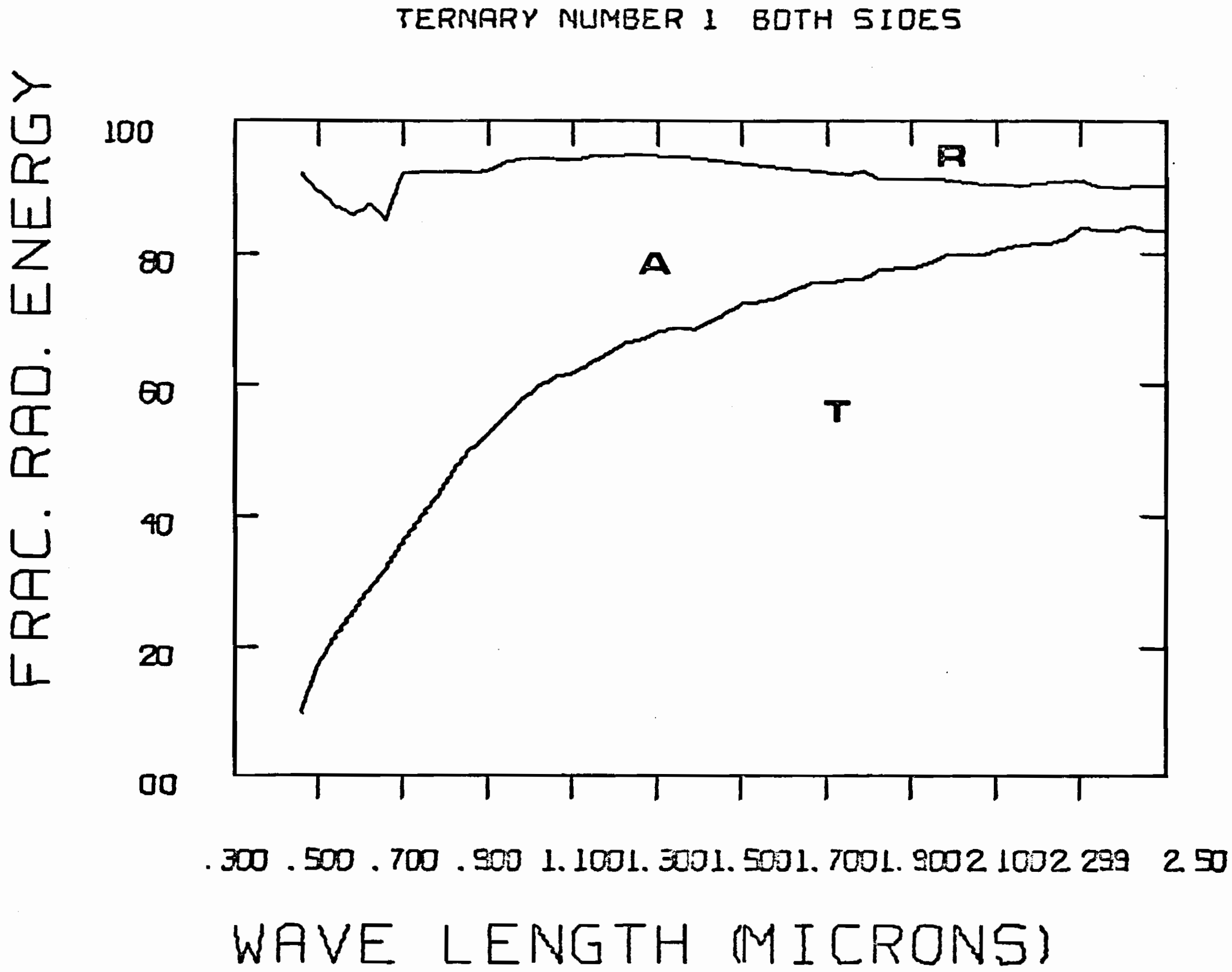

Figure D-52. Optical Properties of 30% Fe_2O_3- 55% Co_3O_4- 15% TiO_2.

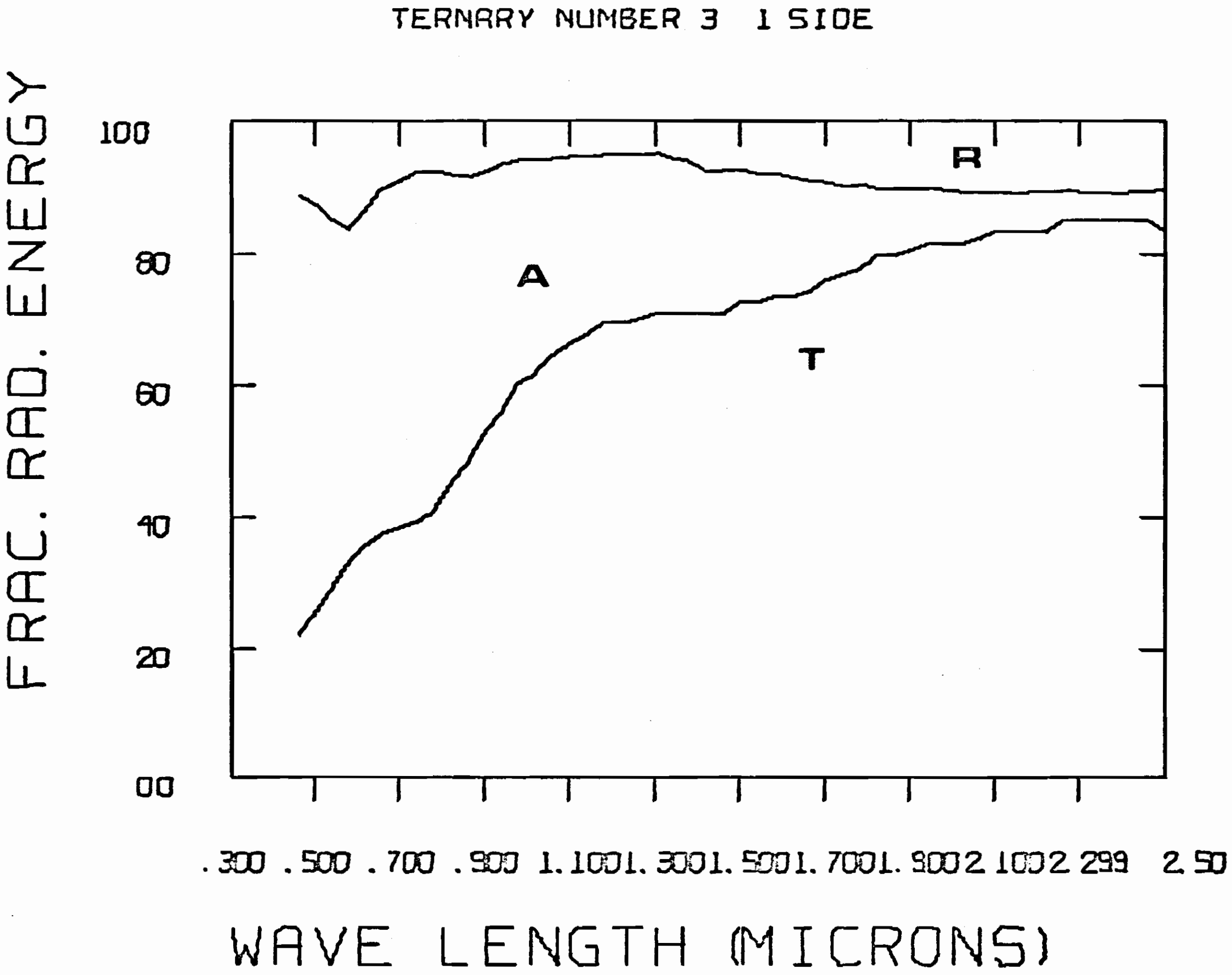

Figure D-53. Optical Properties of 15% Fe_2O_3 - 62% Co_3O_4- 23% TiO_2

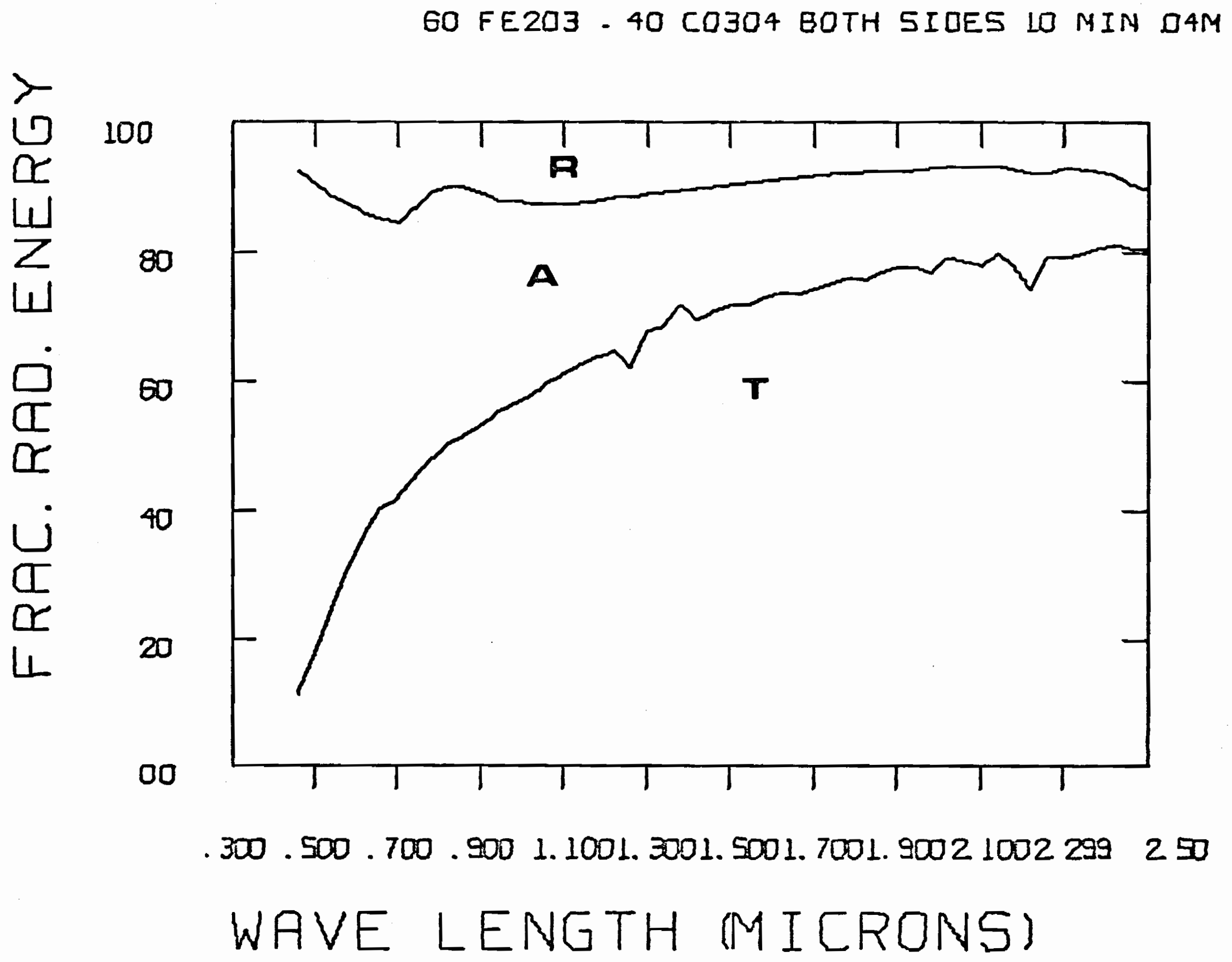

Figure D-54. Optical Properties of 60% Fe_2O_3-40% Co_3O_4.

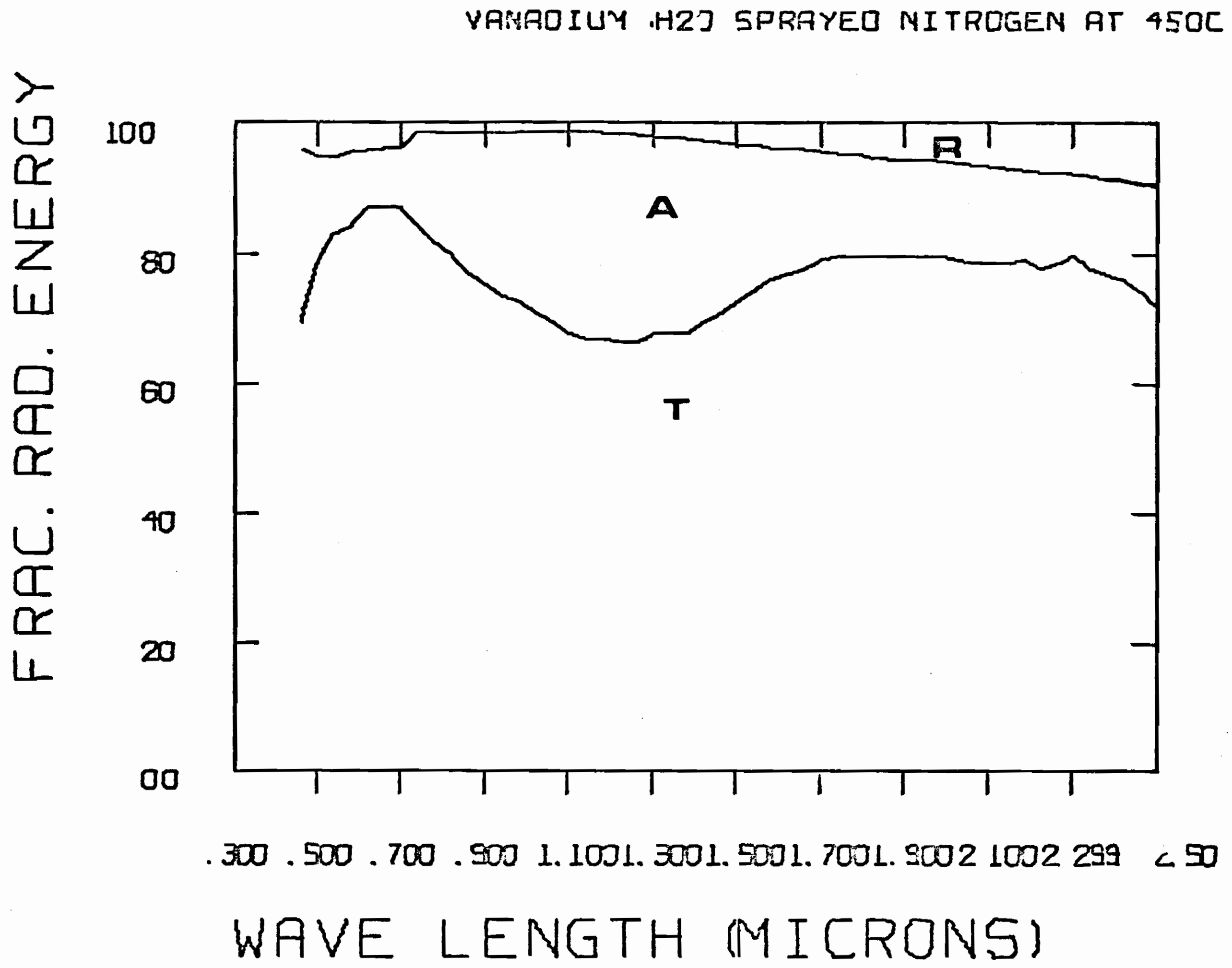

Figure D-55. Optical Properties of VO_xH_y Sprayed with Nitrogen at 450^oC Plus Water.

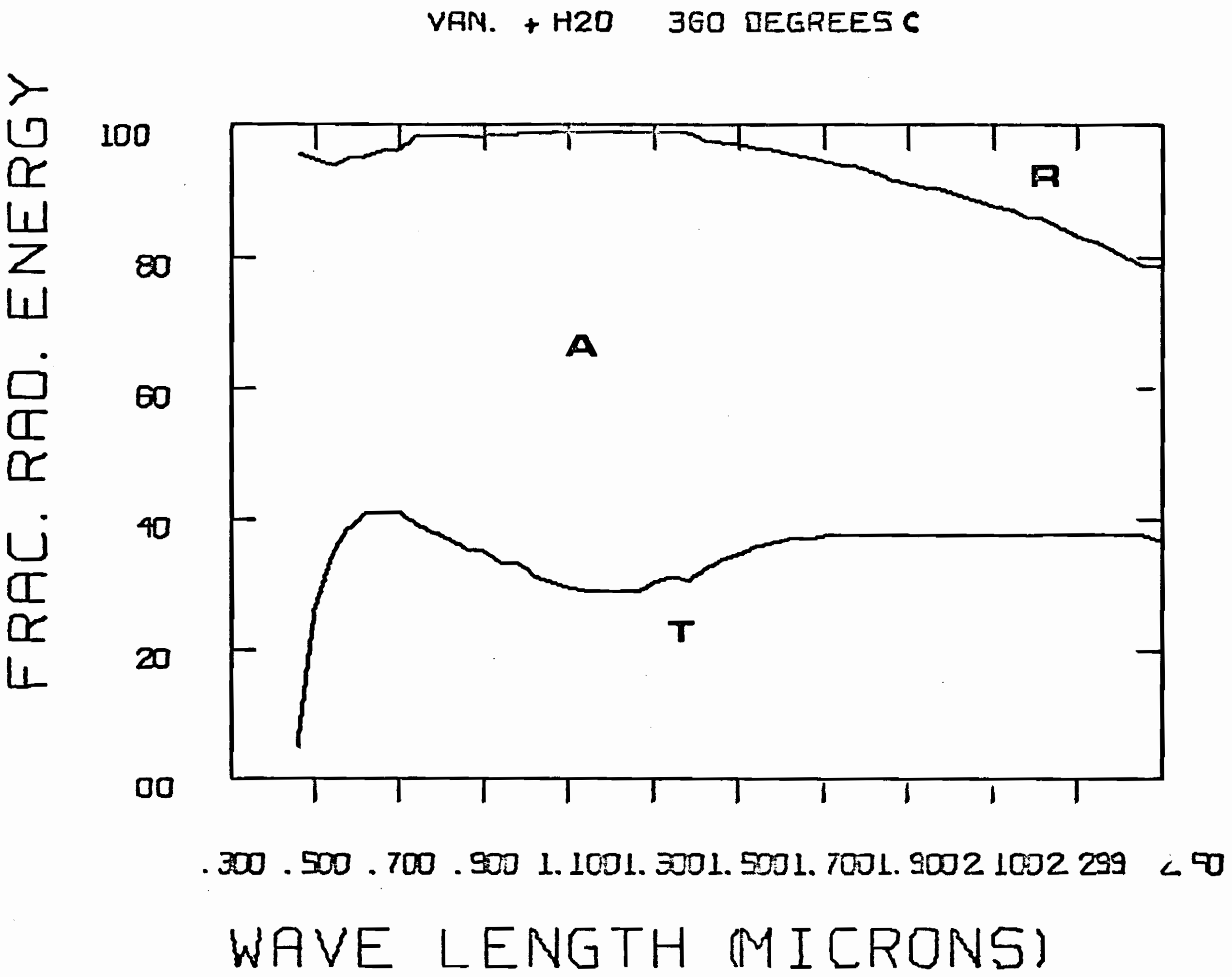

Figure D-56. Optical Properties of VO_xH_y Sprayed with Air and Water 360°C.

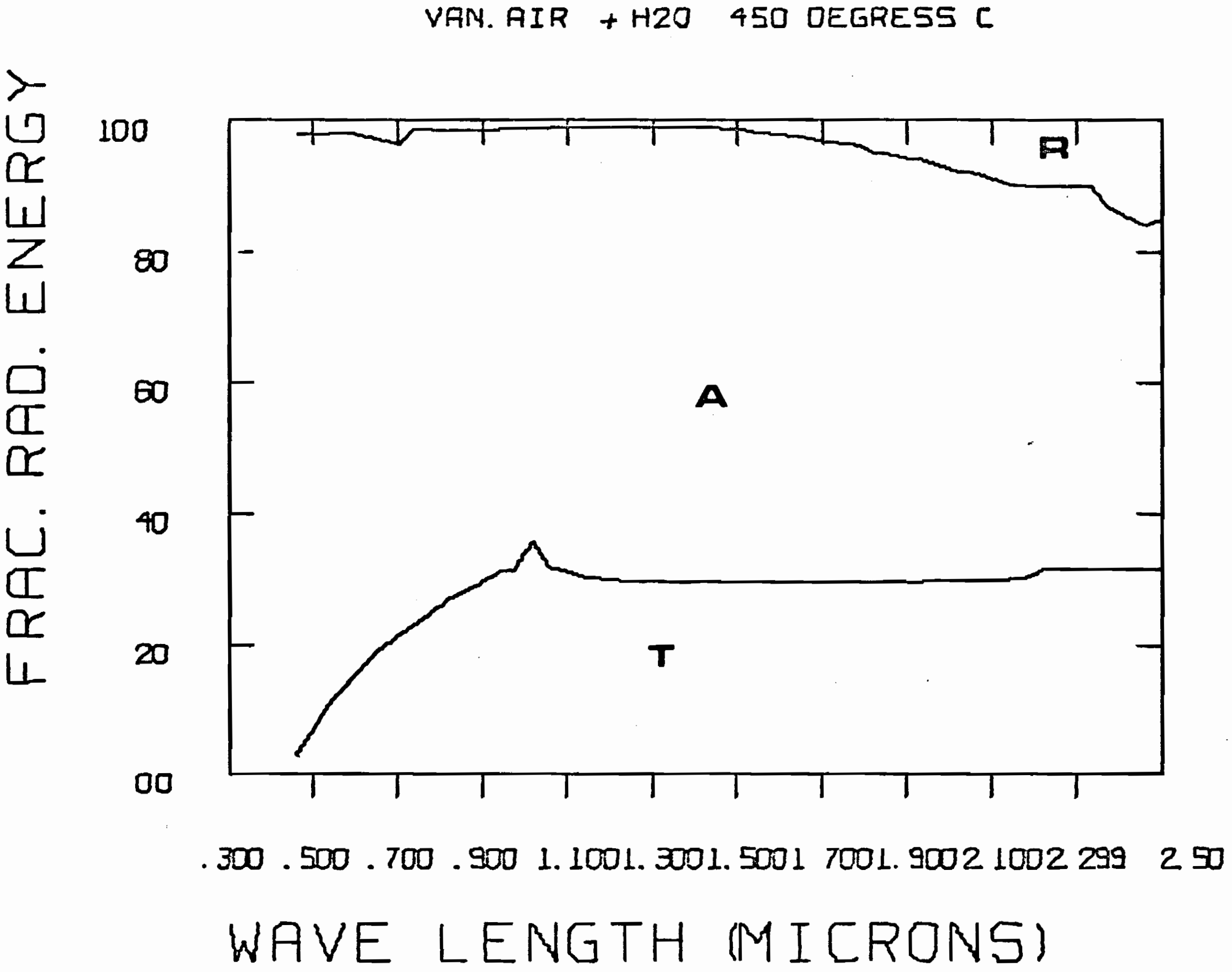

Figure D-57. Optical Properties of VO_xH_y Sprayed with Air and Water at 450°C.

APPENDIX E

Resistance vs $\frac{1}{T}$ for Selected Oxides

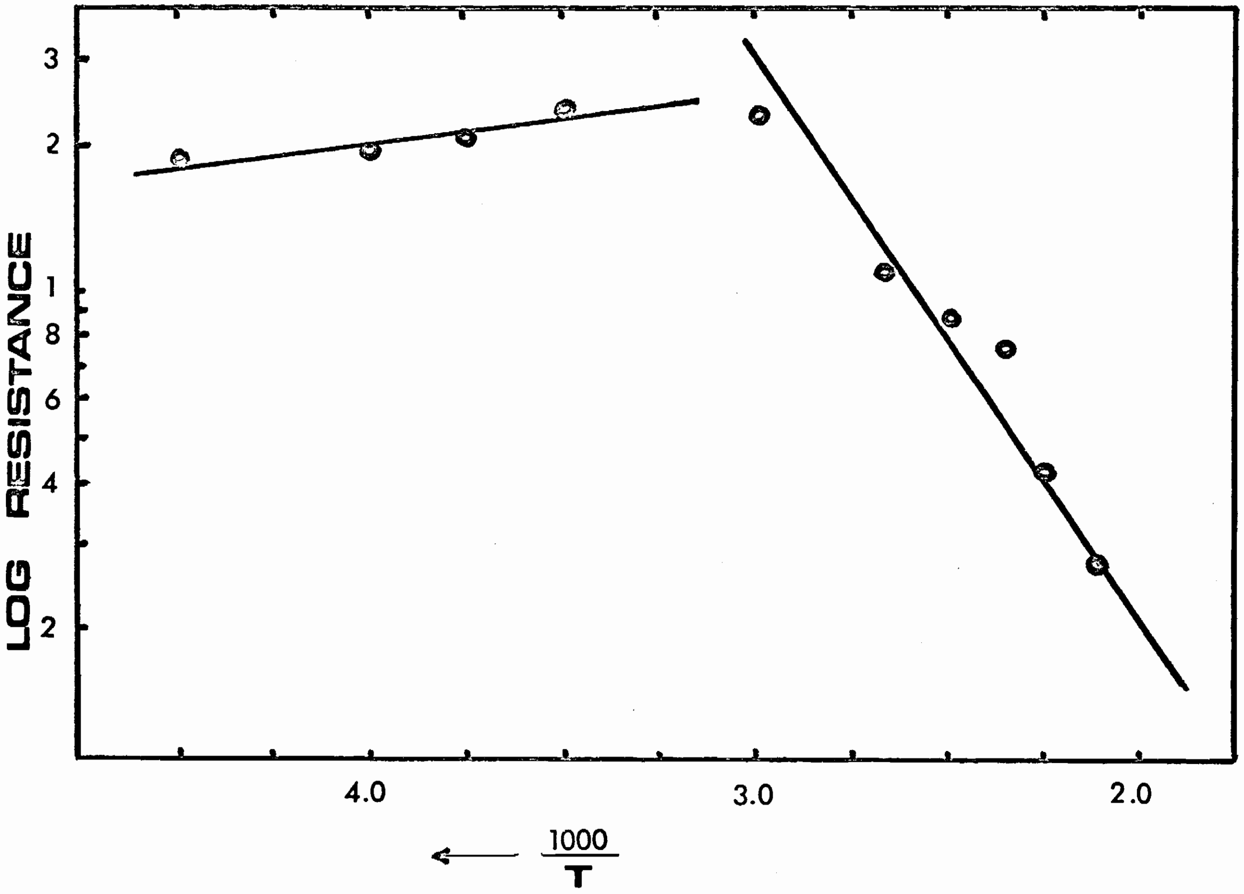

Figure 1-E. Log Resistance as a Function of Temperature for a VO_xH_y Film Sprayed with Nitrogen.

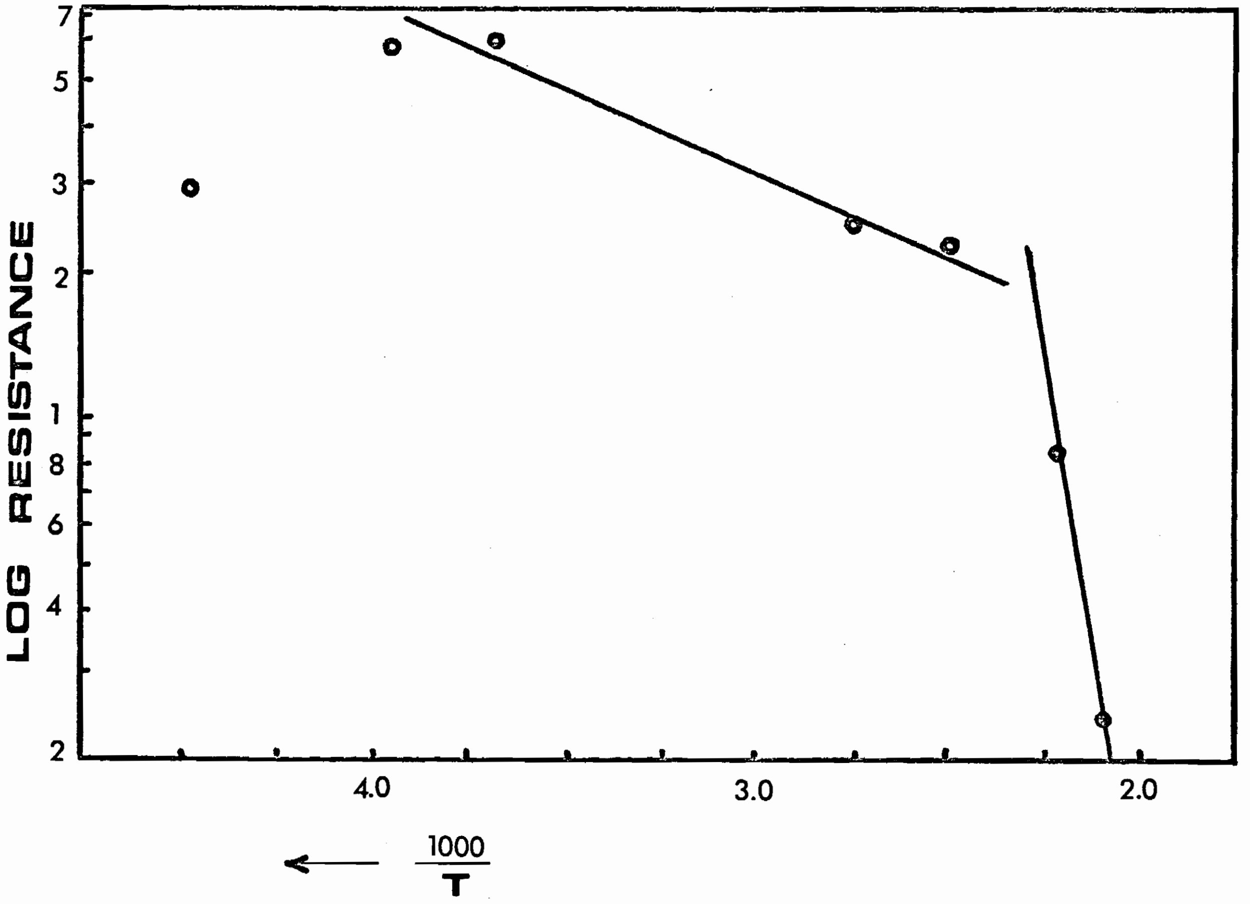

Figure 2-E. Log Resistance as a Function of Temperature for a Co_3O_4 Film Sprayed with Air.

VITA

The author, Thomas R. Viverito, was born in Niagara Falls, New York on September 16, 1951. He attended the elementary and secondary schools in Niagara Falls and graduated from Niagara Falls High School in June 1969.

From the fall of 1969 through the spring of 1973, the author attended and graduated with a Bachelor of Science Degree in Ceramic Engineering from the New York State College of Ceramics at Alfred University in Alfred, New York.

In the summer of 1973 he was employed by the Carborundum Company in Niagara Falls as a member of their Technical Service Group, Refractories and Electronics Division.

He then entered Virginia Polytechnic Institute and State University in the fall of 1973 to begin study leading to a Master of Science Degree in Ceramic Engineering

Thomas R. Viverito

Thomas R. Viverito

SOLAR RADIATION CONTROL BY PYROLYTIC OXIDE THIN FILMS

by

Thomas R. Viverito

(ABSTRACT)

The growing concern for energy conservation is placing many new demands on materials, especially oxide thin films. A few of these new applications include solar collectors, solar reflectors and thermal transparent insulation. The engineer must fully understand how oxide thin films optically behave and what mechanisms govern this behavior before utilizing them for these new applications. Only when oxide thin films are fully understood, will they be used to their potential.

This thesis probes into the basic mechanisms governing the optical properties of oxide thin films. Thin films are complex and their behaviors do not always correspond to those of bulk oxides. Absorption in the oxide films studied is due to electronic excitations and it is also found to be dependent upon crystallinity; the more crystalline films being more absorbing. It was determined that absorbance is related to the semiconducting behavior of the oxides. Absorbance increases when conditions are reducing for n-type oxides and when conditions are oxidizing for p-type oxides. A maximum solar reflectance of 35% was obtained with a Co_3O_4 film that was annealed in $95\%N_2$-$5\%H_2$. Metals such as gold, exhibit higher solar reflectances than both the pure oxides and mixtures of Co_3O_4, Fe_2O_3, SnO_2, TiO_2 and VO_xH_y.

However, configurational designs utilizing the oxide films properties to their greatest advantage could selectively screen solar and thermal energy effectively.